atoms

Interaction of Ionizing Photons with Atomic and Molecular Ions

Edited by
Eugene T. Kennedy, John T Costello and Jean-Paul Mosnier

Printed Edition of the Special Issue Published in *Atoms*

www.mdpi.com/journal/atoms

MDPI

Interaction of Ionizing Photons with Atomic and Molecular Ions

Interaction of Ionizing Photons with Atomic and Molecular Ions

Editors

Eugene T. Kennedy
John T Costello
Jean-Paul Mosnier

MDPI • Basel • Beijing • Wuhan • Barcelona • Belgrade • Manchester • Tokyo • Cluj • Tianjin

Editors

Eugene T. Kennedy
Dublin City University
Ireland

John T Costello
Dublin City University
Ireland

Jean-Paul Mosnier
Dublin City University
Ireland

Editorial Office
MDPI
St. Alban-Anlage 66
4052 Basel, Switzerland

This is a reprint of articles from the Special Issue published online in the open access journal *Atoms* (ISSN 2218-2004) (available at: https://www.mdpi.com/journal/atoms/special_issues/atom_ions).

For citation purposes, cite each article independently as indicated on the article page online and as indicated below:

LastName, A.A.; LastName, B.B.; LastName, C.C. Article Title. *Journal Name* **Year**, *Volume Number*, Page Range.

ISBN 978-3-0365-2430-6 (Hbk)
ISBN 978-3-0365-2431-3 (PDF)

Contents

About the Editors

Eugene T. Kennedy Kennedy is Emeritus Professor of Physics at Dublin City University and a member of the National Centre for Plasma Science and Technology. He was elected Fellow of the Institute of Physics in 1987 and member of the Royal Irish Academy in 2004. He has published exensively on short-wavelength light source developments, plasma diagnostics and the interaction of ionizing photons with atomic and molecular ions. He has served on national and international research bodies, coordinated EU research networks and been an invited researcher at NIST (Wash. DC), HASYLAB and FLASH (DESY Hamburg), LURE and SOLEIL (Paris) and the ALS (Berkeley).

John T Costello is Professor of Physics, former Dean of the Faculty of Science and Health at Dublin City University and a member of the National Centre for Plasma Science and Technology. His research interests lie mainly in intense laser–matter interactions with a special interest in photoionisation processes, most recently in EUV and X-ray Free Electron Laser (FEL) fields. He has served or is serving on editorial boards, advisory boards of international conferences, Institute of Physics committees and the Irish Government Task Force for the Physical Sciences. He is a Fellow of the Institute of Physics and a recipient of the DCU President's Research Award.

Jean-Paul Mosnier holds a faculty position in the School of Physical Sciences at Dublin City University since 1987 and is a member of the National Centre for Plasma Science and Technology. He is currently an Associate Professor and Head of School. He is a member of the Institute of Physics and a Chartered Physicist. His main research interests lie in the areas of atomic and molecular structure and photoionisation dynamics, UV laser ablation and application to pulsed laser deposition, cold plasma applications and astrochemistry and CH^+. He has published extensively in all of these areas.

Preface to "Interaction of Ionizing Photons with Atomic and Molecular Ions"

The interaction of photons with atoms and ions is a fundamental process in nature. Studies of photoionization provide information on the inverse processes of radiative and dielectronic recombination, which is important in many laboratory and astrophysical plasmas. Problems in upper atmospheric physics and chemistry, as well as new astrophysical observations extending into the X-ray region, require laboratory-based experiments to produce key interpretative data. Laser-produced plasmas, High Harmonic Generation, synchrotron and FEL short wavelength sources provide complementary capabilities and new theoretical approaches help us interpret the wide spectrum of results on atomic ions are achievable with these light sources. Studies of the photoionization of molecular ions have been initiated and are expected to become of increasing importance in the future.

This Special Issue book includes original and review papers over the broad range of photoionization studies achievable with atomic and molecular ions, including experiments on relative and/or absolute cross-sections, linear and nonlinear behaviors, new instrumental developments, and current theoretical challenges. Papers describing experimental and theoretical physics insights obtained with laser plasma, synchrotron and short wavelength Free Electron Laser facilities are included.

Eugene T. Kennedy, John T Costello, Jean-Paul Mosnier
Editors

atoms

MDPI

Editorial

Special Issue "Interaction of Ionizing Photons with Atomic and Molecular Ions"

Eugene T. Kennedy *, John T. Costello and Jean-Paul Mosnier

National Centre for Plasma Science and Technology (NCPST), School of Physical Sciences, Dublin City University, D09 V209 Dublin, Ireland; john.costello@dcu.ie (J.T.C.); jean-paul.mosnier@dcu.ie (J.-P.M.)
* Correspondence: eugene.kennedy@dcu.ie

Citation: Kennedy, E.T.; Costello, J.T.; Mosnier, J.-P. Special Issue "Interaction of Ionizing Photons with Atomic and Molecular Ions". *Atoms* **2021**, *9*, 111. https://doi.org/10.3390/atoms9040111

Received: 8 December 2021
Accepted: 9 December 2021
Published: 13 December 2021

The interaction of ionizing photons with atoms or ions is a fundamental process in nature, with laboratory, atmospheric and astrophysical implications. Much of the matter in the universe is in the ionized state and so the results of theoretical and experimental investigations of photoionization of ions are key for the understanding of a wide range of phenomena.

Atomic ions provide an ideal testing ground for the study of the interaction of photons with a many-body system as ions are perfectly reproducible and the basic inter-particle interactions are well known. Systematic studies along isoelectronic and/or isonuclear sequences provide flexibility in experimental and theoretical efforts. Photons in the vacuum ultraviolet, extreme ultraviolet and X-ray regimes can have sufficient energy to excite inner-shell electrons or more than one electron at a time. Hence the study of the photon-ion interactions provides considerable insight into how the complex many-body correlation aspects of the processes can be understood and quantified. Where molecular ions are concerned the experimental and theoretical challenges are even more daunting and it is only in recent years that substantial progress is being made.

The study of ionizing photon-ion interactions in the laboratory requires sources of short wavelength to provide the necessary high-energy photons. In the well-known book "From X-rays to Quarks" by Emile Segré (Nobel Prize winner in 1959) he states on Page 275 "In the 1920s we used to joke that good physicists, once passed to their heavenly rewards, would find apparatus in paradise which, with a twist of some knobs, would give electromagnetic radiation of any desired frequency, intensity, polarization, and direction of propagation".

Developments in short wavelength sources over the last few decades, are coming ever closer to realizing such a "heaven on earth", as far as science at short wavelengths is concerned! For example, photon sources such as laser plasmas, high harmonic generation, synchrotrons and now short wavelength Free Electron Lasers (FELs), are currently available to allow the interaction of ionizing photons with matter to be studied on widely varying photon energy, spatial and time scales. The exploitation of the new source capabilities has required innovative detector solutions. To guide and understand experiments, a concomitant development in theoretical modeling of their complex many-body nature is required.

In the book "Interactions of Ionizing Photons with Atomic and Molecular Ions", based on the proceedings of a Special Issue [1], papers are included which show a variety of recent developments in theory and experiment.

The first of five theoretical papers, written by Gryzlova et al. [2], investigates the photoionization of krypton by intense femtosecond duration pulses, for photon energies (50–80 eV) which lie below the 3d excitation threshold. Sequential ionization processes and results on the time evolution of the 4s and 4p valence shells of Kr and its ions (Kr^+, Kr^{2+} and Kr^{3+}) are described together with the resulting photoelectron spectra. The theoretical approach based on R-matrix calculations uses rate equations with photoionization cross sections in different charge and multiplet states. The study is a precursor to calculations for

higher photon energies where the 3d excitation channel is open and Auger decay makes the dynamics more complex.

Experiments with FELs are often multi-shot in character, where the target systems interact with FEL short wavelength pulses differing from each other in random ways, due to the fact that the individual pulses build up from SASE (Self-Amplified-Spontaneous-Emission) processes. Katravulapally and Nikolopoulos [3] treat the effects of the FEL fluctuations for the special case of the 2s2p Li^+ autoionization lineshape. They employ a perturbative statistical description of the atomic dynamics to investigate the effects of parameters such as peak-intensity, coherence time and pulse duration on the lineshape and the ionization yield.

Hofbrucker et al. [4] note that two-photon ionization is one of the most fundamental nonlinear processes in which two photons are simultaneously absorbed and an electron is emitted. They treat the problem of non-resonant two-photon ionization in magnesium and examine the energy dependence of the resulting photoelectron angular distributions and in particular the angular distribution near the nonlinear Cooper minimum.

Preliminary insights into angle-dependent and angle-integrated spin-polarized photoelectron fluxes, from fullerene anions, are presented by Dolmatov [5]. The characteristics of the phenomenon are discussed within the framework of a simplified semi-empirical methodology where the C_{60} cage is modeled by a spherical annular potential. The key result is that photodetachment of fullerene anions may produce highly spin-polarized photoelectrons.

The final theoretical paper, by Gorczyca et al. [6], uses the R-matrix methodology to address inner-shell photodetachment of the negatively charged Na^- anion near the L-edge threshold. Significant structures are found in the cross section, which are compared to experimental results. Many-body correlation effects are seen to be crucial to the behaviour of the photodetachment cross section.

Several papers deal with experiments carried out at synchrotron facilities on beamlines equipped to examine photon-ion interactions.

Photoelectron spectroscopy of ions remains challenging due to the low density of ion beams but offers advantages over ion yield experiments through the provision of partial photoionization cross sections. Penent et al. [7] describe improvements by a factor of ~20 to an existing cylindrical mirror analyzer, obtained by replacing channeltrons by large microchannel plate detectors in order to perform parallel detection of electrons. The improved performance is illustrated by electron spectra obtained for Si^+ and Xe^{5+} ions at SOLEIL.

Dedicated ion-yield merged photon ion setups at synchrotron facilities such as the Photon Factory (Japan), Aarhus (Denmark), SOLEIL (France) and the ALS at Berkeley (USA) have all contributed to extensive photoionization results for a wide range of atomic ions. The most recent such development is the Photon-Ion Spectrometer (PIPE) at PETRA III in Hamburg, which is capable of very high-resolution investigations over the 250 eV to 3000 eV photon range. In their paper [8] Schippers and Müller show the flexibility and capabilities of PIPE by reviewing recent work on atomic ions of astrophysical interest. Examples include L-shell photoionization of Fe^+, Fe^{2+} and Fe^{3+} ions and single and multiple K-shell photoionization of C^-, C^+, C^{4+}, Ne^+ and Si^{2+}.

Absolute cross sections for K-shell photoionization of N^+ in the 398 to 450 eV photon energy range are reported by Mosnier et al. [9]. The results were obtained from ion yields at the MAIA (Multi-Analysis Ion Apparatus) merged photon-ion beam apparatus at the SOLEIL synchrotron facility. A narrow spectral bandpass of 65 meV was used in the $1s \rightarrow 2p$ region near 400 eV and extended Rydberg series were observed above 415 eV. The results were interpreted using Multi-Configuration-Dirac-Fock and R-matrix theoretical approaches.

Using the same MAIA set-up at SOLEIL, N^{2+} fragments were measured following nitrogen K-shell excitation in the molecular ion NH^+. Carniato et al. [10] show how the high sensitivity of MAIA combined with the high spectral resolution achievable at SOLEIL helped to resolve vibrational structures in the molecular ion. Assignment of the observed resonances was achieved by a detailed ab initio theoretical analysis, including vibrational dynamics, of the core-to-valence and core-to-Rydberg excitations.

The last three papers describe results obtained with laser-produced plasmas.

Scally et al. [11] report on the results of a systematic study of the emission between 10 and 18 nm from plasmas produced with Sn, Pb and lead-tin alloys targets, under a variety of laser irradiation conditions and alloy concentrations. The ion stages contributing to the emission are identified through a collisional radiative model and atomic structure codes. Results obtained with Nd:YAG laser irradiation are compared to optically thinner CO_2 laser plasmas.

Lu et al. [12] report on the photoabsorption spectrum of Bi^+ in the wavelength regime between 37 and 60 nm, recorded by the dual laser plasma technique where separate laser plasmas provide the backlighting short wavelength continuum and the absorbing ions. $5d \rightarrow 6p$ transitions from the ground state of Bi^+ provide the strongest features while transitions from low-lying excited states make small contributions.

The final paper [13] by Wong et al. investigates the use of the Colombant and Tonon Collisional Radiative (CR) Model for the understanding of laser-produced plasmas. The CR model allows ion distributions for a given temperature and density to be calculated. Plots of the collisional ionization, radiative recombination and three-body recombination rate coefficients, ion distributions and peak fractional populations for various elements are included. The importance of dealing correctly with ionization bottlenecks is stressed.

The book overall provides insight into the variety of investigations into the interaction of short wavelength photons with atomic and molecular ions now possible. It is anticipated that investigations of the interaction of energetic photons with ionized matter will further deepen, with the advent of several new FEL facilities under development and which are expected to drive many new innovations and discoveries in the study of light-matter interactions in the short wavelength regime.

Funding: This research received no external funding.

Institutional Review Board Statement: Not applicable.

Informed Consent Statement: Not applicable.

Data Availability Statement: Not applicable.

Conflicts of Interest: The authors declare no conflict of interest.

References

1. Special Issue "Interaction of Ionizing Photons with Atomic and Molecular Ions". Available online: https://www.mdpi.com/journal/atoms/special_issues/atom_ions (accessed on 7 December 2021).
2. Gryzlova, E.V.; Kiselev, M.D.; Popova, M.M.; Zubekhin, A.A.; Sansone, G.; Grum-Grzhimailo, A.N. Multiple Sequential Ionization of Valence n = 4 Shell of Krypton by Intense Femtosecond XUV Pulses. *Atoms* **2020**, *8*, 80. [CrossRef]
3. Katravulapally, T.; Nikolopoulos, L.A.A. Effects of the FEL Fluctuations on the 2s2p Li^+ Auto-Ionization Lineshape. *Atoms* **2020**, *8*, 35. [CrossRef]
4. Hofbrucker, J.; Eiri, L.; Volotka, A.V.; Fritzsche, S. Photoelectron Angular Distributions of Nonresonant Two-Photon Atomic Ionization Near Nonlinear Cooper Minima. *Atoms* **2020**, *8*, 54. [CrossRef]
5. Dolmatov, V.K. Spin-Polarized Photoelectron Fluxes from Fullerene Anions. *Atoms* **2020**, *8*, 65. [CrossRef]
6. Gorczyca, T.W.; Zhou, H.-L.; Hibbert, A.; Hasoglu, M.F.; Manson, S.T. Inner-Shell Photodetachment of Na^- Using R-Matrix Methods. *Atoms* **2020**, *8*, 60. [CrossRef]
7. Penent, F.; Cubaynes, D.; Lablanquie, P.; Palaudoux, J.; Guilbaud, S.; Moustier, O.; Guigand, J.; Bizau, J.-M. Modification of a Cylindrical Mirror Analyzer for High Efficiency Photoelectron Spectroscopy on Ion Beams. *Atoms* **2020**, *8*, 63. [CrossRef]
8. Schippers, S.; Müller, A. Photoionization of Astrophysically Relevant Atomic Ions at PIPE. *Atoms* **2020**, *8*, 45. [CrossRef]
9. Mosnier, J.-P.; Kennedy, E.T.; Bizau, J.-M.; Cubaynes, D.; Guilbaud, S.; Blancard, C.; McLaughlin, B.M. Photoionization Cross-Sections of Carbon-Like N^+ Near the K-Edge (390–440 eV). *Atoms* **2021**, *9*, 27. [CrossRef]
10. Carniato, S.; Bizau, J.-M.; Cubaynes, D.; Kennedy, E.T.; Guilbaud, S.; Sokell, E.; McLaughlin, B.; Mosnier, J.-P. Vibrationally and Spin-Orbit-Resolved Inner-Shell X-ray Absorption Spectroscopy of the NH^+ Molecular Ion: Measurements and ab Initio Calculations. *Atoms* **2020**, *8*, 67. [CrossRef]
11. Scally, E.; O'Reilly, F.; Hayden, P.; Tobin, I.; O'Sullivan, G. An Investigation of Laser Produced Lead-Tin Alloy Plasmas between 10 and 18 nm. *Atoms* **2020**, *8*, 75. [CrossRef]

12. Lu, H.; Varvarezos, L.; Hayden, P.; Kennedy, E.T.; Mosnier, J.-P.; Costello, J.T. The 5d-6p VUV Photoabsorption Spectrum of Bi^+. *Atoms* **2020**, *8*, 55. [CrossRef]
13. Wong, N.L.; O'Reilly, F.; Sokell, E. Investigation of a Collisional Radiative Model for Laser-Produced Plasmas. *Atoms* **2020**, *8*, 52. [CrossRef]

atoms

MDPI

Article

Multiple Sequential Ionization of Valence n = 4 Shell of Krypton by Intense Femtosecond XUV Pulses

Elena V. Gryzlova [1], Maksim D. Kiselev [1,2], Maria M. Popova [1,2], Anton A. Zubekhin [2], Giuseppe Sansone [3] and Alexei N. Grum-Grzhimailo [1,*]

[1] Skobeltsyn Institute of Nuclear Physics, Lomonosov Moscow State University, 119991 Moscow, Russia; gryzlova@gmail.com (E.V.G.); md.kiselev94@gmail.com (M.D.K.); mm.popova@physics.msu.ru (M.M.P.)
[2] Physical Department, Lomonosov Moscow State University, 119991 Moscow, Russia; anton-zubehin@mail.ru
[3] Physikalisches Institut, Albert-Ludwigs-Universität Freiburg Hermann-Herder-Straße 3, 79104 Freiburg, Germany; giuseppe.sansone@physik.uni-freiburg.de
* Correspondence: grum@sinp.msu.ru; Tel.: +7-495-939-4776

Received: 10 October 2020; Accepted: 3 November 2020; Published: 12 November 2020

Abstract: Sequential photoionization of krypton by intense extreme ultraviolet femtosecond pulses is studied theoretically for the photon energies below the 3*d* excitation threshold. This regime with energetically forbidden Auger decay is characterized by special features, such as time scaling of the level population. The model is based on the solution of rate equations with photoionization cross sections of krypton in different charge and multiplet states determined using R-matrix calculations. Predictions of the ion yields and photoelectron spectra for various photon fluence are presented and discussed.

Keywords: photoionization; multiple ionization; ions; free-electron laser; krypton; femtosecond pulses; photoelectron spectroscopy

1. Introduction

Multiple ionization of atoms by intense pulses generated by free-electron laser (FEL) operating in the extreme ultraviolet (XUV) has been observed since the first experiments at the Free-electron LASer in Hamburg (FLASH) [1]. Such studies are of great importance to benchmark theoretical models for the description of simple non-linear process in the XUV. Two regimes can be distinguished in the multiple ionization process:

(i) The photon energy of the FEL is high enough to eject an electron from an inner shell. Within a few femtoseconds the hole is filled by an electron originating from an outer shell, through a single or cascaded Auger decay mechanism. The ultrafast dynamics of the Auger decay competes with the absorption by the target ion of another photon from the same femtosecond FEL pulse. Therefore, ionization of the target often proceeds through a chain of consecutive photoionization and Auger decay events [2]. Usually, the ion yields of the different charge states are measured in the experiment as a function of the FEL pulse parameters and they are compared with the corresponding predictions of theoretical models [3,4]. So far, only a limited number of electronic spectra in this regime have been reported in the literature [2,5].

(ii) The photon energy is not enough for creating a hole in an inner shell and therefore, the Auger process is energetically forbidden, if multiphoton ionisation is neglected. The atom is then ionized only by sequential absorption of photons by valence electrons as far as it is energetically allowed. Sequential photoionization in this regime was observed in noble gases [6–10] and the experimental results were compared with theoretical predictions [11–14]. For these processes, in addition to the ion yield and photoelectron spectra, also the angular distribution and even

angular correlation [6,12,15,16] of two emitted electrons were studied both experimentally and theoretically. The important role of autoionizing resonances was also investigated [10,17,18]. To the best of our knowledge, no studies investigating multiple ionization beyond triple charged ions in the (ii) regime has been reported so far, except a general theoretical formulation for the photoelectron angular distributions in [19].

The current study belongs to the class (ii). Our main purpose is to analyse theoretically and make predictions for sequential ionization of Kr at photon energies in the interval 50–80 eV, i.e., below the excitation threshold of the 3*d*-hole (91.2 eV [20]). In this energy interval the 3*d*-hole is not produced and the Auger decay is excluded. In the next section we describe the process and outline a theoretical approach for modelling the interaction based on the solution of a system of rate equations. In Section 3, we present the results focusing on the time eVolution of the atomic Kr target under the FEL pulse and on the resulting electron spectra. In Section 4 a method for calculating the photoionization cross sections required for the rate equations is described. Examples of the ionization cross sections between electronic multiplet of different charge states of Kr are presented. The last section contains our conclusions.

2. Process Description

Since the Auger decay is energetically forbidden, the main processes, which we consider are photoionization from either the 4*s* or the 4*p* energy levels with emission of a photoelectron e_{ph}

$$\gamma + \mathrm{Kr}^{\mathrm{n}+}\, 4s^k 4p^m \longrightarrow \begin{cases} \mathrm{Kr}^{(\mathrm{n}+1)+}\, 4s^{k-1} 4p^m + e_{ph} \\ \mathrm{Kr}^{(\mathrm{n}+1)+}\, 4s^k 4p^{m-1} + e_{ph} \end{cases} \tag{1}$$

or radiative transition from the 4*p* to the 4*s* level with emission of a fluorescence photon γ_{fl}

$$\mathrm{Kr}^{\mathrm{n}+}\, 4s^k 4p^m \longrightarrow \mathrm{Kr}^{\mathrm{n}+}\, 4s^{k+1} 4p^{m-1} + \gamma_{fl} \tag{2}$$

Sequential ionization of the valence shells of Kr and its ions is schematically shown in Figure 1, where ionization paths between the ionic configurations from neutral Kr to the triply charged ion Kr^{3+} are indicated. "Horizontal" radiation transitions occur between energy levels of a same ion. In fact each indicated level includes all possible multiplet states of the configuration, which were all taken into account in the calculations. For photon energies equal or lower than 50.85 eV, ionization from the $Kr^{3+}\, 4s^k 4p^m$ electron configurations is energetically forbidden. For energies between 50.85 eV and 80 eV ionization channels of $Kr^{3+}\, 4s^k 4p^m$ are allowed, but we neglect them (see below). Thus, we consider the sequential ionization up to triple, three-photon ionization and the scheme in Figure 1 is restricted to transitions up to Kr^{3+}. We do not consider the fine-structure levels of the multiplet states and consider summations over the fine-structure levels. This approach implies that the spectral width of the FEL pulse and resolution of the electron detector are comparable with the fine-structure splitting of the ions: $4s^2 4p^5\, {}^2P^o$ (0.65 eV), $4s^2 4p^4\, {}^3P$ (0.66 eV), $4s^1 4p^5\, {}^3P^o$ (0.69 eV), $4s^2 4p^4\, {}^2D$ (0.20 eV), $4s^2 4p^3\, {}^2P^o$ (0.39 eV), $4s^1 4p^4\, {}^4P$ (0.66 eV), $4s^1 4p^4\, {}^2D$ (0.11 eV), $4s^1 4p^4\, {}^2P$ (0.34 eV). More details on the transitions between the multiplet states in the first three ionization steps from Kr to Kr^{3+} are presented in Table 1.

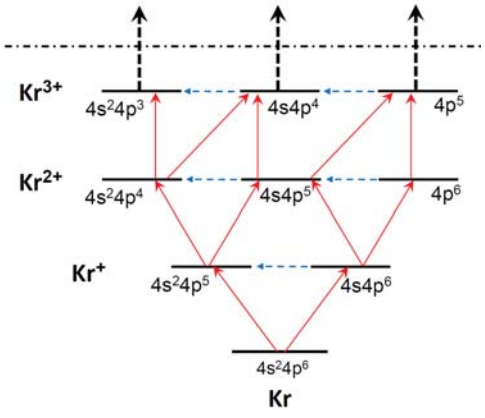

Figure 1. Scheme of transitions in sequential multiphoton ionization of Kr. Solid red arrows—photoionization, dashed blue arrows—radiative transitions. Only configurations are shown without multiplet splitting. The horizontal dash-dotted line indicates the limit for the sequential three-photon triple ionization (see text).

Table 1. List of transitions in sequential three-photon ionization of Kr. Columns and lines correspond to initial and final states of the transitions within the LS-coupling scheme, respectively. Capital letters denote photoelectron lines for further convenience. Numbers after the letters present experimental ionization thresholds [21] for the corresponding transitions in eV, averaged over a multiplet. Transitions not marked by a capital letter are weak and their contribution to the photoelectron spectra is negligible, although they are included in Equations (3).

N	Initial State / Final State	$4s^24p^6\,{}^1S$	$4s^24p^5\,{}^2P^o$	$4s^14p^6\,{}^2S$	$4s^24p^4\,{}^3P$	$4s^24p^4\,{}^1D$	$4s^24p^4\,{}^1S$	$4s^14p^5\,{}^3P^o$	$4s^14p^5\,{}^1P^o$	$4s^04p^6\,{}^1S$
1	$4s^24p^6\,{}^1S$	-	-	-	-	-	-	-	-	-
2	$4s^24p^5\,{}^2P^o$	A, 14.0	-	-	-	-	-	-	-	-
3	$4s^14p^6\,{}^2S$	E, 27.5	-	-	-	-	-	-	-	-
4	$4s^24p^4\,{}^3P$	-	B, 24.4	-	-	-	-	-	-	-
5	$4s^24p^4\,{}^1D$	-	D, 26.2	-	-	-	-	-	-	-
6	$4s^24p^4\,{}^1S$	-	F, 28.5	-	-	-	-	-	-	-
7	$4s^14p^5\,{}^3P^o$	-	I, 38.7	C, 25.2	-	-	-	-	-	-
8	$4s^14p^5\,{}^1P^o$	-	K, 42.0	F, 28.4	-	-	-	-	-	-
9	$4s^04p^6\,{}^1S$	-	-	K, 42.1	-	-	-	-	-	-
10	$4s^24p^3\,{}^4S^o$	-	-	-	G, 35.8	-	-	-	-	-
11	$4s^24p^3\,{}^2D^o$	-	-	-	I, 38.0	G, 36.1	33.8	-	-	-
12	$4s^24p^3\,{}^2P^o$	-	-	-	J, 39.7	H, 37.9	G, 35.6	-	-	-
13	$4s^14p^4\,{}^4P$	-	-	-	L, 50.6	-	-	G, 35.5	-	-
14	$4s^14p^4\,{}^2D$	-	-	-	O, 53.9	M, 52.1	49.8	I, 38.8	G, 36.3	-
15	$4s^14p^4\,{}^2S$	-	-	-	R, 57.4	55.6	53.3	K, 42.3	J, 39.8	-
16	$4s^14p^4\,{}^2P$	-	-	-	Q, 56.4	P, 54.6	M, 52.3	K, 41.4	I, 38.8	-
17	$4s^04p^5\,{}^2P^o$	-	-	-	-	-	-	P, 54.9	M, 52.3	I, 38.7

To follow the dynamics of the state populations, we apply a method of solving rate equations extensively used in the description of sequential ionization of atoms by X-ray FEL pulses (for example [22–29]). For femtosecond pulses the radiative $4p \rightarrow 4s$ transitions can be neglected and the temporal dynamics is dominated by photoionization.

The rate equations for the level populations then take the form (we use atomic units until otherwise indicated)

$$\frac{dN_i(t)}{dt} = j(t) \sum_{j \neq i} \left[\sigma_{j \rightarrow i} N_j(t) - \sigma_{i \rightarrow j} N_i(t) \right] , \qquad i, j = 1, 2, ..., M \tag{3}$$

where $N_i(t)$ is the population of level i, $\sigma_{i\to j}$ is the photoionization cross section from level i of Kr^{n+} to level j of $Kr^{(n+1)+}$, and $j(t)$ is the intensity of the incident radiation, which varies with time according to the pulse shape. M is the number of states, which are accounted for in treating the temporal dynamics of the sequential ionization. In our case $M = 17$ according to Table 1. In the set (3) we do not include shake-up and one-photon double ionization channels [30], but account for the shake-up, as well as autoionizing resonances in the calculation of the photoionization cross sections $\sigma_{i\to j}$. Details of the cross section calculations are presented in Section 4.

The discrete levels can influence the process through two-photon resonance single ionization [31,32]. Photon energies above 50 eV, are above the 4*s* and 4*p* ionization thresholds in Kr and Kr^+ and therefore the two-photon resonance ionization via their discrete states is not possible. However, for energies around 50 eV, the channel of one-photon ionization of the 4*s* electron from Kr^{2+} is closed (see Table 1, lines 13–17). Therefore, the two-photon resonance ionization might occur in the latter case. Nevertheless, we neglect this process, because it can proceed for Kr^{2+} at photon energies around 50 eV only via high Rydberg states with small excitation and ionization probability. For the photon energies higher than ∼58 eV all the 4*s* ionization channels for Kr^{2+} open and the two photon resonance ionization channels disappear.

We assume a temporal Gaussian distribution of the incident photon flux density (number of photons per surface per time):

$$j(t) = j_0 \exp(-t^2/t_p^2)\,, \tag{4}$$

where t_p is related to the full width at half maximum (FWHM) of the pulse, $\mathrm{FWHM} = 2\sqrt{\ln 2}\ t_p$. The photon flux is related to the fluence F, i.e., to the integral number of photons per 1 Å^2 in the entire pulse, as

$$j_0 = \frac{2\sqrt{\ln 2}\ F}{\sqrt{\pi}\ \mathrm{FWHM}} = 0.0063634\ \frac{F\,[\mathrm{ph/Å^2}]}{\mathrm{FWHM}\,[\mathrm{fs}]}\,. \tag{5}$$

Equation (5) is obtained by considering the integral of (4) over time and transforming from atomic units.

For a fixed fluence, Equations (3) are invariant under changes of the time scale, $t \to at$, where a is a constant. This scaling feature breaks down when additional terms not proportional to $j(t)$, such as fluorescence and Auger decays, are added to the right side of (3). Thus, the calculations for a fixed fluence can be performed for a generic pulse duration and then scaled. Our case differs in this respect substantially from previous calculations, where the competing Auger decay had to be included and each pulse duration had to be calculated individually. In this paper we fix the pulse duration to $t_p = 18$ fs (FWHM = 30 fs), which is comparable to the typical pulse duration obtained at the seeded FEL FERMI [33,34].

In order to predict the electron spectrum generated by the pulse, we calculate the probability $P_{ij}(F)$ (which depends on the fluence F) that an ion (atom) in a state i is ionized into the ion in a state j over the entire pulse and build up the function,

$$f_F(\varepsilon) = \sum_{ij} P_{ij}(F) \exp[-(\varepsilon + I_{ij} - \omega)^2/\Gamma^2]\,, \tag{6}$$

where ε is the kinetic energy of the photoelectron at the photon energy ω, I_{ij} is the threshold of ionization of the state i to the state j (binding energy) and Γ represents the resolution of the electron detector. We assumed $\Gamma = 0.42$ eV (corresponding to the resolution FWHM = 0.7 eV), in order to leave the fine structure of levels unresolved, as explained above.

3. Results and Discussion

Our main results are presented in Figures 2 and 3 for the population of the different ionic states and Figure 4 for the photoelectron spectra.

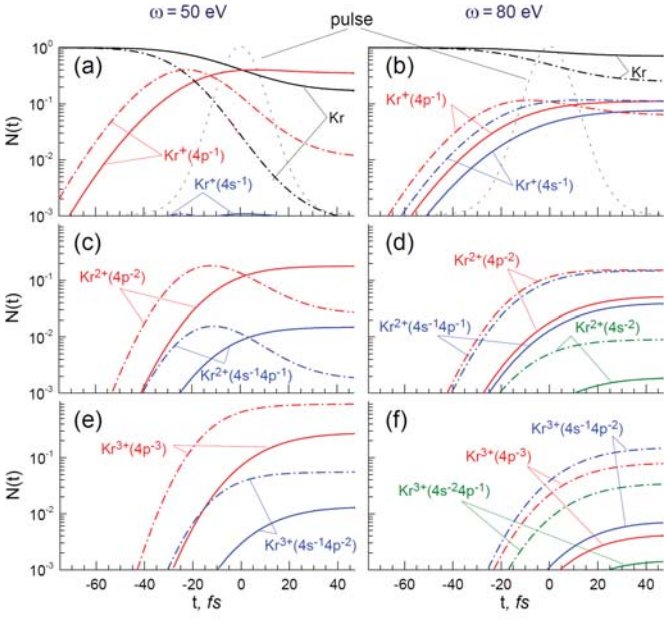

Figure 2. Population of different ion charge states and configurations for two fluences: $F = 100$ ph/Å^2 (solid lines) and $F = 400$ ph/Å^2 (dash-dotted line) for the photon energies 50 eV (**a**,**c**,**e**) and 80 eV (**b**,**d**,**f**). Black lines—ionization of neutral Kr; red lines—ionization to $4s^2 4p^{-n}$ configuration, where n is the ion charge; blue lines—ionization to $4s^{-1}4p^{-n+1}$, green lines—ionization to $4s^{-2}4p^{-n+2}$. The pulse envelope (grey dashed line) is indicated in the upper panels.

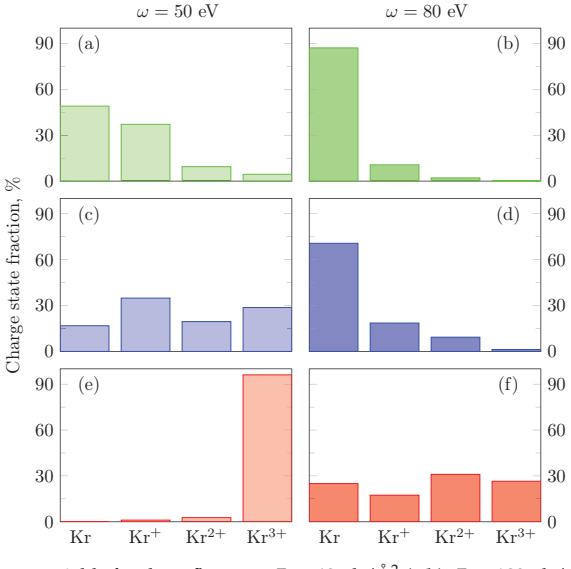

Figure 3. Charge-state yields for three fluences: $F = 40$ ph/Å^2 (**a**,**b**), $F = 100$ ph/Å^2 (**c**,**d**), and $F = 400$ ph/Å^2 (**e**,**f**) for the photon energies 50 eV (**a**,**c**,**e**) and 80 eV (**b**,**d**,**f**).

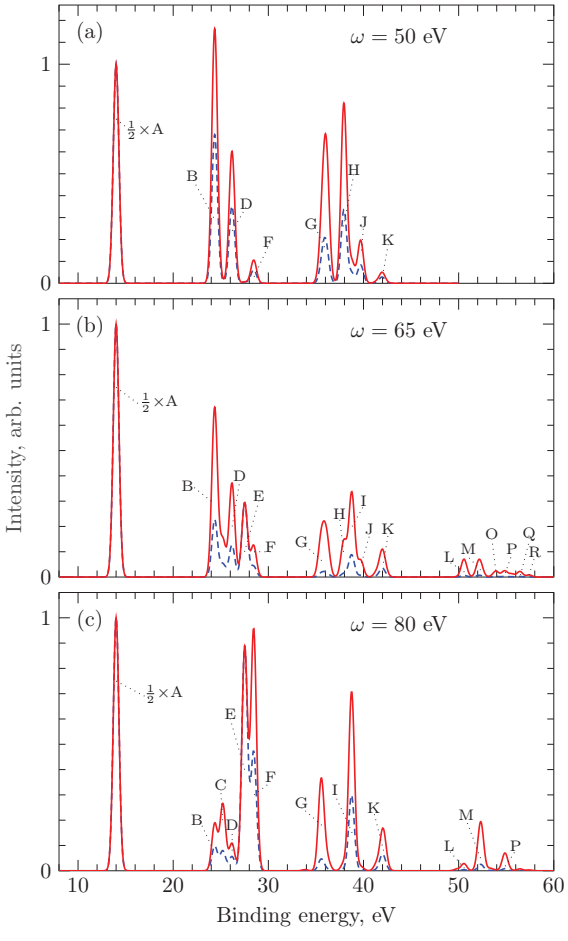

Figure 4. Photoelectron spectrum for different photon energy: $\omega = 50$ eV (**a**), $\omega = 65$ eV (**b**), and $\omega = 80$ eV (**c**). Solid lines: $F = 400$ ph/Å^2; dashed lines: $F = 100$ ph/Å^2. The spectra are normalized in such a way that 1/2 of the main line A equals unity. The spectral features are indicated by capital letters in accordance with Table 1.

3.1. Time Evolution of Population

In Figure 2, we present results obtained with 50 eV (left column) and 80 eV (right column) photon energies and fluences $F = 100$ ph/Å^2 (solid lines) and $F = 400$ ph/Å^2 (dash-dotted lines). We summed up over the populations of different terms within one configuration.

The population of the ionic states Kr^+, Kr^{2+} and Kr^{3+} is presented as a function of time in the first, second and third rows, respectively. Different colors correspond to the configurations without $4s$-hole (red), with one $4s$-hole (blue) and double $4s$-hole (green). With the value of $t_p = 18$ fs the above fluences correspond to intensities between 10^{15} and 10^{16} W/cm^2. As explained above, the curves in Figure 2 remain the same for fixed values of F, after appropriate scaling of the pulse duration and of the timescale. In particular, the final populations of the levels at the end of the pulses are invariant for changes of the pulse duration (for a fixed fluence).

For the photon energy of 50 eV, ionization of the valence $4p$ shell dominates; the configurations Kr^{n+} $4s^2 4p^{-n}$ (red curves in Figure 2a,c,e) are quickly populated, reaching maximum of the population

at slightly different times, depending on the ionic charge and the fluence. As expected, the population maxima are reached at later instants for increasing ionic charge states and decreasing pulse fluences. At the end of the pulse, the populations become constants, because the Auger decay of the holes is energetically forbidden and the fluorescence occur on much longer time scale. The sum of all values presented in Figure 2a,c,e, as well as in Figure 2b,d,f corresponding to the same conditions (time, fluence, photon energy) equals unity.

For the fluence of $F = 400$ ph/Å^2, the majority of the krypton atoms, ∼90.5%, are found after the pulse in the triply charged ionic state in its ground configuration Kr^{3+} $4s^2 4p^3$ (Figure 2e). Configurations of ions with one 4*s*-hole are populated on the level of ∼5.5%, while the amount of ions Kr^{2+} and Kr^{3+} with double 4*s*-holes is negligible. This result is explained by the very small 4*s* ionization cross section in the region of the Cooper minimum around 45 eV (see Section 4). The concentration of neutral atoms at the end of the pulse is also negligible (Figure 2a). The number of singly and doubly charged ions first increases with time, but then it drops down (Figure 2a,c), because the fluence is high enough to further ionize them to Kr^{3+} within the pulse.

For the smaller fluence of $F = 100$ ph/Å^2, already 17% of atoms are left as neutrals (Figure 2a) and the ions are distributed between singly, doubly and triply charged ions with the corresponding concentrations of 35%, 20%, and 29% (Figure 2a,c,e), dominated by ions without 4*s*-holes. At this lower fluence the population of states increases smoothly with time, without showing pronounced maxima.

For the photon energy of 80 eV, the final concentration of the neutral atoms is much higher (compare Figure 2a,b) than for the photon energy of 50 eV, because the 4*p* ionization cross section rapidly decreases with the photon energy in interval from 50 eV to 80 eV. At the same time, the production of ions with the 4*s*-vacancy is much more efficient, because the 4*s* ionization cross section increases in this energy interval, which is just above the corresponding Cooper minimum. At $F = 400$ ph/Å^2 the number of the Kr ions after the pulse in each charge state with a 4*s*-hole exceeds the number of the ions with only 4*p* ionized electrons. Furthermore, the number of Kr ions with the double 4*s*-hole reaches 4.5% of all the target atoms.

Finally, in Figure 3 we present the overall ionic yields at fluences $F = 40$ ph/Å^2, $F = 100$ ph/Å^2 and $F = 400$ ph/Å^2 and photon energies $\omega = 50$ eV and $\omega = 80$ eV. The population of the different ionic states strongly depends on the photon energy and fluence. Figure 3a,b,d show a typical situation for multiple ionization in a regime far from saturation, when the ions with higher charge have smaller yields. Although ionization of Kr^{3+} is energetically possible for 80 eV photons, Figure 3b,d show that at the fluences of $F = 40$ ph/Å^2 and $F = 100$ ph/Å^2 the contribution of higher charge states is negligible. The opposite behavior is shown in Figure 3e, in which nearly all ions are in highest allowed charged state, because a further ionization step is energetically forbidden for the photon energy of 50 eV. In this case the intensity of the radiation and the cross section of the 4*p*-ionization are high enough to promote three 4*p* electrons into the continuum during the pulse. More uniform distribution in Figure 3c,f show an intermediate regime, caused by an interplay between energy dependence of the ionization cross sections and fluence. Note that the last column in Figure 3f actually presents the sum yield (∼25%) of ions with charges three and higher. Although we cut the treatment at Kr^{3+}, the photoelectron spectra presented below, are not influenced by this fact in the considered interval of the electron energies.

3.2. Photoelectron Spectra

The photoelectron spectrum contains much more information on the pathways of the sequential ionization than the ion yield, because it gives information on the relative population of the intermediate states of the process (see Figure 1 and Table 1). This information becomes more detailed by improving the energy resolution of the electron detector and decreasing the pulse spectral bandwidth.

The generated photoelectron spectra for three photon energies, 50 eV, 65 eV, and 80 eV are displayed in Figure 4a–c, respectively.

We considered the modifications of the spectra in a broad range of photon fluences. Figure 4a–c show, as examples, spectra for the two fluences, $F = 100$ ph/Å^2 and $F = 400$ ph/Å^2. As follows from Table 1, lines A and E originate from single ionization of Kr and are produced by absorption of one photon. Lines B, C, D, and F are due to one-photon ionization of Kr^+ and, therefore, in the sequential two-photon double ionization of Kr. Lines G, H, J, L–R are produced in the sequential three-photon triple ionization of Kr. Lines I and K represent an overlap between a few lines from the sequential two- and three-photon ionization. In Figure 4a–c the lines are concentrated in certain groups: three groups for the photon energy of 50 eV and four groups for the photon energies 65 eV and 80 eV. The three groups at $\omega = 50$ eV (Figure 4a) correspond to the line from the $4p$-shell ionization of neutral Kr (electron energy 36 eV), lines from ionization of mostly Kr^+ $4s^24p^5$ (electron energies 21–26 eV) and from ionization of mostly Kr^{2+} $4s^24p^4$ (electron energies 8–14 eV). The fourth group of lines appears at the photon energies 65 eV and 80 eV (Figure 4b,c), when ionization of the $4s$-electron from Kr^{2+} $4s^24p^4$ and Kr^{2+} $4s^14p^5$ is opened. Note that some of the lines in different panels of Figure 4 are not indicated because of negligible contributions to the spectra.

Comparison of Figure 4a,b shows that the intensity of the photoelectron lines drops down for increasing ionic charges at the photon energy of 65 eV faster than at 50 eV, for a fixed fluence. This is caused by the decrease of the $4p$-subshell ionization cross-section with increasing photon energy in this range (see Section 4). For higher photon energies the role of the multiple ionization increases (Figure 4c), due to the increase of the ionization cross-section of the $4s$-subshell after the corresponding Cooper minimum (see Section 4, Figure 5b). The change of the relative contribution of $4s$- and $4p$-ionization channels leads to substantial modifications of the photoelectron spectrum. For example, lines E and I with large contribution from the $4s$-ionization, are not observed at $\omega = 50$ eV, but dominate in their group at $\omega = 80$ eV. This is opposite to neon, where ionization from the subvalence $2s$ shell modifies noticeably the photoelectron spectrum at all photon energies within the (ii) regime [10,15]. We expect that the interference Cooper minimum in the $3s$-ionization of Ar around $\omega = 40$ eV [35,36], leads to modifications of the spectra as function of the photon energy similar to the present Kr case.

Figure 6 shows the fluence dependence of the intensities of some selected spectral lines. The curves clearly indicate the one-, two- and three-photon origin of the spectral features A and EF, I and BCD, and G, respectively. The saturation starts to show up at fluences above 100 ph/Å^2, progressing from the first (one-photon) to the third (three-photon) steps of the sequential ionization process.

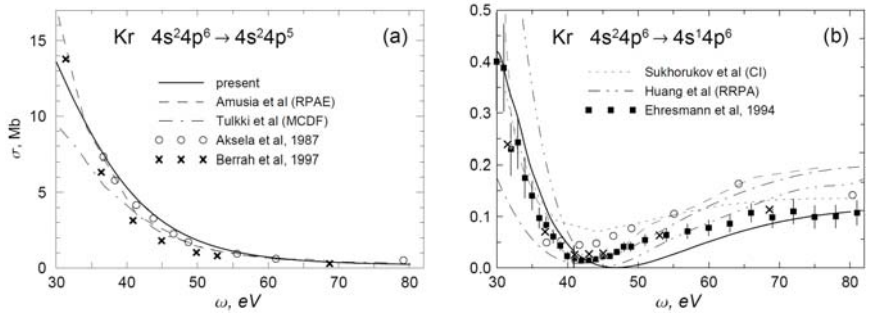

Figure 5. Photoionization cross-sections for the $4p$ (**a**) and $4s$ (**b**) level of Kr. Solid curves — present calculations. Other curves: random phase approximation with exchange (RPAE) from [37] (dashed curve), multichannel Dirac-Fock (MCDF) approximation from [38] (dash-dotted curve), configuration interaction (CI) approximation from [39] (short-dashed curve), relativistic random phase approximation (RRPA) from [40] (dash-dot-dot curve). Experimental data from [41] (squares), [42] (crosses), and [43] (open circles).

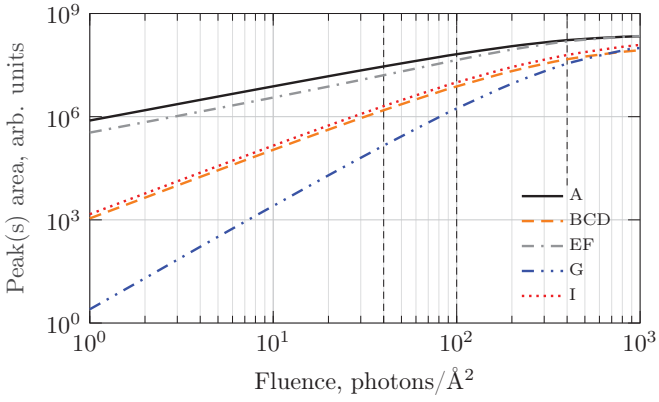

Figure 6. Intensity dependence of different photoelectron lines on the fluence F for the photon energy $\omega = 80$ eV. Vertical dashed lines indicate fluences related to Figures 2–4: 40 ph/Å^2, 100 ph/Å^2, and 400 ph/Å^2.

4. Method of the Cross Section Calculations

Photoionization cross sections of multiplet states $4s^k4p^{m\ 2S+1}L$ for variously charged Kr ions were calculated by the B-spline R-matrix approach [44], which fully takes into account non-orthogonality of the electron functions before and after the ionization. For all the three steps, the basis wave functions of each of the initial nine states listed in Table 1 were obtained in independent Hartee-Fock calculations in the LS-coupling approximation with variation of 4*s* and 4*p* orbitals and the $1s^22s^22p^63s^23p^63d^{10}$ Ar-like core frozen from the self-consistent calculations for the ground state of Kr. The final ionic states (numbers 2–17 in Table 1) were similarly calculated in independent Hartree-Fock calculations with variable 4*s* and 4*p* electron orbitals. For each step, the corresponding set of final ionic states were included in the R-matrix expansion, giving the total angular momentum L_{tot} and spin S_{tot} of the system (final ion + electron) satisfying the dipole selection rules. Overall 19 R-matrix runs were needed for the reactions of the type

$$\gamma + Kr^{n+}\left(4s^k4p^{m\ 2S_i+1}L_i\right) \longrightarrow \underbrace{Kr^{(n+1)+}\left(4s^{k-1}4p^{m\ 2S_f+1}L_f\right) + e(E\ell)}_{L_{tot}\,S_{tot}}, \tag{7}$$

where n = 0, 1, 2 and ℓ are the orbital angular momentum of the photoelectron. Each of the reactions (7) describes a few ionization channels with one of the fixed nine initial states from Table 1 and fixed values of $L_{tot}S_{tot}$, but all possible from 17 final $Kr^{(n+1)+}$ states and ℓ. The ionization cross section to a particular final ionic state is obtained by summation over all corresponding channels with different sets of ℓ, L_{tot}, S_{tot}.

Figure 5 presents photoionization cross sections of the 4*p* (Figure 5a) and 4*s* (Figure 5b) electrons from Kr $4s^24p^6\,{}^1S$, respectively, i.e., for the first step of the sequential ionization. These cross sections can be compared with experiment and other calculations [35,37–43,45,46]. Here and below we use results in the velocity gauge which better agrees with experiment for neutral Kr.

Ionization cross sections for the second step into different multiplet states of the doubly charged ion are shown in Figure 7: ionization from Kr^+ $4s^24p^5\,{}^2P^o$ and from Kr^+ $4s4p^6\,{}^2S$ are displayed in Figure 7a,b, respectively. Figure 8 is related to the third step and shows ionization cross sections from six multiplet states of Kr^{2+} to different multiplet states of Kr^{3+}. The transitions correspond to those indicated in Table 1.

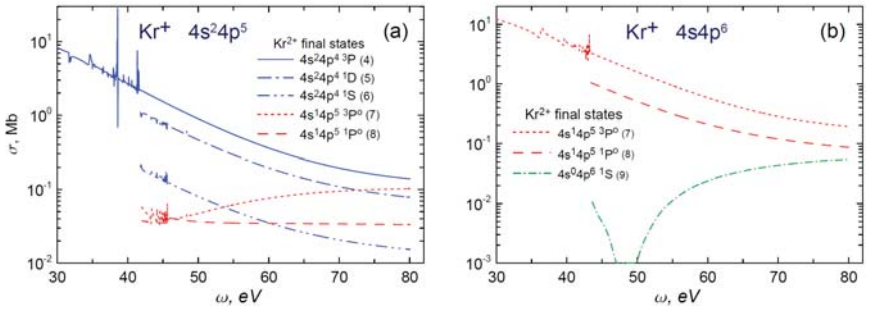

Figure 7. Photoionization cross-sections from the $4s^24p^5\,^2P^o$ (**a**) and $4s^14p^6\,^2S$ state (**b**) of Kr^+. Legends for the curves with the corresponding final Kr^{2+} multiplet states and their numbers (in parenthesis) according to Table 1 are presented. The blue lines in (**a**) correspond to ionization of the $4p$ electron into different terms of the Kr^{2+} $4s^24p^4$ configuration. The green dash-dotted line in (**b**) corresponds to producing of the double-hole state Kr^{2+} $4s^04p^6$. Identical red lines in the both panels show transitions to the same final states from Kr^+ $4s^24p^5$ (panel (**a**)) and Kr^+ $4s4p^6$ (panel (**b**)), respectively.

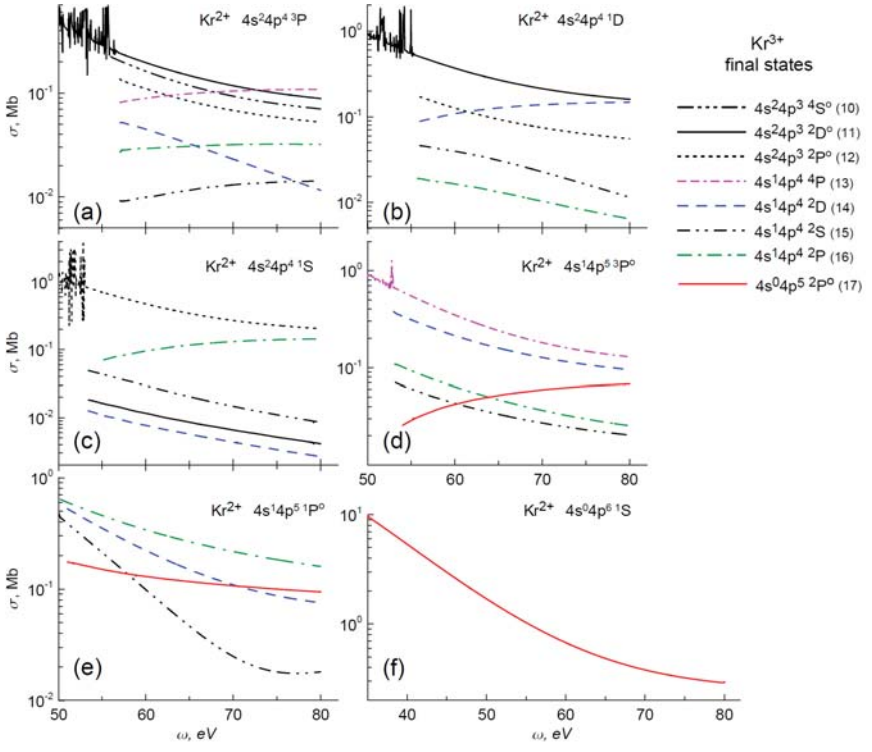

Figure 8. Photoionization cross-sections from different multiplet states of Kr^{2+}. indicated in the panels. Legends for the curves with the corresponding final Kr^{3+} states and their numbers (in parenthesis) according to Table 1 are presented at the right. (See text).

Ionization cross section of a subvalence 4*s* shell in Kr shows a deep interference Cooper minimum around the photon energy of 45 eV [35] (Figure 5b). The position and the depth of the minimum is

very sensitive to the model. In our study the particular value of the 4*s* ionization cross section in the minimum is not so important except the fact that it is at least two orders of magnitude less than the 4*p* ionization cross section. The Cooper minimum occurs in the 4*s* ionization from the Kr^+ $4s^1 4p^6$ state (Figure 7b, green line), but looks moving under the threshold in ionization from the Kr^+ $4s^2 4p^5$ state (Figure 7a, red lines). In the ionization of the doubly charged ion, the appearance of the Cooper minimum strongly depends on the initial and final ion configurations (Figure 8).

There are series of Rydberg autoionizing states with configurations $4s^n 4p^m ({}^{2S_f+1}L_f) np$ in the energy region under consideration. The series appear in the ionization of 4*p* shell at photon energy below the 4*s* ionization threshold for all terms and configurations with only one exception, $4s^0 4p^m$. Besides, the Rydberg series appear in the ionization of 4*s* shell between the split multiplet thresholds, for example between $4s4p^5\,{}^3P^o$ and $4s4p^5\,{}^1P^o$. For the sake of clarity, in Figures 7 and 8, we show only sample resonance structures on the upper curves, obtained in our R-matrix calculations, cutting other curves in the near-threshold region in other cases. Although our calculations automatically accounts for the autoionizing resonances, a careful analysis showed that with the currently available spectral width of intense XUV pulses and the electron detector resolution, it is hardly possible to observe resonance effects in integrated observables such as ionic or electron yields. In order to reveal these resonances, more detailed measurements like photoelectron angular distribution [10,47] or angular correlation functions [18] are needed.

5. Conclusions

Time eVolution and photoelectron spectra in sequential photoionization of atomic krypton by intense femtosecond XUV pulses at the photon energies from 50 eV to 80 eV are studied theoretically. In this regime the Auger decay channel is closed and the ionization proceeds through photoemission of 4*s* and 4*p* electrons. Within our model, the results are applicable to pulses with arbitrary duration within the femtosecond domain, due to the time scaling of the rate equations. Lines from single, double and triple ionization processes are predicted in the photoelectron spectra. The intensity of the lines is proportional to the corresponding power of the fluence up to the saturation fluence of about 10^2 ph/Å^2. The Cooper minimum in the 4*s* ionization cross section influences the time eVolution of the target and eVolution of the photoelectron spectrum with the photon energy. Nevertheless, the population of states with the 4*s*-hole after the pulse can reach tens percents. The present study is a natural step before turning to higher photon energies, when the 3*d* excitation threshold is opened and the Auger decay makes the dynamics more complex.

Author Contributions: The authors have contributed to the manuscript equally. All authors took part in discussions and preparation of the manuscript. All authors have read and agreed to the published version of the manuscript.

Funding: This research was funded by the Russian Foundation for Basic Research, grant number 20-52-12023, and Deutsche Forschungsgemeinschaft, grant number 429805582.

Acknowledgments: The authors benefited greatly from discussions with Oleg Zatsarinny. The research was partly carried out using the equipment of the shared research facilities of HPC computing resources at Lomonosov Moscow State University and of the shared services center "Data Center of Far Eastern Branch of the Russian Academy of Sciences".

Conflicts of Interest: The authors declare no conflict of interests.

References

1. Sorokin, A.A.; Bobashev, S.V.; Feigl, T.; Tiedtke, K.; Wabnitz, H.; Richter, M. Photoelectric Effect at Ultrahigh Intensities. *Phys. Rev. Lett.* **2007**, *99*, 213002. [CrossRef]
2. Young, L.; Kanter, E.P.; Krässig, B.; Li, Y.; March, A.M.; Pratt, S.T.; Santra, R.; Southworth, S.H.; Rohringer, N.; DiMauro, L.F.; et al. Femtosecond electronic response of atoms to ultra-intense X-rays. *Nature* **2010**, *466*, 56–61. [CrossRef]

3. Southworth, S.H.; Dunford, R.W.; Ray, D.; Kanter, E.P.; Doumy, G.; March, A.M.; Ho, P.J.; Krässig, B.; Gao, Y.; Lehmann, C.S.; et al. Observing pre-edge K-shell resonances in Kr, Xe, and XeF_2. *Phys. Rev. A* **2019**, *100*, 022507. [CrossRef]
4. Berrah, N.; Fang, L.; Osipov, T.; Murphy, B.; Bostedtc, C.; Bozek, J. Multiphoton ionization and fragmentation of molecules with the LCLSX-ray FEL. *J. Electron Spectrosc. Relat. Phenom.* **2014**, *196*, 34–37. [CrossRef]
5. Fushitani, M.; Sasaki, Y.; Matsuda, A.; Fujise, H.; Kawabe, Y.; Hashigaya, K.; Owada, S.; Togashi, T.; Nakajima, K.; Yabashi, M.; et al. Multielectron-Ion Coincidence Spectroscopy of Xe in Extreme Ultraviolet Laser Fields: Nonlinear Multiple Ionization via Double Core-Hole States. *Phys. Rev. Lett.* **2020**, *124*, 193201. [CrossRef]
6. Kurka, M.; Rudenko, A.; Foucar, L.; Kühnel, K.U.; Jiang, Y.H.; Ergler, T.; Havermeier, T.; Smolarski, M.; Schössler, S.; Cole, K.; et al. Two-photon double ionization of Ne by free-electron laser radiation: A kinematically complete experiment. *J. Phys. B At. Mol. Opt. Phys.* **2009**, *42*, 141002. [CrossRef]
7. Mondal, S.; Ma, R.; Motomura, K.; Fukuzawa, H.; Yamada, A.; Nagaya, K.; Yase, S.; Mizoguchi, Y.; Yao, M.; Rouzée, A.; et al. Photoelectron angular distributions for the two-photon sequential double ionization of xenon by ultrashort extreme ultraviolet free electron laser pulses. *J. Phys. B At. Mol. Opt. Phys.* **2013**, *46*, 164022. [CrossRef]
8. Braune, M.; Hartmann, G.; Ilchen, M.; Knie, A.; Lischke, T.; Reinköster, A.; Meissner, A.; Deinert, S.; Glaser, L.; Al-Dossary, O.; et al. Electron angular distributions of noble gases in sequential two-photon double ionization. *J. Mod. Opt.* **2016**, *63*, 324. [CrossRef]
9. Ilchen, M.; Hartmann, G.; Gryzlova, E.V.; Achner, A.; Allaria, E.; Beckmann, A.; Braune, M.; Buck, J.; Callegari, C.; Coffee, R.N.; et al. Symmetry breakdown of electron emission in extreme ultraviolet photoionization of argon. *Nat. Commun.* **2018**, *8*, 4659. [CrossRef]
10. Carpeggiani, P.A.; Gryzlova, E.V.; Reduzzi, M.; Dubrouil, A.; Faccialá, D.; Negro, M.; Ueda, K.; Burkov, S.M.; Frassetto, F.; Stienkemeier, F.; et al. Complete reconstruction of bound and unbound electronic wavefunctions in two-photon double ionization. *Nat. Phys.* **2019**, *15*, 170–177. [CrossRef]
11. Kheifets, A.S. Sequential two-photon double ionization of noble gas atoms. *J. Phys. B At. Mol. Opt.* **2007**, *40*, F313–F318. [CrossRef]
12. Fritzsche, S.; Grum-Grzhimailo, A.N.; Gryzlova, E.V.; Kabachnik, N.M. Angular distributions and angular correlations in sequential two-photon double ionization of atoms. *J. Phys. B At. Mol. Opt. Phys.* **2008**, *41*, 165601. [CrossRef]
13. Fritzsche, S.; Grum-Grzhimailo, A.N.; Gryzlova, E.V.; Kabachnik, N.M. Sequential two-photon double ionization of Kr atoms. *J. Phys. B At. Mol. Opt. Phys.* **2009**, *42*, 145602. [CrossRef]
14. Grum-Grzhimailo, A.N.; Gryzlova, E.V.; Meyer, M. Non-dipole effects in the angular distribution of photoelectrons in sequential two-photon atomic double ionization. *J. Phys. B At. Mol. Opt. Phys.* **2012**, *45*, 215602. [CrossRef]
15. Rouzee, A.; Johnsson, P.; Gryzlova, E.; Fukuzawa, H.; Yamada, A.; Siu, W.; Huismans, Y.; Louis, E.; Bijkerk, F.; Holland, D.; et al. Angle-resolved photoelectron spectroscopy of sequential three-photon triple ionization of neon at 90.5 eV photon energy. *Phys. Rev. A* **2011**, *83*, 031401(R). [CrossRef]
16. Gryzlova, E.V.; Grum-Grzhimailo, A.N.; Fritzsche, S.; Kabachnik, N.M. Angular correlations between two electrons emitted in the sequential two-photon double ionization of atoms. *J. Phys. B At. Mol. Opt. Phys.* **2010**, *43*, 225602. [CrossRef]
17. Gryzlova, E.V.; Ma, R.; Fukuzawa, H.; Motomura, K.; Yamada, A.; Ueda, K.; Grum-Grzhimailo, A.N.; Kabachnik, N.M.; Strakhova, S.I.; Rouzée, A.; et al. Doubly resonant three-photon double ionization of Ar atoms induced by an EUV free-electron laser. *Phys. Rev. A* **2011**, *84*, 063405. [CrossRef]
18. Augustin, S.; Schulz, M.; Schmid, G.; Schnorr, K.; Gryzlova, E.V.; Lindenblatt, H.; Meister, S.; Liu, Y.F.; Trost, F.; Fechner, L.; et al. Signatures of autoionization in the angular electron distribution in two-photon double ionization of Ar. *Phys. Rev. A* **2018**, *98*, 033408. [CrossRef]
19. Grum-Grzhimailo, A.N.; Gryzlova, E.V.; Fritzsche, S.; Kabachnik, N.M. Photoelectron angular distributions and correlations in sequential double and triple atomic ionization by free electron lasers. *J. Mod. Opt.* **2016**, *60*, 334–357. [CrossRef]
20. King, G.C.; Tronc, M.; Read, F.H.; Bradford, R.C. An investigation of the structure near the $L_{2,3}$ edges of argon, the $M_{4,5}$ edges of krypton and the $N_{4,5}$ edges of xenon, using electron impact with high resolution. *J. Phys. B At. Mol. Phys.* **1977**, *10*, 2479–2495. [CrossRef]

21. *NIST Atomic Spectra Database (Version 5.7.1)*; National Institute of Standards and Technology: Gaithersburg, MD, USA, 2019. Available online: https://physics.nist.gov/asd (accessed on 9 November 2020).
22. Nakajima, T.; Nikolopoulos, L.A.A. Use of helium double ionization for autocorrelation of an xuv pulse. *Phys. Rev. A* **2002**, *66*, 041402R. [CrossRef]
23. Makris, M.G.; Lambropoulos, P.; Mihelič, A. Theory of Multiphoton Multielectron Ionization of Xenon under Strong 93-eV Radiation. *Phys. Rev. Lett.* **2009**, *102*, 033002. [CrossRef] [PubMed]
24. Son, S.K.; Santra, R. Impact of hollow-atom formation on coherent x-ray scattering at high intensity. *Phys. Rev. A* **2011**, *83*, 033402. [CrossRef]
25. Son, S.K.; Santra, R. Monte Carlo calculation of ion, electron, and photon spectra of xenon atoms in X-ray free-electron laser pulses. *Phys. Rev. A* **2012**, *85*, 063415. [CrossRef]
26. Lorenz, U.; Kabachnik, N.M.; Weckert, E.; Vartanyants, I.A. Impact of ultrafast electronic damage in single-particle x-ray imaging experiments. *Phys. Rev. E* **2012**, *86*, 051911. [CrossRef] [PubMed]
27. Lunin, V.Y.; Grum-Grzhimailo, A.N.; Gryzlova, E.V.; Sinitsyn, D.O.; Petrova, T.E.; Lunina, N.L.; Balabaev, N.K.; Tereshkina, K.B.; Stepanov, A.S.; Krupyanskii, Y.F. Efficient calculation of diffracted intensities in the case of nonstationary scattering by biological macromolecules under XFEL pulses. *Acta Cryst. D* **2015**, *71*, 293–303. [CrossRef]
28. Serkez, S.; Geloni, G.; Tomin, S.; Feng, G.; Gryzlova, E.V.; Grum-Grzhimailo, A.N.; Meyer, M. Overview of options for generating high-brightness attosecond x-ray pulses at free-electron lasers and applications at the European XFEL. *J. Opt.* **2018**, *20*, 024005. [CrossRef]
29. Buth, C.; Beerwerth, R.; Obaid, R.; Berrah, N.; Cederbaum, L.S.; Fritzsche, S. Neon in ultrashort and intense x-rays from free electron lasers. *J. Phys. B At. Mol. Opt. Phys.* **2018**, *51*, 055602. [CrossRef]
30. Ilchen, M.; Mazza, T.; Karamatskos, E.T.; Markellos, D.; Bakhtiarzadeh, S.; Rafipoor, A.J.; Kelly, T.J.; Walsh, N.; Costello, J.T.; O'Keeffe, P.; et al. Two-electron processes in multiple ionization under strong soft-X-ray radiation. *Phys. Rev. A* **2016**, *94*, 013413. [CrossRef]
31. Rudek, B.; Son, S.K.; Foucar, L.; Epp, S.W.; Erk, B.; Hartmann, R.; Adolph, M.; Andritschke, R.; Aquila, A.; Berrah, N.; et al. Ultra-efficient ionization of heavy atoms by intense X-ray free-electron laser pulses. *Nat. Photonics* **2012**, *6*, 858–865. [CrossRef]
32. Rudek, B.; Rolles, D.; Son, S.K.; Foucar, L.; Erk, B.; Epp, S.; Boll, R.; Anielski, D.; Bostedt, C.; Schorb, S.; et al. Resonance-enhanced multiple ionization of krypton at an x-ray free-electron laser. *Phys. Rev. A* **2013**, *87*, 023413. [CrossRef]
33. Allaria, E.; Appio, R.; Badano, L.; Barletta, W.A.; Bassanese, S.; Biedron, S.G.; Borga, A.; Busetto, E.; Castronovo, D.; Cinquegrana, P.; et al. Highly coherent and stable pulses from the FERMI seeded free-electron laser in the extreme ultraviolet. *Nat. Photonics* **2012**, *6*, 699–704. [CrossRef]
34. Finetti, P.; Höppner, H.; Allaria, E.; Callegari, C.; Capotondi, F.; Cinquegrana, P.; Coreno, M.; Cucini, R.; Danailov, M.B.; Demidovich, A.; et al. Pulse Duration of Seeded Free-Electron Lasers. *Phys. Rev. X* **2017**, *7*, 021043. [CrossRef]
35. Amusia, M.Y.; Ivanov, V.K.; Cherepkov, N.A.; Chernysheva, L.V. Interference effects in photoionization of noble gas atoms outer s-shells. *Phys. Lett.* **1972**, *40A*, 361–362. [CrossRef]
36. Lynch, M.J.; Gardner, A.B.; Codling, K.; Marr, G.V. The photoionization of the 3s subshell of argon in the threshold region by photoelectron spectroscopy. *Phys. Lett.* **1973**, *43A*, 237–238. [CrossRef]
37. Amusia, M.; Chernysheva, L.; Yarzhemsky, V. *Handbook of Theoretical Atomic Physics: Data for Photon Absorption, Electron Scattering, and Vacancies Decay*; Springer Science & Business Media: Berlin, Germany, 2012.
38. Tulkki, J.; Aksela, S.; Aksela, H.; Shigemasa, E.; Yagishita, A.; Furusawa, Y. Krypton 4p, 4s, and 3d partial photoionization cross sections below a photon energy of 260 eV. *Phys. Rev. A* **1992**, *45*, 4640–4645. [CrossRef]
39. Sukhorukov, V.L.; Lagutin, B.M.; Petrov, I.D.; Schmoranzer, H.; Ehresmann, A.; Schartner, K.H. Photoionization of Kr near 4s threshold. II. Intermediate-coupling theory. *J. Phys. B At. Mol. Opt. Phys.* **1994**, *27*, 241–256. [CrossRef]
40. Huang, K.N.; Johnson, W.; Cheng, K. Theoretical photoionization parameters for the noble gases argon, krypton, and xenon. *At. Data Nucl. Data Tables* **1981**, *26*, 33–45. doi:10.1016/0092-640X(81)90010-3. [CrossRef]
41. Ehresmann, A.; Vollweiler, F.; Schmoranzer, H.; Sukhorukov, V.L.; Lagutin, B.M.; Petrov, I.D.; Mentzel, G.; Schartner, K.H. Photoionization of Kr 4s: III. Detailed and extended measurements of the Kr 4s-electron ionization cross section. *J. Phys. B At. Mol. Opt. Phys.* **1994**, *27*, 1489–1496. [CrossRef]

42. Berrah, N.; Farhat, A.; Langer, B.; Lagutin, B.M.; Demekhin, P.V.; Petrov, I.D.; Sukhorukov, V.L.; Wehlitz, R.; Whitfield, S.B.; Viefhaus, J.; et al. Angle-resolved energy dependence of the $4p^4nd(^2S_{1/2})$ (n = 4–7) correlation satellites in Kr from 38.5 to 250 eV: Experiment and theory. *Phys. Rev. A* **1997**, *56*, 4545–4553. [CrossRef]
43. Aksela, S.; Aksela, H.; Levasalmi, M.; Tan, K.H.; Bancroft, G.M. Partial photoionization cross sections of Kr 3d, 4s, and 4p levels in the photon energy range 37–160 eV. *Phys. Rev. A* **1987**, *36*, 3449–3450. [CrossRef] [PubMed]
44. Zatsarinny, O. BSR: B-spline atomic R-matrix codes. *Comput. Phys. Commun.* **2006**, *174*, 273–356. [CrossRef]
45. Samson, J.A.R.; Gardner, J.L. Photoionization Cross Sections of the Outer *s*-Subshell Electrons in the Rare Gases. *Phys. Rev. Lett.* **1974**, *33*, 671–673. [CrossRef]
46. Johnson, W.R.; Cheng, K.T. Photoionization of the outer shells of neon, argon, krypton, and xenon using the relativistic random-phase approximation. *Phys. Rev. A* **1979**, *20*, 978–988. [CrossRef]
47. Kiselev, M.D.; Carpeggiani, P.A.; Gryzlova, E.V.; Burkov, S.M.; Reduzzi, M.; Dubrouil, A.; Facciala, D.; Negro, M.; Ueda, K.; Frassetto, F.; et al. Photoelectron spectra and angular distribution in sequential two-photon double ionization in the region of autoionizing resonances of ArII and KrII. *J. Phys. B At. Mol. Phys.* **2020**, accepted. [CrossRef]

atoms

MDPI

Article

Effects of the FEL Fluctuations on the 2s2p Li^+ Auto-Ionization Lineshape

Tejaswi Katravulapally * and Lampros A. A. Nikolopoulos

School of Physical Sciences, Dublin City University, Dublin 9, Ireland; lampros.nikolopoulos@dcu.ie

* Correspondence: katravulapally.tejaswi2@mail.dcu.ie; Tel.: +353-892254459

Received: 30 June 2020; Accepted: 11 July 2020; Published: 14 July 2020

Abstract: The photoionization of Lithium (Li^+) via its doubly-excited state 2s2p ^1P in intense free electron laser (FEL) radiation is studied. A recently developed perturbative statistical description of the atomic dynamics is used to calculate the ionization yield. It is observed that the FEL temporal fluctuations affect the lineshape significantly, strongly dependent on the product of the pulse's coherence time with its intensity, $\sim \tau_c I_0$, which is a measure of the effect of the field in one correlation time. The weak-field long-pulse asymmetric resonant Fano-profile is broadened to resemble a Voight profile. As the intensity increases, the subsequent ionization of Li^{2+} takes over and causes further distortion of the lineshape for Li^+.

Keywords: 2s2p; Lithium-ion; auto-ionization; free electron laser; stochastic average; time dependent density matrix

1. Introduction

The advent of high-order harmonic generation (HOHG) and Free-Electron Laser (FEL) sources in the last two decades has made available radiation which is sufficiently short to compete with sub-femtosecond atomic characteristic times and sufficiently intense to compare and surpass the static interatomic electric fields by orders of magnitudes [1–5]. An important characteristic of this radiation is that it can spatially penetrate the interior of atomic-size systems and interact with the innermost electrons directly; a property which is in complete contrast with intense, long-wavelength, laser (i.e., Ti:Sapphire) where the outermost electrons act as a shield and disallow probe of the inner regions even if the necessary energy is available in the form of multiphoton absroptions. A natural consequence of these breakthrough developments is a shift of the interest to explore and control the dynamics of atomic systems in the short-wavelength radiation regime [1–3,6–8].

In the case of ionization with FEL sources very often the measurements of observables are taken after the target systems have interacted many times with pulses which differ each other in random ways (multishot experiments); then the experimental reports provide only statistically *averaged* values of the observables. For this class of experiments it is inevitable that the temporal fluctuations in the atomic photoionization dynamics should be properly taken into account, in principle, for a fair comparison with the experimental data. This simple fact brings at the forefront a statistical description of the atomic dynamics and in fact there are already a number of works where various theoretical approaches have been applied [9–12].

Recently, we took the effort to develop a perturbative statistical theory which provides the equations-of-motion for the atomic dynamical observables of theoretical and experimental interest (excited population, ionization yield, electron kinetic/angular spectrum, absorption spectrum, etc.) [12]. More specifically we treated the near-resonant photoionization processes as stochastic processes characterized by the fluctuation statistics of the FEL radiation. The FEL was modelled as non-stationary Gaussian stochastic field in line with the model developed by Krinsky and Li [13]; within this model

the FEL statistics has its origin in the self-amplified spontaneous emission (SASE) start-up process, which in turn is treated as a shot-noise stochastic process [14–16].

In the present work we investigate the lineshape of the ionization of Li^+ for FEL fields in the proximity of the $2s2p^1P$ autioinization resonance (AIS). The calculation is based on (a) an ab-initio calculation of the electronic structure and the AIS parameters (position and width of the resonance) [17–20] (b) a formulation of the density matrix elements time-evolution in the Fano basis states (EOMs) [21] (c) the elimination of the continuum state dynamics as well as the subsequent average of the EOMs [12]. Here we do not repeat all the necessary details of the calculations but rather present those steps that are relevant with the particular application to Li^+.

In Section 2 we discuss the calculation method for the atomic structure and the way we extract the Fano parameters from the knowledge of the photoionization cross section and the position and width of the AIS. In Section 3, we present the EOMs for the density matrix elements of the system and in Section 4 their averaged form is presented for the case of a Gaussian, non-stationary FEL field. Finally in Section 5 we investigate the effects of the fluctuations on the lineshape of the ionization yield.

For the presentation of the formulas, atomic units (a.u.) are used throughout the text; For the reader's convenience other units (e.g., eV, fs) are used in the discussion section and the figures caption.

2. Electronic Structure and the Fano Picture of Resonant Ionization

As mentioned, a detailed exposition of the method is included in References [19,20]. Nevertheless, in order to present the logical flow of the calculations we will briefly give the steps involved here; the calculation of the electronic structure [19], the derivation of the density matrix equations [21] and their stochastic average [12] as these are adapted in the present work.

2.1. Atomic Structure Calculations

First we describe the method followed to calculate the transition amplitudes involved in the photoionization process. The Li^+ Hamiltonian in atomic units is given by,

$$\hat{H}_a(\boldsymbol{r_1}, \boldsymbol{r_2}) = \sum_{i=1,2} \hat{h}(\boldsymbol{r_i}) + \hat{V}(\boldsymbol{r_1}, \boldsymbol{r_2}) = \sum_{i=1}^{2} (-\frac{1}{2}\vec{\nabla}_i^2 - \frac{3}{r_i}) + \frac{1}{r_{12}}, \tag{1}$$

where the one-electron Hamiltonians $\hat{h}(\boldsymbol{r_i})$ and the interelectronic potential, $\hat{V}(\boldsymbol{r_1}, \boldsymbol{r_2})$ are defined by inspection.

We consider the interaction of the Li^+ with FEL radiation. Within the non-relativistic approximation a proper Hilbert space to develop a formulation is the one generated by the eigenstates of the total energy, square of the angular momentum and spin operators as well as the corresponding projections, namely, $\hat{H}_a, \hat{L}^2, \hat{S}^2, \hat{L}_z, \hat{S}_z$, where $\hat{L} = \hat{l}_1 + \hat{l}_2$, $\hat{S} = \hat{s}_1 + \hat{s}_2$, where $\hat{l}_i, \hat{s}_i$ are the angular momenta and spin quantum numbers of the two-electrons. Since the interaction between the Li^+ and the FEL radiation does not contain any spin operators and assuming the electric field linearly polarized along the $z-$axis the projection of the total angular momentum and the spin quantum numbers are invariants of the ionization process; which means that the possible states reached, following interaction with the FEL, are singlet states with the same total magnetic quantum number as the ground state, $|g\rangle = |1s^2, {}^1S\rangle$. So in the below all states have $L_z = 0$ and $S = 0, M_S = 0$. The eigenstates are denoted by $|nL\rangle$, the first index representing the eigenenergy, E, and the second one the angular momentum L, values

Having defined the basis, the aim now is the numerical calculation of the two-electron eigenstates of the above Hamiltonian. To this end, the eigenvalue problem to be solved is,

$$\hat{H}_a \Phi_{E_nL}(\boldsymbol{r_1}, \boldsymbol{r_2}) = E_{nL} \Phi_{E_nL}(\boldsymbol{r_1}, \boldsymbol{r_2}), \tag{2}$$

where $\Phi_{E_nL}(\boldsymbol{r_1}, \boldsymbol{r_2})$ are the eigenstates of $\hat{H}_a$ (two-electron field free wavefunctions). The system is assumed to be confined in a sphere of radius R, much larger than the atomic size dimensions. The solution of the partial differential Equation (2) requires the boundary condition to be set, which in our case is to have the wavefunction vanish at the origin and at the boundary, R. Consequently all eigenstates (including the continuum) are now discrete and the bound and continuum states are treated on equal footing. A configuration interaction (CI) approach is employed where the eigenstates are expanded on an *uncorrelated* two-electron basis $\phi^L_{n_1l_1n_2l_2}(\boldsymbol{r_1}, \boldsymbol{r_2})$, formed by Slater determinants of angular momentum coupled one-electron states (configurations) found from the one-electron TISE. More specifically the uncorrelated two-electron basis functions are the eigensolutions of the zero-order Hamiltonian, $\hat{H}_a^{(0)} = \hat{h}_1(\boldsymbol{r_1}) + \hat{h}_2(\boldsymbol{r_2})$, with eigenstates,

$$\phi^L_{n_1l_1n_2l_2}(\boldsymbol{r_1}, \boldsymbol{r_2}) = A_{12} \frac{P_{n_1l_1}(r_1)}{r_1} \frac{P_{n_2l_2}(r_2)}{r_2} \mathcal{Y}^{L0}_{l_1l_2}(\Omega_1, \Omega_2), \tag{3}$$

where $\mathcal{Y}^{LM_L=0}_{l_1l_2}(\Omega_1, \Omega_2)$ are the bipolar spherical harmonics, containing the angular momentum coupling coefficients (Clebsch-Gordon coefficients) and A_{12} is the antisymmetrization operator which acts to exchange the coordinates of the two electrons. The radial functions, $P_{nl}(r)$, are numerically calculated by

$$\left[-\frac{1}{2}\frac{d^2}{dr^2} + \frac{l(l+1)}{2r^2} - \frac{3}{r} \right] P_{nl} = \epsilon_{nl} P_{nl}(r). \tag{4}$$

The radial functions are solved numerically by expanding on a basis of B-Splines with excellent properties for representing continuum states [18,22]. Having solved the numerical calculation of the one-electron states, the two-electron eigenbasis is expanded as,

$$\Phi_{E_nL}(\boldsymbol{r_1}, \boldsymbol{r_2}) = \sum_{n_1l_1n_2l_2} C^{nL}_{n_1l_1n_2l_2} \phi^L_{n_1l_1n_2l_2}(\boldsymbol{r_1}, \boldsymbol{r_2}). \tag{5}$$

Substituting Equation (5) into the TISE and projecting over $\phi^L_{n_1l_1n_2l_2}(\boldsymbol{r_1}, \boldsymbol{r_2})$ converts it to a matrix equation, from which upon diagonalization the eigenenergies E_{nL} and the CI coefficients $C^{nL}_{n_1l_1n_2l_2}$ are obtained.

Assuming the zero-energy level set at the double-ionization threshold, then if a two-electron eigenstate has an energy $E_{nL} < 0$ and both electrons also have negative energy ($\epsilon_1, \epsilon_2 < 0$), then the two-electron state is of bound character. States with energies $E_{nL} > 0$ represent doubly ionized Li with an ejected electron if $\epsilon_1 < 0$ and $\epsilon_2 > 0$ (or vice-versa), and triply ionized Li states and two ejected electrons if $\epsilon_i > 0$ (Note that in Figure 1, the zero-energy level is set equal to the ground state of Li^+) .

Calculation of the two-electron states (bound and continuum) allows the calculation of atomic quantities which are useful to describe interactions with the external environment of the system, for example, collisions, radiation, and so forth. For our particular case we'll be needing the values of the photoionization cross section from the ground state as well as the position and the width of the resonance. Again in the remaining part of this section, we describe swiftly the methodology used.

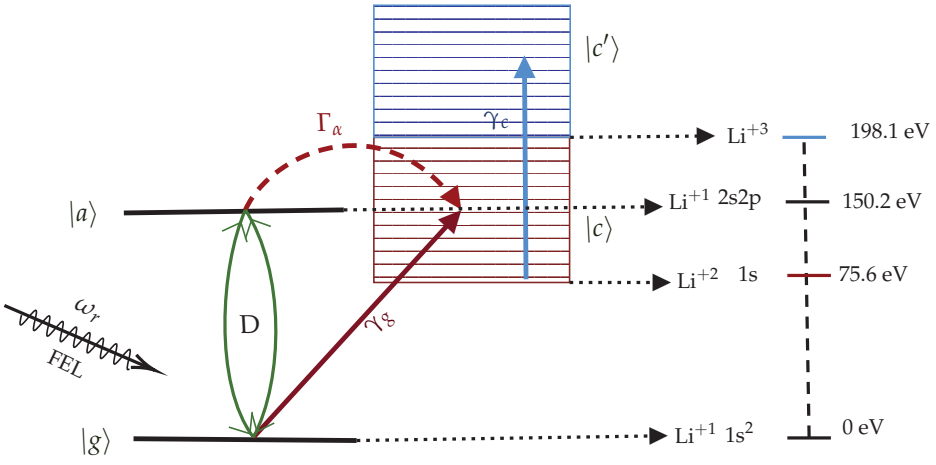

Figure 1. Ionization scheme of Li^+. $|g\rangle$ $1s^2$ is the ground state, $|a\rangle$ 2s2p is the auto-ionizing state, $|c\rangle$ is the continuum above the ionized state of Li^{2+} 1s and the $|c'\rangle$ is the continuum above the ionized state Li^{3+}. The energies depicted on the right are not to scale but only give an idea of the values of the levels.

2.2. Calculation of the Fano Parameters of the AIS

It is convenient to study the ionization process in the Fano-representation which consists to separate the two-electron eigenstates into its bound and continuum part. In Figure 1, the interaction scheme of Li^+ with a FEL pulse is given. The artificial separation of the continuum two-electron wavefunction leads to an effective bound-bound and bound-continuum transition amplitudes which lead to ionization via two different pathways. The first channel initiates with a photon absorption from the ground state, $|g\rangle$, to the artificial Fano-bound state, $|a\rangle$ coupled with the Fano-continuum states, $|c\rangle$, via the interelectronic interaction, V_{ac}, operator; the latter rate of decay is given by the AIS width, Γ_a while the rate of excitation is determined by the dipole transition matrix element, d_{ga}. At the same time, photoionization via a direct transition (d_{gc}) from the ground state to the Fano continuum, $|c\rangle$, is also available. The interference between the two ionization channels ($|g\rangle \rightarrow (d_{ga}) \rightarrow |a\rangle \rightarrow (V_{ac}) \rightarrow |c\rangle$ and $|g\rangle \rightarrow (d_{gc}) \rightarrow |c\rangle$ leads to the well known Fano-asymmetric shape [23].

More specifically, the ground-state $|g\rangle$ ($1s^2$) is considered to be at $E_g = 0$ eV (0 a.u.) and the FEL pulse's central frequency ω is chosen near the resonance energy of $|a\rangle$ (2s2p). The system ionizes into the continuum $|c\rangle$ (ionization potential at 75.6 eV (2.778 a.u.)) characterised by the field-dependent photoionization width $\gamma_g(t)$; also the system, following photon absorption by the field, may excite to the unstable doubly excited auto-ionizing state $|a\rangle$ ($E_a = 150.2$ eV (5.52 a.u.)) with a rate characterized by the field dependent Rabi matrix element $D\mathcal{E}(t)$ coupled with continuum $|c\rangle$. The interference between these two ionizing channels is described by the introduction of the Fano-parameter q_a. Finally, the generated Li^{2+} may further ionize by absorbing one more photon since its ionization potential is 198–75.6 eV (triple ionization of Li ~ 198.1 eV (7.28 a.u.)). We characterize this ionization width as γ_c.

From the above, we see that there arises the need to calculate, $E_a, \Gamma_a, d_{ga}, d_{gc}$ and q_a. Below we give the absolutely necessary formulas for these calculations. The procedure is as follows: (a) from the numerically calculated two-electron states we calculate the photoionization cross section and the position and width of the autoionizing resonance and (b) from these values we calculate the Fano effective parameters, d_{ga}, d_{gc}, q_a.

2.2.1. Photoionization Cross Section and Position, width of the Autoionizing Resonance

The photoionization cross sections of Li^+ in a.u. is calculated by,

$$\sigma_1(E_n) = \frac{4\pi^2}{c}\omega|\langle\Phi_{E_1S}|z_1+z_2|\Phi_{E_nP}\rangle|^2 = \frac{4\pi^2}{c}\omega|d_{1S;nP}|^2, \qquad E_n = E_1+\omega, \tag{6}$$

where ω is the central carrier frequency of the laser field, Φ_{E_1S}, Φ_{E_nP} represent the initial (ground state) and the final (near AIS) states of the system and z_1, z_2 the electron's position operators. A plot of this cross section is given in Reference [20].

Standard theory of the atomic continuum states shows that if the total singly-ionized wave function (above the first ionization threshold) is decomposed as the sum of a bound doubly excited state, its continuum background and all the other zero-order states included, a simple relation for the continuum state's phase shift near the autoionizing states and its position and the width exists:

$$\delta_l(E) = b_0 + b_1E + b_2E^2 + \tan^{-1}\frac{\Gamma_a/2}{E_a - E}, \tag{7}$$

where E_a is the position of the autoionizing state, and Γ_a is the autoionizing width of this state; b_iE^is represent the residual background energy dependence of the phase shift.

With the phase shift, $\delta_l(E)$ calculated numerically, a fit with the above relation provides the values of E_a and Γ_a, shown in Table 1.

Table 1. Atomic parameters in a.u. used for the $Li^+(2s2p)$ AIS resonance.

Parameters	Widths
(E_a, q_a)	(5.52, −2.2)
d_{ga}	0.01527
Γ_a	0.00235
γ_g	0.0819
γ_c	0.0584

The photoionization cross sections of the hydrogenic ion, Li^{++}, is an easier task and calculated by,

$$\sigma_1(\epsilon_{np}) = \frac{4\pi^2}{c}\omega|\langle\phi_{1s}|z|\phi_{np}\rangle|^2 = \frac{4\pi^2}{c}\omega|d_{1s;np}|^2, \qquad \epsilon_{np} = \epsilon_{1s}+\omega, \tag{8}$$

where $\phi_{1s}(\mathbf{r})$ and $\phi_{np}(\mathbf{r})$ are the common eigenstates of the Li^{++} Hamiltonian, angular momentum and its $z-$axis projection. The energies, $\epsilon_{1s}, \epsilon_{np}$ are obtained from the solution of the radial eigenvalue Equation (4). The matrix elements $d_{1s;np}$ have been calculated earlier [19,20].

At this point, for later use, the photoionization yield, caused by a monochromatic field of amplitude E_0 and frequency, ω, should be related with the photoionization cross section. First we need to relate the intensity of a monochromatic electric field with its amplitude. This relation is obtained by taking the time-average of the Poynting vector magnitude, $\mathbf{S}$, $I_0 = \langle S\rangle_t = c\epsilon_0E_0^2/2$ and set $\varepsilon_0 = 1/4\pi$, with ε_0 the vacuum's dielectric constant. This will give $I_0 = cE_0^2/8\pi$. Then by use of standard perturbation theory the ionization yield is related with the photoionization cross section (all quantities in a.u.):

$$\bar{\gamma}_{if} = \sigma_1\frac{I_0}{\omega} = \frac{4\pi^2}{c}\omega|d_{if}|^2\frac{cE_0^2/8\pi}{\omega} = 2\pi|d_{if}|^2\frac{E_0^2}{4} = \gamma_{if}\mathcal{I}, \tag{9}$$

where the bar emphasizes that we refer to a time-averaged ionization rate and $\mathcal{I}$ is defined as the time-averaged intensity $\mathcal{I} = E_0^2/4$. Now γ_{if} represents the average ionization rate when $\mathcal{I} = 1$. The above expression provides the ionization width when the cross section is known, and vice-versa. All the following formulas are expressed in terms of ionization width rather than the photoionization cross section.

2.2.2. Calculation of the Fano Parameters, q_a, d_{ga}, d_{gc}

Having numerically calculated the total photoionization cross section, $\sigma_1(E)$, $E = E_g + \omega$, the position and the width of the autoionizing state, (E_a, Γ_a), we are able to use the Fano approach of the resonant autoionization where the transitions are separated to purely bound-bound and to bound-continuum transitions, as shown in Figure 1. The Fano transition matrix elements to be determined are the q_a,d_{gc} and d_{ga} Fano parameters.

In its simplest form, the Fano parametrization of the dipole photoionization cross section ionization expressed at energy $E = E_g + \omega = E_c = E_{nP}$ is written as,

$$|d_{1S;nP}|^2 = |d_{gc}|^2 \frac{(q+\epsilon)^2}{1+\epsilon^2} = |d_{gc}|^2 (1 + \frac{q_a^2 - 1 + 2q_a\epsilon}{1+\epsilon^2}), \qquad \epsilon = \frac{E - E_a}{\frac{1}{2}\Gamma_a} \tag{10}$$

where $d_{1S;nP}$ is the dipole transition moment in Equation (8). d_{gc} is the dipole transition moment from the ground state to the $|c\rangle$ state and ϵ is the normalized photon energy. In the above parametrization formula, q_a is dimensionless and describes the degree of asymmetry of the resonant line shape,

$$q_a = \frac{d_{ga}}{\pi\, d_{gc} V_{ca}}, \tag{11}$$

where V_{ca} represents the static interelectronic interaction operator $1/r_{12}$. Examination of Equation (10) shows that the ionization profile takes its extrema at the following positions,

$$E_c^{(max)} = E_a + \frac{\Gamma_a}{2q_a}, \qquad E_c^{(min)} = E_a - \frac{1}{2}\Gamma_a q_a. \tag{12}$$

One can select either the minimum or the maximum of the profile to calculate the q_a (given that E_a, Γ_a are known). In fact, knowledge of Γ_a is sufficient since, the E_a can be eliminated by subtracting the above expressions to arrive at,

$$E_c^{(max)} - E_c^{(min)} = \frac{\Gamma_a}{2}(\frac{1}{q_a} + q_a) \qquad \rightarrow \qquad q_a = \frac{E_c^{(max)} - E_c^{(min)}}{\Gamma_a} \pm \sqrt{\left(\frac{E_c^{(max)} - E_c^{(min)}}{\Gamma_a}\right)^2 - 1}. \tag{13}$$

Obviously this formula eliminates any inaccuracy introduced in the calculation by the resonant position.

Following with the calculation of d_{ga} we see from Equation (10) that there is an energy $\bar{E}$ where,

$$q_a^2 + 2q_a\bar{\epsilon} - 1 = 0 \quad \rightarrow \quad \bar{E} = E_a + \frac{\Gamma_a}{2}\frac{1 - q_a^2}{2q_a} \quad \rightarrow \quad |d_{gc}|^2\Big|_{E=\bar{E}} = |d_{1S;nP}|^2\Big|_{E=\bar{E}}. \tag{14}$$

So we can calculate d_{gc} from the above relation and by substituting its value in Equation (11) we obtain d_{ga}, given that $\Gamma_a = 2\pi|V_{\bar{E}}|^2$. This determines the value of d_{ga} up to a sign value, but this can be infered from the ionization profile shape, which also determines the relative sign of d_{ga} and $d_{gc}V_{cg}$. This means that the sign for d_{gc} and V_{cg} (which results to a definite sign for $d_{gc}V_{cg}$) will not affect the dynamics of the ionization; the d_{ga} will obtain a value dependent on this choice and the sign of q_a.

Finally, for later use another useful relation between the Fano parameters is valid:

$$4|d_{ga}|^2 = q_a^2\, \Gamma_a \gamma_g. \tag{15}$$

Following the above methodology for the calculation of the Fano parameters of the $2s2p\ ^1P$ state of Li^+ the obtained values are shown in Table 1.

Having calculated the necessary dynamic parameters for the description of the ionization processes we are now at a position to set up the equation-of-motions (EOMs) for the system's probability

amplitudes. In the present work we'll be using a density-matrix representation to describe the quantum states of the systems and a semiclassical representation of the (stochastic) FEL field.

3. The Density-Matrix EOMs in the Fano Representation

The pulses of FEL radiation differ from shot to shot due to the inherent randomness [13]. This affects the process of obtaining the atomic observables. For a certain class of experiments the observables are the results of multishot interaction with the FEL radiation with the result that any calculation requires the average over an ensemble of shots. Our starting point is to derive the density matrix equation for a FEL field, pretending that it is not fluctuating; this part of derivation is independent on the statistical properties of the field. Having derived these equation we'll be assuming the case of random fluctuations of the FEL field and will proceed with the ensemble averaged form of the density-matrix equations. Both of these steps have been developed and described in detail previously and need not be elaborated with great detail here [12,21]. Nevertheless, some adaptations are still required and as such we will provide here the absolutely necessary information about the calculational methodology for the dynamics.

Our starting point for the first part will be the Liouville equation, $\imath\dot{\hat{\rho}}(t) = [\hat{H}, \hat{\rho}]$ [24]. Here, $\hat{\rho}(t)$ is the density matrix operator and $\hat{H}$ is the Hamiltonian operator which is comprised of the field free Hamiltonian ($\hat{H}_a$) as well as the field-matter interaction operator ($\hat{V}(t)$), that is, $\hat{H} = \hat{H}_a + \hat{D}(t)$. The field-matter interaction operator is given by $\hat{D}(t) = -\hat{d}E(t)$ where $\hat{d}$ characterises the atomic dipole operator and the interacting linearly polarised laser field is modelled as $E(t) = E_o(t)\cos(\omega t + \phi(t))$. This real field relates to the complex field envelope by the relation $\mathcal{E}(t) = \frac{1}{2}E_0(t)e^{-\imath\phi(t)}$. With the complex field modelled as above, we may define the time averaged intensity as $\mathcal{I}(t) = |\mathcal{E}(t)|^2$.

When the interacting field is considered to be having a near resonant frequency, the field free evolution of the density matrices evolve with a time-scale proportional to $\omega \sim |E_a - E_g|$, whereas the presence of the field induces far lower timescales such as $|D_{ag}| << \omega$. This fact can be exploited in eliminating the fast oscillating terms from the system. To this end, we may transform the density matrices into the interaction picture (IP) [21], where the diagonal elements are left intact and the off-diagonal elements are changed by a phase factor. The newly defined density matrix elements are related to the old by $\sigma_{ij}(t) = \rho_{ij}(t)e^{\imath(E_a - E_g)t}$.

It is assumed beforehand that the field-free eigen value problem is solved for the system of Li^+. This gives the eigen state basis on which the density operator is expanded. It is also assumed that the dipole transition matrix elements between the eigen states of the system at play are already known. The final set of modified density matrix equations of motion (EOMs) are given below, in terms of analytic envelopes of the complex field $\mathcal{E}(t)$ and time averaged intensity $\mathcal{I}(t)$.

$$\dot{\sigma}_{gg}(t) = -\gamma_g \mathcal{I}(t)\sigma_{gg}(t) + 2\mathrm{Im}[\mathcal{D}\mathcal{E}(t)\sigma_{ag}(t)], \tag{16a}$$

$$\dot{\sigma}_{aa}(t) = -\Gamma_a \sigma_{aa}(t) - 2\mathrm{Im}[\mathcal{D}^*\mathcal{E}(t)\sigma_{ag}(t)] \tag{16b}$$

$$\dot{\sigma}_{ag}(t) = -\left[\delta + \Delta\mathcal{I}(t)\right]\sigma_{ag}(t) + \imath\mathcal{D}^*\mathcal{E}^*(t)\sigma_{aa}(t) - \imath\mathcal{D}\mathcal{E}^*(t)\sigma_{gg}(t) \tag{16c}$$

$$\dot{\sigma}_{cc}(t) = -\gamma_c \mathcal{I}(t)\rho_{cc}(t) - \dot{\sigma}_{gg}(t) - \dot{\sigma}_{aa}(t). \tag{16d}$$

$Im(z) \equiv (z - z^*)/2\imath$. $\gamma_g = 2\pi|d_{gc}|^2$ and $\gamma_c = 2\pi|d_{1s;\epsilon p}|^2$ are the ionization widths at peak intensity from the Φ_g initial state to the Fano continuum state $|c\rangle$ and from ϕ_{1s} (Li^{2+} ground state) to the continuum state ϕ_{np} (Li^{2+} continuum state), respectively. $\Gamma_a = 2\pi|V_{ac}|^2$ is the autoionization width from the Fano state $|a\rangle$ to the Fano continuum states $|c\rangle$. Δ, δ are the complex peak detunings,

$$\delta = \imath(E_a - E_g - \omega) + \frac{\Gamma_a}{2}, \qquad \Delta = \imath(s_a - s_g) + \frac{\gamma_g}{2}, \tag{17}$$

with s_g, s_a the peak intensity ac-Stark shifts (which are negligible for the intensities considered in this work). Finally, $\mathcal{D}$ is the complex Rabi transition matrix element,

$$\mathcal{D} = d_{ga}(1 - \frac{i}{q_a}), \tag{18}$$

where d_{ga} represents now the real part of the transition matrix element between the ground $|g\rangle$ and the excited $|a\rangle$ state. The interference between the two ionization channels is represented from the imaginary part of $\mathcal{D}$. For $q_a \gg 1$ the indirect ionization channel dominates whereas in the opposite case ionization proceeds via the direct path ($|g\rangle \rightarrow |c\rangle$).

4. The Averaged Density-Matrix EOMs

In the below we first specify the statistical model chosen for the FEL in this work. Based on this model, we provide the corresponding ensemble-averaged EOMs equations for Equations (16). Since the detailed derivation of the averaged EOMs for the density-matrix elements in the Fano representation is presented in Reference [12] here we only provide the final form as they are specified for the chosen model of the FEL field.

4.1. FEL Radiation as a Gaussian, Non-Stationary Stochastic Process

The temporal fluctuations of the field are taken into account by treating the pulse envelope as a stochastic process, more specifically,

$$\mathcal{E}(t) = \mathcal{E}_0(t)\epsilon(t) \tag{19}$$

The $\epsilon(t)$ random process is used to describe the statistical properties of the field whereas the $\mathcal{E}_0(t)$ represents the real slowly varying field envelope. The statistics of the fluctuations are assumed to be fully characterised by the multitime moments (coherences) $\langle \epsilon(t_1)\epsilon(t_2)\ldots\epsilon(t_n)\rangle$. The approach taken here is to assume that the field is a Gaussian stochastic process, which in practice means that its full description requires only the knowledge of its first and second coherence; this is because all the multitime moments are expressed in terms of the first two moments.

More specifically, we assume the model adopted by Krinsky and Li in Reference [13] for FEL radiation where, deterministic part of the field envelope is taken as,

$$\mathcal{E}_0(t) = \mathcal{E}_0 e^{-\hat{\chi}t^2/2\tau_p^2}, \tag{20}$$

where τ_p determines the FWHM duration of the pulse and chirp $\hat{\chi} = 1 - \imath/\sqrt{3}$. The first- and the second- moment of the field are assumed,

$$\langle \epsilon(t)\rangle = 0, \qquad \langle \epsilon(t)\epsilon^*(t-\tau)\rangle = e^{-\tau^2/2\tau_c^2}, \tag{21}$$

where τ_c is the coherence time. With the above assumptions we have for the statistically averaged intensity and the first-order intensity coherence function,

$$\langle \mathcal{I}(t)\rangle = \langle |\mathcal{E}(t)|^2\rangle = \mathcal{E}_0^2 e^{-t^2/\tau_p^2}, \qquad \langle \mathcal{I}(t)\mathcal{I}(t')\rangle = \langle \mathcal{I}(t)\rangle\langle \mathcal{I}(t')\rangle + |\langle \mathcal{E}(t)\mathcal{E}(t')\rangle|^2. \tag{22}$$

The full width half maximum τ_{FWHM} of the average intensity $\langle \mathcal{I}(t)\rangle$ is related to the pulse duration τ_p via $\tau_{FWHM} = 2\tau_p\sqrt{ln2}$. Therefore the FEL is represented as a Gaussian, non-stationary, square-exponentially correlated stochastic process.

4.2. Averaged Form of the EOMs

The presence of the FEL temporal fluctuations render the field to be treated statistically, as a stochastic process, thus making the EOMs for the system to be stochastic differential equations. Let's assume an arbitrary observable as $X(t)$ and consider it as a stochastic process. We can always decompose this into a deterministic and a fluctuating part that is, $X(t) = \langle X(t)\rangle + \widetilde{X}(t)$, where $\langle X(t)\rangle$ is the ensemble average over many shots of the random FEL field and the $\widetilde{X}(t)$ is a fluctuating quantity with zero mean average, $\langle \widetilde{X}(t)\rangle = 0$. For the electric field we have $\langle \mathcal{E}(t)\rangle = 0$ and $\mathcal{E}(t) = \widetilde{\mathcal{E}}(t)$. When $X(t)$ represents the intensity, we have $\mathcal{I}(t) = \langle \mathcal{I}(t)\rangle + \widetilde{\mathcal{I}}(t)$. In the deterministic EOMs Equation (16) the atomic structure parameters are coupled with the field's random variations. Since generally $\langle \sigma_{ij}(t)\mathcal{E}(t)\rangle \neq \langle \sigma_{ij}(t)\rangle\langle \mathcal{E}(t)\rangle$ and $\langle \sigma_{ij}(t)\mathcal{I}(t)\rangle \neq \langle \sigma_{ij}(t)\rangle\langle \mathcal{I}(t)\rangle$ where $i, j = g, a, c$, special statistical methods need to be carefully employed. We have followed a method to obtain the statistical average of the EOMs given the FEL statistical properties; we'll not elaborate the method further here as it has been worked in detail in Reference [12]. We only present the averaged EOMs for the system's density matrix as adapted in the particular Gaussian, non-stationary FEL chosen with statistics as expressed in Equations (19)–(21).

We finally arrive at the following set of averaged density matrix EOMs in the Fano representation:

$$\begin{aligned}\langle \dot{\sigma}_{gg}(t)\rangle = &-\gamma_g\langle \mathcal{I}(t)\rangle\left[1-\gamma_g\tau_c\sqrt{\pi}\frac{\langle I(t)\rangle}{2}+\frac{\Gamma_a\tau_c\sqrt{\pi}}{2\sqrt{2}}\left[(q_a^2-1)U(\frac{\hat{\delta}_-\tau_c}{\sqrt{2}})+2q_aV(\frac{\hat{\delta}_-\tau_c}{\sqrt{2}})\right]\right]\langle\sigma_{gg}(t)\rangle\\ &+(q_a^2+1)\frac{\Gamma_a\gamma_g\tau_c\sqrt{\pi}\langle I(t)\rangle}{2\sqrt{2}}U(\frac{\hat{\delta}_+\tau_c}{\sqrt{2}})\langle\sigma_{aa}(t)\rangle \qquad (23a)\\ \langle \dot{\sigma}_{aa}(t)\rangle = &-\Gamma_a\left[1+\frac{\gamma_g\tau_c\sqrt{\pi}\langle\mathcal{I}(t)\rangle}{2\sqrt{2}}\left[(q_a^2-1)U(\frac{\hat{\delta}_+\tau_c}{\sqrt{2}})-2q_aV(\frac{\hat{\delta}_+\tau_c}{\sqrt{2}})\right]\right]\langle\sigma_{aa}(t)\rangle\\ &+(q_a^2+1)\frac{\Gamma_a\gamma_g\tau_c\sqrt{\pi}\langle I(t)\rangle}{2\sqrt{2}}U(\frac{\hat{\delta}_-\tau_c}{\sqrt{2}})\langle\sigma_{gg}(t)\rangle \qquad (23b)\\ \langle \dot{\sigma}_{cc}(t)\rangle = &-\gamma_c\langle\mathcal{I}(t)\rangle\langle\sigma_{cc}(t)\rangle-\langle\dot{\sigma}_{gg}(t)\rangle-\langle\dot{\sigma}_{aa}(t)\rangle+\gamma_c\tau_c\sqrt{\pi}\frac{\langle I(t)\rangle^2}{2}\left(\gamma_c\langle\sigma_{cc}(t)\rangle-\gamma_g\langle\sigma_{gg}(t)\rangle\right), \qquad (23c)\end{aligned}$$

where the averaged dynamic detunings, $\hat{\delta}_\pm \equiv \hat{\delta}_\pm(t)$, are defined by,

$$\hat{\delta}_\pm(t) = \delta_0 \pm \imath\frac{\Gamma_a - \gamma_g\langle\mathcal{I}(t)\rangle}{2}. \qquad (24)$$

From our atomic-structure calculations we have estimated that the ac-Stark shifts of the bound states and the direct photoionization from the doubly excited state have negligible contribution into dynamics compared to the parameters finally kept in the averaged EOMs.

The $U(z) = U(x,y), V(z) = U(x,y)$ quantities, closely related with the Voight functions, are defined as the real and imaginary of $w(z)$ [25]:

$$w(z) = e^{-z^2}[1-\mathrm{erf}(\imath z)] = U(x,y) + \imath V(x,y), \qquad z = x - \imath y, \qquad (25)$$

where $\mathrm{erf}(z)$ is the error function.

5. Results and Discussion

In this section, we show the results obtained from the averaged EOMs for the Li^+ system for the schematic depicted in the Figure 1. First, we discuss the typical AIS lineshape which is obtained when no fluctuations are included. Then we see how the fluctuation's coherence time of the FEL pulse affects this AIS lineshape. The calculated atomic parameters q_a and Γ_a are in good agreement with those measured in References [26–28] and presented in the Table 1.

5.1. The AIS Line Shape

For a pulse of moderate intensity, free of fluctuations in the amplitude and the phase, the AIS lineshape of Li^+ 2s2p should resemble that of the familiar asymmetric Fano profile [23]. Our findings show that the fluctuations cause a smoothing effect of such sharp asymmetric line shapes. Solving Equation (16) for a deterministic pulse, gives the ionization yield profile depicted by the red-dashed curve of the Figure 2, whereas solving Equation (23) for a Gaussian correlated stochastic pulse, having a coherence time of $\tau_c = 1.3$ fs (53.74 a.u.), gives the ionization yield profile depicted by the black-solid curve of the Figure 2. The peak intensity used is 10^{13} W/cm^2 and the pulse duration used is $\tau_p = 12.7$ fs (525.02 a.u.).

It can be seen that for the same pulse duration and peak intensity we obtain drastically different yield values and lineshapes. The deterministic pulse, as pointed, gives the profile which has a sharp peak and asymmetry around the resonance energy whereas the stochastic pulse gives a smooth peak. The values of the ionization yield are also very different around the resonance but are identical towards the tail-ends. It can be thus concluded that the effects of fluctuations manifest and smooths the lineshape around the resonance, whereas the tail-ends are relatively unaffected.

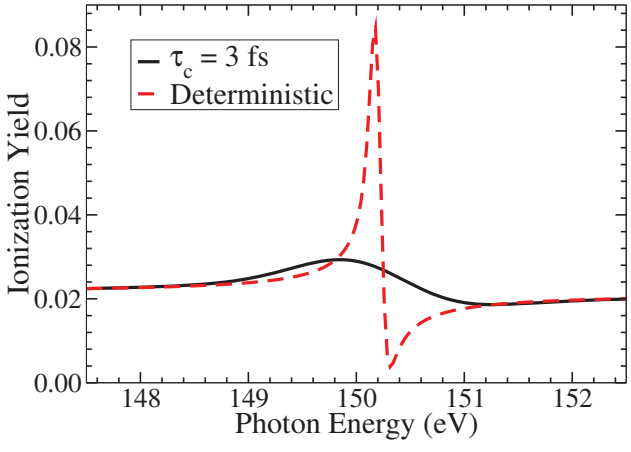

Figure 2. The effect of smoothing the familiar Fano-profile, caused by averaging the fluctuations can be clearly seen in this figure. The red-dashed curve with highest peak is obtained for a deterministic pulse whereas the black-solid curve is obtained for a stochastic pulse with coherence time of 1.3 fs (53.74 a.u.). The peak intensity is 10^{13} W/cm^2 and the pulse duration $\tau_p = 12.7$ fs (525.02 a.u.).

5.2. Effects of the Fluctuation's Coherence Time

For the Gaussian pulse we use the coherence time which is decisive for the ionization dynamics. In Figure 3, we choose four values for the τ_c, 1.3 fs, 3.3 fs, 5.3 fs and 7.3 fs (53.74 a.u., 136.42 a.u., 219.1 a.u. and 301.78 a.u., correspondingly). It can be seen from the said figure that as coherence time increases, the ionization yield around the resonance increases which is accompanied by a narrowing of the AIS lineshape. Ideally, for very large τ_c, these lineshapes tend towards an asymmetric Fano-shape. This trend can be clearly seen here. It can also be observed that the effects of coherence time manifest only around the resonance. Towards the tail ends, the effects are negligible and the yield values are fairly constant.

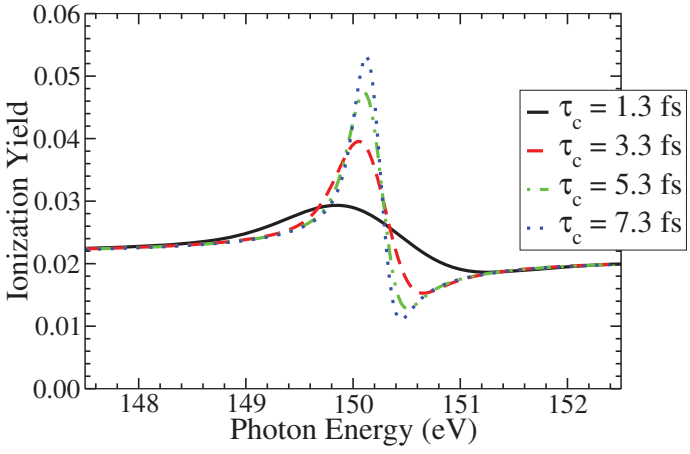

Figure 3. Effect of coherence time on the ionization yield is shown in this plot. As τ_c increases, the ionization yield also increases, near resonance. The peak intensity is 10^{13} W/cm^2 and the pulse duration $\tau_p = 12.7$ fs (525.02 a.u.).

5.3. Effects of the Pulse Duration

Since the pulse duration determines the interaction time with the system it is reasonable to expect that the longer the pulse the more is the ionization yield (this might not be the case under special resonance conditions). Here, we explore the role of pulse duration in affecting the ionization yield for different peak intensities.

In Figure 4, (a) is plotted for the peak intensity of 10^{13} W/cm^2, (b) is for the peak intensity of 10^{14} W/cm^2 and (c) is for the peak intensity of 10^{15} W/cm^2. For (a) and (b) the trend of the yield is that, as pulse duration increases, the yield also increases. But for (c), the trend is reversed. As the peak intensity increases, the yield values decrease. This reversing of the behavior is due to the extra channel of ionization of Li^{2+} from $|c\rangle \rightarrow |c'\rangle$ which is rapidly active at higher peak intensities that is, as peak intensity increases, the population of $|c\rangle$ decreases and the system ionizes into $|c'\rangle$. The same is true with increasing pulse duration as well. That is why, at the highest peak intensity, the ionization yield values are low for the largest pulse duration and high for the smallest pulse duration.

To understand this behavior, we may have to explore the time-evolution of the population of Li^{2+}. In Figure 5, we plot the population of Li^{2+} in time for various peak intensities. The black-solid curve is for the situation when the further channel of ionization is not considered ($\gamma_c = 0$ a.u.) whereas the red-dashed curve is for the current situation where the said channel is present. In the former case, the expected behaviour, namely that by increasing the τ_p increases the ionization yield applies; the plots (a) and (b) depict the rise of populations even after the peak of the pulse (at t = 0 fs) has hit the system. In contrast, for the highest peak intensity, the population of Li^{2+} reaches a maximum before the peak of the pulse and the same population starts to decrease as pulse evolves. This clearly drops the ionization yield values which is the cause for the aforementioned trend-change in Figure 4.

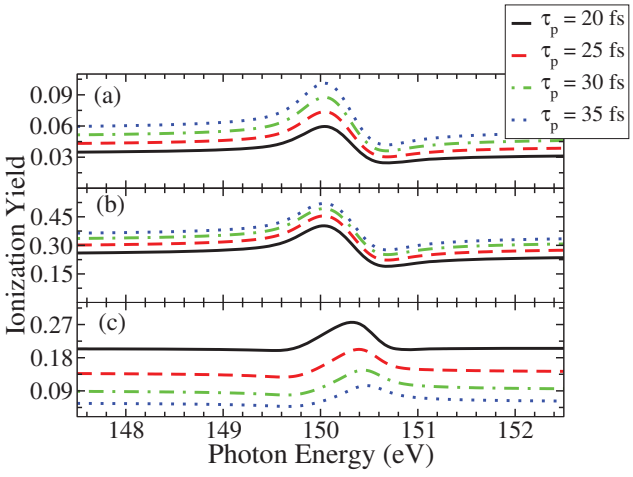

Figure 4. Effect of pulse duration on the ionization yield is shown in this plot. The coherence time used is $\tau_c = 3$ fs (124.02 a.u.) and the peak intensities are: 10^{13} W/cm^2 for (**a**), 10^{14} W/cm^2 for (**b**) and 10^{15} W/cm^2 for (**c**). For lower intensities, as pulse duration increases, the ionization yield also increases. But the pattern flips after certain peak intensity and for the highest peak intensity of 10^{15} W/cm^2, the yield drops as pulse duration increases.

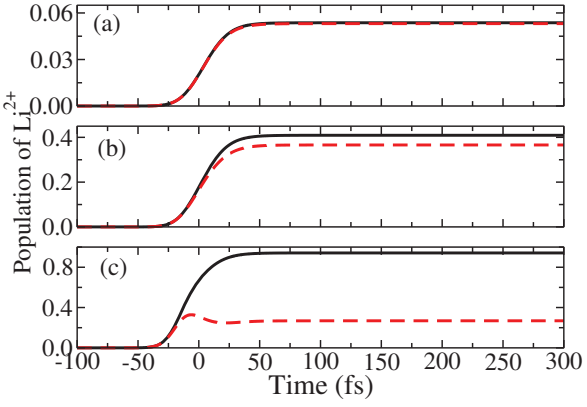

Figure 5. Effect of peak intensity on the population of Li^{2+}. The peak intensities used are: 10^{13} W/cm^2 for (**a**), 10^{14} W/cm^2 for (**b**) and 10^{15} W/cm^2 for (**c**). Black-solid curve is when the further ionization channel is ignored ($\gamma_c = 0$) and the red-dashed curve is when the further ionization channel is considered. The pulse duration $\tau_p = 20$ fs (826.8 a.u.) and the coherence time $\tau_c = 3$ fs (124.02 a.u.). The red-dashed curve suggests that for (**a**) and (**b**) the population grows after the peak intensity at t = 0 fs, but for (**c**) it drops. This causes the change in the trend of ionization of Figure 4.

6. Conclusions

We have investigated the effects of the FEL parameters such as peak-intensity, coherence time and pulse duration on the values of ionization yield of the Li^+ resonance lineshapes. A safe conclusion is that the interaction with a FEL radiation results to lineshapes that may differ from the familiar Fano-like

asymmetry shape. A better insight has been obtained about the role of the temporal fluctuations of the FEL field via their strength and duration.

We have considered the pulsed nature of the FEL by assuming a Gaussian envelope for the field and have taken the first-order coherence function to possess a square-exponential (Gaussian) time dependence, $\sim e^{-(t_1-t_2)^2/2\tau_c^2}$; this choice is different from those that have been assumed so far, when averaging of the EOMs was taken into account as for example $\sim e^{-|t_1-t_2|/2\tau_c}$ of the early lasers of longer-wavelength. The Gaussian-like dependence has been treated to date only within a Monte-Carlo (MC) algorithm type of calculations [9,10]. One of the outcomes is that the dynamics for relatively moderate intensity fields ($\sim 5 \times 10^{14}$ W/cm^2) is determined by directly measured experimental observables, namely its temporal mean intensity and its power spectrum; more accurately, the autocorrelation (AC) functions of the time-integrated electric field amplitude and intensity, $\langle \mathcal{E}(t)\mathcal{E}^*(t')\rangle$ and $\langle \mathcal{I}(t)\mathcal{I}(t')\rangle$, respectively. A second outcome is that the line profile takes the shape of a Voight profile with the Gaussian or the Lorentzian profile to dominate depending on the pulse parameters and the atomic structure.

Author Contributions: All authors have contributed equally to this work. All authors have read and agreed to the published version of the manuscript.

Funding: This research received no external funding.

Acknowledgments: Katravulapaly Tejaswi would like to acknowledge financial support by the Education, Audiovisual and Culture Executive Agency (EACEA) Erasmus Mundus Joint Doctorate Programme Project No. 2011 0033. Also LAAN would like to acknowledge his participation in the COST Action CA18222, 'Attosecond Chemisty'.

Conflicts of Interest: The authors declare no conflict of interest.

Abbreviations

The following abbreviations are used in this manuscript:

AC	Autocorrelation
AIS	Autoionization State
CI	Configuration Interaction
EOMs	Equations of Motion
FEL	Free Electron Laser
FWHM	Full Width at Half Maximum
MC	Monte-Carlo
TISE	Time Independent Schrödinger Equation

References

1. Wabnitz, H.; Bittner, L.; de Castro, A.R.B.; Dohrmann, R.; Gurtler, P.; Laarmann, T.; Laasch, W.; Schulz, J.; Swiderski, A.; von Haeften, K.; et al. Multiple ionization of atom clusters by intense soft X-rays from a free-electron laser. *Nature* **2002**, *420*, 482. [CrossRef]
2. Ackermann, W.; Asova, G.; Ayvazyan, V.; Azima, A.; Baboi, N.; Bahr, J.; Balandin, V.; Beutner, B.; Brandt, A.; Bolzmann, A.; et al. Operation of a free-electron laser from the extreme ultraviolet to the water window. *Nat. Photonics* **2007**, *1*, 336. [CrossRef]
3. Young, L.; Kanter, E.P.; Krässig, B.; Li, Y.; March, A.M.; Pratt, S.T.; Santra, R.; Southworth, S.H.; Rohringer, N.; DiMauro, L.F.; et al. Femtosecond electronic response of atoms to ultra-intense X-rays. *Nature* **2010**, *466*, 56–61. [CrossRef] [PubMed]
4. Allaria, E.; Badano, L.; Bassanese, S.; Capotondi, F.; Castronovo, D.; Cinquegrana, P.; Danailov, M.; D'Auria, G.; Demidovich, A.; De Monte, R.; et al. The FERMI free-electron lasers. *J. Synchrotron Radiat.* **2015**, *22*, 485–491. [CrossRef] [PubMed]
5. Tiedtke, K.; Azima, A.; von Bargen, N.; Bittner, L.; Bonfigt, S.; Düsterer, S.; Faatz, B.; Frühling, U.; Gensch, M.; Gerth, C.; et al. The soft X-ray free-electron laser FLASH at DESY: Beamlines, diagnostics and end-stations. *New J. Phys.* **2009**, *11*, 023029. [CrossRef]

6. Nikolopoulos, L.A.A.; Kelly, T.J.; Costello, J. Theory of ac Stark splitting in core-resonant Auger decay in strong X-ray fields. *Phys. Rev. A* **2011**, *84*, 063419. [CrossRef]
7. Nayak, A.; Dumergue, M.; Kühn, S.; Mondal, S.; Csizmadia, T.; Harshitha, N.; Füle, M.; Kahaly, M.U.; Farkas, B.; Major, B.; et al. Saddle point approaches in strong field physics and generation of attosecond pulses. *Phys. Rep.* **2019**, *833*, 1–52. [CrossRef]
8. Papadogiannis, N.A.; Nikolopoulos, L.A.A.; Charalambidis, D.; Tsakiris, G.D.; Tzallas, P.; Witte, K. On the feasibility of performing non-linear autocorrelation with attosecond pulse trains. *Appl. Phys. B* **2003**, *76*, 721–727. [CrossRef]
9. Rohringer, N.; Santra, R. Resonant Auger effect at high X-ray intensity. *Phys. Rev. A* **2008**, *77*, 053404. [CrossRef]
10. Nikolopoulos, G.M.; Lambropoulos, P. Effects of free-electron-laser field fluctuations on the frequency response of driven atomic resonances. *Phys. Rev. A* **2012**, *86*, 033420. [CrossRef]
11. Mouloudakis, G.; Lambropoulos, P. Effects of field fluctuations on driven autoionizing resonances. *Eur. Phys. J. D* **2018**, *72*, 226. [CrossRef]
12. Katravulapally, T.; Nikolopoulos, L.A.A. Perturbative theory of ensemble-averaged atomic dynamics in fluctuating laser fields. *arXiv* **2020**, arXiv:2006.02477.
13. Krinsky, S.; Li, Y. Statistical analysis of the chaotic optical field from a self-amplified spontaneous-emission free-electron laser. *Phys. Rev. E* **2006**, *73*, 066501. [CrossRef]
14. Rice, S.O. Mathematical analysis of random noise. *Bell Syst. Tech. J.* **1944**, *23*, 282–332. [CrossRef]
15. Evgeny Saldin, E.V. Schneidmiller, M.Y. *The Physics of Free Electron Lasers*; Springer: Berlin/Heidelberg, Germany, 2000.
16. Kim, K.J.; Huang, Z.; Lindberg, R. *Synchrotron Radiation and Free-Electron Lasers*, 1st ed.; Cambridge University Press: Cambridge, UK, 2017.
17. Nikolopoulos, L.A.A.; Nakajima, T.; Lambropoulos, P. Direct versus Sequential Double Ionization of Mg with Extreme-Ultraviolet Radiation. *Phys. Rev. Lett.* **2003**, *90*, 043003. [CrossRef]
18. Nikolopoulos, L.A.A. A package for the ab-initio calculation of one- and two-photon cross sections of two-electron atoms, using a CI B-splines method. *Comput. Phys. Commun.* **2003**, *150*, 140–165. [CrossRef]
19. Hanks, W.; Costello, J.; Nikolopoulos, L. Two- and Three-Photon Partial Photoionization Cross Sections of Li+, Ne8+ and Ar16+ under XUV Radiation. *Appl. Sci.* **2017**, *7*, 294. [CrossRef]
20. Hanks, W. Multi-photon Cross Section of Helium-like Ions Under Soft XUV Fields. Master's Thesis, School of Physical Sciences, Dublin City University, Dublin, Ireland, 2017.
21. Nikolopoulos, L.A.A. *Elements of Photoionization Quantum Dynamics Methods*; Morgan & Claypool Publishers: San Rafael, CA, USA, 2019; pp. 2053–2571. [CrossRef]
22. Bachau, H.; Cormier, E.; Decleva, P.; Hansen, J.E.; Martin, F. Applications of B-splines in Atomic and Molecular Physics. *Rep. Prog. Phys.* **2001**, *64*, 1815. [CrossRef]
23. Fano, U. Effects of Configuration Interaction on Intensities and Phase Shifts. *Phys. Rev.* **1961**, *124*, 1866. [CrossRef]
24. Blum, K. *Density Matrix Theory and Its Applications*; Plenum Press: New York, NY, USA, 1981.
25. *NIST Digital Library of Mathematical Functions*; Release 1.0.27 of 2020-06-15. Available online: http://dlmf.nist.gov/ (accessed on 15 June 2020).
26. Diehl, S.; Cubaynes, D.; Bizau, J.M.; Wuilleumier, F.J.; Kennedy, E.T.; Mosnier, J.P.; Morgan, T.J. New high-resolution measurements of doubly excited states of Li+. *J. Phys. B At. Mol. Opt. Phys.* **1999**, *32*, 4193–4207. [CrossRef]
27. Mosnier, J.P.; Costello, J.; Kennedy, E.; Whitty, W. The photoabsorption spectrum of laser-generated Li+ in the 60–190 eV photon energy range. *J. Phys. B At. Mol. Opt. Phys.* **2000**, *33*, 5203–5214. [CrossRef]
28. Scully, S.W.J.; Álvarez, I.; Cisneros, C.; Emmons, E.D.; Gharaibeh, M.F.; Leitner, D.; Lubell, M.S.; Müller, A.; Phaneuf, R.A.; Püttner, R.; et al. Doubly excited resonances in the photoionization spectrum of Li+: experiment and theory. *J. Phys. B At. Mol. Opt. Phys.* **2006**, *39*, 3957–3968. [CrossRef]

atoms

MDPI

Article

Photoelectron Angular Distributions of Nonresonant Two-Photon Atomic Ionization Near Nonlinear Cooper Minima

Jiri Hofbrucker [1,2,3,*], Latifeh Eiri [1,2], Andrey V. Volotka [1,2] and Stephan Fritzsche [1,2,3]

[1] Helmholtz-Institut Jena, Fröbelstieg 3, D-07743 Jena, Germany; latifeh.iri.iasbs@gmail.com (L.E.); a.volotka@gsi.de (A.V.V.); s.fritzsche@gsi.de (S.F.)
[2] GSI Helmholtzzentrum für Schwerionenforschung GmbH, Planckstrasse 1, D-64291 Darmstadt, Germany
[3] Theoretisch-Physikalisches Institut, Friedrich-Schiller-Universität Jena, Max-Wien-Platz 1, D-07743 Jena, Germany
* Correspondence: j.hofbrucker@gsi.de

Received: 22 July 2020; Accepted: 1 September 2020; Published: 3 September 2020

Abstract: Photoelectron angular distributions of the two-photon ionization of neutral atoms are theoretically investigated. Numerical calculations of two-photon ionization cross sections and asymmetry parameters are carried out within the independent-particle approximation and relativistic second-order perturbation theory. The dependence of the asymmetry parameters on the polarization and energy of the incident light as well as on the angular momentum properties of the ionized electron are investigated. While dynamic variations of the angular distributions at photon energies near intermediate level resonances are expected, we demonstrate that equally strong variations occur near the nonlinear Cooper minimum. The described phenomena is demonstrated on the example of two-photon ionization of magnesium atom.

Keywords: photoionization; nonlinear photoionization; nonlinear interaction; Cooper minimum; angular distributions

1. Introduction

Over the last few decades, studies of nonlinear light-matter interaction have received much attention, both theoretically [1–9] as well as experimentally [10–14]. With the advancement of extreme ultraviolet (EUV) and X-ray light sources such as free-electron lasers (FELs) [15–17], energy restrictions of optical lasers have been removed and new opportunities to investigate ionization of inner-shell electrons of atoms and molecules arose [18]. More importantly, FELs are capable of generating high-brilliance X-ray beams, which enables one to explore the inner-shell electron dynamics [19] but also the multi-photon ionization [11,20]. Modern FEL facilities are even capable to tune the polarization of the intense high-energy beams, which open novel experimental possibilities to investigate the dichroic nature of multi-photon ionization as well as molecular chirality at xuv and X-ray photon energies [21,22].

Two-photon ionization is one of the most fundamental nonlinear (multi-photon) processes, in which two photons are simultaneously absorbed by a target and an electron is emitted. Two-photon ionization can be studied by either detecting the yields of the emitted photoelectrons [23,24], or produced photoions [25] or by collecting the subsequent fluorescence as observed for the two-photon *K*-shell ionization of neutral Ge, Cu, and Co atoms [20,26–28]. From the measured particle yields, it is possible to extract total two-photon ionization cross sections, which gives rise to the ratio of absolute amplitudes for different ionization pathways. Photoelectron angular distributions, on the other hand, provide information not only about the amplitudes, but also the photoelectron phases. One such

experiment was performed at the SACLA FEL [24], where the photoelectron angular distributions of two-photon ionization of helium in the vicinity of $1s2p\ ^1P$ resonances were measured.

In one-photon ionization, the Cooper minimum describes the photon energy at which the (otherwise) dominant ionization channel passes through a local minimum [29]. Such a strong change in the ionization amplitudes is not only imprinted in the total cross section, but even more prominently in the photoelectron angular distributions, where it leads to a breakdown of forward-backward symmetry [14,30]. What is more, the Cooper minimum can be found also in many-photon (nonlinear) ionization of atoms and appears between any two adjacent level resonances of the same angular momentum [31]. We have previously shown, that such a *nonlinear Cooper minimum* enhances the polarization transfer from incident to fluorescence photons [31], and in the case of two-photon *K*-shell ionization, can uniquely reveal multipole contributions in the two-photon ionization process [32]. Furthermore, we have demonstrated that the maximum of elliptical dichroism in photoelectron angular distributions appears near the nonlinear Cooper minimum [5]. Despite the strong effect for elliptically polarized light, the influence of nonlinear Cooper minima on the photoelectron angular distributions of two-photon ionization of atoms has not been studied in detail until today.

The purpose of this paper is to clearly demonstrate the strong effect of nonlinear Cooper minimum upon photoelectron angular distributions in non-resonant two-photon ionization of atoms. This paper is organized as follows. In Section 2, we present our theoretical approach based on second-order perturbation theory and independent-particle approximation. In Section 3, we discuss the impacts of the nonlinear Cooper minimum on photoelectron angular distributions in the two-photon ionization and analyze the importance of the incident photon polarization. Finally, conclusions and outlook are given in Section 4. Relativistic units ($\hbar = c = m = 1$) are used throughout the paper, unless otherwise indicated.

2. Theoretical Background

We here provide a description of two-photon one-electron ionization of neutral atoms, where an atom is initially in a many-electron state $|\alpha_i J_i M_i\rangle$ with total angular momentum J_i and its projection M_i, and where α_i refers to all additional quantum numbers that are necessary for a unique characterization of the state. After the simultaneous interaction of the atom with two identical photons $\gamma(\boldsymbol{k}, \hat{\varepsilon}_\lambda)$ which are characterized by wave vector $\boldsymbol{k}$ and polarization vector $\hat{\varepsilon}_\lambda$, the initial atomic state is excited into a final state. Now, the system contains a singly charged ion $\left|\alpha_f J_f M_f\right\rangle$ and a photoelectron that can be described by the wave function $|\boldsymbol{p}_e m_e\rangle$ with asymptotic momentum $\boldsymbol{p}_e$ and spin projection m_e. The two-photon ionization process can be schematically expressed as

$$|\alpha_i J_i M_i\rangle + 2\gamma(\boldsymbol{k}, \hat{\varepsilon}_\lambda) \rightarrow \left|\alpha_f J_f M_f\right\rangle + |\boldsymbol{p}_e m_e\rangle\,. \tag{1}$$

The two-photon ionization process can be described by density matrix theory, which provides simple access to all possible physical observables as well as control over the polarization of incident and outgoing particles. The final state density matrix of the system after the two-photon ionization process, consisting of both the singly ionized atom and the photoelectron is given by

$$\begin{aligned}\left\langle \alpha_f J_f M_f, \boldsymbol{p}_e m_e \left|\hat{\rho}_f\right| \alpha_f J_f M_f', \boldsymbol{p}_e m_e' \right\rangle = \sum_{M_i M_i'} \sum_{\lambda_1 \lambda_2 \lambda_1' \lambda_2'} \left\langle \alpha_i J_i M_i, \boldsymbol{k}\lambda_1 \boldsymbol{k}\lambda_2 \left|\hat{\rho}\right| \alpha_i J_i M_i', \boldsymbol{k}\lambda_1' \boldsymbol{k}\lambda_2' \right\rangle \\ \times M^{\lambda_1 \lambda_2}_{J_i M_i J_f M_f m_e} M^{\lambda_1' \lambda_2' *}_{J_i M_i' J_f M_f' m_e'}.\end{aligned} \tag{2}$$

Since the neutral atom and the two photons are initially in a product state, the incident density matrix can be decomposed as follows

$$\left\langle \alpha_i J_i M_i, \boldsymbol{k}\lambda_1 \boldsymbol{k}\lambda_2 \left|\hat{\rho}\right| \alpha_i J_i M_i', \boldsymbol{k}\lambda_1' \boldsymbol{k}\lambda_2' \right\rangle = \left\langle \alpha_i J_i M_i \left|\hat{\rho}_i\right| \alpha_i J_i M_i' \right\rangle \left\langle \boldsymbol{k}\lambda_1 \left|\hat{\rho}_\gamma\right| \boldsymbol{k}\lambda_1' \right\rangle \left\langle \boldsymbol{k}\lambda_2 \left|\hat{\rho}_\gamma\right| \boldsymbol{k}\lambda_2' \right\rangle, \tag{3}$$

where the neutral atom is initially taken to be in an unpolarized ground state. Hence, its density matrix simplifies to

$$\left\langle \alpha_i J_i M_i \left| \hat{\rho}_i \right| \alpha_i J_i M_i' \right\rangle = \frac{1}{[J_i]} \delta_{M_i M_i'}. \tag{4}$$

The photon density matrices $\left\langle \boldsymbol{k}\lambda \left| \hat{\rho}_\gamma \right| \boldsymbol{k}\lambda' \right\rangle$ define the degree and direction of polarization of the incoming light and can be conveniently expressed in the helicity representation via Stokes parameters

$$\left\langle \boldsymbol{k}\lambda \left| \hat{\rho}_\gamma \right| \boldsymbol{k}\lambda' \right\rangle = \begin{pmatrix} 1+P_3 & P_1 - iP_2 \\ P_1 + iP_2 & 1-P_3 \end{pmatrix}. \tag{5}$$

Since both photons arise from the same source, they both have equivalent wave vector $\boldsymbol{k}$, energy ω and degree of polarization as defined by the linear (P_1, P_2) and circular (P_3) Stokes parameters. The interaction of the two photons with the neutral atom is calculated within second-order perturbation theory. Within this theory, the interaction is described by the transition amplitude $M^{\lambda_1\lambda_2}_{J_i M_i J_f M_f m_e}$, which takes the form

$$M^{\lambda_1\lambda_2}_{J_i M_i J_f M_f m_e} = \sum\!\!\!\!\!\!\int_{\nu} \frac{\left\langle \alpha_f J_f M_f, \boldsymbol{p}_e m_e \left| \hat{R}(\boldsymbol{k}, \hat{\varepsilon}_{\lambda_2}) \right| \alpha_\nu J_\nu M_\nu \right\rangle \left\langle \alpha_\nu J_\nu M_\nu \left| \hat{R}(\boldsymbol{k}, \hat{\varepsilon}_{\lambda_1}) \right| \alpha_i J_i M_i \right\rangle}{E_i + \omega - E_\nu}. \tag{6}$$

In the above relation, the summation runs over the complete spectrum of intermediate states $|\alpha_\nu J_\nu M_\nu\rangle$. The operator $\hat{R}$ represents the (one-particle) electron-photon interaction operator and can be represented in the second quantization formalism as

$$\hat{R}(\boldsymbol{k}, \hat{\varepsilon}_\lambda) = \sum_{lm} \langle l \left| \boldsymbol{\alpha} \cdot \boldsymbol{A}_\lambda(\omega) \right| m \rangle \, a_l^\dagger a_m, \tag{7}$$

where the wave functions $|l\rangle$ and $|m\rangle$ denote the single-electron initial and final states, and where the electron creation and annihilation operators is represented by $a^\dagger$ and a, respectively. Furthermore, $\boldsymbol{\alpha}$ indicates the vector of the Dirac matrices and $\boldsymbol{A}_\lambda(\omega)$ is the photon wave function. The transition amplitude (6) can be further simplified, by using the multipole decomposition of the photon field $\boldsymbol{A}_\lambda(\omega)$ into spherical tensors

$$\boldsymbol{A}_\lambda(\omega) = 4\pi \sum_{JMp} i^{J-p} [\hat{\boldsymbol{\varepsilon}}_\lambda \cdot \boldsymbol{Y}^{(p)*}_{JM}(\hat{\boldsymbol{k}})] \boldsymbol{a}^{(p)}_{JM}(\boldsymbol{r}). \tag{8}$$

In expression (8), the vector spherical harmonics are represented by $\boldsymbol{Y}^{(p)}_{JM}(\hat{\boldsymbol{k}})$ and the electric and magnetic components of the electromagnetic field are described with index ($p = 1$) and ($p = 0$), respectively. Also, the vector functions $\boldsymbol{a}^{(p)}_{JM}(\boldsymbol{r})$ are sometimes referred to as multipole potentials. Furthermore, by choosing $\hat{\boldsymbol{k}}$ as the quantization axis, the dot product of the polarization vector with the vector spherical harmonics becomes

$$[\hat{\boldsymbol{\varepsilon}}_\lambda \cdot \boldsymbol{Y}^{(p)}_{JM}(\hat{\boldsymbol{k}})] = \sqrt{\frac{[J]}{8\pi}} (-\lambda)^p \delta_{\lambda M}. \tag{9}$$

By making use of the independent-particle approximation and by applying the electron creation and annihilation operators to the initial state, the final state of the system after an ionization process can be written as

$$\left| \alpha_f J_f M_f, \boldsymbol{p}_e m_e \right\rangle = \sum_{m_a M} \left\langle j_a - m_a, J_i M \right| \left. J_f M_f \right\rangle (-1)^{j_a - m_a} a^\dagger_{p_e m_e} a_{n_a j_a l_a m_a} \left| \alpha_i J_i M \right\rangle, \tag{10}$$

where $\langle .., .. | .. \rangle$ represents a Clebsch–Gordan coefficient. The annihilation operator $a_{n_a j_a l_a m_a}$ describes the creation of a vacancy with a single (active) electron with quantum numbers n_a, j_a, l_a, m_a in the initial atomic state. Such description of the final state wave function of the system (photoion and photoelectron) enables us to reduce the many-electron transition amplitude into a single electron amplitude, see [33,34] for details. Further simplification of the transition amplitude arises from expanding of the continuum electron wave function into its partial waves

$$|\boldsymbol{p}_e m_e\rangle = \frac{1}{\sqrt{\varepsilon_e |\boldsymbol{p}_e|}} \sum_{jm_j} \sum_{lm_l} i^l e^{-i\Delta_{jl}} \left\langle lm_l, 1/2 m_e \,|\, jm_j \right\rangle |\varepsilon_e j l m_j\rangle \, Y^*_{lm_l}(\hat{p}_e), \tag{11}$$

with the photoelectron energy $\varepsilon_e = \sqrt{\boldsymbol{p}_e^2 + m^2}$, the phase factor Δ_{jl} and the spherical harmonics $Y^*_{lm_l}(\hat{p}_e)$ that particularly depend on the direction of the emitted electron. Applying all the above expansions as well as the Wigner-Eckart theorem to Equation (6) the transition amplitude can be written for initially closed shell atoms as

$$\begin{aligned} M^{\lambda_1\lambda_2}_{J_i M_i J_f M_f m_e} = & \sum_{p_1 J_1} \sum_{p_2 J_2} \sum_{n_n j_n l_n m_n} i^{J_1 - p_1 + J_2 - p_2} \sqrt{\frac{[J_1, J_2]}{[j_n, j_a]}} (-\lambda_1)^{p_1} (-\lambda_2)^{p_2} \\ \times & \sum_{jm_j} \sum_{lm_l} (-i)^l e^{i\Delta_{jl}} \left\langle lm_l, 1/2 m_e \,|\, jm_j \right\rangle Y_{lm_l}(\hat{p}_e) (-1)^{j - m_j} \\ \times & \left\langle jm_j, J_2 - \lambda_2 \,|\, j_n m_n \right\rangle \sum_{m_a} \left\langle j_a - m_a, J_i M_i \,|\, J_f M_f \right\rangle \left\langle j_n m_n, J_1 - \lambda_1 \,|\, j_a m_a \right\rangle \\ \times & \frac{\left\langle \varepsilon_e j l \left\| \alpha \cdot \boldsymbol{a}^{(p_2)}_{J_2} \right\| n_n j_n l_n \right\rangle \left\langle n_n j_n l_n \left\| \alpha \cdot \boldsymbol{a}^{(p_1)}_{J_1} \right\| n_a j_a l_a \right\rangle}{E_{n_a j_a} + \omega - E_{n_n j_n}}, \end{aligned} \tag{12}$$

where $[J] = 2J + 1$. The angle-differential two-photon ionization cross section can be simply obtained from the density matrix of the final state of our system by tracing out all quantum numbers of the photoion as well as spin of the photoelectron

$$\begin{aligned} \frac{d\sigma}{d\Omega} = & \frac{8\pi^3 \alpha^2}{\omega^2} \sum_{J_f M_f m_e} \left\langle \alpha_f J_f M_f, \boldsymbol{p}_e m_e \left| \hat{\rho}_f \right| \alpha_f J_f M_f, \boldsymbol{p}_e m_e \right\rangle \\ = & \frac{8\pi^3 \alpha^2}{\omega^2} \frac{1}{[J_i]} \sum_{\lambda_1 \lambda_2 \lambda'_1 \lambda'_2} \left\langle \boldsymbol{k}\lambda_1 \left| \hat{\rho}_\gamma \right| \boldsymbol{k}\lambda'_1 \right\rangle \left\langle \boldsymbol{k}\lambda_2 \left| \hat{\rho}_\gamma \right| \boldsymbol{k}\lambda'_2 \right\rangle \sum_{J_f M_f M_i m_e} M^{\lambda_1\lambda_2}_{J_i M_i J_f M_f m_e} M^{\lambda'_1 \lambda'_2 *}_{J_i M_i J_f M_f m_e}. \end{aligned} \tag{13}$$

The photoelectron angular distributions of the two-photon ionization can be factorized using the asymmetry parameters β_m, together associated with the mth-order Legendre polynomials $\mathcal{P}_m$ as follows

$$\frac{d\sigma}{d\Omega} = \frac{\sigma}{4\pi} \sum_{m=1} [1 + \beta_m \mathcal{P}_m(\cos\Phi)], \tag{14}$$

where σ represents the total (angle-integrated) two-photon ionization cross section. The meaning of the angle Φ depends on the incident photon polarization. For ionization of atoms by linearly polarized light, Φ is the angle in the polarization plane, measured from the polarization direction. For ionization of atoms by circularly polarized light the angle represents the angle between photon propagation and electron emission directions. Since we shall analyze below the energy dependence of the photoelectron angular distributions, the asymmetry parameters β_m provide a convenient way of presenting this dependence. Moreover, in the scenario considered below, the asymmetry parameters β_2 and β_4 are fully sufficient to describe the presented results as the contributions from all higher orders are negligible.

3. Results and Discussions

Although the formalism presented in the previous section applies generally and is independent of the particular choice of the atom, we here present our results on the example of nonsequential two-photon ionization of magnesium atoms. Furthermore, the photoelectron angular distributions corresponding to the release of an electron from an individual subshell share similar characteristics if their total angular momentum is the same. Here, we shall restrict ourselves to two-photon ionization of the 1*s* and $2p_{1/2}$ electrons only. Further spin contributions were included in the calculations of the presented results, however, they were found to be negligible. For the sake of simpler future discussion, we will restrict ourselves to the nonrelativistic limit, where the electron spin is ignored. Moreover, we will describe the ionization within single-active electron approximation, and refer to single-electron ionization pathways (see Figure 1 for schematic representation of electric dipole pathways in two-photon ionization of 1*s* and $2p_{1/2}$ electrons). This ignores coupling of this active electron with other electrons of the atom and replaces the interaction with the other electrons to simply their mean potential. An effective potential is also widely used in calculations of multi-photon ionization using solutions of time-dependent Schrödinger equation, which for long pulse lengths are in agreement with time-independent perturbation theory [7]. In our previous work [31], we evaluated the uncertainty in our calculations due to the choice of the screening potential by using a number of different potential models. There are approaches beyond the independent-particle approximation (see, e.g., [4]), however, they are usually applied for ionization by soft XUV photon energies and cannot be applied for deep inner-shell ionization. There are currently no approaches which utilize full many-electron calculation for calculation of two-photon ionization of inner-shell electrons. However, a full many-electron calculation of two-photon ionization process is planned to be integrated in the publicly available atomic structures and processes computing software JAC [35] in near future.

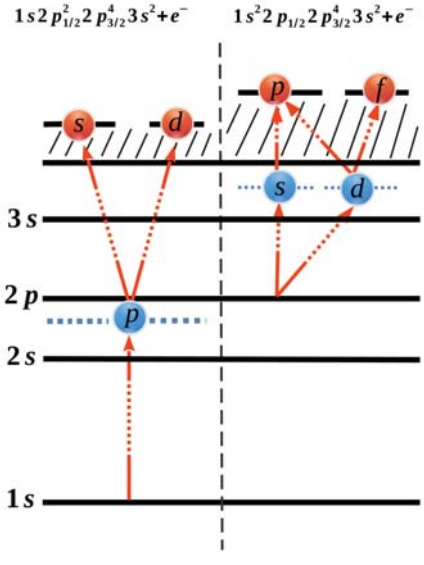

Figure 1. Schematic diagram of possible electric dipole ionization pathways for two-photon ionization of a 1*s* (**left**) and $2p_{1/2}$ (**right**) electrons of neutral magnesium. The possible electric dipole ionization pathways in the single-active-electron picture are represented by red arrows. At the nonlinear Cooper minimum, the ionization pathways with highest angular momentum (right-most pathways) have zero contribution to the process. This has a significant impact upon all physical observables associated with the process.

Our results for two-photon ionization of $1s$ and $2p_{1/2}$ electrons of magnesium are presented in Figure 2. The first row presents the total cross section for two-photon ionization of the $1s$ (left) and $2p_{1/2}$ (right) electrons of magnesium. The total cross sections are presented for incident photon energies in the range of the first corresponding resonances, which can be seen as a local increase of the value of the total cross section. Between each pair of intermediate resonances with total orbital angular momentum of $l_n = l_a + 1$ due to the partial wave of the outgoing electron, there is a local minimum called nonlinear Cooper minimum. Such minimum appears due to zero contribution of the (otherwise) dominant ionization channel and is marked in Figure 2 with a vertical dashed line, see Ref. [31] for detailed explanation of the minimum. As seen from this figure, the drop in the total cross section is larger for the two-photon ionization by circularly polarized photons. This can be easily understood from the selection rules. For ionization by circularly polarized light, the only electric dipole ionization pathway of the photoelectron is $l_a \to l_a + 1 \to l_a + 2$, which by the Fano's propensity rules [36], is generally the dominant ionization pathway. Therefore, while electric dipole interaction contributions vanish at the nonlinear Cooper minimum for ionization by circularly polarized light, other electric dipole channels remain in the case of two-photon ionization by linearly polarized light, resulting in significantly higher total cross sections. Similar to the Cooper minimum in one-photon ionization, the nonlinear Cooper minimum has an impact not only on the total cross section, but is even more pronounced in photoelectron angular distributions.

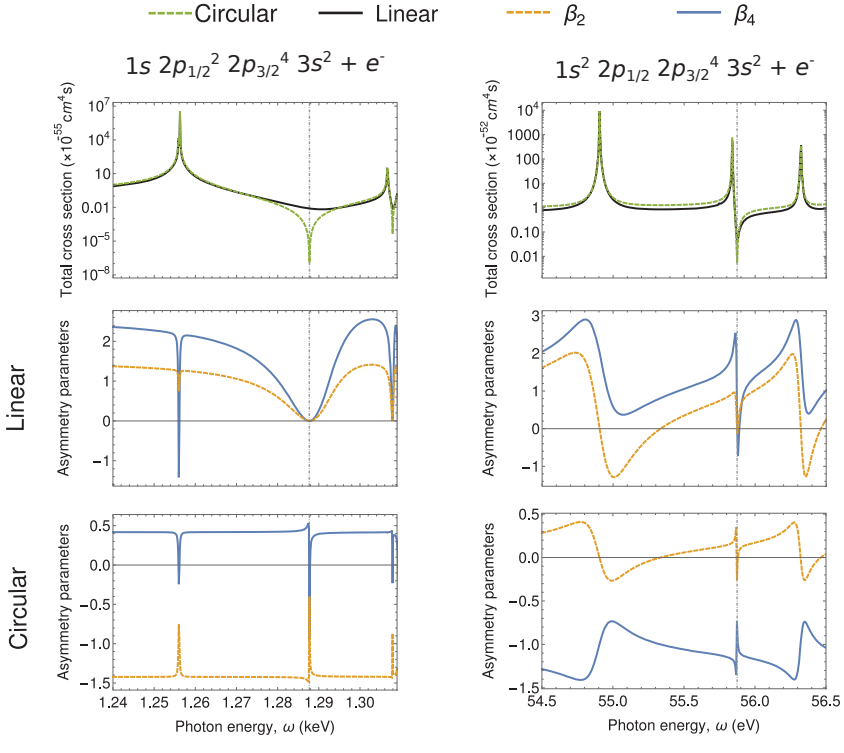

Figure 2. Two-photon ionization of $1s$ (**left**) and $2p_{1/2}$ (**right**) electrons of neutral magnesium. Local minima in the total ionization cross section (first row) can be clearly seen. These so called nonlinear Cooper minima arise due to a zero contribution from the otherwise dominant ionization channel. The minima are even more strongly imprinted in the photoelectron angular distributions both for ionization of magnesium by linearly (second row) as well as circularly (last row) polarized light.

The angular distributions of two-photon ionization of the $1s$ and $2p$ electrons of neutral magnesium is presented in the second and third rows of Figure 2. The photoelectron angular distributions are described using the asymmetry parameters (see Equation (14)) for ionization by linearly (middle) and circularly (bottom) polarized light, and their dependence on incident photon energy is plotted. Strong variation of the photoelectron angular distributions is predicted both, if the incident photon energies match intermediate level resonances as well as near to the nonlinear Cooper minima. While the influence of intermediate resonances has been discussed before [4,37], the variation at nonlinear Cooper minima have not been discussed until now. We will, therefore, concentrate on the variation of angular distributions at the nonlinear Cooper minima only. Significant differences can be seen for different angular momentum of the created hole as well as polarization of the incident photons. For two-photon ionization of $1s$ electrons by linearly polarized light, two nonrelativistic electric dipole ionization pathways are possible, $s \to p \to s$ and $s \to p \to d$. Since the the latter pathway vanishes at the nonlinear Cooper minimum, the distribution is predominantly determined by an electron partial wave with spherical symmetry. As a result, both asymmetry parameters drop to zero at the Cooper minimum. For the two-photon ionization of s electrons by circularly polarized light, in contrast, only the $s \to p \to d$ pathway is allowed by the selection rules. However, as mentioned before, this pathway vanishes at the nonlinear Cooper minimum, and hence, the distribution at this energy is determined purely by higher multipole order. Similar argumentation can be carried out for the two-photon ionization of p electrons. However, in this case, more pathways contribute to the process which leads to less intuitive explanation.

Explicit photoelectron distributions of two-photon ionization of $1s$ (left) and $2p_{1/2}$ (right) electrons of neutral magnesium by linearly polarized light are presented in Figure 3. The distributions are presented in the polarization plane for three incident photon energies, one matching the nonlinear Cooper minimum (solid black), one matching an intermediate resonance ($2p_{1/2}$ and $3d$ for ionization of $1s$ and $2p_{1/2}$ electrons, respectively, plotted with long dashed green curve) and one which does not match either of these extrema (short dashed orange). The presented distributions have been normalized to the value of the corresponding total cross section. While the photon energy matching neither extrema represents a typical photoelectron angular distribution, strong variation can be clearly seen at photon energies matching either an intermediate level resonance or the nonlinear Cooper minimum. In the case of two-photon ionization of $1s$ electrons at the Cooper minimum by linearly polarized light, the photoelectron distribution becomes spherically symmetric, as discussed before. For two-photon ionization of $2p_{1/2}$ electrons, on the other hand, the dominant ionization direction is perpendicular to the photon polarization direction. This counter-intuitive results arises from the vanishing contributions of the otherwise dominant ionization pathway and relatively stronger contributions of pathways with lower angular momentum.

Accurate measurement of the energy position of nonlinear Cooper minima would allow to critically evaluate the theoretical representation of the complete electron spectrum of atoms. As can be seen from Figure 2, measurements of the total cross sections could be too insensitive for an accurate determination of the position this minimum, especially since the accuracy of the experimentally determined cross sections suffer higher uncertainties due to beam parameters employed in the experiment. Photoelectron angular distributions, on the other hand, are independent of the intensity of the incident beam and hence, can lead to more precise extraction of the position of the Cooper minimum. Moreover, Figure 2 also shows that the distributions vary very dynamically near the nonlinear Cooper minimum of the dominant ionization channel ($l_a \to l_a + 1 \to l_a + 2$). Nonlinear Cooper minima can be found between any pair of intermediate resonances of the same angular momentum, and hence, their detection is not restricted to a particular atom or incident beam energies. It is these properties that make the photoelectron spectroscopy a promising tool for the first determination of Cooper minima in multiphoton ionization.

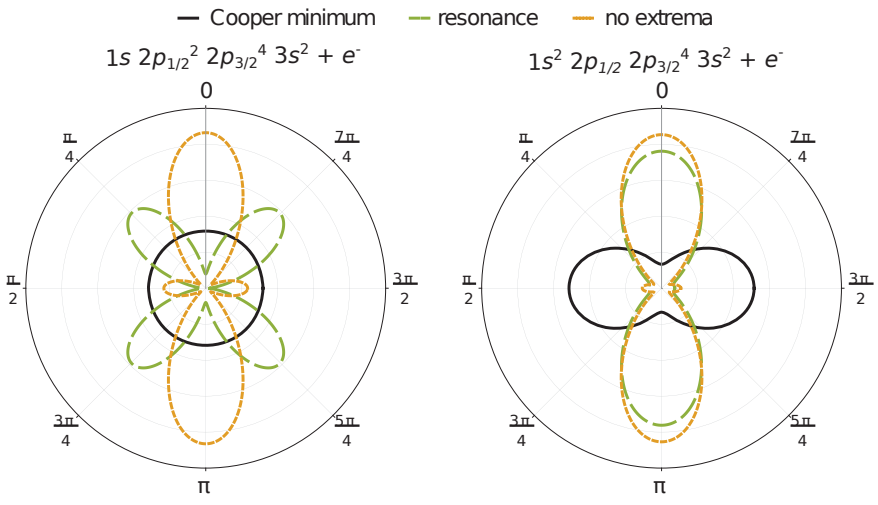

Figure 3. Photoelectron angular distributions of two-photon ionization of 1*s* (**left**) and $2p_{1/2}$ (**right**) electrons of neutral magnesium atoms by linearly polarized light. The distributions were normalized to the total cross section. For ionization of each shell, distributions corresponding to three different photon energies are presented. Incident photon energy matching either the nonlinear Cooper minimum in solid black (1.288 keV and 55.88 eV for ionization of 1*s* and $2p_{1/2}$ electrons, respectively), an intermediate level resonance ($2p_{1/2}$ and 3*d* for ionization of 1*s* and $2p_{1/2}$ electrons, respectively) in long-dashed green (1.256 keV and 55.835 eV) or an energy, which does not match either extrema in short-dashed orange (1.260 keV and 54.50 eV). From the plot, it can be clearly seen that the photoelectron angular distributions at the nonlinear Cooper minima are always distinct.

4. Conclusions

The photoelectron angular distributions of two-photon ionization of 1*s* and $2p_{1/2}$ electrons of neutral magnesium have been investigated theoretically. The energy dependence of the angular distribution was presented in terms of asymmetry parameters. In particular, the distributions in the vicinity of nonlinear Cooper minimum are discussed and their strong variation near the minimum is demonstrated. Such a dynamic variation of the angular distributions near the nonlinear Cooper minimum can be utilized, for instance, for determining the position of the minima, as well as for the phase extraction near the minima from experiment, where the different amplitudes have comparable amplitudes.

Author Contributions: J.H. and L.E. have written the manuscript with the input from A.V.V., Figure 1 was created by L.E., the used numerical tools were programmed by J.H. and A.V.V., the two authors also performed the calculations of the presented results. S.F. supervised the project throughout its duration. All authors have read and agreed to the published version of the manuscript.

Funding: This research received no external funding.

Conflicts of Interest: The authors declare no conflict of interest.

References

1. Nikolopoulos, L.A.A.; Lambropoulos, P. Multiphoton ionization of helium under uv radiation: Role of the harmonics. *Phys. Rev. A* **2006**, *74*, 063410. [CrossRef]
2. Rohringer, N.; Santra, R. X-ray nonlinear optical processes using a self-amplified spontaneous emission free-electron laser. *Phys. Rev. A* **2007**, *76*, 033416. [CrossRef]
3. Florescu, V.; Budriga, O.; Bachau, H. Two-photon ionization of hydrogen and hydrogenlike ions: Retardation effects on differential and total generalized cross sections. *Phys. Rev. A* **2012**, *86*, 033413. [CrossRef]

4. Lagutin, B.M.; Petrov, I.D.; Sukhorukov, V.L.; Demekhin, V.; Knie, A.; Ehresmann, A. Relativistic, correlation, and polarization effects in two-photon photoionization of Xe. *Phys. Rev. A* **2017**, *95*, 063414. [CrossRef]
5. Hofbrucker, J.; Volotka, A.V.; Fritzsche, S. Maximum elliptical dichroism in atomic two-photon ionization. *Phys. Rev. Lett.* **2018**, *121*, 053401. [CrossRef]
6. Wang, M.-X.; Liang, H.; Xiao, X.-R.; Chen, S.-G.; Peng, L.-Y. Time-dependent perturbation theory beyond the dipole approximation for two-photon ionization of atoms. *Phys. Rev. A* **2019**, *99*, 023407. [CrossRef]
7. Gryzlova, E.; Popova, M.M.; Grum-Grzhimailo, A.N.; Staroselskaya, E.I.; Douguet, N.; Bartschat, K. Coherent control of the photoelectron angular distribution in ionization of neon by a circularly polarized bichromatic field in the resonance region. *Phys. Rev. A* **2019**, *100*, 063417. [CrossRef]
8. Boll, D.I.R.; Martini, L.; Fojón, O.A.; Palacios, A. Off-resonance-enhanced polarization control in two-color atomic ionization. *Phys. Rev. A* **2020**, *101*, 013428. [CrossRef]
9. Venzke, J.; Jaroń-Becker, A.; Becker, A. Ionization of helium by an ultrashort extreme-ultraviolet laser pulse. *J. Phys. B: At. Mol. Opt. Phys.* **2020**, *53*, 085602. [CrossRef]
10. Dodhy, A.; Compton, R.N.; Stockdale J.A.D. Photoelectron angular distributions for near-threshold two-photon ionization of cesium and rubidium atoms. *Phys. Rev. Lett.* **1985**, *54*, 422. [CrossRef]
11. Meyer, M.; Cubaynes, D.; Glijer, D.; Dardis, J.; Hayden, P.; Hough, P.; Richardson, V.; Kennedy, E.T.; Costello, J.T.; Radcliffe, P.; et al. Polarization control in two-color above-threshold ionization of atomic helium. *Phys. Rev. Lett.* **2008**, *101*, 193002. [CrossRef] [PubMed]
12. Ishikawa, K.L.; Kawazura Y.; Ueda, K. Two-photon ionization of atoms by ultrashort laser pulses. *J. Mod. Opt.* **2010**, *57*, 999. [CrossRef]
13. Richardson, V.; Li, W.B.; Kelly, T.J.; Costello, J.T.; Nikolopoulos, L.A.A.; Düsterer, S.; Cubaynes, D.; Meyer, M. Dichroism in the above-threshold two-colour photoionization of singly charged neon. *J. Phys. B: At. Mol. Opt. Phys.* **2012**, *45*, 085601. [CrossRef]
14. Ilchen, M.; Hartmann, G.; Gryzlova, E.V.; Achner, A.; Allaria, E.; Beckmann, A.; Braune, M.; Buck, J.; Callegari, C.; Coffee, R.N.; et al. Symmetry breakdown of electron emission in extreme ultraviolet photoionization of argon. *Nat. Commun.* **2018**, *9*, 4659. [CrossRef] [PubMed]
15. Shintake, T.; Tanaka, H.; Hara, T.; Tanaka, T.; Togawa, K.; Yabashi, M.; Otake, Y.; Asano, Y.; Bizen, T.; Fukui, T.; et al. A compact free-electron laser for generating coherent radiation in the extreme ultraviolet region. *Nature Photon.* **2008**, *2*, 555. [CrossRef]
16. Emma, P.; Akre, R.; Arthur, J.; Bionta, R.; Bostedt, C.; Bozek, J.; Brachmann, A.; Bucksbaum, P.; Coffee, R.; Decker, F.-J.; et al. First lasing and operation of an ångstrom-wavelength free-electron laser. *Nature Photon.* **2010**, *4*, 641. [CrossRef]
17. Pabst, S. Atomic and molecular dynamics triggered by ultrashort light pulses on the atto- to picosecond time scale. *Eur. Phys. J. Spec. Top.* **2013**, *221*, 1. [CrossRef]
18. Pellegrini, C.; Marinelli, A.; Reiche, S. The physics of X-ray free-electron lasers. *Rev. Mod. Phys.* **2016**, *88*, 015006. [CrossRef]
19. Tamasaku, K.; Nagasono, M.; Iwayama, H.; Shigemasa, E.; Inubushi, Y.; Tanaka, T.; Tono, K.; Togashi, T.; Sato, T.; Katayama, T.; et al. Double core-hole creation by sequential attosecond photoionization. *Phys. Rev. Lett.* **2013**, *111*, 043001. [CrossRef]
20. Tamasaku, K.; Shigemasa, E.; Inubushi, Y.; Inoue, I.; Osaka, T.; Katayama, T.; Yabashi, M.; Koide, A.; Yokoyama, T.; Ishikawa, T. Nonlinear spectroscopy with X-ray two-photon absorption in metallic copper. *Phys. Rev. Lett.* **2018**, *121*, 083901. [CrossRef]
21. Lutman, A.A.; MacArthur, J.P.; Ilchen, M.; Lindahl, A.O.; Buck, J.; Coffee, R.N.; Dakovski, G.L.; Dammann, L.; Ding, Y.; Dürr, H.A.; et al. Polarization control in an X-ray free-electron laser. *Nature Photon.* **2016**, *10*, 468. [CrossRef]
22. Ilchen, M.; Douguet, N.; Mazza, T.; Rafipoor, A.J.; Callegari, C.; Finetti, P.; Plekan, O.; Prince, K.C.; Demidovich, A.; Grazioli, C.; et al. Circular dichroism in multiphoton ionization of resonantly excited He^+ ions. *Phys. Rev. Lett.* **2017**, *118*, 013002. [CrossRef] [PubMed]
23. Richardson, V.; Costello, J.T.; Cubaynes, D.; Düsterer, S.; Feldhaus, J.; van der Hart, H.W.; Juranić, P.; Li, W.B.; Meyer, M.; Richter, M.; et al. Two-photon inner-shell ionization in the extreme ultraviolet. *Phys. Rev. Lett.* **2010**, *105*, 013001. [CrossRef] [PubMed]

24. Ma, R.; Motomura, K.; Ishikawa, K.L.; Mondal, S.; Fukuzawa, H.; Yamada, A.; Ueda, K.; Nagaya, K.; Yase, S.; Mizoguchi, Y.; et al. Photoelectron angular distributions for the two-photon ionization of helium by ultrashort extreme ultraviolet free-electron laser pulses. *J. Phys. B: At. Mol. Opt. Phys.* **2013**, *46*, 164018. [CrossRef]
25. Richter, M.; Amusia, M.Y.; Bobashev, S.V.; Feigl, T.; Juranić, P.N.; Martins, M.; Sorokin, A.A.; Tiedtke, K. Extreme ultraviolet laser excites atomic giant resonance. *Phys. Rev. Lett.* **2009**, *102*, 163002. [CrossRef] [PubMed]
26. Tamasaku, K.; Shigemasa, E.; Inubushi, Y.; Katayama, T.; Sawada, K.; Yumoto, H.; Ohashi, H.; Mimura, H.; Yabashi, M.; Yamauchi, K.; et al. X-ray two-photon absorption competing against single and sequential multiphoton processes. *Nature Photon.* **2014**, *8*, 313. [CrossRef]
27. Szlachetko, J.; Hoszowska, J.; Dousse, J.-C.; Nachtegaal, M.; Błachucki, W.; Kayser, Y.; Sá, J.; Messerschmidt, M.; Boutet, S.; Williams, G.J.; et al. Establishing nonlinearity thresholds with ultraintense X-ray pulses. *Sci. Rep.* **2016**, *6*, 33292. [CrossRef]
28. Tyrała, K.; Milne, C.; Wojtaszek, K.; Wach, A.; Czapla-Masztafiak, J.; Kwiatek, W.M.; Kayser, Y.; Szlachetko, J. Cross-section determination for one- and two-photon absorption of cobalt at hard-X-ray energies. *Phys. Rev. A* **2019**, *99*, 052509. [CrossRef]
29. Cooper, J.W. Photoionization from outer atomic subshells. A model study. *Phys. Rev.* **1962**, *128*, 681. [CrossRef]
30. Pradhan, G.B.; Jose, J.; Deshmukh, P.C.; LaJohn, L.A.; Pratt, R.H.; Manson, S.T. Cooper minima: A window on nondipole photoionization at low energy. *J. Phys. B: At. Mol. Opt. Phys.* **2011**, *44*, 201001. [CrossRef]
31. Hofbrucker, J.; Volotka, A.V.; Fritzsche, S. Fluorescence polarization as a precise tool for understanding nonsequential many-photon ionization. *Phys. Rev. A* **2019**, *100*, 011401(R). [CrossRef]
32. Hofbrucker, J.; Volotka, A.V.; Fritzsche, S. Breakdown of the electric dipole approximation at Cooper minima in direct two-photon ionization. *Sci. Rep.* **2020**, *10*, 3617. [CrossRef] [PubMed]
33. Hofbrucker, J.; Volotka, A.V.; Fritzsche, S. Relativistic calculations of the non-resonant two-photon ionization of neutral atoms. *Phys. Rev. A* **2016**, *94*, 063412. [CrossRef]
34. Hofbrucker, J.; Volotka, A.V.; Fritzsche, S. Photoelectron distribution of nonresonant two-photon ionization of neutral atoms. *Phys. Rev. A* **2017**, *96*, 013409. [CrossRef]
35. Fritzsche, S. A fresh computational approach to atomic structures, processes and cascades. *Comput. Phys. Commun.* **2019**, *240*, 1. [CrossRef]
36. Fano, U. Propensity rules: An analytical approach. *Phys. Rev. A* **1985**, *32*, 617. [CrossRef]
37. Petrov, I.D.; Lagutin, B.M.; Sukhorukov, V.L.; Novikovskiy, N.M.; Demekhin, V.; Knie, A.; Ehresmann A. Many-electron character of two-photon above-threshold ionization of Ar. *Phys. Rev. A* **2019**, *99*, 013408. [CrossRef]

atoms

MDPI

Article

Spin-Polarized Photoelectron Fluxes from Fullerene Anions

Valeriy K. Dolmatov

Department of Physics and Earth Science, University of North Alabama, Florence, AL 35630, USA; vkdolmatov@una.edu

Received: 30 July 2020; Accepted: 24 September 2020; Published: 29 September 2020

Abstract: Initial insights into spin-polarized photoelectron fluxes from fullerene anions are presented here. Both the angle-dependent and angle-integrated degrees of spin polarization of said photoelectron fluxes are discussed. Empty $C_{60}^{-}(2p)$ and endohedral $H@C_{60}^{-}(2p)$ and $He@C_{60}^{-}(2p)$ anions, where the attached electron resides in a $2p$ state, are chosen as case studies. We uncover the characteristics of the phenomenon in the framework of a semi-empirical methodology where the C_{60} cage is modeled by a spherical annular potential, rather than aiming at a rigorous study. It is found that the spin-polarization degree of photoelectron fluxes from fullerene anions can reach large values, including a nearly complete polarization, at/in specific values/domains of the photoelectron momentum. This is shown to correlate with an inherent feature of photoionization of fullerenes, the abundance of resonances, known as confinement resonances, in their photodetachment spectra owing to a large empty space inside fullerenes. Moreover, the results obtained can serve as a touchstone for future studies of the phenomenon by more rigorous theories and/or experiments to reveal the significance of interactions omitted in the present study.

Keywords: spin-polarization; fullerene anions; endohedral fullerene anions; photodetachment

1. Introduction

Photoionization/photodetachment of various neutral ($q = 0$) and charged ($q \neq 0$) fullerenes, $C_N^{\pm q}$, and their endohedral counterparts, $A@C_N^{\pm q}$ (where A is the atom encapsulated inside $C_N^{\pm q}$ cage), has been the subject of experimental as well as intense systematic theoretical studies for many years now, see, e.g., [1–24] (and references therein). However, the subject of spin-polarized photoelectron fluxes from fullerene anions (or neutral $A@C_N$, for that matter) was provisionally touched briefly only in [25,26], to the best of the author's knowledge. Meanwhile, fundamentally, the topic of spin-polarized electron beams is of significance to both basic and applied sciences [27]. The present paper remedies the situation by producing novel results and findings related to spin-polarized photoelectron fluxes from fullerene anions.

We investigate and predict peculiarities in spin-polarized photoelectron fluxes upon photodetachment of a $C_{60}^{-}(2p)$ fullerene, where an external electron is captured into a $2p$-state in the field of the C_{60} cage.

Moreover, with the impetus of work [15], where it was predicted that the embedded into a neutral C_{60} fullerene cage atom, A, can qualitatively modify the photoionization spectrum of the C_{60} cage itself, we study how the photodetachment properties of fullerene anions can be affected by the embedded atom inside a hollow interior of $C_{60}^{-}(2p)$. Such systems are referred to as $A@C_{60}^{-}(2p)$ endohedral fullerene anions. We choose the $H@C_{60}^{-}(2p)$ and $He@C_{60}^{-}(2p)$ endohedral anions for case studies and demonstrate how their photodetachment parameters differ from those of the empty $C_{60}^{-}(2p)$.

Furthermore, we investigate how accounting for polarization of the fullerene cage by the outgoing photoelectron affects the spin polarization degree of the emitted photoelectrons.

The culmination point of the the present work is the prediction that photodetachment of fullerene anions can serve as a tool for the production of highly spin-polarized electron beams.

The present paper, thus, provides a broad initial investigation into spin-polarized photoelectron fluxes from fullerene anions, albeit being carried out within a simple (semi-)empirical model. The latter is similar in its spirit to the (semi-)empirical model originally suggested in [4] and later in [5] for studying of photodetachment of $C_{60}^-(n\ell)$. There, the C_{60} cage was modeled by an infinitesimally thin Dirac-bubble potential, $U(r) = A\delta(r - r_C)$ (r_C is the radius of the C_{60} skeleton) which binds an external electron into a $n\ell$ state, thereby turning C_{60} into a $C_{60}^-(n\ell)$ fullerene anion. A more realistic model, however, must account for a finite thickness of the fullerene cage. This is exactly what we do in the present paper. Namely, we model the C_{60} cage by a spherical annular potential of a certain inner radius, r_{in}, and finite thickness, Δ. This is because such model has been proven [18,20,28,29] (and references therein) to produce results in a reasonably good agreement with both the experimental photoionization spectrum of endohedral $Xe@C_{60}^+$ [20] and differential elastic electron scattering off C_{60} [30], particularly when polarization of the C_{60} cage by the outgoing photoelectron was accounted by theory [18,28,29]. Such modeling was also shown [31] to result in a semi-quantitative agreement with some of the most prominent features of the $e^- - C_{60}$ total elastic electron scattering cross section predicted by a far more sophisticated ab initio molecular-Hartree-Fock approximation. Thus, in the present paper, we utilize the described model, combine it with Cherepkov's theory [32,33] of spin-polarized photoelectron fluxes from atomic targets, and demonstrate that the emitted photoelectrons from fullerene anions can have a high degree of spin polarization.

It is clear that, of course, photodetachment of a fullerene anion is a much more complicated process than the simplified model suggests. It is a multifaceted problem. It presents a challenge to theory. In the present work, we peel off only a "facet" related to the inherent geometry of C_{60} to learn if there is something worthy of attention hidden behind the "facet", instead of performing rigorous high-level calculations of the phenomenon. One of a higher-level study could be the investigation of the impact of the surface and volume plasmons photoexcited in a fullerene anion by the incoming electromagnetic radiation, as in the case of photoionization of positive fullerene ions [13]. These plasmon excitations can induce a rather strong collective effect in about $\hbar\omega = 10$ to 50 eV domain of the photon energy. However, as is discussed in the end of Section 2.2 of the paper, the binding energy, E_{2p}, of a $2p$ attached electron in $C_{60}^-(2p)$, $H@C_{60}^-(2p)$ and $He@C_{60}^-(2p)$ is approximately -2.65 eV. Therefore, the plasmon effect on photodetachment of these fullerene anions should start matter at the photoelectron momenta $k = \sqrt{2(\hbar\omega + E_{2p})} \geq 0.7$ a.u. Thus, in the range of k's up to $k \approx 0.7$ a.u. one can reasonably expect that the utilized in the present work model is usable, to a good approximation. Furthermore, as will be shown below, the spin-polarization characteristics of the ejected photoelectrons depend on the $\frac{d_{\ell-1}}{d_{\ell+1}}$ ratio of the $d_{\ell-1}$ and $d_{\ell+1}$ dipole photodetachment amplitudes. This might result in a partial cancelation of the plasmon effects and, thus, in their weakened impact on the spin-polarization parameters of the ejected photoelectrons. Therefore, one can reasonably expect that the model is still usable for studying spin-polarized fluxes of photoelectrons even at the values of $k > 0.7$ a.u. Anyway, such calculated results are needed to reveal a role of collective effects in the subject of study that would remain undetermined otherwise. Accounting for collective effects themselves is beyond the scope of the present paper. As such, the present study may be the impetus for future rigorous theoretical or experimental studies of the phenomenon.

In addition, the present study also carries an alternative significance regardless of its relevance to fullerene anions. It relates to a topic of the structure and spectra of confined quantum systems in whole. To date, confined systems have been scrutinized intensely worldwide by exploiting various sorts of imaginable external confinements [34–41] (and references therein). As a perspective, the present work, too, contributes something new to the knowledge box on confined quantum systems in general.

Atomic units (a.u.) are used throughout the text, assuming the electronic charge $|e^-|$, mass m and Planck's constant $\hbar$ are equal to unity: $|e^-| = m = \hbar = 1$.

2. Review of Theory

2.1. Cherepkov'S Theory of Spin-Polarized Photoelectron Fluxes from Atoms

To date, theory and experiment on the production of spin-polarized electrons have been developed to a high degree [27,32,33,42] (and references therein).

In the present paper, we follow Cherepkov's work [32,33] on spin-polarized photoelectron fluxes upon photoionization of a $n\ell$-subshell ($\ell \geq 1$) of an unpolarized atom. We focus on the simplest case of theory. Namely: (a) A photoionized $n\ell_j$ atomic subshell is a single-electron subshell having the definite total angular momentum j, $j = \ell \pm \frac{1}{2}$, (b) a photon flux is circularly-polarized and it is propagating along the Z-axis of the XYZ coordinate system, (c) the photoelectron has a definite spin projection, $\mu = \pm\frac{1}{2}$, on the Z axis. The corresponding differential photoionization cross section, $\frac{d\sigma_j}{d\Omega} \equiv I_j(\omega, \theta, \mu)$, by a right-hand circularly-polarized photon is [32]:

$$I_j(\omega, \theta, \mu) = \frac{\sigma^j_{\rm tot}(\omega)}{8\pi}\left\{1 + A_j(\omega){\rm sign}\mu - \left[\frac{1}{2}\beta(\omega) + \gamma_1(\omega){\rm sign}\mu\right] P_2(cos\theta)\right\}. \quad (1)$$

Here, $P_2(\cos\theta)$ is a Legendre polynomial, θ is the photoelectron emission angle relative to the Z axis, $\sigma^j_{\rm tot}$ is the photoionization cross section of a $n\ell_j$ ($\ell \geq 1$) single-electron outer subshell of the atom, $\beta(\omega)$ is the well-known angular-asymmetry parameter of the photoelectron angular distribution, and $A_j(\omega)$ and $\gamma_1(\omega)$ are spin-polarization parameters [32]:

$$\beta = \frac{\ell(\ell-1)d^2_{\ell-1} + (\ell+1)(\ell+2)d^2_{\ell+1} - 6\ell(\ell+1)d_{\ell-1}d_{\ell+1}\cos(\delta_{\ell+1} - \delta_{\ell-1})}{(2\ell+1)[\ell^2_{\ell-1} + (\ell+1)d^2_{\ell+1}]}, \quad (2)$$

$$A_j = (-1)^{j-\ell-\frac{1}{2}}\frac{\ell(\ell+1)(d^2_{\ell+1} - d^2_{\ell-1})}{(2j+1)[\ell d^2_{\ell-1} + (\ell+1)d^2_{\ell+1}]}, \quad (3)$$

$$\gamma_1 = (-1)^{j-\ell-\frac{1}{2}}\frac{2\ell(\ell+1)[(\ell+2)d^2_{\ell+1} - (\ell-1)d^2_{\ell-1} + 3d_{\ell-1}d_{\ell+1}\cos(\delta_{\ell+1} - \delta_{\ell-1})]}{(2j+1)(2\ell+1)[\ell d^2_{\ell-1} + (\ell+1)d^2_{\ell+1}]}, \quad (4)$$

$$d_{\ell\pm1} = \int_0^\infty r^2 R_{n\ell}(r)R_{\ell\pm1}(r)dr. \quad (5)$$

Here, $d_{\ell\pm1}$ are the radial parts of the photoionization amplitudes for the ejection of an $n\ell$-electron into $\epsilon, \ell \pm 1$ continuum spectra, ϵ is the kinetic energy of the photoelectron, $R_{n\ell}(r)$ and $R_{\epsilon,\ell\pm1}(r)$ are the radial parts of the corresponding wavefunctions of the initial and final states, $\delta_{\ell\pm1}$ are phases of the photoelectron wavefunctions.

The angular dependence of the the spin-polarization degree of a photoelectron flux, $P_j(\theta)$, is defined [32] as

$$P_j(\theta) = \frac{I_j(\theta, \frac{1}{2}) - I_j(\theta, -\frac{1}{2})}{I_j(\theta, \frac{1}{2}) + I_j(\theta, -\frac{1}{2})} = \frac{A_j - \gamma_1 P_2(\cos\theta)}{1 - \frac{1}{2}\beta P_2(\cos\theta)}. \quad (6)$$

The total, i.e., angle-integrated degree of the photoelectron spin polarization, P_j, is obtained by the integration, separately, of the numerator and denominator of Equation (6) with respect to the solid angle, $d\Omega$. As a result, one finds [32] that P_j is the same as the A_j parameter, Equation (3):

$$P_j = A_j \tag{7}$$

The most interesting and important situation for getting strongly spin-polarized photoelectron fluxes, is when (a) a normally inferior transition, $d_{\ell-1}$, turns into a dominant transition compared to a normally superior transition, $d_{\ell+1}$, i.e., when $d_{\ell-1} > d_{\ell+1}$, and (b) a photoionized atomic subshell is a np-subshell ($\ell = 1$) with the total angular momentum $j = \ell - \frac{1}{2} = \frac{1}{2}$. Indeed, when $d_{\ell-1} > d_{\ell+1}$, Equations (3) and (7) say [32]:

$$P_{j=\ell-\frac{1}{2}}\Big|_{d_{\ell-1}>d_{\ell+1}} \leq \frac{\ell+1}{2\ell}\Big|_{\ell=1} \leq 1 \text{ and } P_{j=\frac{1}{2}}\Big|_{d_{\ell-1}\gg d_{\ell+1}} \approx 1, \text{ whereas } P_{j=\ell+\frac{1}{2}} \leq \frac{1}{2}. \tag{8}$$

In other words, photoionization of a $np_{\frac{1}{2}}$ subshell may result in an almost completely spin-polarized photoelectron flux, $P_{\frac{1}{2}} \approx 1$, regardless of the angle of emission of a $np_{\frac{1}{2}}$-photoelectron, when $d_{\ell-1} \gg d_{\ell+1}$. It is precisely for this reason that, in the present paper, we choose fullerene anions where the attached electron is a $p_{\frac{1}{2}}$-electron and study the phenomenon of spin-polarized photoelectron fluxes upon $p_{\frac{1}{2}}$-photodetachment.

2.2. Modeling Fullerene Anion Photodetachment

As mentioned above, we model (replace) the C_{60} cage by a $U_C(r)$ spherical annular potential of the inner radius, r_{in}, finite thickness, Δ, and depth, U_0, as in many other studies, e.g., [8–11,18,20,21,28,29] (and references therein):

$$U_C(r) = \begin{cases} -U_0, & \text{if } r_{in} \leq r \leq r_{in} + \Delta \\ 0 & \text{otherwise.} \end{cases}$$

A $C_{60}^-(n\ell)$ anion, then, is formed by binding of an external electron into a $n\ell$ state by the $U_C(r)$ potential. This model of a fullerene anion is similar in its spirit to modeling C_{60} by the Dirac-bubble potential [4,5]. Next, we expand our model for $C_{60}^-(n\ell)$ to an $A@C_{60}^-$ endohedral anion, simply by positioning the A atom at the center of the $U_C(r)$ potential. Furthermore, we complete our model of fullerene anions by an approximate accounting for polarization of C_{60} by the outgoing photoelectron. Generally, this is a too complicated task to be approached rigorously as, e.g., in work [43] (and references therein) on photodetachment of free atomic anions. However, it is not the aim of the present work to develop a rigorous theory (model). Instead, we focus on gaining the first meaningful insight into the subject of study. Thus, the C_{60} polarization potential is approximated by a semi-empirical static dipole polarization potential, $V_\alpha(r)$, as in [18,28,29] (and references therein):

$$V_\alpha(r) = -\frac{\alpha}{2(r^2+b^2)^2}. \tag{9}$$

Here, α is the static dipole polarizability of C_{60} ($\alpha \approx 850$ a.u. [44]), and b is a free parameter of the order of the fullerene size. Such accounting for polarization of C_{60} by the outgoing photoelectron has recently been proven to result in a reasonable agreement between calculated angle-differential elastic electron scattering off C_{60} [28,29] and experiment [30], as well as between the calculated [18] photoionization cross section of Xe@C_{60} and experiment [20].

Thus, the total model Hamiltonian, $\hat{\mathcal{H}}(r)$, for the bound and continuum states of the $C_{60}^-(n\ell)$ and $A@C_{60}^-(n\ell)$ anions is as follows:

$$\hat{\mathcal{H}}(r) = U_C(r) + \hat{H}^{HF} + V_\alpha(r). \tag{10}$$

Here, $\hat{H}^{\rm HF}$ is the Hartree-Fock Hamiltonian of the system "encapsulated A atom plus an external electron".

Correspondingly, the bound energy, $E_{n\ell}$, and the radial part, $P_{n\ell}(r)$, of the wavefunctions of the attached $n\ell$ electron, or its continuum-state wavefunction, $P_{\epsilon\ell}(r)$, are the solutions of the following radial equation:

$$-\frac{1}{2}\frac{d^2P_{n/\epsilon\ell}}{dr^2}+\left[\frac{\ell(\ell+1)}{2r^2}+\hat{\mathcal{H}}(r)\right]P_{n/\epsilon\ell}(r),=E_{n/\epsilon\ell}P_{n/\epsilon\ell}(r). \tag{11}$$

Here,

$$P_{n\ell}(r)|_{r\to 0,\infty}=0,\ \text{whereas}\ \ P_{\epsilon\ell}(r)|_{r\gg 1}\to\sqrt{\frac{2}{\pi}}\sin\left(kr-\frac{\pi\ell}{2}+\delta_\ell(\epsilon)\right), \tag{12}$$

where $\delta_\ell(\epsilon)$ is the phase of the continuum state wavefunction and k is the photoelectron momentum.

Lastly, when solving Equation (11), we use the following values for the model adjustable parameters of the $U_{\rm C}(r)$ potential: $r_{\rm in}\approx 5.8$, $\Delta\approx 1.9$, $U_0\approx 0.302$ and $b\approx 8$ a.u. This is because these values of the parameters were shown earlier to result in a reasonably good agreement between calculated [18,28,29] and experimental data on both elastic electron scattering off C_{60} [30] and photoionization of $Xe@C_{60}^+$ [20]. A would-be drawback of this potential regarding its application to $2p$ photodetachment of a $C_{60}^-(2p)$ anion is that it produces a $2p$ state bound by approximately -2 eV versus the known value of the -2.65 eV of electron affinity of C_{60} [45]. If we adjust U_0 to produce a $2p$ state bound by -2.65 eV, then $U_0=0.347$ a.u. The question, then, is whether the use of $U_0=0.302$ a.u. is justified for the present study. We have carefully analyzed this situation by performing parallel calculations for a $C_{60}^-(2p)$ anion (i.e., one with the use of $U_0=0.302$ a.u. and the other one with the use of $U_0=0.347$ a.u.). Namely, we calculated the corresponding P_{2p} radial wavefunction, $\sigma_{2p\to s}$ and $\sigma_{2p\to d}$ partial photodetachment cross sections, β_{2p} photoelectron angular-asymmetry parameter, γ_1 spin-polarization parameter as well as the $A_1=P_{j=\frac{1}{2}}$ spin-polarization degree of ejected photoelectrons. Moreover, the stated calculations were performed with and without account for polarization of C_{60} by the outgoing photoelectron. Calculated data are presented in the Appendix A. They show that there is a negligible difference in the $P_{2p}(r)$ radial functions of a $2p$ bound-state between the two calculated sets of data. Likewise, there are only insignificant differences between the photdetachment characteristics, plotted versus the photoelectron momentum, $k=\sqrt{2(\hbar\omega+E_{2p})}$, calculated with the use of both potentials. Because of a semi-quantitative nature of the present study, these insignificant differences can hardly matter at all. More so, when polarization of C_{60} by the outgoing photoelectron is considered, there is practically no difference in $\sigma_{2p\to s}$, $\sigma_{2p\to d}$, β_{2p}, γ_1 and $A_1=P_{j=\frac{1}{2}}$ between the two sets of calculated data plotted versus k. In terms of the photon energy, "competing" graphs obtained with the use of $U_0=0.302$ a.u. can simply be shifted by 0.65 eV to match the threshold of $E_{2p}=-2.65$ eV, if wanted. Therefore, it does not, actually, matter which of the two values of U_0 to use to proceed with the planned study. We prefer to operate with $U_0\approx 0.302$ a.u., for the sake of consistency with a series of our former calculations. This is more so, because such defined $U_{\rm C}(r)$ pseudo-potential led us previously to a reasonable agreement between calculated and experimental data on photoionization of $Xe@C_{60}^+$ and elastic electron scattering off C_{60}, as was mentioned above. Moreover, we plot calculated photodetachment parameters versus the photoelectron momentum k, because it eliminates the necessity to know the exact value of the E_{2p} binding energy.

3. Results and Discussion

Let us first get a quantitative information about the one-electron configurations of the $C_{60}^-(2p)$, $H@C_{60}^-(2p)$ and $He@C_{60}^-(2p)$ anions. To do so, let us utilize Equation (11), where we exclude the V_α polarization potential. This is because V_α is irrelevant to the ground-states of the anions. Calculated

radial functions of the attached $2p$ electron, $P_{2p}(r)$, as well as the $1s$ radial functions, $P_{1s}(r)$, of the encapsulated H and He atoms are plotted in Figure 1.

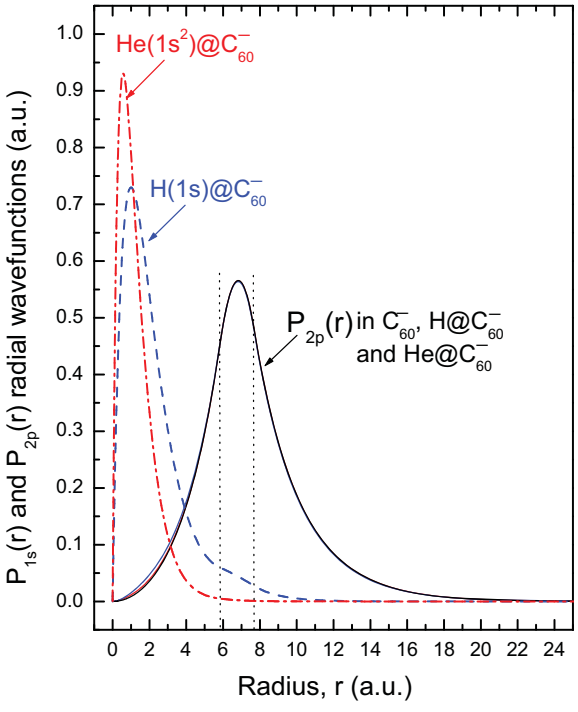

Figure 1. Calculated $P_{1s}^{H}(r)$ and $P_{1s}^{He}(r)$ radial functions of the encapsulated H and He atoms, as well as the $P_{2p}(r)$ radial function of the attached $2p$-electron in the $C_{60}^{-}(2p)$, $H@C_{60}^{-}(2p)$ and $He@C_{60}^{-}(2p)$ fullerene anions, as marked. Note: the $P_{2p}(r)$ functions in these anions are practically indistinguishable from one another. Vertical dotted lines mark the boundaries of the C_{60} shell.

Note how the calculated bound $P_{2p}(r)$ functions in these anions are practically indistinguishable from one another with an insignificant exception at small r's. Hence, if one to expect differences in photoionization characteristics between these anions, they will be due to the differences between the electron densities affecting the photoelectron wave primarily inside the hollow interior of C_{60}.

Calculated $\sigma_{2p\to s}$ and $\sigma_{2p\to d}$ partial photodetachment cross sections of $C_{60}^{-}(2p)$, $H@C_{60}^{-}(2p)$ and $He@C_{60}^{-}(2p)$ are depicted in Figure 2.

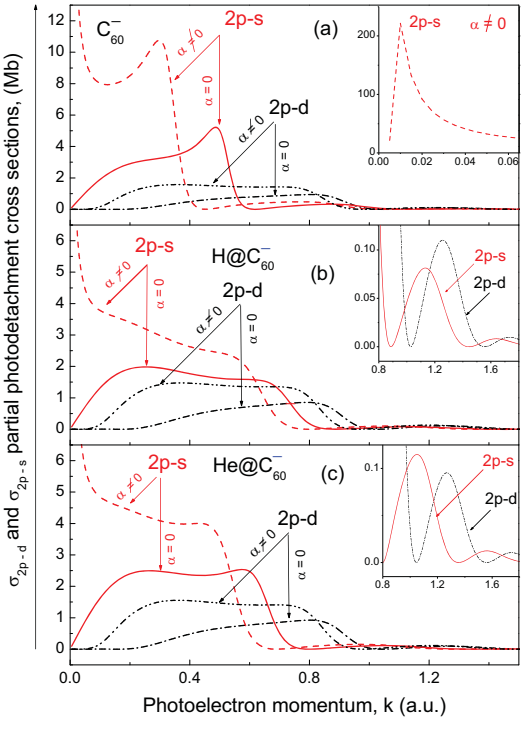

Figure 2. Partial $\sigma_{2p\to s}$ and $\sigma_{2p\to d}$ photodetachment cross sections of (**a**) $C_{60}^-(2p)$, (**b**) H@$C_{60}^-(2p)$ and (**c**) He@$C_{60}^-(2p)$ calculated without account ($\alpha = 0$) and with account ($\alpha \neq 0$) for polarization of the fullerene anions by the outgoing photoelectron, as marked. Inserts: $\sigma_{2p\to s}$ and $\sigma_{2p\to d}$ plotted on an extended k-scale, as marked.

Firstly, which is of primary importance to the present paper, one can see that $\sigma_{2p\to s}$ exceeds considerably $\sigma_{2p\to d}$ in the interval of k from threshold to several tenths' a.u. Then, again, $\sigma_{2p\to s} \gg \sigma_{2p\to d}$, at selected higher values of k. The latter is because $\sigma_{2p\to s}$ is oscillating, resonantly, in anti-phase relative to the oscillating $\sigma_{2p\to d}$, as is clearly demonstrated in inserts in Figure 2b,c. Note, resonance oscillations in $\sigma_{2p\to s}$ and $\sigma_{2p\to d}$ emerge at lower values of k as well, albeit they are less sharp. For C_{60}^-, the resonance oscillations in $\sigma_{2p\to s}$ and $\sigma_{2p\to d}$ were first uncovered in [4] and re-discovered in [5]. They are similar in nature to resonances that have been extensively scrutinized in photoionization of the A atom of A@C_{60} endohedral fullerenes for some time now, see, e.g., [8,11,12,14,18–24] (and references therein). The resonances are due to the interference of the photoelectron waves scattered off the inner and outer walls of the C_{60} cage. Following [46], these resonances are commonly referred to as the confinement resonances. The demonstrated fact that $\sigma_{2p\to s}$ can considerably exceed $\sigma_{2p\to d}$ not only when $\sigma_{2p\to d}$ is nearly a zero at the resonance minima, but also when $\sigma_{2p\to d}$ is fairly large (at lower values of k), is an outstanding feature of the photodetachment of fullerene anions. It is precisely because of this feature that fullerene anions can serve as new sources of highly spin-polarized electron beams, as will soon be shown in the present paper.

Secondly, note how $\sigma_{2p\to s}$ and $\sigma_{2p\to d}$ of H@$C_{60}^-(2p)$ and He@$C_{60}^-(2p)$ differ from those of empty $C_{60}^-(2p)$. We attribute this primarily to the additional scattering of the photoelectron wave off the encapsulated atom inside C_{60} compared to the case of empty $C_{60}^-(2p)$. Thus, the photodetachment

parameters of fullerene anions can be tailored to one's needs by encapsulating an atom inside the C_{60}^- cage.

Thirdly, one can see that accounting for polarization of the fullerene anions by the outgoing photoelectron affects strongly both the magnitudes and k-dependence of $\sigma_{2p\to s}$ and $\sigma_{2p\to d}$. Especially strong changes are incurred by the polarization effect to $\sigma_{2p\to s}$ at low photoelectron momenta. Very near the threshold the changes are dramatic, resulting in an extremely narrow resonance in $\sigma_{2p\to s}$. The latter is depicted in insert in Figure 2a, for C_{60}^-.

The angle-integrated degrees of the photoelectron spin polarization, $P_{j=\frac{1}{2}}$, upon photodetachment of $C_{60}^-(2p)$, $H@C_{60}^-(2p)$ and $He@C_{60}^-(2p)$, calculated without ($\alpha = 0$) and with ($\alpha \neq 0$) account for polarization of the C_{60} cage by the outgoing photoelectron, are depicted in Figure 3.

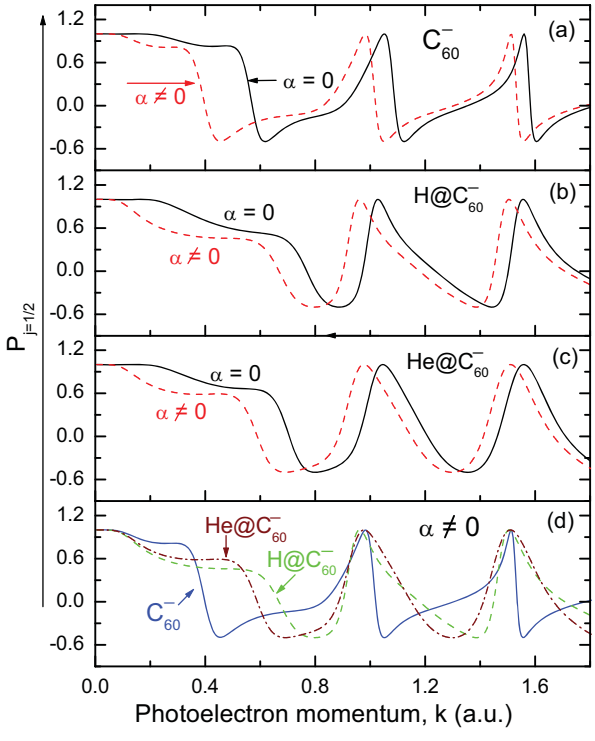

Figure 3. The angle-integrated degree of photoelectron spin polarization, $P_{j=\frac{1}{2}}$, upon photodetachment of the fullerene anions calculated without account ($\alpha = 0$) and with account ($\alpha \neq 0$) for polarization of the C_{60} cage by the outgoing photoelectron, as marked. (**a**) $P_{j=\frac{1}{2}}$ for $C_{60}^-(2p)$. (**b**) $P_{j=\frac{1}{2}}$ for $H@C_{60}^-(2p)$. (**c**) $P_{j=\frac{1}{2}}$ for $He@C_{60}^-(2p)$. (**d**) Calculated $P_{j=\frac{1}{2}}$s for $C_{60}^-(2p)$, $H@C_{60}^-(2p)$ and $He@C_{60}^-(2p)$ graphed on the same plot to ease the comparison between them.

Owing to the fact that $\sigma_{2p\to s}$ exceeds, considerably, $\sigma_{2p\to d}$ at/in specific values/domains of k, the $P_{j=\frac{1}{2}}$ degree reaches large values in there, including the value of $P_{j=\frac{1}{2}} \approx 1$. This is in accordance with Cherepkov's theory, Equation (8). The resonances in $P_{j=\frac{1}{2}}$ are due to confinement resonances in the $2p \to d$ and $2p \to s$ photodetachment amplitudes. Next, note how accounting for the polarizability of C_{60} results in decreasing the value of $P_{j=\frac{1}{2}}$ in a domain of k's from threshold to about 0.5 a.u. Lastly, note (see Figure 3d) how the encapsulation of an atom A into the $C_{60}^-(2p)$ cage generally broadens

the domains of k's where $P_{j=\frac{1}{2}}$ is large. Thus, in principle, spin-polarized photoelectron fluxes from fullerene anions can be controlled, to some extent, by embedding an atom into the C_{60}^- cage.

To calculate the angular dependence of the spin-polarization degree, $P_j(\theta)$, of the photoelectron fluxes from fullerene anions, one needs to know the angular-asymmetry parameters, γ_1 and β in addition to $A_j = P_j$. Calculated γ_1 and β are depicted in Figure 4.

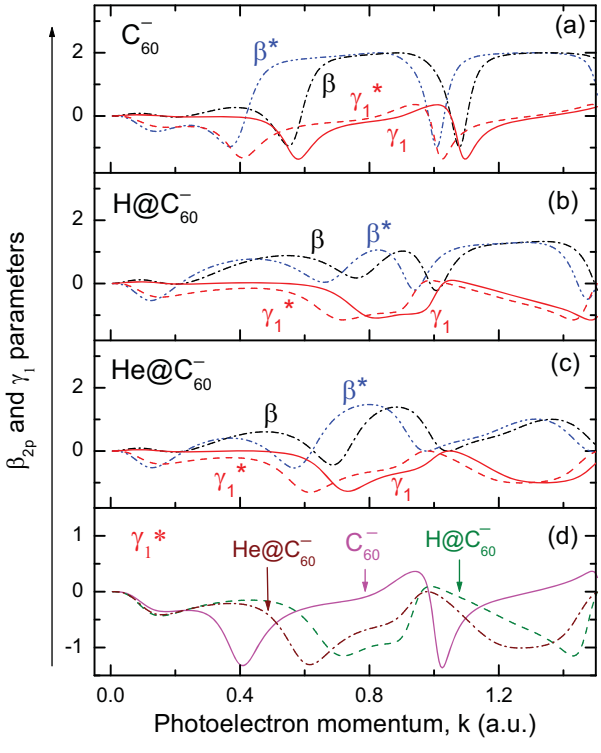

Figure 4. Calculated γ_1 and β photoelectron angular-asymmetry parameters upon $2p$-photodetachment of (**a**) $C_{60}^-(2p)$, (**b**) $H@C_{60}^-(2p)$ and (**c**) $He@C_{60}^-(2p)$, as marked. Labels: γ_1/γ_1^* and β/β^* are calculated data without/with account for polarizability of C_{60}, respectively. (**d**) Calculated γ_1^* for $C_{60}^-(2p)$, $H@C_{60}^-(2p)$ and $He@C_{60}^-(2p)$ graphed on the same plot to ease the comparison between them.

Similar to $\sigma_{2p\to s}$, $\sigma_{2p\to d}$ and $P_{j=\frac{1}{2}}$, the angular-asymmetry parameters are affected significantly both by the effect of polarization of the C_{60} cage by the outgoing photoelectron and encapsulation of H and He into the fullerene cage. The latter is specifically demonstrated by Figure 4d for enhanced clarity.

We now explore the angular dependence of the spin-polarization degree, $P_{j=\frac{1}{2}}(\theta)$, of the photoelectron fluxes from $C_{60}^-(2p)$, $H@C_{60}^-(2p)$ and $He@C_{60}^-(2p)$. We investigate $P_{j=\frac{1}{2}}(\theta)$ at two different values of the photoelectron momentum, k, where $\sigma_{2p\to s}$ significantly exceeds a fairly large $\sigma_{2p\to d}$. In photodetachment of $C_{60}^-(2p)$, this happens at $k \approx 0.485$ a.u. when polarizability of C_{60} is neglected ($\alpha = 0$) and at $k \approx 0.3$ a.u. in the case of $\alpha \neq 0$. Calculated $P_{j=\frac{1}{2}}(\theta)$, at $k = 0.485$ a.u., is depicted in Figure 5.

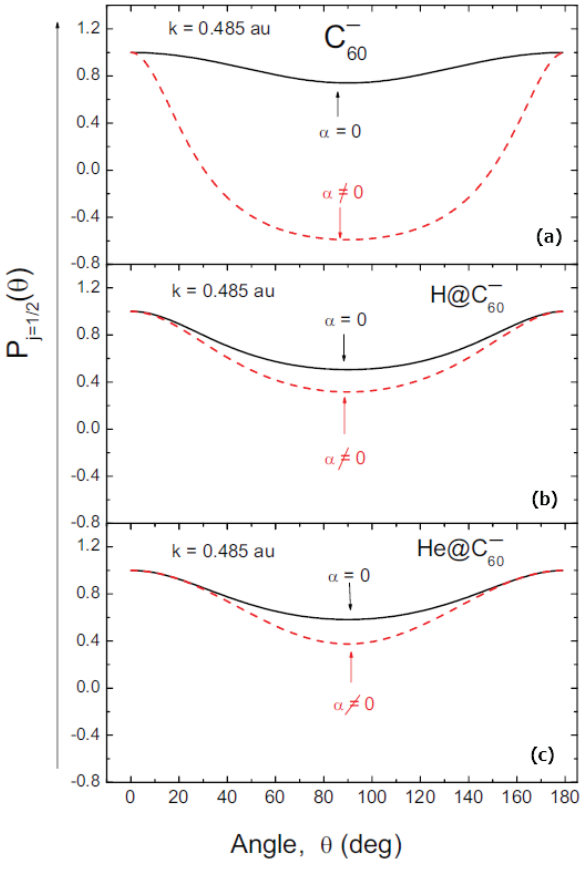

Figure 5. The angle-dependent degree of spin-polarization of photoelectron fluxes, $P_{j=\frac{1}{2}}(\theta)$, upon photodetachment of **(a)** $C_{60}^-(2p)$, **(b)** $H@C_{60}^-(2p)$ and **(c)** $He@C_{60}^-(2p)$ calculated at $k = 0.485$ a.u. without account ($\alpha = 0$) and with account ($\alpha \neq 0$) for polarization of the fullerene cage by the outgoing photoelectron, as marked.

Note how accounting for polarizability of C_{60} changes $P_{j=\frac{1}{2}}(\theta)$ for C_{60}^- dramatically, both quantitatively and qualitatively, including its sign change in a broad range of the emission angles, approximately from 30 to 150°. On the other hand, said polarization of the fullerene cage affects the spin-polarization degree of the photoelectrons from $H@C_{60}^-(2p)$ and $He@C_{60}^-(2p)$ significantly weaker. Moreover, the $P_{j=\frac{1}{2}}(\theta)$s, calculated for $H@C_{60}^-(2p)$ and $He@C_{60}^-(2p)$, differ relatively little from each other. Hence, the angle-dependent degree of the photoelectron spin polarization is somewhat insensitive to the kind of an atom encapsulated inside the C_{60}^- cage, at least in the present case study.

Calculated $P_{j=\frac{1}{2}}(\theta)$s, at $k = 0.3$ a.u., are plotted in Figure 6.

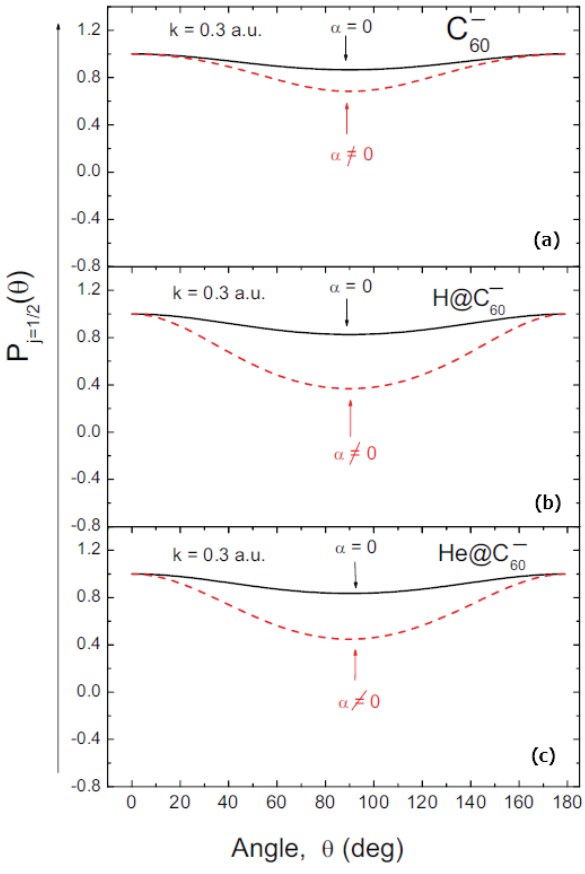

Figure 6. The angle-dependent degree of spin-polarization of the photoelectron fluxes, $P_{j=\frac{1}{2}}(\theta)$, upon photodetachment of (**a**) $C_{60}^{-}(2p)$, (**b**) $H@C_{60}^{-}(2p)$ and (**c**) $He@C_{60}^{-}(2p)$ calculated at $k = 0.3$ a.u. without account ($\alpha = 0$) and with account ($\alpha \neq 0$) for polarization of the fullerene cage by the outgoing photoelectron, as marked.

Overall, the behavior of $P_{j=\frac{1}{2}}(\theta)$ at $k = 0.3$ a.u. is similar to that of $P_{j=\frac{1}{2}}(\theta)$ at $k = 0.485$ a.u. It is similar in the respect that (a) accounting for polarizability of C_{60} only decreases the possible values of $P_{j=\frac{1}{2}}(\theta)$ regardless of the presence or absence of an atom inside C_{60}^{-}, (b) the encapsulation of an atom inside C_{60}^{-} results, overall, in decreased values of $P_{j=\frac{1}{2}}(\theta)$, and (c) the $P_{j=\frac{1}{2}}(\theta)$s for the endohedral fullerene anions differ relatively little from each other. On a contrasting side, however, polarization of C_{60} by the outgoing photoelectron impacts $P_{j=\frac{1}{2}}(\theta)$ of empty $C_{60}^{-}(2p)$, at $k = 0.3$. a.u., only relatively insignificantly compared to the caused dramatic changes in $P_{j=\frac{1}{2}}(\theta)$ at $k = 0.485$ a.u.

4. Conclusions

In the present paper, we have provided a glimpse into spin-polarized photoelectron fluxes from fullerene anions. The key result is that photodetachment of fullerene anions may serve as a tool for producing highly spin-polarized photoelectron fluxes. This was shown to be due to a specific feature of photodetachment of fullerene anions-the presence of the domains of the photoelectron energies/momenta where a $d_{\ell-1}$ photodetachment amplitude exceeds by far a $d_{\ell+1}$ amplitude. Accounting for interactions omitted in the present study will likely change the details

of the reported results. However, it is unlikely that the omitted interactions would obliterate the very existence of the domains of the photoelectron momenta where the key inequality, $d_{\ell-1} \gg d_{\ell+1}$, takes place. Thus, the prediction of highly spin-polarized photoelectrons from fullerene anions should be qualitatively and semi-quantitatively accurate. It would be interesting to learn how the reported results would differ from those obtained in the framework of a rigorous theory. In this respect, let us stress once again that a similar simple model has been reasonably successful in the qualitative and quantitatively description of experimental and other theoretical data on both the $4d$ photoionization of Xe@C_{60}^{+} and differential elastic electron scattering off C_{60}.

Funding: This research received no external funding.

Conflicts of Interest: The author declares no conflict of interest.

Appendix A. Comparison of Calculated Data Obtained with the Use of $U_0 = 0.302$ and 0.347 a.u.

We demonstrate by Figure A1 that there are only insignificant differences between calculated $P_{2p}(r)$ radial wavefunctions, as well as $\sigma_{2p\to s}$, $\sigma_{2p\to d}$, β_{2p}, γ_1 and $P_{j=\frac{1}{2}}$ calculated with the use of $U_0 = 0.302$ and 0.347 a.u. for $U_C(r)$, Equation (9). Calculations were performed both with and without account for polarizability, α, of C_{60}. Thus, any of the potential depths fits, to a good approximation, to study spin-polarization photoelectron fluxes from fullerene anions.

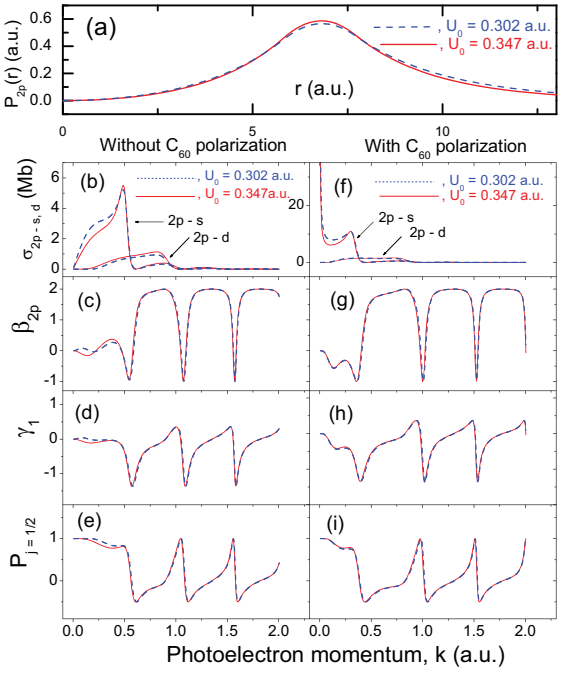

Figure A1. Calculated data for a $C_{60}^{-}(2p)$ anion obtained with the use of the depths $U_0 = 0.302$ a.u. (dashed lines) and 0.347 (solid lines) a.u. for the $U_C(r)$ pseudo-potential, Equation (9), as marked in the figure. (**a**) The $P_{2p}(r)$ radial part of the wavefunction of the attached $2p$ electron. (**b**–**e**) Calculated, without account for polarizability of C_{60}, $\sigma_{2p\to s}$ and $\sigma_{2p\to d}$ photodetachment cross sections, β_{2p} photoelectron angular-asymmetry parameter, γ_1 spin-polarization parameter and the $P_{j=\frac{1}{2}}$ angle-integrated degree of photoelectron spin polarization. (**f**–**i**) The same as (**b**–**e**) but with account for polarizability of C_{60}.

References

1. Kato, T. Absorption and emission spectra for C_{60}. *Laser Chem.* **1994**, *52*, 155. [CrossRef]
2. Bilodeau, R.C.; Gibson, N.D.; Walter, C.W.; Esteves-Macaluso, D.A.; Schippers, S.; Mü ller, A.; Phaneuf, R.A.; Aguilar, A.; Hoener, M.; Rost, J.M.; et al. Single-Photon Multiple Detachment in Fullerene Negative Ions: Absolute Ionization Cross Sections and the Role of the Extra Electron. *Phys. Rev. Lett.* **2013**, *111*, 043003. [CrossRef]
3. Müller, A.; Martins, M.; Kilcoyne, A.L.D.; Phaneuf, R.A.; Hellhund, J.; Borovik, A.; Holste, K.; Bari, S.; Buhr, T.; Klumpp, S.; et al. Photoionization and photofragmentation of singly charged positive and negative $Sc_3N@C_{80}$ endohedral fullerene ions. *Phys. Rev. A* **2019**, *99*, 063401. [CrossRef]
4. Lohr, L.L.; Blinder, S.M. Electron photodetachment from a Dirac bubble potential. A model for the fullerene negative ion C_{60}^-. *Chem. Phys. Lett.* **1992**, *198*, 100. [CrossRef]
5. Amusia, M.Y.; Baltenkov, A.S.; Krakov, B.G. Photodetachment of negative C_{60}^- ions. *Phys. Lett. A* **1998**, *243*, 99. [CrossRef]
6. Korol, A.V.; Solov'yov, A.V. Vacancy decay in endohedral atoms: the role of an atom's non-central position. *J. Phys. B* **2011**, *44*, 085001. [CrossRef]
7. Baltenkov, A.S.; Msezane, A.Z. Doubly-charged Negative Ion of C_{60}^- Molecule. *Proc. Dyn. Syst. Appl.* **2016**, *7*, 239.
8. Kumar, A.; Varma, H.R.; Deshmukh, P.C.; Manson, S.T.; Dolmatov, V.K.; Kheifets, A.S. Wigner photoemission time delay from endohedral anions. *Phys. Rev. A* **2016**, *94*, 043401. [CrossRef]
9. Chaudhuri, S.K.; Mukherjee, P.K.; Fricke, B. Spectroscopy of low lying transitions of He confined in a fullerene cage. *Eur. Phys. J. D* **2016**, *70*, 196. [CrossRef]
10. Dolmatov, V.K. Impact of fullerene polarizability on Wigner time delay in photodetachment of fullerene anions C_N^-. *J. Phys. Conf. Ser.* **2017**, *875*, 022013. [CrossRef]
11. Puska, M.J.; Nieminen, R.M. Photoabsorption of atoms inside C_{60}. *Phys. Rev. A* **1993**, *47*, 1181. [CrossRef] [PubMed]
12. Baltenkov, A.S. Resonances in photoionization cross sections of inner subshells of atoms inside the fullerene cage. *J. Phys. B* **1999**, *32*, 2745. [CrossRef]
13. Scully, S.W.J.; Emmons, E.D.; Gharaibeh, M.F.; Phaneuf, R.A.; Kilcoyne, A.L.D.; Schlachter, A.S.; Schippers, S.; Müller, A.; Chakraborty, H.S.; Madjet, M.E.; et al. Photoexcitation of a volume plasmon in C_{60} ions. *Phys. Rev. Lett.* **2005**, *94*, 065503. [CrossRef] [PubMed]
14. Shields, D.; De, R.; Madjet, M.E.; Manson, S.T.; Chakraborty, H.S. Photoemission from hybrid states of $Cl@C_{60}$ before and after a stabilizing charge transfer. *J. Phys. B* **2020**, *53*, 125101. [CrossRef]
15. McCune, M.A.; De, R.; Madjet, M.E.; Chakraborty, H.S. First prediction of the direct effect of a confined atom on photoionization of the confining fullerene. *J. Phys. B* **2010**, *43*, 181001. [CrossRef]
16. McCune, M.A.; Madjet, M.E.; Chakraborty, H.S. Reflective and collateral photoionization of an atom inside a fullerene: Confinement geometry from reciprocal spectra. *Phys. Rev. A* **2009**, *80*, 011201(R). [CrossRef]
17. McCune, M.A.; Madjet, M.E.; Chakraborty, H.S. Unique role of orbital angular momentum in subshell-resolved photoionization of C_{60}. *J. Phys. B* **2008**, *41*, 201003. [CrossRef]
18. Dolmatov, V.K.; Edwards, A. Role of polarizability of a C_N fullerene cage in $A@C_N$ photoionization and $e^- - C_N$ scattering: the size effect. *J. Phys. B* **2019**, *52*, 105001. [CrossRef]
19. Baltenkov, A.S.; Manson, S.T.; Msezane, A.Z. Jellium model potentials for the C_{60} molecule and the photoionization of endohedral atoms, $A@C_{60}$. *J. Phys. B* **2015**, *48*, 185103. [CrossRef]
20. Phaneuf, R.A.; Kilcoyne, A.L.D.; Aryal, N.B.; Baral, K.K.; Esteves-Macaluso, D.A.; Thomas, C.M.; Hellhund, J.; Lomsadze, R.; Gorczyca, T.W.; Ballance, C.P.; et al. Probing confinement resonances by photoionizing Xe inside a C_{60}^+ molecular cage. *Phys. Rev. A* **2013**, *88*, 053402. [CrossRef]
21. Gorczyca, T.W.; Hasoglu, M.F.; Manson, S.T. Photoionization of endohedral atoms using R-matrix methods: Application to $Xe@C_{60}$. *Phys. Rev. A* **2012**, *86*, 033204. [CrossRef]
22. Li, B.; O'Sullivan, G.; Dong, C. Relativistic R-matrix calculation photoionization cross section of Xe and $Xe@C_{60}$. *J. Phys. B* **2013**, *46*, 155203. [CrossRef]
23. Korol, A.V.; Solov'yov, A.V. Confinement resonances in the photoionization of endohedral atoms: Myth or reality? *J. Phys. B* **2010**, *43*, 201004. [CrossRef]

24. Amusia, M.Y.; Baltenkov, A.S.; Chernysheva, L.V.; Felfli, Z.; Msezane, A.Z. Dramatic distortion of the 4*d* giant resonance by the C_{60} fullerene shell. *J. Phys. B* **2005**, *38*, L169. [CrossRef]
25. Dolmatov, V. On fullerene anions as sources of spin-polarized electrons. In Proceedings of the 12th European Conference on Atoms Molecules and Photons: Extended Abstracts (ECAMP 2016), Frankfurt am Main, Germany, 5–9 September 2016; p. 8.
26. Edwards, A.C.; Lane, C.G.; Dolmatov, V.K. Spin-polarized electrons upon nondipole photodetachment of fullerene anions. *J. Phys. Conf. Ser.* **2017** *875*, 032032. [CrossRef]
27. Heinzmann, U.; Dil, J.H. Spin-orbit-induced photoelectron spin polarization in angle-resolved photoemission from both atomic and condensed matter targets. *J. Phys. B* **2012**, *24*, 173001. [CrossRef]
28. Dolmatov, V.K.; Amusia, M.Y.; Chernysheva, L.V. On the $e^- - C_{60}$ elastic angle-differential scattering cross section. *J. Phys. Conf. Ser.* **2020**, *1412*, 182011. [CrossRef]
29. Amusia, M.Y.; Chernysheva, L.V.; Dolmatov, V.K. Angle-differential elastic-electron scattering off C_{60}: A simple semi-empirical theory versus experiment. *J. Phys. B* **2019**, *52*, 085201. [CrossRef]
30. Tanaka, H.; Boesten, L.; Onda, K.; Ohashi, O. Cross-beam experiment for the scattering of low-energy electron grom gas phase C_{60}. *J. Phys. Soc. Jpn.* **1994**, *63*, 485. [CrossRef]
31. Winstead, C.; McKoy, V. Elastic electron scattering by fullerene, C_{60}. *Phys. Rev. A* **2006**, *73*, 012711. [CrossRef]
32. Cherepkov, N.A. Angular distribution of photoelectrons with a given spin orientation. *Sov. Phys. JETP* **1974**, *38*, 463.
33. Cherepkov, N.A. Spin polarization of photoelectrons ejected from unpolarized atoms. *J. Phys. B* **1983**, *12*, 1279. [CrossRef]
34. Jaskólski, W. Confined many-electron systems. *Phys. Rep.* **1996**, *271*, 1. [CrossRef]
35. Buchachenko, A.L. Compressed atoms. *J. Phys. Chem. B* **2001**, *105*, 5839. [CrossRef]
36. Sabin, J.R.; Brändas, E.; Cruz, S.A. (Eds.) *Advances in Quantum Chemistry: Theory of Confined Quantum Systems. Part* 1; Academic: New York, NY, USA, 2009; Volume 57, pp. 1–334.
37. Sabin, J.R.; Brändas, E.; Cruz, S.A. (Eds.) *Advances in Quantum Chemistry: Theory of Confined Quantum Systems. Part* 2; Academic: New York, NY, USA, 2009; Volume 58, pp. 1–297.
38. Connerade, J.-P.; Kengkanb, P.; Semaounea, R. Confined Atoms in Clusters, Bubbles, Dots and Fullerenes. *J. Chin. Chem. Soc.* **2001**, *48*, 265. [CrossRef]
39. Connerade, J.-P. 2013 From Pauli's birthday to "Confinement Resonances" —A potted history of Quantum Confinement. *J. Phys. Conf. Ser.* **2013**, *438*, 012001. [CrossRef]
40. Sen, K.D. (Ed.) *Electronic Structure of Quantum Confined Atoms and Molecules*; Springer: New York, NY, USA, 2014; pp. 1–253.
41. Ley-Koo, E. Recent progress in confined atoms and molecules: Superintegrability and symmetry breakings. *Rev. Mex. Fis.* **2018**, *64*, 326. [CrossRef]
42. Chakraborty, H.S.; Deshmukh, P.C.; Manson, S.T. Interchannel-coupling effects in the spin polarization of energetic photoelectrons. *Phys. Rev. A* **2003**, *67*, 052701. [CrossRef]
43. Ivanov, V.K. Theoretical studies of photodetachment. *Radiat. Phys. Chem.* **2004**, *70*, 345. [CrossRef]
44. Amusia, M.Y.; Baltenkov, A.S. On the possibility of considering the fullerene shell C_{60} as a conducting sphere. *Phys. Lett. A* **2006**, *360*, 294. [CrossRef]
45. Wang, L.-S.; Conceicao, J.; Jin, C.; Smalley, R.E. Threshold photodetachment of cold C_{60}^-. *Chem. Phys. Lett.* **1991**, *182*, 5. [CrossRef]
46. Connerade, J.-P.; Dolmatov, V.K.; Manson, S.T. On the nature and origin of confinement resonances. *J. Phys. B* **2000**, *33*, 2279. [CrossRef]

atoms

MDPI

Article

Inner-Shell Photodetachment of Na^- Using R-Matrix Methods

T. W. Gorczyca [1,*], H.-L. Zhou [2], A. Hibbert [3], M. F. Hasoglu [4] and S. T. Manson [2]

1 Department of Physics, Western Michigan University, Kalamazoo, MI 49008, USA
2 Department of Physics and Astronomy, Georgia State University, Atlanta, GS 30303, USA; phyhlz@gmail.com (H.-L.Z.); smanson@gsu.edu (S.T.M.)
3 School of Mathematics and Physics, Queen's University of Belfast, Belfast BT7 1NN, UK; a.hibbert@qub.ac.uk
4 Department of Computer Engineering, Hasan Kalyoncu University, Sahinbey 27100, Gaziantep, Turkey; mfatih.hasoglu@hku.edu.tr
* Correspondence: thomas.gorczyca@wmich.edu

Received: 18 August 2020; Accepted: 15 September 2020; Published: 21 September 2020

Abstract: Inner-shell photodetachment of Na^- near the L-edge threshold was investigated using the R-matrix method. Significant structure was found in the cross section, and this structure is shown to be related to the complicated correlated electron dynamics endemic in negative ions. Comparison with experiment suggests that the absolute values of the measured cross section might be too small by a factor of two.

Keywords: photodetachment; inner-shell phenomena

PACS: 34.80.Lx; 31.15.vj; 32.80.Zb

1. Introduction

Photodetachment is a highly correlated process [1–5]. Correlation is required to accurately characterize the initial state wave function of a negative ion, or even to get the initial state bound in many cases. As a well-studied example, the (uncorrelated) Hartree-Fock energy level for the simplest H^- anion lies above the hydrogen atomic energy level [6]. For the final state wave function in the photodetachment process, correlation in the form of interchannel coupling has been found to be quite important. Since correlation dominates the photodetachment process, studying photodetachment is an excellent venue for understanding the correlated dynamics of electrons in atomic negative ions. Studies of outer-shell photodetachment have a long history [1–5]. More recently, principally over the past two decades, investigations of inner-shell photodetachment have been performed, both theoretical and experimental, particularly He^- and Li^- [7–16]. Much has been done on heavier anions, as well; see, e.g., Refs. [17,18] and references therein. Inner-shell photodetachment of atomic anions is also of particular interest because the initial-state wave function of the transition remains almost exactly the same as in the neutral atom, but the final-state wave functions can differ dramatically. This is due to rather different fields experienced in the anion and neutral atom by the emerging photoelectron. The differences of the inner-shell cross section between the atom and the negative ion are entirely due to the different outer-shell electronic structure, which is highly correlated in the case of a negative ion. This correlated photodetachment process can be used to quantify the spectroscopy of the tenuously bound valence electrons, a photoelectron probe of the many-body dynamics inherent in the binding of the negative ion. The simplest multielectron negative ions, beyond the tractable two-electron H^- case, are He^- and Li^- and their photodetachment has been dealt with extensively already [7–16]. The inner-shell photodetachment of Na^-, which lies below Li^- in the periodic table, has been studied

experimentally [19], and calculations that included many-body dynamics have been performed [20,21]. Neither of those calculations could reproduce, even qualitatively, the sharp resonance that is attributed to a multiple-electron excitation process [19]. This means that important physics was not included in those calculations. To improve upon the situation, R-matrix methods are used here for the calculations since they are able to account for initial state correlations and final state interchannel coupling, thereby including coupling with detachment-plus-excitation channels. A version of the Belfast R-matrix methodology that has been modified to accommodate photodetachment has been employed [15].

In the next section, a brief discussion of the theoretical methods employed is given, along with the results of our calculations of the relevant discrete state energies of Na and Na^-. The following section presents the photodetachment cross section and a comparison with experiment and previous calculations. The final section presents a summary and conclusions.

2. Theoretical Methods

In carrying out the present R-matrix calculations for the Na^- photodetachment near the $2p$ thresholds, we begin with the exact same structure as used in our earlier R-matrix study for Na^- [22]. To recap briefly, an atomic orbital basis is generated using the atomic structure program CIV3 [23]. The $1s$, $2s$, $2p$, and $3s$ orbitals are obtained from a Hartree-Fock calculation for the $1s^22s^22p^63s$ ground state of the Na target, whereas the $(3p, 3d, 4s, 4p, 4d,$ and $4f)$ orbitals are each optimized on their corresponding frozen-core $1s^22s^22p^6nl$ states ($n = 3, 4$), completing the physical, outer-shell-optimized orbital basis for the lowest Na target states. An additional basis of pseudoorbitals ($5s, 5p, 5d,$ and $5f$) is obtained from multi-configuration optimizations on the $1s^22s^22p^53l3l'$ inner-shell vacancy states, thus adding consistent correlation additions to both the Na and Na^- states.

The 14 CIV3 orbitals, 10 physical and 4 treated as correlation pseudoorbitals, are used to construct the first 7 singly-excited Na target states, and 37 inner-shell-excited states. These are all bounded within the R-matrix radius determined to be 56.2 a.u. A separate, orthogonal basis of 50 continuum orbitals is used to represent the photodetached electron beyond the R-matrix radius. The "bound" and "continuum" orbitals are then coupled together to represent all Na^- states: the initial $1s^22s^22p^63s^2(^1S)$ Na^- state, the e^- + Na scattering states, and the inner-shell-excited resonance states such as the dominant resonance just below the $1s^22s^22p^53s4s$ threshold, as will be seen.

We also include an additional, important component in the calculations, that of a pseudoresonance removal procedure [24]. A highly-correlated R-matrix basis, without proper care, can lead to an over-completeness of the bound $N + 1 = 12$-electron Na^- bound or quasibound (resonance) state basis, or the e^- + Na scattering states. This in turn causes unphysical *pseudoresonances* to arise in the computed cross sections. The R-matrix method usually uses an orthonormal orbital basis, constraining the continuum orbital basis to be orthogonal to the bound-orbital basis. To compensate for the subspace projected out of the wavefunction Hilbert space by this enforced orthogonality, additional, so-called $(N + 1)$-electron configurations must be added back into the full wavefunction basis. However, the exact choice of linear combinations of $(N + 1)$-electron configurations needed requires examination. A linear algebra method for choosing the minimum basis needed to span the $N + 1 = 12$-electron states determines the minimal rotated basis needed, yielding a reduced basis of linear combinations of configurations. The "continuum" orbitals are generated in the first step of the R-matrix calculation [25,26] by using a model core potential and appropriate surface boundary conditions, along with necessary Laguerre or Gram-Schmidt orthogonalization to the bound-orbital basis.

The resultant energies for the Na 11-electron target states are shown in Table 1, and compared to the NIST values [27]. We only use doublet states of Na, not quartet states or higher, since our final-symmetry $^1P^o$ singlet states must be composed from a doublet electron coupled to the Na target state. In addition, shown in Table 1 is the electron affinity of Na (photodetachment threshold energy) along with experiment [28]. From this table, it is evident that the agreement between theory and experiment for both the electron affinity and the states of the neutral Na atom is quite good.

Table 1. R-matrix energies of the Na target states compared to the NIST values [27], the NIST Na^+ ground state energy, and the R-matrix electron affinity of Na^- compared to experiment [28].

Term State	R-matrix (Ryd)	EXP (Ryd)
$Na^- 2p^6 3s^2$	−0.0395	−0.0403
$2p^6 3s(^2S)$	0.00000	0.00000
$2p^6 3p(^2P)$	0.15827	0.15462
$2p^6 4s(^2S)$	0.23623	0.23456
$2p^6 3d(^2D)$	0.26720	0.26584
$2p^6 4p(^2P)$	0.27809	0.27585
$2p^6 5S(^2S)$		0.30255
$2p^6 4d(^2D)$	0.31606	0.31483
$2p^6 4f(^2F)$	0.31651	0.31518
⋮		
$Na^+ 2p^6(^1s)$		0.37772
⋮		
$2p^5 3s^2(^2P)$	2.26134	2.26550
$2p^5 3s3p(^2D)$	2.47510	2.46049
$2p^5 3s3p(^2P)$	2.47950	2.46751
$2p^5 3s3p(^2S)$	2.50273	2.48991
$2p^5 3s3p(^2S)$	2.58706	2.55864
$2p^5 3s3p(^2D)$	2.58870	2.55624
⋮		

3. Results and Discussion

To understand the physics of what goes on in the vicinity of each threshold, it is important to keep in mind that near-threshold negative-ion photodetachment cross sections behave very differently from cross sections for photoionization of neutral systems or positive ions. First of all, in the photoionization process, there are an infinity of autoionizing (Feshbach) resonances below each threshold [29], while in photodetachment there generally are none or, at most, one or two [5]. Secondly, while photoionization cross sections have a finite value at threshold [29], photodetachment cross sections are zero at threshold, which means that photodetachment cross sections always rise from threshold [5]. The results of the photodetachment cross section calculations over a broad L-edge energy region are depicted in Figure 1, along with the experimental results [19]; the qualitative agreement is excellent. All of the structure observed in the experiment is also seen in the calculated results, including the resonance maximum just above the first inner-shell threshold, the structure associated with the $2p^5 3s3p$ thresholds, the sharp Feshbach resonance just above 36 eV, and the gradual rise of the cross section with energy above these resonances.

The maximum in the cross section just above the first inner-shell threshold, at about 31.3 eV, is the result of the ordinary photodetachment rise from zero, plus a resonance which we assign to be the $2p^5 3s^2(\epsilon s, ns)$ resonance. This occurs because in the negative ion, the $2p^5 3s^2 ns$ excitation lies *above* the $2p^5 3s^2$ threshold. This is similar to what was found recently in Li^- [30]. This resonance has both shape and Feshbach characteristics, which demonstrates how different negative ions are compared to their neutral atom counterparts; even the language of neutral atoms is inadequate to describe certain negative ion phenomena. In addition, it is evident that the calculation seriously overestimates the size of this near-threshold resonance. This occurs because the present calculation omits the post collision interaction (PCI) effect [31,32], whereby a slow (near-threshold) photoelectron from an inner shell can be recaptured and the energy transferred to a fast photoelectron associated with photoemission from an outer shell via interchannel coupling. This was found to be quite important in the threshold behavior of the inner-shell photodetachment of Li^- [14,15]. As discussed below, however, there are reasons to believe that PCI is not very important in this case.

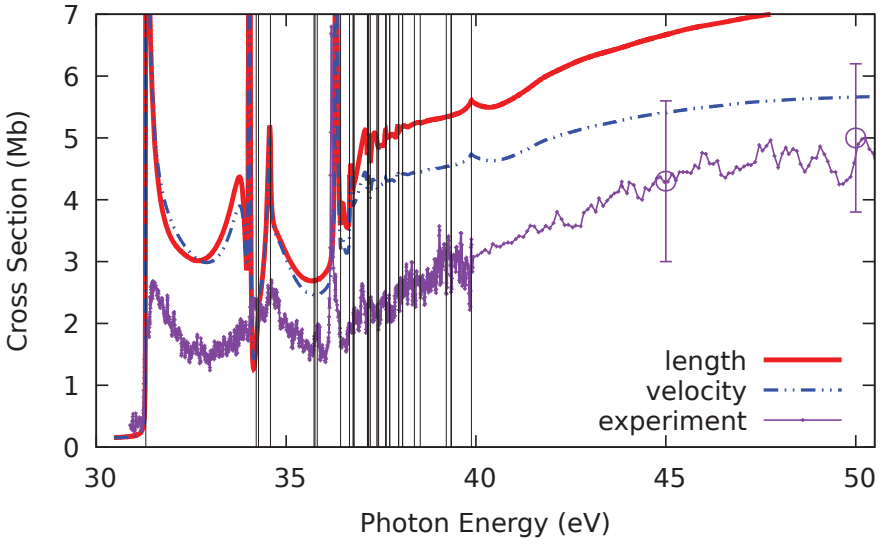

Figure 1. Calculated R-matrix Na^- photodetachment cross sections compared to experiment [28]. The calculated inner-shell thresholds are shown as vertical black lines.

In the region of the $2p^5 3s3p$ thresholds—in the 34 eV region—the calculated results exhibit a complex series of structures that is only hinted at in the somewhat unresolved experimental results. The calculation does, however, reproduce the valleys in the cross section both between the threshold maximum and the $2p^5 3s3p$ threshold regions, and above this region, as well. It is likely that one of the resonances that theory predicts is too high here due to associated PCI effects. In any case, the fact that length and velocity results are almost identical in this region lends credence to the theoretical predictions, thereby suggesting that this energy region be scrutinized with greater experimental resolution.

Between the sharp resonance just above 36 eV and about 40 eV, theory shows a number of small resonances associated with the many inner-shell thresholds in this region. While it is not entirely clear, due to the finite resolution, the experimental results also seem to show a number of resonances, as well. Above about 40 eV, the cross sections, both theoretical and experimental, are more or less smooth and increasing. The increasing behavior arises from the $2p \rightarrow \epsilon p$ shape resonance that is also known in the inner-shell photoionization of neutral Na [33]. Furthermore, with increasing energy, it is reasonable to expect that the $2p$ photodetachment cross section should approach the $2p$ photoionization cross section of neutral Na. This is because, as mentioned earlier, the initial state $2p$ wave functions are essentially the same in both cases, and in the final states, a fast (as opposed to a slow, near-threshold) photoelectron barely interacts with the outer shells so that the final state wave functions, in the region of the $2p$ subshell, are very close, as well. In the atomic case, the $2p$ cross section, 20 eV above threshold, is about 9 Mb [33], as compared to roughly half that value for the photodetachment experiment [28], as seen in Figure 1. This suggests that the absolute normalization of the experimental photodetachment cross section might be too small by a factor of two or so. Furthermore, multiplying the experimental cross section by a factor of two would bring that scaled cross section into quite good quantitative agreement with the R-matrix calculation.

To further investigate this point, a calculation of $2p$ ionization in neutral Na has been performed using the same methodology as the Na^- calculation, and the results are shown in Figure 2 as compared to the Na^- results. It is clear that the Na $2p$ cross sections at higher energies agree quite well with the Na^- results, as suggested above, in both length and velocity formulations. Furthermore, the calculated

Na cross sections are in substantial agreement with earlier experimental and calculated results for neutral Na [33]. For these reasons, then, it would seem to be a really good idea to look again experimentally at the Na^- photodetachment cross section, particularly at the absolute normalization.

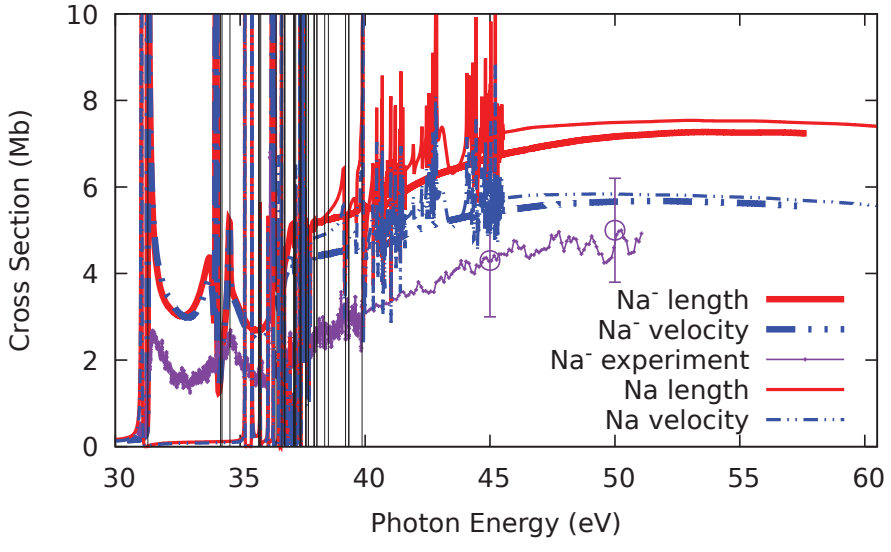

Figure 2. Present R-matrix Na photoionization cross sections compared to present R-matrix Na^- photodetachment cross sections, in length and velocity gauges. The calculated inner-shell thresholds are shown as vertical black lines.

The resonance just above 36 eV is difficult to see in Figure 1, so a blow-up of that region of the cross section in given in Figure 3. This resonance lies just below the $2p^5 3s4s$ doublet thresholds, and we conclude that it is a Feshbach $2p^5 3s4s^2\ ^1P$ resonance. The reason that $2p \rightarrow 4s$ photoexcitation is chosen, rather than the usually dominant $2p \rightarrow 3d$ "giant resonance" transition, is that the $3d$ orbital in the Na^- $3p^6 3s3d$ and $2p^5 3s^2 3d$ state is so much more diffuse than the tightly-bound $2p$ orbital that the *dynamic* transition factor is diminished in the latter transition, despite the larger $2p \rightarrow 3d$ *geometric* factor. Considering the one-electron frozen-core transition, this resonance must be associated with the $(2p^5 3s)[^1P]4s(^2P)$ threshold, as opposed to the $(2p^5 3s)[^3P]4s(^2P)$ threshold, as suggested earlier [19]. The theoretical resonance is seen to lie about 0.1 eV above the experimental resonance, and the shapes are more or less the same. However, it is also seen that the theoretical resonance peak is about a factor of two larger than the experimental peak, further suggesting that the absolute normalization of the experimental cross section might be off by as much as a factor of two. Since this difference is roughly the same over the entire energy range, even in the threshold region, it was thought that the PCI effect ia not great in this case, so it has been omitted.

A comparison with the two previous calculations [20,21] is given in Figure 4, along with the experimental results. As mentioned earlier, neither of the earlier calculations showed a sharp Feshbach resonance just above 36 eV because neither of them included the relevant detachment-plus-excitation channels. Both show resonant-like behavior near threshold that is not associated with Feshbach resonances. It is also of interest to note that both earlier calculations predict cross sections that are closer to the magnitude of the experiment, which argues somewhat against our notion that the absolute magnitude of the published experimental results is off by a factor of two. Again, an experimental re-examination of the Na^- photodetachment cross section is required to settle the issue.

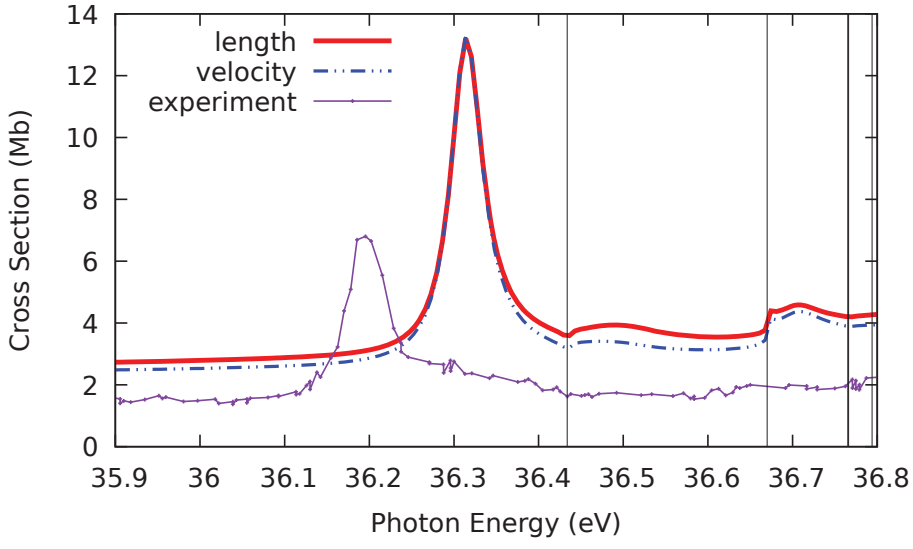

Figure 3. Photodetachment of Na^- near the Feshbach resonance just above 36 eV. The calculated inner-shell thresholds are shown as vertical black lines.

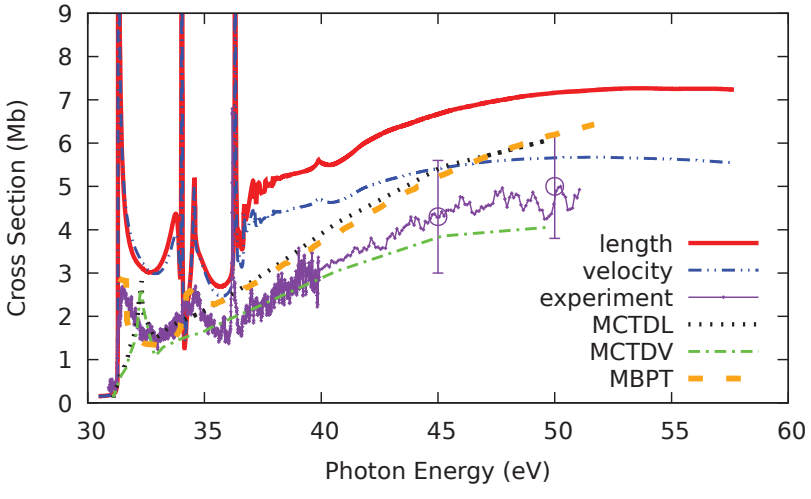

Figure 4. Photodetachment of Na^-: Present R-matrix cross sections compared to earlier theoretical results: the Multiconfiguration Tamm-Damcoff results [21] in length (MCTDL) and velocity (MCTDV) forms, as well as many-body perturbation theory (MBPT) results [20].

Another point of importance is the agreement between length and velocity in the present calculation. From the inner-shell detachment threshold to about 37 eV, the agreement between the two gauges is seen to be excellent. This agreement strongly suggests (but does not prove) that the present calculation is reliable in this energy region. At the higher energies, the agreement is not quite as good, with a roughly 20% difference between length and velocity gauge results, but is sill not terrible. The disagreement in this region is likely due to the omission of the myriad of $2p^5nln'l'$ states of Na in the close-coupling expansion.

4. Summary and Conclusions

The inner-shell photodetachment cross section of Na^- has been calculated using R-matrix methodology. The results show excellent *qualitative* agreement with experiment, including the sharp Feshbach resonance just above 37 eV that was absent in previous calculations. The disagreement with experiment at the first $2p$ threshold is mainly due to the PCI effect which is not included in the present calculation. Overall, the calculated cross section is about a factor of two larger than the experimental result, and this is problematical. Owing to the agreement of length and velocity gauges in the calculation, along with the agreement of the theoretical Na^- cross section with the $2p$ photoionization cross section of neutral Na, it is suggested that the measured inner-shell photodetachment cross section of Na^- is too small by a factor of about two; it is strongly suggested that this matter be re-examined experimentally.

Many-body correlation effects were seen to be not merely important but crucial to the behavior of the inner-shell Na^- photodetachment cross section. The initial state of Na^- is not even bound without the inclusion of correlation. And the various structures seen in the photodetachment cross section are intimately tied up with correlation in the final-state wave function, effects that are absent (or much diminished) in the corresponding photoionization of neutral Na. The situation can be thought of in the framework of a simple conceptual model. An ionizing photon excites inner-shell electron, and the photoelectron emerges through the cloud of outer-shell electrons. On its way out, the photoelectron can scatter inelastically off an outer-shell electron, giving up some of its energy and exciting the outer-shell electron, resulting in a final state of photoemission-plus-excitation; from a quantum mechanical point of view, this is just interchannel coupling. For the photodetachment process, this inelastic excitation process is very strong, since the outer-shell electrons are bound so weakly in a negative ion, yielding a cross section replete with significant inner-shell photodetachment-plus-excitation channels and structures. For the neutral photoionization process, the same model applies, but the outer-shell electrons are much more tightly bound so that the probability of the excitation process is very much smaller. For this reason, then, although the photoionization-plus-excitation process does, in fact, occur for neutral Na, it is so much smaller than the main photoionization cross section that it is hardly noticeable. This shows clearly why the study of photodetachment is such an excellent venue for investigating many-body correlation in atomic systems.

Author Contributions: Conceptualization, T.W.G., H.-L.Z., A.H. and S.T.M.; methodology, T.W.G., H.-L.Z., A.H., M.F.H. and S.T.M.; software, T.W.G., H.-L.Z., A.H.; validation, T.W.G., H.-L.Z., A.H., M.F.H. and S.T.M.; formal analysis, T.W.G., H.-L.Z., A.H., M.F.H. and S.T.M.; investigation, T.W.G. and S.T.M.; resources, T.W.G. and S.T.M.; data curation, T.W.G., H.-L.Z., A.H. and M.F.H.; writing—original draft preparation, T.W.G. and S.T.M.; writing—review and editing, T.W.G., H.-L.Z., A.H. and S.T.M.; visualization, A.H.; supervision, T.W.G. and S.T.M.; project administration, T.W.G. and S.T.M.; funding acquisition, T.W.G. and S.T.M. All authors have read and agreed to the published version of the manuscript.

Funding: T.W.G. was supported in part by NASA (NIX11AF32G). S.T.M. was supported by the U.S. Department of Energy, Office of Basic Sciences, Division of Chemical Science, Geosciences and Biosciences under Grant No. DE-FG02-03ER15428.

Conflicts of Interest: The authors declare no conflict of interest.

References

1. Buckman, S.J.; Clark, C.W. Atomic negative-ion resonances. *Rev. Mod. Phys.* **1994**, *66*, 539–655. [CrossRef]
2. Ivanov, V.K. Many-body effects in negative ion photodetachment. *J. Phys. B At. Molec. Opt. Phys.* **1999**, *32*, R67–R101. [CrossRef]
3. Andersen, T. Atomic negative ions: structure, dynamics and collisions. *Phys. Rep.* **2004**, *394*, 157–313. [CrossRef]
4. Gorczyca, T.W. Inner-shell photodetachment dynamics. *Radiat. Phys. Chem.* **2004**, *70*, 407–415. [CrossRef]
5. Pegg, D. Photodetachment. In *Springer Handbook of Atomic, Molecular, and Optical Physics*; Springer: Berlin/Heidelberg, Germany, 2006; pp. 891–899.

6. Froese Fischer, C. A general multi-configuration Hartree-Fock program. *Comput. Phys. Commun.* **1991**, *64*, 431–454. [CrossRef]
7. Kim, D.S.; Zhou, H.L.; Manson, S.T. Photodetachment of the 1s2s2p ^{4}P state of He^- from threshold to 100 eV. *Phys. Rev. A* **1997**, *55*, 414–425. [CrossRef]
8. Kjeldsen, H.; Andersen, P.; Folkmann, F.; Kristensen, B.; Andersen, T. Inner-shell photodetachment of Li^-. *J. Phys. B At. Molec. Opt. Phys.* **2001**, *34*, L353–L357. [CrossRef]
9. Zhou, H.L.; Manson, S.T.; Voky, L.; Feautrier, N.; Hibbert, A. Dramatic Structure in the Photodetachment of Inner Shells of Negative Ions: Li^-. *Phys. Rev. Lett.* **2001**, *87*, 023001. [CrossRef]
10. Berrah, N.; Bozek, J.D.; Wills, A.A.; Turri, G.; Zhou, H.L.; Manson, S.T.; Akerman, G.; Rude, B.; Gibson, N.D.; Walter, C.W.; et al. K-Shell Photodetachment of Li^-: Experiment and Theory. *Phys. Rev. Lett.* **2001**, *87*, 253002. [CrossRef]
11. Berrah, N.; Bozek, J.D.; Turri, G.; Akerman, G.; Rude, B.; Zhou, H.L.; Manson, S.T. K-Shell Photodetachment of He^-: Experiment and Theory. *Phys. Rev. A* **2002**, *88*, 093001.
12. Zatsarinny, O.; Gorczyca, T.W.; Froese Fischer, C. Photodetachment of He^- 1s2s2p $^4P^o$ in the region of the 1s threshold. *J. Phys. B At. Molec. Opt. Phys.* **2002**, *35*, 4161–4178. [CrossRef]
13. Sanz-Vicario, J.L.; Lindroth, E. Resonant triply excited states in the photodetachment of He^- 1s2s2p $^4P^o$. *Phys. Rev. A* **2002**, *65*, 060703. [CrossRef]
14. Sanz-Vicario, J.L.; Lindroth, E.; Brandefelt, N. Photodetachment of negative helium ions below and above the 1s ionization threshold: A complex scaled configuration-interaction approach. *Phys. Rev. A* **2002**, *66*, 052713. [CrossRef]
15. Gorczyca, T.W.; Zatsarinny, O.; Zhou, H.L.; Manson, S.T.; Felfli, Z.; Msezane, A.Z. Postcollision recapture in the K-shell photodetachment of Li^-. *Phys. Rev. A* **2003**, *68*, 050703. [CrossRef]
16. Bilodeau, R.C.; Bozek, J.D.; Ackerman, G.D.; Aguilar, A.; Berrah, N. Photodetachment of He^- near the 1s threshold: Absolute cross-section measurements and postcollision interactions. *Phys. Rev. A* **2006**, *73*, 034701. [CrossRef]
17. Dumitriu, I.; Bilodeau, R.C.; Gorczyca, T.W.; Walter, C.W.; Gibson, N.D.; Rolles, D.; Pešić, Z.D.; Aguilar, A.; Berrah, N. Inner-shell photodetachment from $N\,i^-$: A giant Feshbach resonance. *Phys. Rev. A* **2017**, *96*, 023405. [CrossRef]
18. Perry-Sassmannshausen, A.; Buhr, T.; Borovik, A.; Martins, M.; Reinwardt, S.; Ricz, S.; Stock, S.O.; Trinter, F.; Müller, A.; Fritzsche, S.; et al. Multiple Photodetachment of Carbon Anions via Single and Double Core-Hole Creation. *Phys. Rev. Lett.* **2020**, *124*, 083203. [CrossRef]
19. Covington, A.M.; Aguilar, A.; Davis, V.T.; Alvarez, I.; Bryant, H.C.; Cisneros, C.; Halka, M.; Hanstorp, D.; Hinojosa, G.; Schlachter, A.S.; et al. Correlated processes in inner-shell photodetachment of the Na^- ion. *J. Phys. B At. Molec. Opt. Phys.* **2001**, *34*, L735–L740. [CrossRef]
20. Ivanov, V.K.; Yatsyshin, P.I. Resonances in the cross section of photodetachment of 2 p electrons from negative ions Na^-. *J. Tech. Phys.* **2009**, *54*, 7–12. [CrossRef]
21. Jose, J.; Pradhan, G.B.; Radojevic, V.; Manson, S.T.; Deshmukh, P.C. Inner Shell Photodetachment of Na- Using The Multi-Configuration Tamm-Dancoff Approximation. *Pub. Astronom. Obs. Belgrade* **2010**, *89*, 29–32.
22. Zhou, H.L.; Manson, S.T.; Hibbert, A.; Gorczyca, T.W. Inner-shell Photodetachment of Na^-. *Bull. Am. Phys. Soc.* **2006**, *51*, 151.
23. Hibbert, A. CIV3—A general program to calculate configuration interaction wave functions and electric-dipole oscillator strengths. *Comput. Phys. Commun.* **1975**, *9*, 141–172. [CrossRef]
24. Gorczyca, T.W.; Robicheaux, F.; Pindzola, M.S.; Griffin, D.C.; Badnell, N.R. Elimination of electron-ion pseudoresonances associated with approximate target wave functions. *Phys. Rev. A* **1995**, *52*, 3877–3888. [CrossRef] [PubMed]
25. Burke, P.G. *R-Matrix Theory of Atomic Collisions*; Springer: New York, NY, USA, 2011.
26. Berrington, K.A.; Eissner, W.B.; Norrington, P.H. RMATRX1: Belfast atomic R-matrix codes. *Comput. Phys. Commun.* **1995**, *92*, 290–420. [CrossRef]
27. Ralchenko, Y.; Kramida, A.E.; Reader, J.; NIST ASD Team. NIST Atomic Spectra Database (ver. 4.1.0). National Institute of Standards and Technology. 2011. Available online: http://physics.nist.gov/asd (accessed on 1 April 2020).
28. Andersen, T.; Haugen, H.K.; Hotop, H. Binding Energies in Atomic Negative Ions: III. *J. Phys. Chem. Ref. Data* **1999**, *28*, 1511–1533. [CrossRef]

29. Starace, A.F. Theory of Atomic Photoionization. *Handbuch Physik* **1982**, *31*, 1–121.
30. Gorczyca, T.W.; Manson, S.T. Outer-Shell Photodetachment of Li^- Near Inner-Shell Thresholds. *J. Phys. B At. Molec. Opt. Phys.* **2020**, *53*, 195203. [CrossRef]
31. Russek, A.; Mehlhorn, W. Post-collision interaction and the Auger lineshape. *J. Phys. B At. Molec. Phys.* **1986**, *19*, 911–927. [CrossRef]
32. Kuchiev, M.Y.; Sheinerman, S.A. The post collision interaction in the inner-shell photoionisation of Ar and Xe. *J. Phys. B At. Molec. Phys.* **1985**, *18*, L551–L556. [CrossRef]
33. Cubaynes, D.; Voky, L.; Wuilleumier, F.J.; Rouvellou, B.; Hibbert, A.; Faucher, P.; Bizau, J.M.; Journel, L.; Saraph, H.E.; Bely-Dubau, F. Inner-shell photoionization of sodium: Experiment and theory. *Phys. Rev. A* **1998**, *57*, 4432–4451. [CrossRef]

atoms

MDPI

Article

Modification of a Cylindrical Mirror Analyzer for High Efficiency Photoelectron Spectroscopy on Ion Beams

Francis Penent [1,*], Denis Cubaynes [2,3], Pascal Lablanquie [1], Jérôme Palaudoux [1], Ségolène Guilbaud [2], Olivier Moustier [2], Jérôme Guigand [2] and Jean-Marc Bizau [2,3]

[1] Laboratoire de Chimie Physique-Matière et Rayonnement (UMR 7614), Sorbonne Université, CNRS, F-75005 Paris, France; pascal.lablanquie@upmc.fr (P.L.); jerome.palaudoux@sorbonne-universite.fr (J.P.)

[2] Institut des Sciences Moléculaires d'Orsay (ISMO), CNRS, Univ. Paris Paris-Sud, Université Paris-Saclay, F-91405 Orsay, France; denis.cubaynes@universite-paris-saclay.fr (D.C.); segolene.guilbaud@universite-paris-saclay.fr (S.G.); olivier.moustier@universite-paris-saclay.fr (O.M.); jerome.Guigand@universite-paris-saclay.fr (J.G.); jean-marc.bizau@universite-paris-saclay.fr (J.-M.B.)

[3] Synchrotron SOLEIL, L'Orme des Merisiers, Saint-Aubin, BP 48, F-91192 Gif-sur-Yvette, France

* Correspondence: francis.penent@upmc.fr

Received: 1 September 2020; Accepted: 24 September 2020; Published: 25 September 2020

Abstract: An existing cylindrical mirror analyzer (CMA) that was initially equipped with eight channeltrons detectors has been modified to install large micro-channel plate detectors to perform parallel detection of electrons on an energy range corresponding to ~12% of the mean pass energy. This analyzer is dedicated to photoelectron spectroscopy of ions ionized by synchrotron radiation. The overall detection efficiency is increased by a factor of ~20 compared to the original analyzer. A proof of principle of the efficiency of the analyzer has been done for Xe^{5+} and Si^{+} ions and will allow photoelectron spectroscopy on many other ionic species.

Keywords: photoionization; electron spectroscopy; ion beam; synchrotron radiation

1. Introduction

Photoionization of atomic ions is a major importance to understand laser-produced laboratory and astrophysical plasmas (OPACITY and IRON projects [1,2]). Most experimental results on ionic species concern photoabsorption experiments for which photoion spectrometry has allowed the determination of absolute cross-sections for a variety of ions using the technique of merged ion and photon beams [3–5]. Recent insights have also been provided by other techniques, for instance by choosing C^{+} ions and detecting C^{4+} to unravel triple Auger decay [6], or by fluorescence spectroscopy with ion traps [7]—that is a nowadays an adaptation of the historical spectroscopy on plasma discharges—to study the emission spectra of ions. To go further in the interpretation of the ionization processes, it is necessary to understand how resonances, due for instance to the excitation of an inner-shell electron to a vacant orbital, will decay when different channels are possible (autoionization, Auger decay, cascade processes . . .) to obtain partial cross sections. To unravel such processes, electron spectroscopy can be a very helpful technique. Here, contrary to the usual field of application of electron spectroscopy to neutral gas target or to surfaces, the difficulty comes from the very low ion density in an ion beam, typically six orders of magnitude lower than the density of a neutral gas target. It is hence very difficult to perform electron spectroscopy with ionic targets. While for ion spectrometry it is possible to use a long interaction region (~1 m) with overlapping ion and photon beams and to detect all the different charged states of the ion after magnetic deflection, it remains very difficult to improve the efficiency of electron spectroscopy with ion beams [8]. Due to reduced length of the source (~1 cm)

and acceptance solid angle (~1%) of the analyzer, the electron count rates are typically three or four orders of magnitude lower than the ion count rates. Moreover, the electron signal often appears on a high background resulting from ionization of the residual gas by the photon beam from collisions even in ultra-high vacuum conditions (~10^{-10} hPa). Increasing the ion target density (if possible?) is not a real option since the charge of the ion beam will induce a shift and a broadening of the photoelectron peaks. Increasing the photon flux is possible by moving from synchrotron to X-ray free-electron laser (XFEL) sources but experiments remain nevertheless difficult [9]. Using 4π detection analyzers as magnetic-bottle electron spectrometers could appear as a possible option, but the Doppler-shift with ion velocity of the electron spectra becomes a real limitation [10] to perform electron spectroscopy with acceptable resolution. While it could be possible to use zero-degree electron spectroscopy [11–13] to limit the Doppler broadening, it seems that this possibility was never explored on synchrotron centers.

All these difficulties explain why experiments reporting electron spectroscopy with ion beams are scarce. For a long time, only two experimental results were published: on Ca^+ giant resonance [14,15] and on Xe^+ [16].

After the pioneering work on Ca^+ [14,15] at the Super-ACO synchrotron at Orsay, the cylindrical mirror analyzer (CMA) analyzer that was used to perform these experiments [17] was installed on the PLEIADES beamline of SOLEIL synchrotron to be used with the MAIA (multi analysis ion apparatus) set-up [18]. The analyzer equipped with eight channeltrons was used to study Xe^{5+} ionization processes on 4d → nf resonances [19]. To extract the true electron signal from a high background, it was necessary to detect the product Xe^{6+} ion in coincidence with the electron and to subtract the random coincidences. The method was efficient to study Xe^{5+} resonances decay [19] with true electron count rates of about 1 e^-/s needing long acquisition time.

With the same set-up, it was further possible to extract the Xe^+(4d) photoelectron signal at 120.7 eV photon energy [20], the results were validated by cross-checking with core-valence double ionization of Xe [20] and have clearly shown that the first published results on Xe^+ [16] were not correct for some unknown reason. That proves, if necessary, how difficult electron spectroscopy with ion targets may be.

Although these recent results [19,20] are encouraging, with third-generation synchrotron sources, the electron count rates remain very small for most of the ions to study even when the photon energy is tuned on a resonance. Hence, long accumulation times are necessary that are not always compatible with the time allocated to a given experiment on the synchrotron (typically one or two weeks continuously).

2. Experimental Approach

This was the motivation to modify our CMA analyzer to increase its detection efficiency. This analyzer was first described in reference [15,17] and was designed to perform angle resolved photoelectron spectroscopy on ions using eight channeltrons. The source volume of the analyzer, defined by two ~6 mm slits in the two inner cylinders of the analyzer (R_0 = 39 mm and R_{int} = 73 mm), is about 20 mm long (Figure 2 in [17]), although the main contribution is due to the central 6 mm zone which is not cut by the first slit. This analyzer can be inserted on the MAIA set-up, which is a permanent installation on the PLEIADES beamline at SOLEIL for the study of ionic species [18], and comes in place of the chamber used for ion spectrometry with merged ion and photon beams. The analyzer exit slit, in front of the channeltrons, was also 6 mm (see Figure 10 in [18]). The 8 channeltrons (~15 mm entrance cone) were positioned between the two inner cylinders of the CMA on the image focal ring (point to ring focusing [17]). To obtain a complete energy spectra on a broad energy range it is necessary to scan the analyzer voltage (difference between the potential of inner and outer cylinders).

Our simple idea was to open wide (>80 mm) the exit slit of the analyzer in order to replace the channeltrons by micro-channel plate detectors as it is usually done for the most frequently used 180° hemispherical deflector electron energy analyzer. The electron energy is deduced from the impact position of the electrons on the micro-channel plates (MCP) detector, thanks to position encoding systems (delay-line or phosphor screen with charge-coupled device (CCD) camera detector). With a cylindrical mirror analyzer, the focusing conditions (between the source and the image points), that

are a general rule for any electron analyzer [21], were defined in [17] to build this analyzer for a point to ring focusing, but they cannot be fulfilled for a point to cylinder focusing on a broad energy range. Although some prospective studies exist [22], where a point to cylinder focusing seems possible on a broad energy range for a modified CMA analyzer, this was not verified here. Nevertheless, since ultimate energy resolution is not the goal of our analyzer that aims to have the highest possible luminosity, we have relied on a simple electron trajectories simulation using SIMION® [23] to verify how the analyzer works in a given energy range.

2.1. SIMION Simulations with Cylindrical Symmetry

The real analyzer uses 15 guard rings that are polarized through a resistive chain to follow the 1/r variation of the potential. For sake of simplicity, an "ideal" CMA analyzer was simulated with SIMION in cylindrical symmetry with 1 mm SIMION graphic unit (gu). Due to the averaging property of the Laplace equation, no noticeable differences exist between the ideal and the real CMA at a few cm from the guard rings inside the analyzer, and the electron trajectories are absolutely similar. This "ideal" cylindrical analyzer allows to see how the electrons travel from the source point to the detector. We fixed the analyzer voltage to 0 V for the inner cylinder and −24 V for the outer cylinder, any other value is obtained by scaling all voltages. The potential between the two cylinders is $V(r) = (V_{in} - V_{out})\left(\frac{R_{out}R_{in}}{R_{out}-R_{in}}\right)\left(\frac{1}{r} - \frac{1}{R_{in}}\right) + V_{in}$ with (R_{in} = 73 mm, R_{out} = 226 mm).

For electrons created at the source point on the axis of the analyzer, we can see in Figure 1a that the focusing that is obtained for the central energy (29 eV) where the exit slit for the channeltrons detectors was initially positioned is no longer valid for all energies. The point to ring focusing conditions are not on a cylinder but rather on a cone frustum (best focus line). When the real size of the interaction volume (L~20 mm, R~1 mm) and the angular acceptance of the entrance slits are taken into account, the energy dispersion and the extension of the image for each energy remain however very good (Figure 1b). Since the radius of the ion and photon beams are about 1 mm, we do not consider the trajectories of electrons starting off axis that would spiral inside the analyzer. The analyzer is big enough (R_{in} = 73 mm, R_{out} = 226 mm, L = 500 mm) to make this problem not critical. However, it is necessary to keep the photon and ion beams on the analyzer axis to avoid a tilt of the image circle that would give different z on the detector for the same energy but different azimuth angle.

2.2. Mechanical Construction of the Analyzer

Since, at the moment, no cylindrical detector exist that could be installed after a cylindrical mesh (R_{in}, V_{in}) at the exit of analyzer, the cylindrical symmetry is broken when a detector is installed. Note that such detector could eventually have been developed with microsphere molding between two cylinders [24].

A first idea could have been to replace the eight channeltrons by eight MCP chevron assemblies located at ($0° + n \times 45°$; n = 0–7) angles with respect to the photon polarization (for direct determination of β asymmetry parameter at 0° and 90°). However, a cheaper option with only 6 MCP (L ~ 80 mm, w ~ 30 mm) was chosen ($0° + n \times 60°$; n = 0–5). The space available between the two inner cylinders allowed the insertion of 6 MCP assemblies on a hexagonal holder (see Figure 2). Compared to 8 channeltrons with 6mm slits the detection area is multiplied by (80/6) × (30/15) × (6/8) = 20, but the open area ratio (OAR) of the MCP being 70% a gain of ~14 is expected. This means than an increase in efficiency by about one order of magnitude and, consequently, experiments that would have need one week of continuous accumulation can be done in less than one day.

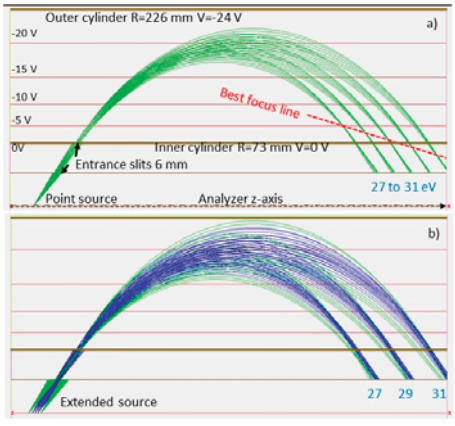

Figure 1. (**a**) SIMION® simulation of electron trajectories, starting from a source point, inside an ideal cylindrical analyzer for energies from 27 to 31 eV with V_{in}–V_{out} = 24 V (the field varies as 1/r) and elevation angles from 50° to 60° (around the 54.4° magic angle). The two 6 mm entrance slits limit the acceptance angle. The focus on the inner cylinder is for K.E. ~ 29 eV. (**b**) Simulation for an extended source. The trajectories of electrons starting from the central 6 mm zone (blue trajectories) are not cut by the first slit, while electron from the two zones of 7 mm before and after are limited by the most inner slit. They induce an asymmetric broadening of the electron peak.

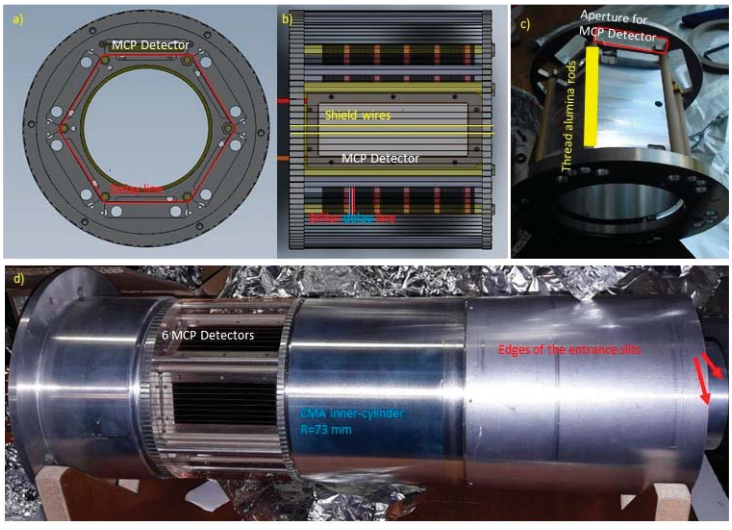

Figure 2. (**a**,**b**) The drawing of the detector. (**c**) hexagonal holder for the 0.5 mm threaded alumina rod on which the bifilar delay line is coiled. (**d**) The cylindrical mirror analyzer (CMA) inner cylinder with detectors installed. Longitudinal wires at the same potential allow the electrons to reach the micro-channel plates (MCP). The whole system is inserted in the CMA analyzer. Electrical connections (MCP polarization, delay line) go out on the left side of the image.

The position encoding along z is done with a bifilar delay line coiled around 6 alumina rods (Figure 2c) with 0.5 mm thread. Two copper wires (0.13 mm) were wound parallel simultaneously with a 1 mm step around the six alumina rods with a constant tension of 30 g along 85 mm to create a bifilar delay-line (see Figure 2a,b). A single turn corresponds to ~30 cm of wire length (1 mm along z and

~1 ns in time propagation), the total length of the line is ~25 m and corresponds to a time propagation of ~83 ns. The duralumin holder (Figure 2c) prevents flexion of the alumina rods when 85 turns are wound and avoids loosening of the coil. The electrical resistance of the wire is 30 ohms and does not induce a strong attenuation of the electron signal that propagates towards the two ends of the bifilar delay line. Position encoding was performed thanks to a time-to-digital converter (TDC-V4) [25] with 125 ps time resolution by measuring the time difference ($T_1 - T_2$) of the signal that have propagated toward the two ends of the line. To be sure that the signals at the two ends correspond to the same electron the time ($T_1 + T_2 - 2T_0$) must correspond to the delay line propagation time of 83 ns ± ΔT (with ΔT ≈ 2 ns). T_0 corresponds to the time of arrival of the electron on the MCP and is given by the signals $S_{1–6}$ on the back of any of the 6 MCPs (S_1 OR S_2 … OR S_6) that initiates the TDC acquisition process. The signal from each channel plate chevron assembly was taken on the backside and decoupled from the high voltage by a capacitance out of the vacuum chamber.

As seen in Figure 1a, with 80 mm long detector it is possible to detect simultaneously energies from 27 to 31 eV. That corresponds to ΔE/E ≈ 14%. The energy dispersion is linear with z in a very good approximation on the central 70 mm long zone of the MCP, however, due to some edge effects with the real detector (MCP holder thickness, delay-line termination), a ~5 mm zone on the two sides of the detector was securely excluded from the analysis by software filtering and limits ΔE/E to about 12%.

The rectangular MCPs were manufacture by Hamamatsu® and are 87 × 37 mm outer dimensions with 81 × 32.5 mm active area. The detector consists of two MCPs in chevron position that are inserted in a PEEK holder and polarized thanks to thin 0.1 mm rectangular copper frames. Metallic frames of 98 × 48 mm (visible in Figure 2b,d) allow to secure the two MCPs, and the insertion of the detector between the two inner cylinders with a groove in PEEK rods. Although the hexagonal shape of the detector does not match the cylindrical symmetry, the distance (~1 cm) between the shield wires (Figure 2b), that are at the potential of the inner cylinder of the CMA, and the front MCP, on which the electron are accelerated to ~200 eV, is not critical and a circle is projected as a straight line on the MCP. Six detectors can be installed at 60° from each other, but, unfortunately, due to a crack in one set of MCPs only 5 could be installed. The whole system (Figure 2d) with the detectors is than inserted in the CMA analyzer.

The insertion of the detector into the analyzer can be seen in Figure 3.

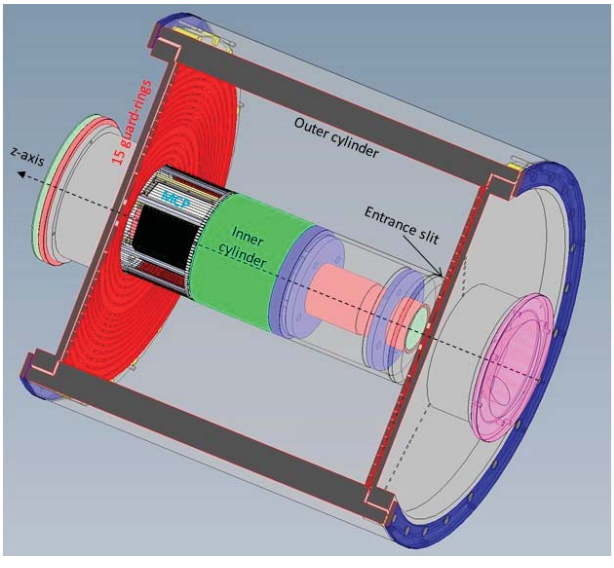

Figure 3. 3D sectional plan of the real CMA analyzer showing all the electrodes and the insertion of the MCP detectors. The ion beam travels along the z-axis inside the most inner cylinder R_0.

2.3. Optimization of the Analyzer

Since a single delay-line is used to detect the signal from different MCPs, the potential of the back MCP (about 1800 V) must be the same for all MCPs in order to optimize the detection of the electron cloud on the wires that are polarized at +200 V and +150 V with respect to the MCP back. The MCP must have similar impedances and signal amplification factor. They were manufactured in the same process and the impedances were measured to match the same characteristics. A single detector was tested in a first step of the analyzer development and the MCP characteristics were slightly different from the next ones. Consequently, the amplification of the different MCP could be different when the same potential is applied to polarize the MCPs. This makes the adjustment of discriminator threshold critical.

Another difficulty is due to the length of connecting cables from the vacuum flange to the MCP (about 1 m) that are not exactly matched in impedance with the bifilar delay line. This induces some rebounds in the electron signal. Hopefully, since the electron count rates remain low it was possible to broaden the signal to 200 ns to kill the rebounds in the logic NIM or TTL signals. Another problem is some cross-talk between the different MCP detectors. In the present configuration, is would be rather difficult to deduce beta parameter from the count rate on different MCPs positioned at different azimuthal angles.

The signal at each end of the delay line is a differential signal because the electrons are collected on the higher potential wire (cf. Roentdek® [26]) and is very clean. The signal from the back MCP is noisier. The ultrahigh vacuum conditions and the limited space for the MCP assemblies do not allow to use in-vacuum capacitors and resistors close enough from the detector to filter out the MCP signal. The connection of signal cables is also critical because tin solder cannot be used due to baking of the analyzer at more than 100 °C to reach ultrahigh vacuum. This baking was also critical for the delay line detector and the copper wires were relaxed and eventually short-circuited after baking operation.

Nevertheless, most of these little (but time consuming due to ultra-high vacuum constraints) problems could be reduced and the analyzer operated as expected.

The calibration of the analyzer is done by introducing neon gas target in the chamber to a pressure of 10^{-7} hPa. By changing the analyzer voltage and/or the photon energy, the 2p photoelectron peak (Figure 4) is moved from one edge to the other of the MCP and allows a precise calibration of the electron energy with the position on the detector. This procedure allows also to verify that no major distortion due to bad focusing conditions occur. Since the channel plates were only detection quality ones, and not imaging quality for cost limitations, it is necessary to move the photoelectron peak on all positions on the MCP to have an average detection efficiency on the whole area. The position is linearized as a function of the analyzer voltage and an electron spectra is collected (Figure 4).

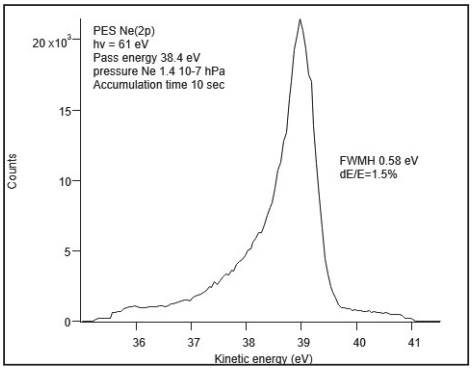

Figure 4. Ne 2p photoelectron peak. The resolution ΔE/E is 1.5% thanks to the 1 mm precision encoding with the delay line. The peak asymmetry towards lower energy can be explained by the focusing at lower z of electrons created out of the central zone seen in Figure 2b.

The control of all the experimental parameters (photon energy, analyzer voltages) and the acquisition is done with different Labview procedures [18].

After the ionization event, the time of arrival of the electrons to the detector and of the signal at the end of the delay line are less than 100 ns, but in order to extract the true electron signal the product ion is detected in coincidence with the photoelectron. The product ions are detected after magnetic q/m deflection and energy analysis by an electrostatic deflector before detection by MCPs with a typical efficiency of 50% (if the ions are fast enough). A phosphor screen and a CCD camera are used to center the product ions on the MCP by adjusting the current in the analyzing magnet and the deflector potentials. The time of flight (TOF) of ions to the detector depends on the velocity of the ion and is typically a few μs, much longer than electron TOF. The TDC window is opened for a time long enough for the arrival of the ion to the detector. In practice this time is also a limit for the electron count rate since no other electron should initiate another timing measurement.

3. Experimental Results

3.1. Results on Xe^{5+}

Xe^{5+} 4d inner-shell photoionization was measured in a previous experiment [19] with the original configuration of the analyzer with 8 channeltrons. The experiment was repeated with the modified analyzer, after baking of the CMA, during another experimental session of 21 shifts. In Figure 5 we compare the two spectra on Xe^{5+} ions [19] at 94.4 eV photon energy (4d → 4f resonance) with the 8 channeltrons detector (lower panel Figure 5b) and with the analyzer equipped with 5 MCPs detectors (upper panel Figure 5a). This last spectrum was obtained by scanning the CMA pass energy between 26 and 37.5 eV with 0.5 eV step. We observe two lines corresponding to the Xe^{6+} $5s^2$ final state starting from Xe^{5+} $5p\ ^2P_J$ J = 1/2 and 3/2 levels: $Xe^{5+}[Kr]5s^25p\ ^2P_{1/2;3/2}$ + hν(94.4 eV) → $Xe^{5+}4d^95s^25p4f$ → Xe^{6+} $5s^2$ + e^-.

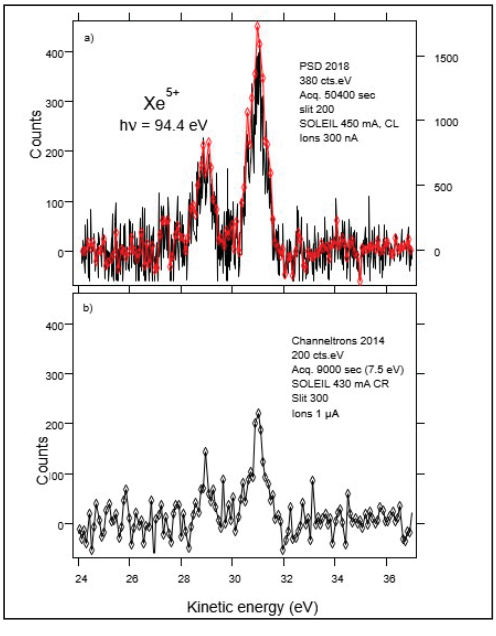

Figure 5. Comparison of electron spectra in Xe^{5+} (4d → 4f) resonance with different detection systems: (**a**) Position sensitive detector with 5 MCPs versus (**b**) 8 channeltrons. The energy step is 20 meV in (**a**) and 100 meV in (**b**). To make the comparison easier, the red curve in (**a**) was summed on 5 points to compare the counts rate (right scale) with (**b**) with the same 100 meV steps.

It was obtained in 14 h with much better statistics and also better energy resolution because the resolution in position with the delay line encoder is 1 mm while the slit in front of the channeltron was 6 mm. The energy step coherent with the resolution in position in Figure 5 was 100 meV with the channeltron and 20 meV with the MCPs.

The quality of the spectrum is clearly improved, the gain in efficiency is close to one order of magnitude but remains difficult to precisely quantify because the overlap between the photon and ion beams was not measured in these experiments and many other parameters (ion current, acquisition time, photon flux, . . .) changed between the two experiments taken with 4 years interval.

3.2. Results on Si^+

In Figure 6 we present the electron spectra on the strongest 2p → 3d resonance of Si^+ at 111.74 eV [27] corresponding to Si^+ $2p^{-1}3s^23p3d\ ^2D_{5/2}$ configuration. This spectra was first obtained with the analyzer equipped with only one MCP assembly. We can see on this spectra that the preferential decay channel correspond to an Auger decay with a spectator 3d electron leading to Si^{2+} $3s3d\ ^3D$. This dominant decay channel corresponds to a filling of the 2p hole by a 3s electron with ejection of the 3p electron. There is no evidence of participator Auger decay of the 3d electron giving Si^{2+} ion in its ground state $2p^63s^2\ ^1S$ that would involve filling of the 2p hole by a 3p electron and ejection of the 3d electron. It seems however that the $3s3p\ ^1P$ state can be reached by filling of the 2p hole by a 3s electron and ejection of the 3d electron. Some other peaks, at lower kinetic energy, correspond certainly to Auger decay with shake-up of the 3d electron.

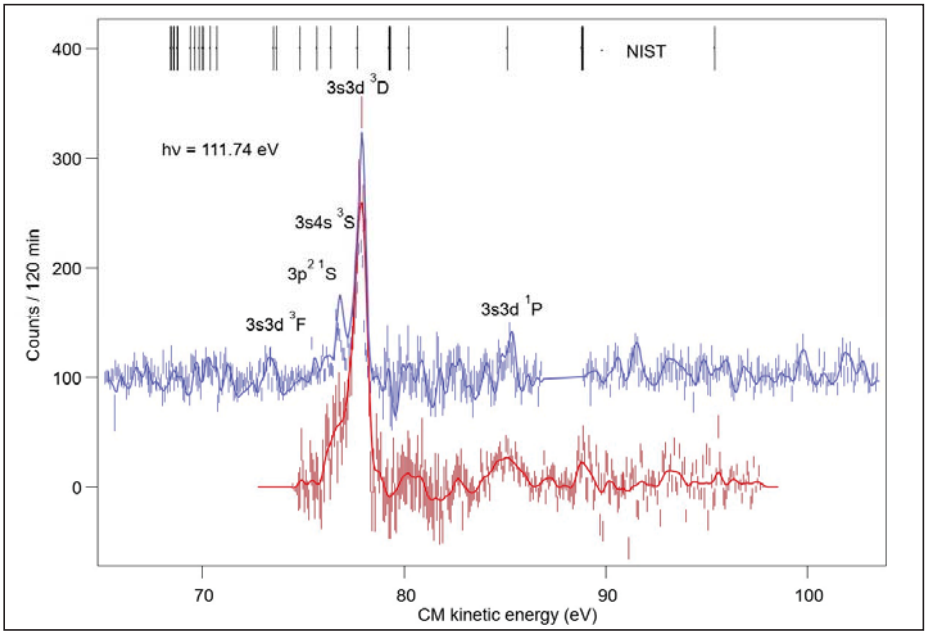

Figure 6. Electron spectra on Si^+ 2p → 3d $^2D_{5/2}$ resonance (two different energy scans). The black lines correspond to the energy levels from NIST for Si^{2+} [28].

This confirms that the electron spectra provide essential additional information to the results obtained by ion spectrometry [27]. The final Si^{2+} states are excited states that can only decay by emission of a photon that could be detected by optical spectroscopy.

4. Conclusions

We have proved by the present results on a few examples that the concept of parallel energy detection with a CMA analyzer is a very good option although the optimal focusing is not achieved for all electron energies. We have modified our CMA analyzer to install large MCPs detectors. The Si^+ and Xe^{5+} examples show that electron spectroscopy can be performed in a reasonable time when absolute cross section are of tens of Mb and not only giant resonances. This could be extended to molecular ions of astrophysical interest as CH^+, SiH^+, OH^+ [29] and possibly to $CH_n{}^+$, $SiH_n{}^+$. Although some improvements are still possible and desirable, this analyzer is a good tool to perform photoelectron spectroscopy with ion beams with an angular acceptance about 0.7% of 4π solid angle around the 54.4° magic angle. One practical problem is the need of impedance matching between all MCP assemblies to insure the same detection efficiency in order to determine partial angular (azimuthal) distributions of photoelectrons. Hence the global cost of the detection system may also be an issue. Some improvements remain possible to precisely adjust the detection efficiency of the 6 MCPs set-up. By installing a grid just in front of the MCP at a potential of ~200 V, it is possible to adjust independently the voltage of the front MCP (typically 200 ± 50 V) to reach the same amplification for all the detectors, since it is necessary to keep the same voltage on the back of all the MPC to have the same extension of the electron cloud on the delay line. The decoupling of the signal—to avoid cross-talk that is also a crucial issue to determine angular distribution—would need vacuum capacitors and resistors compatible with an ultra-high vacuum and some miniature high voltage connectors (not commercially available) providing reliable connections to avoid any soldering. Another difficulty with ultrahigh vacuum is the need of baking that can loosen fixations. When one week is allocated for an experiment it is not possible to make any repair in a short delay with these constraints. To obtain the precise angular distribution, it is certainly possible to use a ceramic printed circuit board to create a bifilar delay line in a direction perpendicular to the wires. There is enough space available between the wires and the hexagonal holder to insert such a system. This could be an ultimate development of the position sensitive detector for z and θ determination.

Author Contributions: Conceptualization: F.P., D.C. and J.-M.B., software: O.M. and J.-M.B.; formal analysis: J.-M.B., P.L., S.G. and D.C.; investigation: F.P., D.C., P.L., J.P., S.G., O.M., J.G. and J.-M.B.; resources: J.G. and O.M.; data curation: J.-M.B., D.C. and F.P.; writing—original draft preparation, F.P.; writing—review and editing, F.P., D.C. and J.-M.B.; visualization, F.P., D.C., J.G. and J.-M.B., supervision, F.P., D.C. and J.-M.B.; project administration, F.P., D.C. and J.-M.B.; funding acquisition, F.P., D.C. and J.-M.B. All authors have read and agreed to the published version of the manuscript.

Funding: This research has been done within the LABEX Plas@par project, and received financial state aid managed by the Agence Nationale de la Recherche, as part of the programme "Investissements d'Avenir" under the reference ANR-11-IDEX-0004-02.

Acknowledgments: The experiment was performed at SOLEIL Synchrotron (France) at the PLEIADES beam line, with the approval of the SOLEIL Peer Review Committee (Project N° 20160251, 20170042, 20181434). We thank the PLEIADES beam staff for help during the experiments.

Conflicts of Interest: The authors declare no conflict of interest. The funders had no role in the design of the study; in the collection, analyses, or interpretation of data; in the writing of the manuscript, or in the decision to publish the results.

References

1. Seaton, M.J. The Opacity Project. *AIP Conf. Proc.* **1995**, *322*, 117.
2. Hummer, D.G.; Berrington, K.A.; Eissner, W.; Pradhan, A.K.; Saraph, H.E.; Tully, J.A. Atomic data from the IRON Project. 1: Goals and methods. *Astron. Astrophys.* **1993**, *279*, 298–309.
3. Kjeldsen, H. Photoionization cross sections of atomic ions from merged-beam experiments. *J. Phys. B At. Mol. Opt. Phys.* **2006**, *39*, R325–R377. [CrossRef]
4. Müller, A. Precision studies of deep-inner-shell photoabsorption by atomic ions. *Phys. Scr.* **2015**, *90*, 54004. [CrossRef]

5. Schippers, S.; Muller, A. Photoionization of Astrophysically Relevant Atomic Ions at PIPE. *Atoms* **2020**, *8*, 45. [CrossRef]
6. Müller, A.; Borovik, A., Jr.; Buhr, T.; Hellhund, J.; Holste, K.; Kilcoyne, A.L.D.; Klumpp, S.; Martins, M.; Ricz, S.; Viefhaus, J.; et al. Observation of a Four-Electron Auger Process in Near-K-Edge Photoionization of Singly Charged Carbon Ions. *Phys. Rev. Lett.* **2015**, *114*, 013002. [CrossRef]
7. Kühn, S.; Shah, C.; Lopez-Urrutia, J.R.C.; Fujii, K.; Steinbrügge, R.; Stierhof, J.; Togawa, M.; Harman, Z.; Oreshkina, N.S.; Cheung, C.; et al. High Resolution Photoexcitation Measurements Exacerbate the Long-Standing Fe XVII Oscillator Strength Problem. *Phys. Rev. Lett.* **2020**, *124*, 225001. [CrossRef]
8. Windelius, O.; Aguilar, A.; Bilodeau, R.C.; Juarez, A.M.; Rebolledo-Salgado, I.; Pegg, D.J.; Röhlen, J.; Castel, T.; Welander, J.; Hanstorp, D.; et al. A collinear angle-resolved photoelectron spectrometer. *Nucl. Instrum. Methods Phys. Res. Sect. B Beam Interact. Mater.* **2017**, *410*, 144–152. [CrossRef]
9. Förstel, M.; Jordon-Thaden, B.; Domesle, C.; Arion, T.; Lischke, T.; Mucke, M.; Lammich, L.; Pedersen, H.B.; Klumpp, S.; Martins, M.; et al. Electron Spectroscopy on an Ion Beam at FLASH. *Hasylab Annu. Rep.* **2009**. Available online: https://www.academia.edu/24518735/Electron_Spectroscopy_on_an_Ion_Beam_at_FLASH (accessed on 31 August 2020).
10. Domesle, C.; Jordon-Thaden, B.; Lammich, L.; Förstel, M.; Hergenhahn, U.; Wolf, A.; Pedersen, H.B. Photoelectron spectroscopy of O^- at 266 nm: Ratio of ground- and excited-state atomic oxygen. Production and channel-resolved photoelectron anisotropy parameters. *Phys. Rev. A* **2010**, *82*, 033402. [CrossRef]
11. Itoh, A.; Schneider, T.; Schiwietz, G.; Roller, Z.; Platten, H.; Nolte, G.; Schneider, D.; Stolterfoht, N. Selective production of Auger electrons from fast projectile ions studied by zero-degree Auger spectroscopy. *J. Phys. B At. Mol. Phys.* **1983**, *16*, 3965. [CrossRef]
12. Penent, F.; Grouard, J.-P.; Montmagnon, J.-L.; Hall, R.I. Translation electron spectroscopy study of the $^1p^0$ shape resonance of H^- excited in H^- rare-gas collisions (0.5–6 keV). *J. Phys. B At. Mol. Opt. Phys.* **1991**, *24*, 173. [CrossRef]
13. Zouros, T.J.M.; Lee, D.H. Zero Degree Auger Electron Spectroscopy of Projectile Ions. In *Accelerator-Based Atomic Physics Techniques and Applications*; Shafroth, S.M., Austin, J.C., Eds.; American Institute of Physics: Woodbury, NY, USA, 1997; Chapter 13, pp. 426–479.
14. Bizau, J.M.; Cubaynes, D.; Richter, M.; Wuilleumier, F.J.; Obert, J.; Putaux, J.C.; Morgan, T.J.; Källne, E.; Sorensen, S.; Damany, A. First observation of photoelectron spectra emitted in the photoionization of a singly charged-ion beam with synchrotron radiation. *Phys. Rev. Lett.* **1991**, *67*, 576–579. [CrossRef]
15. Al Moussalami, S.; Bizau, J.M.; Rouvellou, B.; Cubaynes, D.; Journel, L.; Wuilleumier, F.J.; Obert, J.; Putaux, J.C.; Morgan, T.J.; Richter, M. First angle-resolved photoelectron measurements following inner-shell resonant excitation in a singly charged ion. *Phys. Rev. Lett.* **1996**, *76*, 4496–4499. [CrossRef] [PubMed]
16. Gottwald, A.; Gerth, C.; Richter, M. 4d photoionization of free singly charged xenon ions. *Phys. Rev. Lett.* **1999**, *82*, 2068–2070. [CrossRef]
17. Rouvellou, B.; Bizau, J.M.; Cubaynes, D.; Journel, L.; Al Moussalami, S.; Wuilleumier, F.J. A dedicated electron spectrometer for photoionization studies of atomic ions with synchrotron radiation. *J. Electron. Spectrosc. Relat. Phenom.* **1995**, *76*, 237–243. [CrossRef]
18. Bizau, J.M.; Cubaynes, D.; Guilbaud, S.; El Eassan, N.; Al Shorman, M.M.; Bouisset, E.; Guigand, J.; Moustier, O.; Marié, A.; Nadal, E.; et al. A merged-beam setup at SOLEIL dedicated to photoelectron–photoion coincidence studies on ionic species. *J. Electron. Spectrosc. Relat. Phenom.* **2016**, *210*, 5–12. [CrossRef]
19. Bizau, J.-M.; Cubaynes, D.; Guilbaud, S.; Penent, F.; Lablanquie, P.; Andric, L.; Palaudoux, J.; Al Shorman, M.M.; Blancard, C. Photoelectron Spectroscopy of Ions: Study of the Auger Decay of the 4d→nf (n = 4, 5) Resonances in Xe^{5+} Ion. *Phys. Rev. Lett.* **2016**, *116*, 103001. [CrossRef]
20. Khalal, M.A.; Lablanquie, P.; Andric, L.; Palaudoux, J.; Penent, F.; Bučar, K.; Žitnik, M.; Püttner, R.; Jänkälä, K.; Cubaynes, D.; et al. 4d-inner-shell ionization of Xe^+ ions and subsequent Auger decay. *Phys. Rev. A* **2017**, *96*, 013412. [CrossRef]
21. Granneman, E.H.A.; van der Wiel, J.M. *Handbook of Synchrotron Radiation*; Koch, E.E., Eastman, D.E., Farge, Y., Eds.; North-Holland: Amsterdam, The Netherlands; New York, NY, USA; Oxford, UK, 1983; Volume 1A, pp. 367–456.
22. Read, F. The parallel cylindrical mirror electron energy analyzer. *Rev. Sci. Instrum.* **2002**, *73*, 1129. [CrossRef]
23. Manura, D.; Dahl, D. *SIMION® 8.1 User Manual*; Scientific Instrument Services, Inc.: Ringoes, NJ, USA, 2008. Available online: http://simion.com/ (accessed on 31 August 2020).

24. Tremsin, A.S.; Pearson, J.F.; Lees, J.E.; Fraser, G.W. The Microsphere Plate: A new type of electron multiplier. *Nucl. Instrum. Methods Phys. Res. Sect. A Accel. Spectrometers Detect. Assoc. Equip.* **1996**, *368*, 719–730. [CrossRef]
25. Universite Paris-Saclay. Available online: http://www.ismo.u-psud.fr/IMG/pdf/tdc-v4_notice_utilisateur.pdf (accessed on 31 August 2020).
26. Jagutzki, O.; Mergel, V.; Ullmann-Pfleger, K.; Spielberger, L.; Spillmann, U.; Dörner, R.; Schmidt-Böcking, H. A broad-application microchannel-plate detector system for advanced particle or photon detection tasks: Large area imaging, precise multi-hit timing information and high detection rate. *Nucl. Instrum. Methods Phys. Res. A* **2002**, *477*, 244–249. [CrossRef]
27. Kennedy, E.T.; Mosnier, J.-P.; Van Kampen, P.; Cubaynes, D.; Guilbaud, S.; Blancard, C.; McLaughlin, B.M.; Bizau, J.-M. Photoionization cross sections of the aluminumlike Si^+ ion in the region of the 2p threshold (94–137 eV). *Phys. Rev. A* **2014**, *90*, 063409. [CrossRef]
28. Ralchenko, Y.; Kramida, A.E.; Reader, J.; NIST ASD Team. *NIST Atomic Spectra Database*; version 4.0.1; National Institute of Standards and Technology: Gaithersburg, MD, USA, 2011. Available online: http://physics.nist.gov/asd3 (accessed on 31 August 2020).
29. Mosnier, J.-P.; Kennedy, E.T.; van Kampen, P.; Cubaynes, D.; Guilbaud, S.; Sisourat, N.; Puglisi, A.; Carniato, S.; Bizau, J.-M. Inner-shell photoexcitations as probes of the molecular ions CH^+, OH^+, and SiH^+: Measurements and theory. *Phys. Rev. A* **2016**, *93*, 061401. [CrossRef]

atoms

MDPI

Review

Photoionization of Astrophysically Relevant Atomic Ions at PIPE

Stefan Schippers [1,*] and Alfred Müller [2]

[1] I. Physikalisches Institut, Justus-Liebig-Universität Gießen, Heinrich-Buff-Ring 16, 35392 Giessen, Germany
[2] Institut für Atom- und Molekülphysik, Justus-Liebig-Universität Gießen, Leihgesterner Weg 217, 35392 Giessen, Germany; Alfred.Mueller@iamp.physik.uni-giessen.de
* Correspondence: stefan.schippers@physik.uni-giessen.de

Received: 20 July 2020; Accepted: 14 August 2020; Published: 18 August 2020

Abstract: We review recent work on the photoionization of atomic ions of astrophysical interest that has been carried out at the photon-ion merged-beams setup PIPE, a permanently installed end station at the XUV beamline P04 of the PETRA III synchrotron radiation source operated by DESY in Hamburg, Germany. Our results on single and multiple *L*-shell photoionization of Fe^+, Fe^{2+}, and Fe^{3+} ions, and on single and multiple *K*-shell photoionization of C^-, C^+, C^{4+}, Ne^+, and Si^{2+} ions are discussed in astrophysical contexts. Moreover, these experimental results bear witness of the fact that the implementation of the photon-ion merged-beams method at one of the world's brightest synchrotron light sources has led to a breakthrough for the experimental study of atomic inner-shell photoionization processes with ions.

Keywords: photoionization; multiple ionization; many-electron processes; absolute cross sections; synchrotron radiation

1. Introduction

Much of the baryonic matter in the Universe is in a plasma state. The interpretation of the astronomical observations of cosmic plasmas requires a quantitative understanding of the quantum processes that lead to the emission or absorption of photons and that govern the charge balance of atoms and ions in a plasma. The photoionization and photoabsorption of atomic ions are important in connection with radiation transport, e.g., in stars [1] or kilonovae [2] and whenever a cosmic plasma is within the line of sight between the observer and a radiation source such as, e.g., a star, an X-ray binary, or an active galactic nucleus. Absorption spectra that were recorded by X-ray telescopes contain spectral signatures of the atomic ions contained in the plasma [3]. The most prominent features are due to the cosmically most abundant elements. Next to hydrogen and helium these are C, N, O, Ne, Mg, Si, S, and Fe [4]. The astrophysically motivated atomic-data needs concerning these and other elements from the Periodic Table have been highlighted repeatedly (see, e.g., [5–10]).

Here, we briefly review recent progress in experimental photoionization that has been accomplished while using interacting photon and ion beams at one of the world's brightest third generation synchrotron light sources. We present experimental cross sections for *L*-shell photoionization of Fe^+, Fe^{2+}, and Fe^{3+} ions, and for *K*-shell photoionization of C^-, C^+, C^{4+}, Ne^+, and Si^{2+} ions. In addition, we discuss the relevance of our results for the modeling of astrophysical plasmas.

2. Experimental Technique

The photoionization of ions by a single photon requires photon energies that exceed the ionization potential of the ion to be investigated. For stable atomic ions, these range from 10 eV for Ba^+ to 132 keV

for U^{91+} [11]. Thus, photon energies from the vacuum ultraviolet (VUV) to the hard X-ray bands are needed for investigating photoionization of ions across the entire periodic table. Powerful laboratory sources for these types of radiation are hot plasmas and synchrotron light sources, which both have been used for photoabsorption and photoionization studies with atomic ions. The dual laser plasma (DLP) technique [12] uses a laser-generated hot plasma as a back-lighter for absorption measurements with ions in a second laser-generated plasma. In contrast to the broad spectral distribution of the radiation from a hot plasma, synchrotron radiation has a much narrower photon-energy bandwidth and it is freely tunable over large energy ranges. Moreover, modern third generation synchrotron light sources provide a high photon flux, which is a prime necessity for experiments with dilute targets, such as ions, whose mutual electrostatic repulsion entails low particle densities. The density of ionic targets can be increased in ion traps, where the ion cloud can be compressed by external fields and its density can be increased by applying cooling techniques. Nevertheless, the signal rates from such arrangements are usually still rather low and, therefore, photoionization of trapped atomic ions has been performed in only a few cases [13–18], so far.

The photon-ion merged-beams technique [19–21] makes up for the diluteness of the ionic target by providing a large spatial overlap between the photon beam and the ion beam. Corresponding experimental setups were installed at several synchrotron light sources [19,22–28]. The most recent development is the use of a XUV laser for a photon-ion merged-beams experiment in a heavy-ion storage ring [29,30]. Figure 1 sketches the photon-ion merged-beams setup PIPE [27], which is permanently installed at the variable polarization XUV beam line P04 [31] of the PETRA III synchrotron light source operated by DESY in Hamburg, Germany. Different types of ion sources can be mounted, such that a large variety of ion beams can be produced. In the past years, experiments at PIPE have been performed with positive and negative atomic ions, small molecular ions, and endohedral fullerene ions [32]. After extraction from the ion source, which is operated on a potential of typically 6 kV, the ions are separated in the analyzing magnet according to their mass-to-charge ratio. Subsequently, the selected ion beam is brought to a coaxial overlap with the photon-beam by adjusting the electrostatic ion-optical elements of the ion beam line accordingly. The length of the overlap region is 1.7 m. The demerging magnet separates the more highly charged product ions from the primary ions. The demerging-magnet field strength is adjusted, such that one selected product-ion charge state is directed onto a single-particle detector that counts the product ions, which hit the detector with keV energies, with practically 100% efficiency. The combination of a large interaction volume, a record-high photon flux (more than 10^{12} s^{-1} at 0.01% bandwidth across the entire 250–3000 eV P04 energy range), and a highly efficient and largely background-free product-detection scheme provides a world-unique sensitivity for photon-interaction studies with ionized matter in the gas phase.

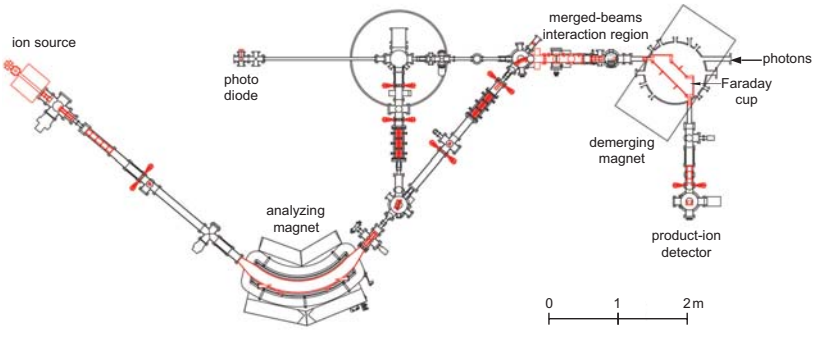

Figure 1. Sketch of the photon-ion merged-beams setup PIPE (Photon-Ion spectrometer at PETRA III). Ion-optical elements, such as focusing lenses, beam deflectors, collimating slits and Faraday cup are drawn in red color. This figure is a differently labeled version of Figure 2 from [33] (reproduced by permission of the AAS).

An asset of the merged-beam technique, which is particularly important for applications in astrophysics, is its capability to provide absolute photoionization cross sections. To this end, the photon flux, $\phi_{\rm ph}$, at PIPE is monitored with a calibrated photodiode and the primary ion current, $I_{\rm ion}$, is measured with a large Faraday cup that is located inside the demerging-magnet vacuum chamber (Figure 1). From these experimental quantities and the measured product-ion count rate, R, the absolute cross section can be calculated as

$$\sigma = R \frac{q\, e\, v_{\rm ion}}{\eta\, I_{\rm ion}\, \phi_{\rm ph}\, \mathcal{F}_L}, \tag{1}$$

where qe and $v_{\rm ion}$ are the charge and the velocity of the primary ion and η is the detection efficiency (usually $\eta = 1.0$). The factor $\mathcal{F}_L$ quantifies the mutual spatial overlap of the ion beam and the photon beam (see [27] for details). It is determined by beam-profile measurements using slit scanners that probe the beam overlap at three different locations along the photon-ion interaction region. Figure 2 shows beam profiles that are measured at its center. This procedure results in a systematic uncertainty of the absolute cross-section scale of typically 15% at a confidence level of 90% [27].

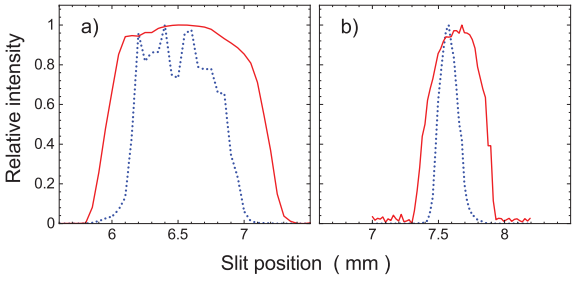

Figure 2. Measured horizontal (**a**) and vertical (**b**) beam profiles at the center of the interaction region [33] (reproduced by permission of the AAS). The red full and blue dashed curves represent the ion-beam (Ne^+) and photon-beam profiles, respectively.

The systematic uncertainty of the P04 photon-energy scale is typically ±30–200 meV after a calibration to absorption features in gases has been applied. As discussed in considerable detail in [33], the remaining uncertainty is primarily due to the uncertainties of the calibration standards that are currently available in the soft X-ray range. Considering the ppm accuracies that can be obtained at hard X-ray beamlines with crystal monochromators, this situation for soft X-rays seems unsatisfying and calls for better calibration standards. As proposed in [34] (see also below), few-electron ions could serve this purpose since the theoretical uncertainties of photoionization-resonance positions for such fundamental atomic systems are on the meV level if state-of-the-art atomic theory is applied (see, e.g., [34–36]).

3. L-Shell Ionization of Low-Charged Iron Ions

A particular astrophysical data need was addressed in a sequence of measurements with the low-charged iron ions Fe^+ [37], Fe^{2+} [38], and Fe^{3+} [39]. These ions and neutral iron atoms form the gaseous iron fraction in the interstellar medium [40]. Another fraction of iron is chemically bound to interstellar dust grains. This fraction is an important parameter for tracing the evolution of the stellar mass distribution and, more generally, of the chemical evolution of the universe [41]. The abundance of iron in the interstellar medium can be inferred from astronomical X-ray observations of Fe L-shell features, and high-resolution data from X-ray satellites can be used to discriminate between the gaseous and solid forms of iron in the interstellar medium [42]. This requires laboratory data for L-shell absorption by solid iron compounds and by iron in the gas-phase. The available data for solids have been compiled in [43] and $2p$ absorption of neutral iron vapour was experimentally studied in [44,45]. However, data for L-shell photoionization of low-charged iron ions have not

been available prior to our recent measurements at PIPE, except for relative cross sections for single and double photoionization of Fe^+ [18]. Further work on *L*-shell photoionization was only carried out for the higher charge states Fe^{6+}–Fe^{10+} [46] and Fe^{14+} [17]. In addition, a number of merged beams experiments have been performed on valence shell photoionization of Fe^+ [47], Fe^{4+} [48], Fe^{2+}–Fe^{6+} [49], and of Fe^{3+}, Fe^{5+}, and Fe^{7+} [50].

Most of these previous studies only considered single ionization and in some cases also double ionization. At PIPE, cross sections could be measured for *m*-fold photoionization of Fe^+, Fe^{2+}, and Fe^{3+} with *m* ranging from 1 to 5 and, in the case of Fe^+ [37], even to 6. As an example, Figure 3 displays cross sections for up to five-fold ionization of Fe^{3+} [39]. The cross-section scale spans several orders of magnitude ranging from several Mb to below one kb. Such low cross sections can only be accessed because of the high photon flux from the PETRA III synchrotron and because of the high selectivity and practically background-free detection of the product ions in the PIPE setup. All of the cross sections displayed in Figure 3 show the same resonance features, which are associated with the excitation of a $2p$ or a $2s$ electron to a higher *nl* subshell. The two most prominent ones in the energy range 700–730 eV are due to $2p \rightarrow 3d$ excitations. The separation of the two peaks corresponds to the $2p_{3/2} - 2p_{1/2}$ spin-orbit splitting amounting to about 15 eV. The resonances in the range 740–760 eV are dominated by $2p \rightarrow 4d$ excitations according to atomic structure calculations that were carried out in support of the Fe^{3+} experiment [39]. At energies below ~770 eV, double ionization is the dominant channel. That energy corresponds to the threshold for direct $2p$ ionization. The theoretical value for the threshold energy is 766.9 eV [51]. In contrast to $2p$ excitation, which occurs below this threshold and results in net double ionization, the $2p$ ionization process increases the ion charge state by one and, consequently, net triple ionization is the dominant ionization channel once direct ionization becomes energetically possible.

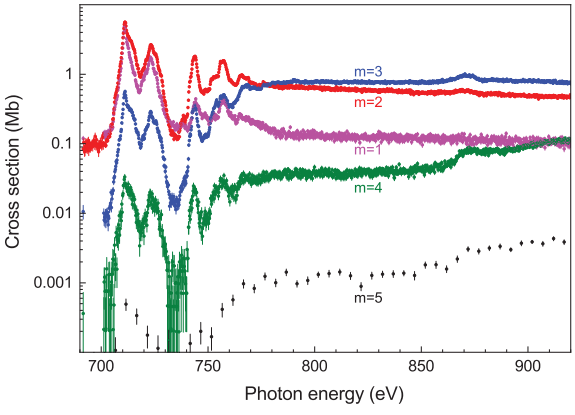

Figure 3. Experimental cross sections (1 Mb = 10^{-18} cm^2) for *m*-fold ionization of Fe^{3+} ions in the energy range 690–920 eV that contains the thresholds for $2p$ and $2s$ ionization [39]. The observed resonance structures are associated with the excitation of a $2p$ or a $2s$ electron to a higher atomic subshell and subsequent autoionization.

The charge state distribution that results from inner-shell ionization is rather broad as compared to valence ionization, as can bee seen from Figure 3. This is due to the multitude of deexcitation pathways that open up, once a *L*-shell hole is created. The deexcitation cascade involves radiative and autoionization transitions. The theoretical calculation of these cascades and the resulting product charge-state fractions is of considerable complexity. Already almost three decades ago, such calculations were performed for astrophysically relevant ions, including iron, by Kaastra and Mewe [52], who had to make simplifications to keep the computations tractable. Modern computers allow one to follow cascades in more detail and to include also many-electron processes such as

autoionization accompanied by shake processes. This approach, which was taken in our supporting calculations for Fe^{+}–Fe^{3+} [37–39], reproduced the experimental findings better than the earlier work of Kaastra and Mewe, but still leaves room for improvement. We just mention here that cascade calculations addressing *L*-shell ionization of Fe^{2+} were also carried out by Kučas et al. [53,54]. Their results are compared with our measured product charge-state fraction in [38].

Because all significant ionization processes have been measured, one can very well approximate the Fe^{3+} absorption cross section by the sum of all cross sections for *m*-fold ionization with $1 \leq m \leq 5$. In Figure 4 (left panels), the experimental absorption cross section for Fe^{+}–Fe^{3+} [37–39] are compared with the widely used theoretical results of Verner et al. [51]. Their calculations comprised only direct ionization processes and, therefore, do not reproduce the resonance features that are associated with $2p$ (and $2s$) excitation, which dominate the absorption cross sections below the $2p$ threshold and which are important for inferring iron abundances from astronomical X-ray absorption spectra. The resonance structures are significantly different for the different charge states, such that a discrimination between these in the astronomical observations is feasible. As can be seen from the right panels of Figure 4, this is also true for the higher iron charge states. The displayed ionization cross sections for Fe^{6+}–Fe^{10+} [46] were measured at the MAIA setup [28] at SOLEIL. They exhibit rather large statistical uncertainties as compared to the data from PIPE. This is due to the lower photon flux at SOLEIL when compared to PETRA III and also due to the fact that it is more difficult to obtain intense ion beams for more highly charged ions.

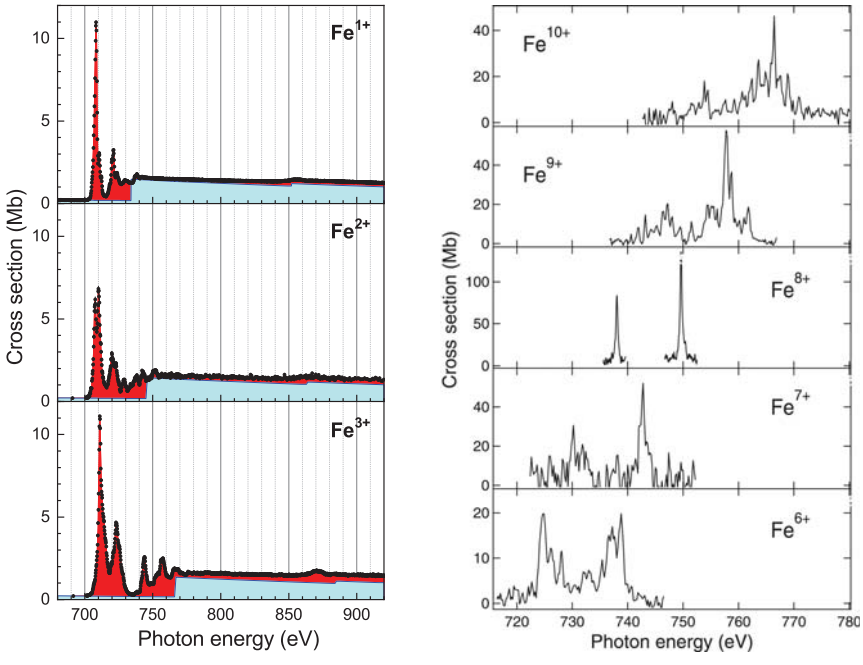

Figure 4. Left panels: Experimental cross sections (symbols) from PIPE for photoabsorption of Fe^{+} [37], Fe^{2+} [38], and Fe^{3+} [39]. The uncertainty of the experimental energy scale amounts ± 0.2 eV. The light-shaded full curves are theoretical cross sections provided by Verner et al. [51]. The steps in the theoretical cross sections occur at the computed thresholds for direct ionization of a $2p$ or a $2s$ electron. The photoionization resonances that dominate the experimental spectra below the $2p$ thresholds were not considered in the theoretical calculations. Right panels: Experimental cross sections for single ionization of Fe^{6+}–Fe^{10+} ions measured at SOLEIL [46] (reproduced by permission of the AAS).

4. K-Shell Ionization of Light Ions

Deep inner-shell photoionization of atomic ions has been reviewed five years ago by Müller [55]. This earlier review covers a large part of the data that were measured prior to the start of the experimental program at PIPE in 2013. Table 1 provides a comprehensive compilation of merged-beams studies on *K*-shell ionization of positive and negative atomic ions, which cover a time span of two decades. In the present review, we concentrate on the recent results from PIPE for Ne^+, C^-, C^+, C^{4+}, and Si^{2+} ions.

Table 1. List of published experimental cross sections for *K*-shell photoionization of atomic ions with atomic numbers $Z \geq 2$ from photon-ion merged-beams experiments at the synchrotron light sources ALS (Berkeley, CA, USA), ASTRID (Aarhus, Denmark), PETRA III (Hamburg, Germany), SOLEIL (Saint-Aubin, France), and SPring-8 (Hyogo, Japan). Columns 3 and 5 provide the experimental photon-energy range and the year of publication, respectively.

Z	Ion	Energy Range (eV)	Light Source	Year	Reference
2	He^+	80–140	ASTRID	2001	[56]
2	He^-	38–44	ALS	2002	[57]
2	He^-	43–44	ALS	2004	[58]
3	Li^-	56–70	ASTRID	2001	[59]
3	Li^-	56–66	ALS	2001	[60]
3	Li^+	149–181	ALS	2006	[61]
5	B^-	187–196	ALS	2007	[62]
5	B^+	193–210	ALS	2014	[63]
5	B^{2+}	195–235	ALS	2010	[64]
6	C^-	280–285	ALS	2003	[65]
6	C^-	281–282	ALS	2006	[66]
6	C^-	282–1000	PETRA III	2020	[67]
6	C^+	287–290	ALS	2004	[68]
6	C^+	286–326	PETRA III	2015	[69]
6	C^+	286–326	PETRA III	2018	[70]
6	C^{2+}	292–323	ALS	2005	[71]
6	C^{3+}	300–338	ALS	2009	[72]
6	C^{4+}	358–439	PETRA III	2018	[34]
7	N^+	399–406	SOLEIL	2011	[73]
7	N^+	390–435	PETRA III	2019	[74]
7	N^+	415–440	SOLEIL	2020	[75]
7	N^{2+}	404–442	SOLEIL	2014	[76]
7	N^{3+}	412–414	SOLEIL	2013	[77]
7	N^{4+}	421–460	SOLEIL	2013	[77]
8	O^-	526–536	ALS	2012	[78]
8	O^-	524–543	PETRA III	2016	[79]
8	O^+	525–540	SPRING-8	2002	[80]
8	O^+	526–620	SOLEIL	2015	[81]
8	O^{2+}	526–620	SOLEIL	2015	[81]
8	O^{3+}	540–600	SOLEIL	2014	[82]
8	O^{4+}	550–670	SOLEIL	2017	[83]
8	O^{5+}	561–570	SOLEIL	2017	[83]
9	F^-	660–1000	PETRA III	2018	[84]
10	Ne^+	841–858	SPRING-8	2001	[25]
10	Ne^+	840–925	PETRA III	2017	[33]
10	Ne^{2+}	850–863	SPRING-8	2001	[25]
10	Ne^{3+}	853–873	SPRING-8	2001	[85]
14	Si^{2+}	1830–1880	PETRA III	2020	[86]

4.1. K-Shell Photoionization of Ne^+

X-ray emission and absorption lines of singly charged neon are frequently encountered in the spectra recorded by X-ray observatories. They originate from a variety of cosmic objects, such as stellar coronae, X-ray binaries, supernova remnants, the interstellar medium, galaxies, and active galactic nuclei (see, e.g., [87]). Figure 5 shows experimental cross sections for single, double, and triple ionization of Ne^+ ions [33] that contain prominent resonance lines associated with the excitation of

a 1*s* electron to a higher *np* subshell. As discussed above already for iron, here the absorption cross section can also be well approximated by the cross-section sum over the different final ion charge states. In Figure 5d, the experimental absorption cross section thus derived is compared to state-of-the-art theoretical results of Gorzcyca et al. [42,88,89] and Witthoeft et al. [90]. At energies above 900 eV, i.e., at energies well above the threshold for direct *K*-shell ionization, where the cross section in the displayed energy range is essentially flat, all of the results agree excellently with one another. However, there are significant discrepancies concerning the photoionization resonances.

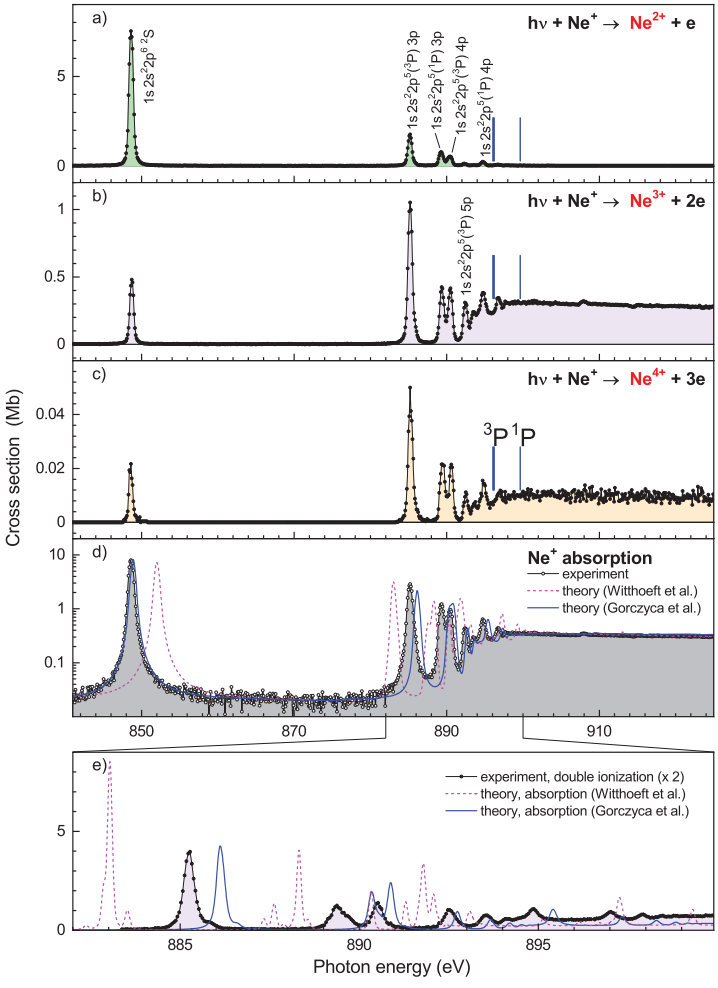

Figure 5. Cross sections for (**a**) single ionization, (**b**) double ionization, and (**c**) triple ionization of Ne^+ ions [33] measured with a photon energy bandwidth of 500 meV. The experimental cross section in panel (**d**) is the sum of the cross sections displayed in panels (**a**–**c**). It represents the Ne^+ absorption cross section, which is compared with the theoretical cross sections of Gorzcyca et al. [42,88,89] and Witthoeft et al. [90]. Panel (**e**) presents a comparison between the theoretical results with a high-resolution measurement (113 meV photon-energy bandwidth) of the cross section for double ionization (multiplied by a factor of 2) over a narrower energy range. For the comparisons, the theoretical cross sections were convolved with gaussians with full-widths-at-half-maximum of 500 meV in panel (**d**) and 113 meV in panel (**e**).

As detailed in [33], accurate resonance positions, resonance widths, and resonance strengths could be retrieved from the measured absolute cross sections. Even more detailed information on Auger transition rates and fluorescence yields could be obtained, in particular, for the $1s\,2s^2\,2p^6\;{}^2S_{1/2} \rightarrow 1s^2\,2s^2\,2p^5\;{}^2P_{1/2,\,3/2}\;K\alpha$ transitions. The theoretical resonance positions differ from the experimental ones by much more than the ± 0.2 eV uncertainty of the experimental energy scale, as can be seen in Figure 5d,e. Moreover, there are also discrepancies concerning resonance widths and fine-structure splittings not only between experiment and theory but also between both state-of-the-art theoretical calculations. This is most probably due to different computational approximations of the two different approaches, e.g., by choosing different, naturally limited sets of basis states in close-coupling calculations whose convergence is not always obvious. Clearly, experimental benchmarking is vitally needed for the accurate location of resonance lines and, thus, for their unambiguous identification in absorption and emission spectra from astronomical observations. One should also be aware of the fact that accurate line strengths are required for inferring elemental abundances from astrophysical line spectra. At the current level of theoretical accuracy, these quantities apparently also need to be checked against laboratory results.

4.2. K-Shell Photoionization of Carbon Ions: C^-, C^+, C^{4+}

Carbon is the fourth most abundant element in the Solar system [4]. High charge states of carbon such as C^{4+} occur in many of the cosmic objects mentioned in the introduction. In our vicinity, C^{4+} is found in the solar wind, where its abundance has been shown to significantly depend on photoionization by the solar EUV and X-ray radiation [91]. Lower-charged carbon, in particular C^+, plays a decisive role in the interstellar chemistry [92]. In fact, most of the molecules that have been detected in the interstellar medium to date are organic [93]. Some of these carbon containing molecules are negatively charged [94]. However, the atomic ion C^- has not been detected in any cosmic object. Potentially, this could be due to a lack of corresponding atomic data, since the *K*-shell absorption cross section has become available for a wide range of photon energies only recently [67] (see below). As can be seen from Table 1, merged-beams experiments on *K*-shell ionization of carbon ions were carried out at the ALS and at PETRA III (PIPE) covering the charge states -1, 1, 2, 3, and 4. In addition to this work on carbon *K*-shell ionization of atomic ions, there are also related studies with the carbon containing molecules CH^+ [95], $La_3N@C_{80}^+$ [96], and $Sc_3N@C_{80}^+$ [97], which are not discussed here.

Figure 6 showcases some of the highlights obtained from photon-ion merged beams experiments with atomic carbon ions at PIPE. The displayed absorption and ionization cross sections for C^-, C^+, and C^{4+} are distinctly different from one another. This allows one to discriminate between these ions in astronomical X-ray absorption spectra. The spectra of the positive ions are dominated by photoionization resonances of primary ions being initially in the ground level or in a long-lived excited metastable level. The C^+ ion beam contained a 9:1 mixture of ions in the $1s^2\,2s^2\,2p\;{}^2P$ ground term and in the metastable $1s^2\,2s\,2p^2\;{}^4P$ term [70]. The C^{4+} beam was a mixture of $C^{4+}(1s^2\;{}^1S_0)$ and $C^{4+}(1s\,2s\;{}^3P_1)$ ions with the metastable fraction amounting to 0.105 [34]. In the C^- beam, all ions were initially in the $1s^2\,2s^2\,2p^3\;{}^4S$ ground term. Unfortunately, there is no general method for determining the fraction of metastable ions in an ion beam (for special cases see, e.g., [98–100]). For C^+, the ion-beam composition was inferred from a detailed comparison between measured and calculated absorption cross sections. This approach is somewhat dissatisfying since it relies on the accuracy of the theoretical methods, which is generally difficult to assess. In exceptional cases, one can relate the experimental photoionization cross sections to experimental cross sections for the time inverse process of photorecombination by employing the principle of detailed balance [63,72,101]. This method could be applied to C^{4+} while using the measured absolute cross section for photorecombination of C^{5+} ions from a storage-ring experiment [102].

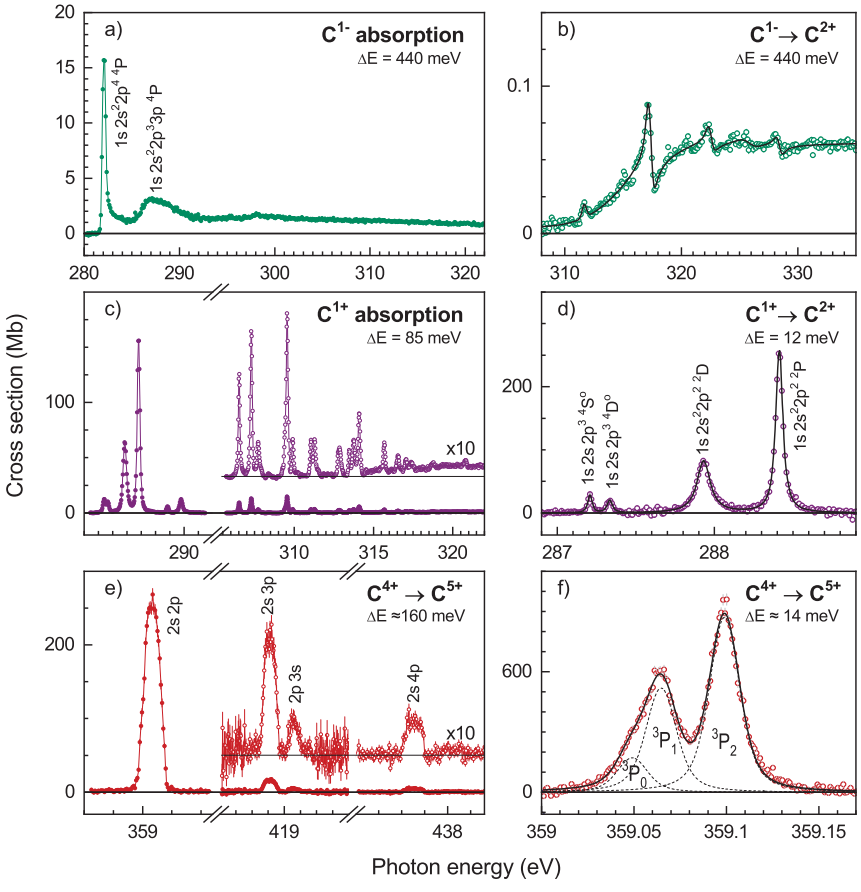

Figure 6. Experimental cross sections for photoabsorption and (multiple) photoionization of C^- [67] {panels (**a**,**b**)}, C^+ [70] {panels (**c**,**d**)}, and C^{4+} [34] {panels (**e**,**f**)}. The C^+ and C^{4+} ion beams were mixtures of ground-level and excited metastable ions (see text). For each measurement the experimental photon-energy bandwidth ΔE is specified. The left panels provide overviews, the right panels feature cross-section details that were measured partly with significantly smaller photon-energy bandwidths. For a better display of the data in panel (**b**), a smooth cross section was subtracted that represented the direct ionization of a 1*s* electron (see [67] for details). The full black lines in panels (**b**,**d**,**f**) result from resonance fits to the experimental data. The uncertainty of the experimental photon-energy scale is ±200 meV for C^-, ±30 meV for C^+, and (depending on photon energy) ±40 meV up to ±50 meV for C^{4+}.

Figure 6a displays the C^- absorption cross section. Only two relatively weak resonance features can be discerned. Generally, negative ions support less resonances than positive ions because the potential that binds the extra electron in a negative ion is comparatively shallow. Nevertheless, a number of hitherto mostly unknown resonances were discovered in the C^- photoionization cross sections measured at PIPE, as can been seen in Figure 6a,b. From a fundamental point of view, investigations of negative ions are interesting because their structure and dynamics is governed by strong correlation effects [103]. The $1s^2\,2s^2\,2p^3\;{}^4S \rightarrow 1s\,2s^2\,2p^4\;{}^4P$ resonance at about 282 eV (Figure 6a) was already experimentally studied earlier by Walter et al. [66]. These authors found that it can be well described by an asymmetric Breit–Wigner line shape, which, in addition to the resonance itself, accounts for the *K*-shell ionization threshold that occurs just 0.1 eV below the resonance energy.

The broader resonance peaking at ∼287 eV (Figure 6a) is outside the experimental energy range of the earlier work. It has been tentatively assigned to $1s^2\,2s^2\,2p^3\;{}^4S \rightarrow 1s\,2s^2\,2p^2\,3p\;{}^4P$ excitations [67]. The weak resonances at higher energies that are only visible in the experimental cross section for net triple ionization (Figure 6b) could not be unambiguously assigned. They exhibit asymmetric Fano line shapes that are caused by quantum mechanical interference of the resonance channel with direct $1s + 2s$ double ionization, which sets in at about 310 eV [67]. We just mention here that also double core-hole creation by direct $1s + 1s$ ionization was observed in the five-fold ionization channel of the C^- experiment.

Additionally, for C^+ and C^{4+}, the most prominent resonances in the cross sections displayed in Figure 6c–f are associated with $1s \rightarrow np$ excitations with $n \geq 2$. The resonance structure is more complicated for C^+ than for C^{4+} because of the larger number of open subshells and the correspondingly larger number of fine-structure levels of the excited $C^+(1s\,2s^2\,2p\,np)$ and $C^+(1s\,2s\,2p^2\,np)$ configurations as compared to the $C^{4+}(2s\,np)$ configurations. The latter are exclusively excited from the metastable $C^{4+}(1s\,2s\;{}^3P_1)$ ions. Their excitation from the $C^{4+}(1s^2\;{}^1S_0)$ ground level would be very much less efficient, since this requires the simultaneous rearrangement of both electrons and the required photon energy would be almost 300 eV higher.

The careful evaluation of the measured data allows for one to extract a considerable amount of detail concerning resonance parameters and deexcitation pathways. For example, the measurement of the strengths and widths of the $C^+(1s\,2s^2\,2p^2)$ resonances in the single, double and threefold ionization channels provided unambiguous evidence and quantitative results for the elusive triple-Auger process, which is a manifestation of a genuine four-particle interaction [69,70]. The widths (and asymmetry parameters) of narrow resonances can be extracted from high-resolution measurements by fitting (Fano-)Voigt line profiles [104] to the measured data (Figure 6b,d,f). Moreover, high photon-energy resolving powers $E/\Delta E$ facilitate the separation of individual fine-structure components, as shown in Figure 6f for the $C^{4+}(2s\,2p\;{}^3P)$ resonance, where $E/\Delta E = 25{,}800$ was reached [34]. This result is unique, since the fine-structure of resonance terms associated with deep inner-shell excitations has not yet been resolved in any other photoionization experiment with ions.

The original paper on the photoionization of C^{4+} [34] also comprises state-of-the-art theoretical calculations using relativistic many-body perturbation theory (RMBPT) [105] with quantum electrodynamical (QED) additions [106]. An in-depth discussion of these calculations is beyond the scope of the present review, but we want to point out that the C^{4+} photoionization resonances were calculated with an exceptionally high accuracy at an estimated uncertainty of the resonance energies of less than ±1 meV. At present, such an accuracy can only be achieved for few-electron ions where the description of electron-electron–interaction effects is well under control. At the given level of theoretical uncertainty of resonance energies for He-like ions, these resonances can be potentially used to establish new photon-energy calibration standards that are up to two orders of magnitude more accurate than what is currently available in the soft X-ray range, as is discussed in detail in [33,34]. Like many other technical applications, the field of X-ray astronomy will certainly greatly benefit from such a development.

4.3. K-Shell Ionization of Silicon Ions

K-shell photoabsorption by silicon is used to trace its abundance in the interstellar medium, where it is, to a large part, contained in dust particles [107]. Only a small fraction of the interstellar silicon is expected to be in the gas-phase. Recently, it has been suggested that gas phase absorption data for silicon ions are required for an accurate modelling of the astronomically observed Si *K*-edge absorption features [108]. This has motivated theoretical work on the photoabsorption of silicon atoms and ions [90,109–111]. At PIPE, we have recently measured cross sections for single and multiple photoionization of low-charged Si^+, Si^{2+}, ans Si^{3+} ions. Figure 7 shows preliminary results for the *K*-shell photoionization of $Si^{2+}([\mathrm{Ne}]\,3s^2\;{}^1S_0)$ [86]. The experimental cross section, which has not yet been put on an absolute scale, has strong resonance contributions associated with $1s \rightarrow 3p$ and

$1s \rightarrow 4p$ excitations. A more careful, currently ongoing analysis will reveal whether there are also smaller contributions from excitations to higher shells. The cross-section rise at energies above 1860 eV is caused by direct $1s$ ionization. The theoretically predicted threshold energy for this process is 1852 eV [51], which is in reasonable accord with the experimental finding when considering the fact that a photon-energy calibration has still to be applied to the experimental energy scale. It should be pointed out that PIPE is currently the only photon-ion merged-beams setup where photon energies beyond 1000 eV available.

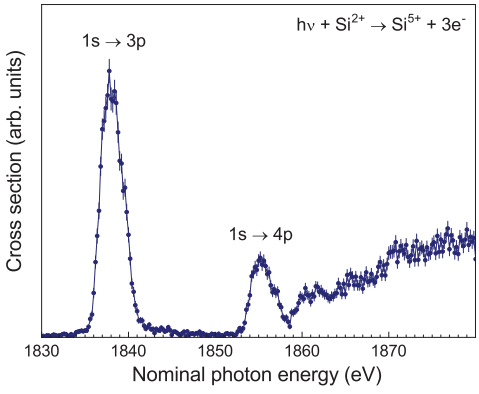

Figure 7. Experimental cross section for *K*-shell triple ionization of Si^{2+}. These preliminary data from [86] are not on an absolute cross section scale, and the photon energy scale has not been calibrated, yet.

5. Conclusions and Outlook

It is fair to state that the implementation of the photon-ion merged-beams technique at a world-leading synchrotron beamline has led to a breakthrough for experimental inner-shell ionization studies with ions. The high sensitivity of the PIPE setup allows one to measure cross sections on a sub-kilobarn level and, thus, to gain insight in multiple ionization processes in unprecedented detail. This facilitates the observation of rare multi-electron processes, such as, e.g., the triple-Auger process. At present, the merged-beams method is the only experimental approach that can independently provide absolute cross sections, which is of particular value for the application of atomic cross-section data in astrophysics. A draw-back is that the ion beams are often mixtures of ground-level and excited metastable ions and that there is no general method to quantitatively determine the ion-beam composition. In special cases, these can be inferred, e.g., by applying the principle of detailed balance to comparisons with experimental cross sections for photorecombination, which is the time inverse process of photoionization. In general, the use of state-prepared ion beams is desirable. Photoionization experiments with state-prepared ions in traps have been demonstrated, but the associated particle losses seem discouraging. Moreover, trap-based methods cannot generally provide absolute cross sections. Another route towards state preparation is taken at ion storage rings, where photon-ion merged-beams experiments with portable XUV light sources based on high-harmonic generation are currently being devised. In the foreseeable future, synchrotron based photon-ion merged-beams setups will continue to deliver the bulk of experimental data on the photoionization of ions [112].

Author Contributions: Both authors contributed to the writing of the text. Authors have read and agreed to the published version of the manuscript.

Funding: Financial support was provided by the German Federal Ministry of Education and Research (BMBF, grant numbers 05K10RG1, 05K16RG1, 05K19RG3) and by Deutsche Forschungsgemeinschaft (DFG, grant numbers Mu1068/22-1, Schi378/12-1).

Acknowledgments: The authors are grateful to their collaborators for their contributions to the work at PIPE reviewed here, who are, in alphabetical order, Sadia Bari, Dietrich Bernhardt, Alexander Borovik, Ticia Buhr, Jonas Hellhund, Pierre-Michel Hillenbrand, Kristof Holste, David Kilcoyne, Stephan Klumpp, Michael Martins, Alexander Perry-Sassmannshausen, Ron Phaneuf, Simon Reinwardt, Sandor Ricz, Daniel Savin, Jörn Seltmann, Kaja Schubert, Florian Trinter, Jens Viefhaus, and Patrick Wilhelm. We also thank Randolf Beerwerth, Stephan Fritzsche, Paul Indelicato, Eva Lindroth, and Sebastian Stock for their theory contributions to our joint work, and the staff of the PETRA III beamline P04 for their excellent support.

Conflicts of Interest: The authors declare no conflict of interest. The founding sponsors had no role in the design of the study; in the collection, analyses, or interpretation of data; in the writing of the manuscript, and in the decision to publish the results.

References

1. Pain, J.C.; Gilleron, F.; Comet, M. Detailed opacity calculations for astrophysical applications. *Atoms* **2017**, *5*, 22. [CrossRef]
2. Tanaka, M.; Kato, D.; Gaigalas, G.; Kawaguchi, K. Systematic Opacity Calculations for Kilonovae. *Mon. Not. R. Astron. Soc.* **2020**, *496*, 1369. [CrossRef]
3. Paerels, F.B.S.; Kahn, S.M. High-resolution X-ray spectroscopy with Chandra and XMM-Newton. *Annu. Rev. Astron. Astrophys.* **2003**, *41*, 291–342. [CrossRef]
4. Asplund, M.; Grevesse, N.; Sauval, A.J.; Scott, P. The chemical composition of the Sun. *Annu. Rev. Astron. Astrophys.* **2009**, *47*, 481–522. [CrossRef]
5. Ferland, G.J. Quantitative spectroscopy of astronomical plasmas. *Annu. Rev. Astron. Astrophys.* **2003**, *41*, 517–554. [CrossRef]
6. Kallman, T.R.; Palmeri, P. Atomic data for X-ray astrophysics. *Rev. Mod. Phys.* **2007**, *79*, 79–133. [CrossRef]
7. Savin, D.W.; Brickhouse, N.S.; Cowan, J.J.; Drake, R.P.; Federman, S.R.; Ferland, G.J.; Frank, A.; Gudipati, M.S.; Haxton, W.C.; Herbst, E.; et al. The impact of recent advances in laboratory astrophysics on our understanding of the Cosmos. *Rep. Prog. Phys.* **2012**, *75*, 036901. [CrossRef]
8. Smith, R.K.; Brickhouse, N.S. Atomic Data Needs for Understanding X-ray Astrophysical Plasmas. *Adv. Atomic Mol. Opt. Phys.* **2014**, *63*, 271–321. [CrossRef]
9. Lynas-Gray, A.E.; Basu, S.; Bautista, M.A.; Colgan, J.; Mendoza, C.; Tennyson, J.; Trampedach, R.; Turck-Chièze, S. Current State of Astrophysical Opacities: A White Paper. In Proceedings of the Second Workshop on Astrophysical Opacities, Kalamazoo, MI, USA, 1–4 August 2017; Volume 515, p. 115.
10. Smith, R.; Hahn, M.; Raymond, J.; Kallman, T.; Ballance, C.P.; Polito, V.; Zanna, G.D.; Gu, L.; Hell, N.; Cumbee, R.; et al. Roadmap on cosmic EUV and X-ray spectroscopy. *J. Phys. B* **2020**, *53*, 092001. [CrossRef]
11. Kramida, A.; Ralchenko, Y.; Reader, J.; Team, N.A. *NIST Atomic Spectra Database*; Version 5.7.1; Technical Report; National Institute of Standards and Technology: Gaithersburg, MD, USA, 2019. Available online: http://physics.nist.gov/asd (accessed on 1 July 2020).
12. Kennedy, E.T.; Costello, J.T.; Mosnier, J.P.; van Kampen, P. VUV/EUV ionising radiation and atoms and ions: Dual laser plasma investigations. *Radiat. Phys. Chem.* **2004**, *70*, 291–321. [CrossRef]
13. Kravis, S.D.; Church, D.A.; Johnson, B.M.; Meron, M.; Jones, K.W.; Levin, J.; Sellin, I.A.; Azuma, Y.; Mansour, N.B.; Berry, H.G.; et al. Inner-shell photoionization of stored positive ions using synchrotron radiation. *Phys. Rev. Lett.* **1991**, *66*, 2956–2959. [CrossRef] [PubMed]
14. Thissen, R.; Bizau, J.M.; Blancard, C.; Coreno, M.; Dehon, C.; Franceschi, P.; Giuliani, A.; Lemaire, J.; Nicolas, C. Photoionization cross section of Xe^+ ion in the pure $5p^5\ ^2P_{3/2}$ ground level. *Phys. Rev. Lett.* **2008**, *100*, 223001. [CrossRef] [PubMed]
15. Bizau, J.M.; Blancard, C.; Coreno, M.; Cubaynes, D.; Dehon, C.; Hassan, N.E.; Folkmann, F.; Gharaibeh, M.F.; Giuliani, A.; Lemaire, J.; et al. Photoionization study of Kr^+ and Xe^+ ions with the combined use of a merged-beam set-up and an ion trap. *J. Phys. B* **2011**, *44*, 055205. [CrossRef]
16. Simon, M.C.; Crespo López-Urrutia, J.R.; Beilmann, C.; Schwarz, M.; Harman, Z.; Epp, S.W.; Schmitt, B.L.; Baumann, T.M.; Behar, E.; Bernitt, S.; et al. Resonant and near-threshold photoionization cross sections of Fe^{14+}. *Phys. Rev. Lett.* **2010**, *105*, 183001. [CrossRef]
17. Simon, M.C.; Schwarz, M.; Epp, S.W.; Beilmann, C.; Schmitt, B.L.; Harman, Z.; Baumann, T.M.; Mokler, P.H.; Bernitt, S.; Ginzel, R.; et al. Photoionization of N^{3+} and Ar^{8+} in an electron beam ion trap by synchrotron radiation. *J. Phys. B* **2010**, *43*, 065003. [CrossRef]

18. Hirsch, K.; Zamudio-Bayer, V.; Ameseder, F.; Langenberg, A.; Rittmann, J.; Vogel, M.; Möller, T.; Issendorff, B.; Lau, J.T. 2p X-ray absorption of free transition-metal cations across the 3d transition elements: Calcium through copper. *Phys. Rev. A* **2012**, *85*, 062501. [CrossRef]
19. Lyon, I.C.; Peart, B.; West, J.B.; Dolder, K. Measurements of absolute cross sections for the photoionisation of Ba^+ ions. *J. Phys. B* **1986**, *19*, 4137–4147. [CrossRef]
20. Kjeldsen, H. Photoionization cross sections of atomic ions from merged-beam experiments. *J. Phys. B* **2006**, *39*, R325–R377. [CrossRef]
21. Schippers, S.; Kilcoyne, A.L.D.; Phaneuf, R.A.; Müller, A. Photoionization of ions with synchrotron radiation: From ions in space to atoms in cages. *Contemp. Phys.* **2016**, *57*, 215–229. [CrossRef]
22. Bizau, J.M.; Cubaynes, D.; Richter, M.; Wuilleumier, F.J.; Obert, J.; Putaux, J.C.; Morgan, T.J.; Källne, E.; Sorensen, S.; Damany, A. First observation of photoelectron spectra emitted in the photoionization of a singly charged-ion beam with synchrotron radiation. *Phys. Rev. Lett.* **1991**, *67*, 576–579. [CrossRef]
23. Oura, M.; Kravis, S.; Koizumi, T.; Itoh, Y.; Kojima, T.M.; Sano, M.; Sekioka, T.; Kimura, M.; Okuno, K.; Awaya, Y. Experimental setups for photoionization of multiply charged ions by synchrotron radiation. *Nucl. Instrum. Methods B* **1994**, *86*, 190. [CrossRef]
24. Kjeldsen, H.; Folkmann, F.; Knudsen, H.; Rasmussen, M.S.; West, J.B.; Andersen, T. Absolute photoionization cross cection of K^+ ions from the $3p$ to the $3s$ threshold. *J. Phys. B* **1999**, *32*, 4457–4465. [CrossRef]
25. Yamaoka, H.; Oura, M.; Kawatsura, K.; Hayaishi, T.; Sekioka, T.; Agui, A.; Yoshigoe, A.; Koike, F. Photoionization of singly and doubly charged neon ions following inner-shell excitation. *Phys. Rev. A* **2001**, *65*, 012709. [CrossRef]
26. Covington, A.M.; Aguilar, A.; Covington, I.R.; Gharaibeh, M.F.; Hinojosa, G.; Shirley, C.A.; Phaneuf, R.A.; Álvarez, I.; Cisneros, C.; Dominguez-Lopez, I.; et al. Photoionization of Ne^+ using synchrotron radiation. *Phys. Rev. A* **2002**, *66*, 062710. [CrossRef]
27. Schippers, S.; Ricz, S.; Buhr, T.; Borovik, A., Jr.; Hellhund, J.; Holste, K.; Huber, K.; Schäfer, H.J.; Schury, D.; Klumpp, S.; et al. Absolute cross sections for photoionization of Xe^{q+} ions ($1 \leq q \leq 5$) at the 3d ionization threshold. *J. Phys. B* **2014**, *47*, 115602. [CrossRef]
28. Bizau, J.M.; Cubaynes, D.; Guilbaud, S.; Eassan, N.E.; Shorman, M.M.A.; Bouisset, E.; Guigand, J.; Moustier, O.; Marié, A.; Nadal, E.; et al. A merged-beam setup at SOLEIL dedicated to photoelectron-photoion coincidence studies on ionic species. *J. Electron Spectrosc. Relat. Phenom.* **2016**, *210*, 5–12. [CrossRef]
29. Lestinsky, M.; Andrianov, V.; Aurand, B.; Bagnoud, V.; Bernhardt, D.; Beyer, H.; Bishop, S.; Blaum, K.; Bleile, A.; Borovik, A.; et al. Physics book: CRYRING@ESR. *Eur. Phys. J. Spec. Top.* **2016**, *225*, 797–882. [CrossRef]
30. Borovik, A.; Weber, G.; Hilbert, V.; Lin, H.; Pfäfflein, P.; Zhu, B.; Hahn, C.; Lestinsky, M.; Schippers, S.; Stöhlker, T.; et al. Development of a detector to register low-energy, charge-changed ions from ionization experiments at CRYRING@ESR. *J. Phys. Conf. Ser.* **2020**, *1412*, 242003. [CrossRef]
31. Viefhaus, J.; Scholz, F.; Deinert, S.; Glaser, L.; Ilchen, M.; Seltmann, J.; Walter, P.; Siewert, F. The variable polarization XUV beamline P04 at PETRA III: Optics, mechanics and their performance. *Nucl. Instrum. Methods A* **2013**, *710*, 151–154. [CrossRef]
32. Schippers, S.; Buhr, T.; Borovik, A., Jr.; Holste, K.; Perry-Sassmannshausen, A.; Mertens, K.; Reinwardt, S.; Martins, M.; Klumpp, S.; Schubert, K.; et al. The photon-ion merged-beams experiment PIPE at PETRA III - The first five years. *X-ray Spectrom.* **2020**, *49*, 11. [CrossRef]
33. Müller, A.; Bernhardt, D.; Borovik, A., Jr.; Buhr, T.; Hellhund, J.; Holste, K.; Kilcoyne, A.L.D.; Klumpp, S.; Martins, M.; Ricz, S.; et al. Photoionization of Ne atoms and Ne^+ ions near the K edge: Precision spectroscopy and absolute cross sections. *Astrophys. J.* **2017**, *836*, 166. [CrossRef]
34. Müller, A.; Lindroth, E.; Bari, S.; Borovik, A., Jr.; Hillenbrand, P.M.; Holste, K.; Indelicato, P.; Kilcoyne, A.L.D.; Klumpp, S.; Martins, M.; et al. Photoionization of metastable heliumlike $C^{4+}(1s\,2s\,{}^3S_1)$ ions: Precision study of intermediate doubly excited states. *Phys. Rev. A* **2018**, *98*, 033416. [CrossRef]
35. Yerokhin, V.A.; Surzhykov, A.; Müller, A. Relativistic configuration-interaction calculations of the energy levels of the $1s^2 2l$ and $1s\,2l\,2l'$ states in lithiumlike ions: Carbon through chlorine. *Phys. Rev. A* **2017**, *96*, 042505; Erratum in **2017**, *96*, 069901. [CrossRef]
36. Machado, J.; Bian, G.; Paul, N.; Trassinelli, M.; Amaro, P.; Guerra, M.; Szabo, C.I.; Gumberidze, A.; Isac, J.M.; Santos, J.P.; et al. Reference-free measurements of the $1s^2\,2s\,2p\,{}^2P^o_{1/2,3/2} \rightarrow 1s^2\,2s\,{}^2S_{1/2}$ and $1s\,2s\,2p\,{}^4P_{5/2} \rightarrow 1s^2\,2s\;{}^2S_{1/2}$ transition energies and widths in lithiumlike sulfur and argon ions. *Phys. Rev. A* **2020**, *101*, 062505. [CrossRef]

37. Schippers, S.; Martins, M.; Beerwerth, R.; Bari, S.; Holste, K.; Schubert, K.; Viefhaus, J.; Savin, D.W.; Fritzsche, S.; Müller, A. Near L-edge single and multiple photoionization of singly charged iron ions. *Astrophys. J.* **2017**, *849*, 5. [CrossRef]
38. Schippers, S.; Beerwerth, R.; Bari, S.; Buhr, T.; Holste, K.; Kilcoyne, A.L.D.; Perry-Sassmannshausen, A.; Phaneuf, R.A.; Reinwardt, S.; Savin, D.W.; et al. Near L-edge single and multiple photoionization of doubly charged iron ions. In preparation.
39. Beerwerth, R.; Buhr, T.; Perry-Sassmannshausen, A.; Stock, S.O.; Bari, S.; Holste, K.; Kilcoyne, A.L.D.; Reinwardt, S.; Ricz, S.; Savin, D.W.; et al. Near L-edge single and multiple photoionization of triply charged iron ions. *Astrophys. J.* **2019**, *887*, 189. [CrossRef]
40. Jensen, A.G.; Snow, T.P. New insights on interstellar gas-phase iron. *Astrophys. J.* **2007**, *669*, 378–400. [CrossRef]
41. Jenkins, E.B. A unified representation of gas-phase element depletions in the interstellar medium. *Astrophys. J.* **2009**, *700*, 1299. [CrossRef]
42. Juett, A.M.; Schulz, N.S.; Chakrabarty, D.; Gorczyca, T.W. High-resolution X-ray spectroscopy of the interstellar medium. II. neon and iron absorption edges. *Astrophys. J.* **2006**, *648*, 1066. [CrossRef]
43. Miedema, P.S.; de Groot, F.M.F. The iron L edges:Fe 2p X-ray absorption and electron energy loss spectroscopy. *J. Electron Spectrosc. Relat. Phenom.* **2013**, *187*, 32–48. [CrossRef]
44. Richter, T.; Godehusen, K.; Martins, M.; Wolff, T.; Zimmermann, P. Interplay of intra-atomic and interatomic effects: An investigation of the 2*p* core level spectra of atomic Fe and molecular $FeCl_2$. *Phys. Rev. Lett.* **2004**, *93*, 023002. [CrossRef] [PubMed]
45. Martins, M.; Godehusen, K.; Richter, T.; Wernet, P.; Zimmermann, P. Open shells and multi-electron interactions: Core level photoionization of the 3d metal atoms. *J. Phys. B* **2006**, *39*, R79–R125. [CrossRef]
46. Blancard, C.; Cubaynes, D.; Guilbaud, S.; Bizau, J.M. Absolute photoionization cross section for Fe^{6+} to Fe^{10+} ions in the photon energy region of the 2p-3d resonance lines. *Astrophys. J.* **2018**, *853*, 32. [CrossRef]
47. Kjeldsen, H.; Kristensen, B.; Folkmann, F.; Andersen, T. Measurements of the absolute photoionization cross section of Fe^+ ions from 15.8 to 180 eV. *J. Phys. B* **2002**, *35*, 3655–3668. [CrossRef]
48. Bizau, J.M.; Blancard, C.; Cubaynes, D.; Folkmann, F.; Kilbane, D.; Faussurier, G.; Luna, H.; Lemaire, J.L.; Blieck, J.; Wuilleumier, F.J. Experimental and theoretical studies of the photoionization cross section of Fe^{4+}. *Phys. Rev. A* **2006**, *73*, 020707. [CrossRef]
49. El Hassan, N.; Bizau, J.M.; Blancard, C.; Cosse, P.; Cubaynes, D.; Faussurier, G.; Folkmann, F. Photoionization cross sections of iron isonuclear sequence ions: Fe^{2+} to Fe^{6+}. *Phys. Rev. A* **2009**, *79*, 033415. [CrossRef]
50. Gharaibeh, M.F.; Aguilar, A.; Covington, A.M.; Emmons, E.D.; Scully, S.W.J.; Phaneuf, R.A.; Müller, A.; Bozek, J.D.; Kilcoyne, A.L.D.; Schlachter, A.S.; et al. Photoionization measurements for the iron isonuclear sequence Fe^{3+}, Fe^{5+}, and Fe^{7+}. *Phys. Rev. A* **2011**, *83*, 043412. [CrossRef]
51. Verner, D.A.; Yakovlev, D.G.; Band, I.M.; Trzhaskovskaya, M.B. Subshell photoionization cross sections and ionization energies of atoms and ions from He to Zn. *Atomic Data Nucl. Data Tables* **1993**, *55*, 233–280. [CrossRef]
52. Kaastra, J.S.; Mewe, R. X-ray emission from thin plasmas. I - Multiple Auger ionisation and fluorescence processes for Be to Zn. *Astron. Astrophys. Suppl. Ser.* **1993**, *97*, 443–482.
53. Kučas, S.; Drabužinskis, P.; Kynienė, A.; Masys, Š.; Jonauskas, V. Evolution of radiative and Auger cascades following 2*s* vacancy creation in Fe^{2+}. *J. Phys. B* **2019**, *52*, 225001. [CrossRef]
54. Kučas, S.; Drabužinskis, P.; Jonauskas, V. Radiative and Auger cascade following 2*p* vacancy creation in Fe^{2+}. *Atomic Data Nucl. Data Tables* **2020**, 101357. [CrossRef]
55. Müller, A. Precision studies of deep-inner-shell photoabsorption by atomic ions. *Phys. Scr.* **2015**, *90*, 054004. [CrossRef]
56. Andersen, P.; Andersen, T.; Folkmann, F.; Ivanov, V.K.; Kjeldsen, H.; West, J.B. Absolute cross sections for the photoionization of 4d electrons in Xe^+ and Xe^{2+} ions. *J. Phys. B* **2001**, *34*, 2009–2019. [CrossRef]
57. Berrah, N.; Bozek, J.D.; Turri, G.; Akerman, G.; Rude, B.; Zhou, H.L.; Manson, S.T. K-shell photodetachment of He^-: Experiment and theory. *Phys. Rev. Lett.* **2002**, *88*, 093001. [CrossRef]
58. Bilodeau, R.C.; Bozek, J.D.; Aguilar, A.; Ackerman, G.D.; Turri, G.; Berrah, N. Photoexcitation of He^- hollow-ion resonances: Observation of the $2s\,2p^2\ {}^4P$ state. *Phys. Rev. Lett.* **2004**, *93*, 193001. [CrossRef]
59. Kjeldsen, H.; Andersen, P.; Folkmann, F.; Kristensen, B.; Andersen, T. Inner-shell photodetachment of Li^-. *J. Phys. B* **2001**, *34*, L353–L357. [CrossRef]

60. Berrah, N.; Bozek, J.D.; Wills, A.A.; Turri, G.; Zhou, H.L.; Manson, S.T.; Akerman, G.; Rude, B.; Gibson, N.D.; Walter, C.W.; et al. K-shell photodetachment of Li^-: Experiment and theory. *Phys. Rev. Lett.* **2001**, *87*, 253002. [CrossRef]
61. Scully, S.W.J.; Álvarez, I.; Cisneros, C.; Emmons, E.D.; Gharaibeh, M.F.; Leitner, D.; Lubell, M.S.; Müller, A.; Phaneuf, R.A.; Püttner, R.; et al. Doubly excited resonances in the photoionization spectrum of Li^+: Experiment and theory. *J. Phys. B* **2006**, *39*, 3957–3968. [CrossRef]
62. Berrah, N.; Bilodeau, R.C.; Dumitriu, I.; Bozek, J.D.; Gibson, N.D.; Walter, C.W.; Ackerman, G.D.; Zatsarinny, O.; Gorczyca, T.W. Shape resonances in the absolute K-shell photodetachment of B^-. *Phys. Rev. A* **2007**, *76*, 032713. [CrossRef]
63. Müller, A.; Schippers, S.; Phaneuf, R.A.; Scully, S.W.J.; Aguilar, A.; Cisneros, C.; Gharaibeh, M.F.; Schlachter, A.S.; McLaughlin, B.M. K -shell photoionization of Be-like boron (B^+) ions: experiment and theory. *J. Phys. B* **2014**, *47*, 135201. [CrossRef]
64. Müller, A.; Schippers, S.; Phaneuf, R.A.; Scully, S.W.J.; Aguilar, A.; Cisneros, C.; Gharaibeh, M.F.; Schlachter, A.S.; McLaughlin, B.M. K-shell photoionization of ground-state Li-like boron ions [B^{2+}]: Experiment and theory. *J. Phys. B* **2010**, *43*, 135602. [CrossRef]
65. Gibson, N.D.; Walter, C.W.; Zatsarinny, O.; Gorczyca, T.W.; Ackerman, G.D.; Bozek, J.D.; Martins, M.; McLaughlin, B.M.; Berrah, N. K-shell photodetachment from C^-: Experiment and theory. *Phys. Rev. A* **2003**, *67*, 030703(R). [CrossRef]
66. Walter, C.W.; Gibson, N.D.; Bilodeau, R.C.; Berrah, N.; Bozek, J.D.; Ackerman, G.D.; Aguilar, A. Shape resonance in K-shell photodetachment from C^-. *Phys. Rev. A* **2006**, *73*, 062702.02. [CrossRef]
67. Perry-Sassmannshausen, A.; Buhr, T.; Borovik, A., Jr.; Martins, M.; Reinwardt, S.; Ricz, S.; Stock, S.O.; Trinter, F.; Müller, A.; Fritzsche, S.; et al. Multiple photodetachment of carbon anions via single and double core-hole creation. *Phys. Rev. Lett.* **2020**, *124*, 083203. [CrossRef]
68. Schlachter, A.S.; Sant'Anna, M.M.; Covington, A.M.; Aguilar, A.; Gharaibeh, M.F.; Emmons, E.D.; Scully, S.W.J.; Phaneuf, R.A.; Hinojosa, G.; Álvarez, I.; et al. Lifetime of a K-shell vacancy in atomic carbon created by $1s \rightarrow 2p$ photoexcitation of C^+. *J. Phys. B* **2004**, *37*, L103–L109. [CrossRef]
69. Müller, A.; Borovik, A., Jr.; Buhr, T.; Hellhund, J.; Holste, K.; Kilcoyne, A.L.D.; Klumpp, S.; Martins, M.; Ricz, S.; Viefhaus, J.; et al. Observation of a four-electron Auger process in near-K-edge photoionization of singly charged carbon ions. *Phys. Rev. Lett.* **2015**, *114*, 013002. [CrossRef]
70. Müller, A.; Borovik, A.; Buhr, T.; Hellhund, J.; Holste, K.; Kilcoyne, A.L.D.; Klumpp, S.; Martins, M.; Ricz, S.; Viefhaus, J.; et al. Near-K-edge single, double, and triple photoionization of C^+ ions. *Phys. Rev. A* **2018**, *97*, 013409. [CrossRef]
71. Scully, S.W.J.; Aguilar, A.; Emmons, E.D.; Phaneuf, R.A.; Halka, M.; Leitner, D.; Levin, J.C.; Lubell, M.S.; Püttner, R.; Schlachter, A.S.; et al. K-shell photoionization of Be-like carbon ions: Experiment and theory for C^{2+}. *J. Phys. B* **2005**, *38*, 1967–1975. [CrossRef]
72. Müller, A.; Schippers, S.; Phaneuf, R.A.; Scully, S.W.J.; Aguilar, A.; Covington, A.M.; Álvarez, I.; Cisneros, C.; Emmons, E.D.; Gharaibeh, M.F.; et al. K-shell photoionization of li-like carbon ions [C^{3+}]: experiment, theory and comparison with time-reversed photorecombination. *J. Phys. B* **2009**, *42*, 235602. [CrossRef]
73. Gharaibeh, M.F.; Bizau, J.M.; Cubaynes, D.; Guilbaud, S.; El Hassan, N.; Al Shorman, M.M.; Miron, C.; Nicolas, C.; Robert, E.; Blancard, C.; et al. K-shell photoionization of singly ionized atomic nitrogen: experiment and theory. *J. Phys. B* **2011**, *44*, 175208. [CrossRef]
74. Bari, S.; Inhester, L.; Schubert, K.; Mertens, K.; Schunck, J.O.; Dörner, S.; Deinert, S.; Schwob, L.; Schippers, S.; Müller, A.; et al. Inner-shell X-ray absorption spectra of the cationic series NH_y^+ (y = 0–3). *Phys. Chem. Chem. Phys.* **2019**, *21*, 16505–16514. [CrossRef] [PubMed]
75. McLaughlin, B.M.; Mosnier, J.P.; Kennedy, E.T.; Sokell, E.; Bizau, J.M.; Cubaynes, D.; Guilbaud, S.; Carniato, S. K-shell Photoionization of the N^+, NH^+ and NH_2^+ ions. *J. Phys. Conf. Ser.* **2020**, *1412*, 142007. [CrossRef]
76. Gharaibeh, M.; El Hassan, N.; Shorman, M.A.; Bizau, J.; Cubaynes, D.; Guilbaud, S.; Sakho, I.; Blancard, C.; McLaughlin, B. K-shell photoionization of B-like atomic nitrogen ions: Experiment and theory. *J. Phys. B* **2014**, *47*, 065201. [CrossRef]
77. Al Shorman, M.M.; Gharaibeh, M.F.; Bizau, J.M.; Cubaynes, D.; Guilbaud, S.; El Hassan, N.; Miron, C.; Nicolas, C.; Robert, E.; Sakho, I.; et al. K-shell photoionization of Be-like and Li-like ions of atomic nitrogen: Experiment and theory. *J. Phys. B* **2013**, *46*, 195701. [CrossRef]

78. Gibson, N.D.; Bilodeau, R.C.; Walter, C.W.; Hanstorp, D.; Aguilar, A.; Berrah, N.; Matyas, D.J.; Li, Y.G.; Alton, R.M.; Lou, S.E. K-shell photodetachment from O^-. *J. Phys. Conf. Ser.* **2012**, *388*, 022102. [CrossRef]
79. Schippers, S.; Beerwerth, R.; Abrok, L.; Bari, S.; Buhr, T.; Martins, M.; Ricz, S.; Viefhaus, J.; Fritzsche, S.; Müller, A. Prominent role of multielectron processes in K-shell double and triple photodetachment of oxygen anions. *Phys. Rev. A* **2016**, *94*, 041401. [CrossRef]
80. Kawatsura, K.; Yamaoka, H.; Oura, M.; Hayaishi, T.; Sekioka, T.; Agui, A.; Yoshigoe, A.; Koike, F. The $1s-2p$ resonance photoionization measurement of O^+ ions in comparison with an isoelectronic species Ne^{3+}. *J. Phys. B* **2002**, *35*, 4147–4153. [CrossRef]
81. Bizau, J.M.; Cubaynes, D.; Guilbaud, S.; Al Shorman, M.M.; Gharaibeh, M.F.; Ababneh, I.Q.; Blancard, C.; McLaughlin, B.M. K-shell photoionization of O^+ and O^{2+} ions: Experiment and theory. *Phys. Rev. A* **2015**, *92*, 023401. [CrossRef]
82. McLaughlin, B.; Bizau, J.; Cubaynes, D.; Shorman, M.A.; Guilbaud, S.; Sakho, I.; Blancard, C.; Gharaibeh, M. K-shell photoionization of B-like oxygen (O^{3+}) ions: Experiment and theory. *J. Phys. B* **2014**, *47*, 115201. [CrossRef]
83. McLaughlin, B.M.; Bizau, J.M.; Cubaynes, D.; Guilbaud, S.; Douix, S.; Shorman, M.M.A.; Ghazaly, M.O.A.E.; Sakho, I.; Gharaibeh, M.F. K-shell photoionization of O^{4+} and O^{5+} ions: Experiment and theory. *Mon. Not. R. Astron. Soc.* **2017**, *465*, 4690–4702. [CrossRef]
84. Müller, A.; Borovik, A., Jr.; Bari, S.; Buhr, T.; Holste, K.; Martins, M.; Perry-Sassmannshausen, A.; Phaneuf, R.A.; Reinwardt, S.; Ricz, S.; et al. Near-K-edge double and triple detachment of the F^- negative ion: Observation of direct two-electron ejection by a single photon. *Phys. Rev. Lett.* **2018**, *120*, 133202. [CrossRef] [PubMed]
85. Oura, M.; Yamaoka, H.; Kawatsura, K.; Kimata, J.; Hayaishi, T.; Takahashi, T.; Koizumi, T.; Sekioka, T.; Terasawa, M.; Itoh, Y.; et al. Photoionization of Ne^{3+} ions in the region of the $1s2p$ autoionizing resonance. *Phys. Rev. A* **2001**, *63*, 014704. [CrossRef]
86. Buhr, T.; Stock, S.O.; Perry-Sassmannshausen, A.; Reinwardt, S.; Martins, M.; Ricz, S.; Müller, A.; Fritzsche, S.; Schippers, S. Photoionization of low-charged silicon ions. *J. Phys. Conf. Ser.* **2020**, *1412*, 152024. [CrossRef]
87. Liao, J.Y.; Zhang, S.N.; Yao, Y. Wavelength measurements of K transitions of oxygen, neon, and magnesium with X-ray absorption lines. *Astrophys. J.* **2013**, *774*, 116. [CrossRef]
88. Gorczyca, T.W. Auger decay of the photoexcited $1s^{-1}np$ Rydberg series in neon. *Phys. Rev. A* **2000**, *61*, 024702. [CrossRef]
89. Gatuzz, E.; Garcia, J.; Kallman, T.R.; Mendoza, C.; Gorczyca, T.W. ISMabs: A comprehensive X-ray absorption model for the interstellar medium. *Astrophys. J.* **2015**, *800*, 29. [CrossRef]
90. Witthoeft, M.C.; Bautista, M.A.; Mendoza, C.; Kallman, T.R.; Palmeri, P.; Quinet, P. K-shell photoionization and photoabsorption of Ne, Mg, Si, S, Ar, and Ca. *Astrophys. J. Suppl. Ser.* **2009**, *182*, 127–130. [CrossRef]
91. Landi, E.; Lepri, S.T. Photoionization in the Solar wind. *Astrophys. J.* **2015**, *812*, L28. [CrossRef]
92. Larsson, M.; Geppert, W.D.; Nyman, G. Ion chemistry in space. *Rep. Prog. Phys.* **2012**, *75*, 066901. [CrossRef]
93. Tielens, A.G.G.M. The molecular universe. *Rev. Mod. Phys.* **2013**, *85*, 1021–1081. [CrossRef]
94. Millar, T.J.; Walsh, C.; Field, T.A. Negative ions in space. *Chem. Rev.* **2017**, *117*, 1765–1795. [CrossRef] [PubMed]
95. Mosnier, J.P.; Kennedy, E.T.; van Kampen, P.; Cubaynes, D.; Guilbaud, S.; Sisourat, N.; Puglisi, A.; Carniato, S.; Bizau, J.M. Inner-shell photoexcitations as probes of the molecular ions CH^+, OH^+, and SiH^+: Measurements and theory. *Phys. Rev. A* **2016**, *93*, 061401. [CrossRef]
96. Hellhund, J.; Borovik A., Jr.; Holste, K.; Klumpp, S.; Martins, M.; Ricz, S.; Schippers, S.; Müller, A. Photoionization and photofragmentation of multiply charged $Lu_3N@C_{80}$ ions. *Phys. Rev. A* **2015**, *92*, 013413. [CrossRef]
97. Müller, A.; Martins, M.; Kilcoyne, A.L.D.; Phaneuf, R.A.; Hellhund, J.; Borovik, A.; Holste, K.; Bari, S.; Buhr, T.; Klumpp, S.; et al. Photoionization and photofragmentation of singly charged positive and negative $Sc_3N@C_{80}$ endohedral fullerene ions. *Phys. Rev. A* **2019**, *99*, 063401. [CrossRef]
98. Voulot, D.; Gillen, D.R.; Thompson, W.R.; Gilbody, H.B.; McCullough, R.W.; Errea, L.; Macias, A.; Mendez, L.; Riera, A. First studies of state-selective electron capture in collisions of state-prepared ions with atomic hydrogen; the case of C^{2+}–H(1s). *J. Phys. B* **2000**, *33*, L187–L192. [CrossRef]

99. Covington, A.M.; Aguilar, A.; Covington, I.R.; Gharaibeh, M.; Shirley, C.A.; Phaneuf, R.A.; Álvarez, I.; Cisneros, C.; Hinojosa, G.; Bozek, J.D.; et al. Photoionization of metastable O^+ ions: Experiment and theory. *Phys. Rev. Lett.* **2001**, *87*, 243002. [CrossRef]
100. Benis, E.P.; Madesis, I.; Laoutaris, A.; Nanos, S.; Zouros, T.J.M. Mixed-state ionic beams: An effective tool for collision dynamics investigations. *Atoms* **2018**, *6*, 66. [CrossRef]
101. Schippers, S.; Müller, A.; Ricz, S.; Bannister, M.E.; Dunn, G.H.; Bozek, J.D.; Schlachter, A.S.; Hinojosa, G.; Cisneros, C.; Aguilar, A.; et al. Experimental link of photoionization of Sc^{2+} to photorecombination of Sc^{3+}: An application of detailed balance in a unique atomic system. *Phys. Rev. Lett.* **2002**, *89*, 193002. [CrossRef]
102. Wolf, A.; Berger, J.; Bock, M.; Habs, D.; Hochadel, B.; Kilgus, G.; Neureither, G.; Schramm, U.; Schwalm, D.; Szmola, E.; et al. Experiments with highly-charged ions in the storage ring TSR. *Z. Phys. D* **1991**, *21*, S69–S75. [CrossRef]
103. Andersen, T. Atomic negative ions: Structure, dynamics and collisions. *Phys. Rep.* **2004**, *394*, 157–313. [CrossRef]
104. Schippers, S. Analytical expression for the convolution of a Fano line profile with a gaussian. *J. Quant. Spectrosc. Radiat. Transf.* **2018**, *219*, 33–36. [CrossRef]
105. Lindroth, E.; Argenti, L. Atomic resonance states and their role in charge-changing processes. *Adv. Quantum Chem.* **2012**, *63*, 247. [CrossRef]
106. Indelicato, P.; Gorveix, O.; Desclaux, J.P. Multiconfigurational Dirac-Fock studies of two-electron ions. II. Radiative corrections and comparison with experiment. *J. Phys. B* **1987**, *20*, 651. [CrossRef]
107. Zeegers, S.T.; Costantini, E.; Rogantini, D.; de Vries, C.P.; Mutschke, H.; Mohr, P.; de Groot, F.; Tielens, A.G.G.M. Dust absorption and scattering in the silicon K-edge. *Astron. Astrophys.* **2019**, *627*, A16. [CrossRef]
108. Schulz, N.S.; Corrales, L.; Canizares, C.R. Si K edge structure and variability in Galactic X-ray binaries. *Astrophys. J.* **2016**, *827*, 49. [CrossRef]
109. Witthoeft, M.C.; García, J.; Kallman, T.R.; Bautista, M.A.; Mendoza, C.; Palmeri, P.; Quinet, P. K-shell photoionization of Na-like to Cl-like ions of Mg, Si, S, Ar, and Ca. *Astrophys. J. Suppl. Ser.* **2011**, *1992*, 7. [CrossRef]
110. Kučas, S.; Karazija, R.; Momkauskaitė, A. Cascades after K-vacancy production in atoms and ions of light elements. *Astrophys. J.* **2012**, *750*, 90. [CrossRef]
111. Hasoglu, M.F.; Gorczyca, T.W. X-Ray Absorption by Interstellar Atomic Gases near the K Edges of C, O, Ne, Mg, and Si and the L Edge of Fe. *ASP Conf. Ser.* **2018**, *515*, 275.
112. Ueda, K.; Sokell, E.; Schippers, S.; Aumayr, F.; Sadeghpour, H.; Burgdörfer, J.; Lemell, C.; Tong, X.M.; Pfeifer, T.; Calegari, F.; et al. Roadmap on photonic, electronic and atomic collision physics: I. Light–matter interaction. *J. Phys. B* **2019**, *52*, 171001. [CrossRef]

atoms

MDPI

Article

Photoionization Cross-Sections of Carbon-Like N^+ Near the K-Edge (390–440 eV)

Jean-Paul Mosnier [1,*], Eugene T. Kennedy [1], Jean-Marc Bizau [2,3], Denis Cubaynes [2,3], Ségolène Guilbaud [2], Christophe Blancard [4,5] and Brendan M. McLaughlin [6]

[1] National Centre for Plasma Science and Technology (NCPST), School of Physical Sciences, Dublin City University, Dublin 9, Ireland; eugene.kennedy@dcu.ie
[2] Institut des Sciences Moléculaires d'Orsay, UMR 8214, Rue André Rivière, Bâtiment 520, Université Paris-Saclay, F-91405 Orsay, France; jean-marc.bizau@universite-paris-saclay.fr (J.-M.B.); denis.cubaynes@universite-paris-saclay.fr (D.C.); segolene.guilbaud@universite-paris-saclay.fr (S.G.)
[3] Synchrotron SOLEIL, L'Orme des Merisiers, Saint-Aubin, BP 48, CEDEX, F-91192 Gif-sur-Yvette, France
[4] CEA, DAM, DIF, F-91297 Arpajon, France; christophe.blancard@cea.fr
[5] Commissariat à l'Énergie Atomique et aux Énergies Alternatives, Laboratoire Matière en Conditions Extrêmes, Université Paris-Saclay, 91680 Bruyères le Châtel, France
[6] Centre for Theoretical Atomic, Molecular and Optical Physics (CTAMOP), School of Mathematics and Physics, The David Bates Building, 7 College Park, Queen's University Belfast, Belfast BT7 1NN, UK; bmcl104@gmail.com
* Correspondence: jean-paul.mosnier@dcu.ie

Abstract: High-resolution K-shell photoionization cross-sections for the C-like atomic nitrogen ion (N^+) are reported in the 398 eV (31.15 Å) to 450 eV (27.55 Å) energy (wavelength) range. The results were obtained from absolute ion-yield measurements using the SOLEIL synchrotron radiation facility for spectral bandpasses of 65 meV or 250 meV. In the photon energy region 398–403 eV, $1s \longrightarrow 2p$ autoionizing resonance states dominated the cross section spectrum. Analyses of the experimental profiles yielded resonance strengths and Auger widths. In the 415–440 eV photon region $1s \longrightarrow (1s2s^22p^{2\,4}P)np$ and $1s \longrightarrow (1s2s^22p^{2\,2}P)np$ resonances forming well-developed Rydberg series up $n = 7$ and $n = 8$, respectively, were identified in both the single and double ionization spectra. Theoretical photoionization cross-section calculations, performed using the R-matrix plus pseudo-states (RMPS) method and the multiconfiguration Dirac-Fock (MCDF) approach were bench marked against these high-resolution experimental results. Comparison of the state-of-the-art theoretical work with the experimental studies allowed the identification of new resonance features. Resonance strengths, energies and Auger widths (where available) are compared quantitatively with the theoretical values. Contributions from excited metastable states of the N^+ ions were carefully considered throughout.

Keywords: atomic data; inner-shell photoionization; atomic nitrogen ion

Citation: Mosnier, J.-P.; Kennedy, E.T.; Bizau, J.-M.; Cubaynes, D.; Guilbaud, S.; Blancard, C.; McLaughlin, B.M. Photoionization Cross-Sections of Carbon-Like N^+ Near the K-Edge (390–440 eV). *Atoms* **2021**, *9*, 27. https://doi.org/10.3390/atoms9020027

Academic Editor: Luca Argenti

Received: 2 April 2021
Accepted: 6 May 2021
Published: 11 May 2021

1. Introduction

X-ray spectra obtained by Chandra from sources such as Capella, Procyon, and HR 1099 provide challenges for contemporary plasma spectral modelling codes. For example, the X-ray spectrum of the bright blazar Mkn 421 observations by the Chandra LETG+HRC-S and subsequent modelling of the spectra indicated that high quality photoionization cross-section data of atomic carbon and its ions were required [1]. More recently, photoionization cross-section measurements on the atomic oxygen ion sequence [2–4] were used to interpret the O VI differences between satellite observations in the UV spectra of galactic and extra-galactic sight lines compared to ground based measurements made at the SOLEIL synchrotron radiation facility [5,6].

Nitrogen is ubiquitous in astrophysical environments and the sixth most populous element in the cosmos. The photoionization of atomic nitrogen species has been the subject

of a number of laboratory investigations. 1*s* photoionization of neutral nitrogen was investigated by Stolte et al. [7] while Gharaibeh et al. measured K-shell cross-sections in N^+ (carbon-like) [8] and N^{2+} (B-like) [9], Al-Shorman et al. investigated N^{3+} and N^{4+} [10]. Recently, ion yield spectra following X-ray absorption in the K threshold region of the N^+, NH^+, $NH_2{}^+$ and $NH_3{}^+$ species were obtained by Bari et al. [11]. For N^+, these authors measured the double-ionisation yield (N^{3+}) and provided resonance assignments based on both ab initio CI calculations using the General Atomic and Molecular Electronic Structure System (GAMESS) package [12] and the results of [8]. Inner-shell photoionization and Auger processes in atomic nitrogen species have also been the subject of a number of theoretical works, see for example [13,14].

In this paper, we report high resolution absolute photoionization (PI) cross-section measurements for the singly ionised carbon-like atomic nitrogen ion N^+ over the photon energy range 398–450 eV, covering the full 1s excitation region and photon energies beyond the K-threshold. N^+ was one of the first ions to be studied on the Multi-Analysis Ion Apparatus (MAIA) photon-ion merged-beam facility at SOLEIL [8]. This early investigation was limited to the narrow 398–406 eV photon energy range and succeeded in detecting resonance features belonging to the strongest $1s \longrightarrow 2p$ excitation only. Recent substantial improvements (discussed below) to the MAIA apparatus enabled us to: (1) detect the $1s \longrightarrow 2p$ resonances with much improved statistical significance leading to the observation and assignment of several additional features; (2) estimate the $1s \longrightarrow 2p$ experimental Auger widths and compare with theoretical values; (3) observe and identify regular series of $1s \longrightarrow np$ $(n \geq 3)$ resonances leading up to the K-shell ionisation limits and (4) provide improved absolute cross section measurements in both the single and double-ionisation channels.

State-of-the-art theoretical work from the Multi Configurational Dirac-Fock (MCDF) and R-matrix with pseudo-states (RMPS) methods are bench marked against these measurements. The comparison with theory allows the interpretation of resonance features found in the experimental spectra and an estimation of the metastable content of the ion beam.

2. Experimental Details

The present work was performed on the MAIA photon-ion merged-beam set-up available at the site of the SOLEIL synchrotron radiation facility [15]. MAIA allows the high-quality synchrotron photon beam to interact with a counter-propagating ion beam within a well-defined overlap region, and has been used for the last decade to investigate the relative and absolute cross section inner-shell photoionization behaviours of a range of atomic ions, see for example [16–18]. More recently, similar studies on molecular species were initiated, see for example [19–21]. Photoelectron-photo-ion coincidence studies on ionic species can also be performed with MAIA [17].

Comprehensive descriptions of the apparatus and procedures used to obtain cross-sections in free ions are available from Bizau et al. [15] and so only an outline of the main points is presented here. Molecular nitrogen was introduced into an electron cyclotron resonance (ECR) plasma source and heated by microwaves to produce ionisation. N^+ ions, after extraction at a 4 kV voltage on the source, were selected from other multiply charged nitrogen ions by a dipole magnet and guided via an electrostatic deflector into the region of overlap with the counter-propagating monochromatized photon beam. The interaction of the synchrotron photons with the N^+ ions resulted in the production of either N^{2+} or N^{3+} photo-ions which were separated, after exit from the interaction region, by a tuneable dipole magnet and detected by a channel plate detector. Photon energy scans of the N^{2+} and N^{3+} count rates were acquired to map out the relative single and double photoionization cross section behaviours, respectively. Absolute measurements of the N^{2+} and N^{3+} photon yield cross-section values were also carried out at a number of photon energies.

In a merged-beam experiment the ionisation cross section value $\sigma(E)$ is obtained from:

$$\sigma(E) = \frac{S(E)e^2\eta v q}{IJ\epsilon \int_0^L \frac{dz}{\Delta x \Delta y F(z)}}, \quad (1)$$

where $S(E)$ is the counting rate of the photo-ions produced by the synchrotron photons of energy E, e is the electron charge, η is the efficiency of the photodiode used to characterise the photon beam, v is the velocity of the ions in the interaction region due to the extracting voltage, q is the charge on the ion, I is the current produced by the calibrated photodiode, J is the ion current, ϵ is the efficiency of the channel plates used to measure the photo-ions and the integral takes account of the beam overlap geometry with z which defines the ion beam propagation direction.

Table 1 provides a summary of the experimental parameters for the present experiments under the experimental conditions prevailing during the measurement of the absolute cross section near the maximum of the strongest resonance at 400 eV. The aforementioned experimental developments included an increased photon flux and an improved understanding and calibration of the merged beam configuration. The ion current J has doubled and the reduced form factor F_{xy} reflects a tighter and better-defined interaction region. Most significantly, the signal-to-noise ratio for the experiment has been very much improved. Finally, of most significance for the absolute cross section measurements, a new ion detector involving focusing optics now ensures maximum collection efficiency of the photo-ions produced due to photoionization in the merged beam overlap region. Comparison with Gharaibeh et al. [8] shows a substantial gain in overall performance and sensitivity due to the significant improvement of key experimental parameters. This is the justification for the revised cross-sectional values presented in the current work.

Table 1. Values of experimental parameters used to evaluate the absolute photoionization cross-section at 400 eV photon energy.

Experimental Parameter	Value
Photo-ion counting rate S (s^{-1})	1030
Noise (s^{-1})	60
Ion beam velocity v (ms^{-1})	2.1×10^5
Photon brilliance (photons/0.1%BP)	6×10^{12}
Ion current J (nA)	80
Channel plates efficiency ϵ	0.55
Form factor F_{xy}	13

Photon energies were determined by calibrating with the well-known $1s \longrightarrow \pi^*$ and $2p \longrightarrow 3d$ transitions in N_2 [22] and Ar [23] gas, respectively, corrected for the Doppler shift resulting from the velocity of the N^+ ions. The estimated energy uncertainty is 60 meV. Different photon energy bandpasses were used depending on the spectral region under investigation. For the strongest resonances in the 400 eV region a minimum photon bandpass of 65 meV was used for optimum spectral resolution, whereas for the higher lying resonances (425–450 eV) a mean energy bandpass of 225 meV was used. When carrying out measurements of the cross sections on an absolute basis a bandpass of 280 meV was used. We estimate the total relative experimental uncertainty in the absolute values of the cross sections to be no greater than 15%.

A complication in the interpretation of the MAIA experimental measurements may arise due to the possible presence in the overlap region of ions in long-lived metastable states that have remained populated during the journey from the ECR plasma source (this is the case for the present N^+ experiment). The measured photo-ion spectra thus comprise ground and metastable initial states contributions, the relative strength of which depends in a non-trivial manner on the source (ECR plasma) conditions prevailing at extraction.

Detailed comparisons between theoretical and experimental results can be used effectively to estimate the metastable fraction, e.g., [24].

3. Theory

3.1. Relevant Decay Processes

Photon inner-shell excitation of a N^+ ion in either the ground or metastable states produces highly energetic 1*s* hole states that may decay via autoionization (resonant Auger process), forming a stable N^{2+} ion and releasing a free electron. From the initial $1s^22s^22p^2\,{}^3P_{0,1,2}$ ground levels of N^+, $1s \longrightarrow np$ photo-excitation processes ($n \geq 2$) produce $1s2s^22p^3 {}^3S, {}^3P, {}^3D$ $(n = 2)$ or $\left(1s2s^22p^{2\,4,2}P\right)np\ {}^3S,\ \ {}^3P,\ \ {}^3D$ $(n > 2)$ inner-shell states that autoionize into the $(1s^22s^22p\ {}^2P{+}\epsilon s_{1/2})$ or $(1s^22s^22p\ {}^2D{+}\epsilon d_{3/2,5/2})$ continua (channels) by Coulomb interactions, according to the $\Delta S = \Delta L = \Delta J = 0$ *LS* coupling selection rules, leaving the ion in the ground state configuration of N^{2+}. This decay scheme corresponds to the $KL_{2,3}L_{2,3}$ Auger process. Other Auger processes, namely KL_1L_1 or $KL_1L_{2,3}$ are possible that would leave the ion in the core-excited configurations $1s^22p^3$ or $1s^22s2p^2$. More final state channels are open if the 1*s* electron is excited to 3*p* (higher *np*) states for the 3*p* (higher *np*) electron can now either participate or spectate in the Auger process [1] with the final core state configurations $\left(1s^22s2p^2\right)$, $\left(1s^22s^22p\right)$ or $\left(1s^22s^23p\right)$, $\left(1s^22s2p3p\right)$, $\left(1s^22p^23p\right)$, respectively, e.g., [25].

As noted earlier, the measured cross section data may be complicated by the presence of metastable states in the sample ion beam. Theoretical interpretation, thus, requires the computation of all the PI cross-sections from the relevant initially populated states that contribute. In the present case, these are $1s^22s^22p^2\ {}^1D_2$ (1.90 eV),${}^1S_0$ (4.05 eV) and $1s^22s2p^3{}^5S_2$ (5.80 eV), which all lie within a few eV above the ground state [26]. The $1s^22s2p^3\ {}^5S_2$ state is radiatively coupled to the $1s^22s^22p^2{}^3P_{1,2}$ ground *J*-levels with a total lifetime of 5.6 ms [27]. This time is sufficiently long for the initially extracted ions excited in the $1s^22s^22p^2{}^3P_{1,2}$ states to reach the interaction zone in our apparatus. Following $1s \longrightarrow np$ $(n \geq 2)$ photo-excitation of $1s^22s2p^3{}^5S_2$, autoionization decay processes such as $N^+\ 1s2s\left(2p^3{}^3P\right)np\ {}^5P \longrightarrow N^{2+}\ 1s^22s2p^2\ {}^4P{+}\epsilon s_{1/2}$ are allowed and similarly for $1s \longrightarrow np$ $(n \geq 2)$ excitations in the $1s^22s^22p^2{}^1D_2$ and ${}^1S_0$ metastable states.

This brief analysis shows that the strength of the signal measured in this work in the single-ionization channel (N^{2+}), at a given photon energy, will comprise simultaneous contributions from a variety of possible Auger decay processes involving several initial state channels. Theoretical modelling comprising the most important of these channels is necessary for the interpretation of the experimental data.

Further ionisation may also result from the initial X-ray absorption. The $N^{3+}\ 1s^22s^2\ {}^1S$ state lies about 77.0 eV [26] above the $N^+\ 1s^22s^22p^2\ {}^3P$ ground state and, thus, double-photoionization processes are, in principle, energetically possible following K-shell excitation in N^+. Double-Auger decay, Auger cascade and electron shake-off are possible atomic processes that may contribute to double-ionization in the present case. For some of the final state configurations mentioned above, e.g., $1s^22p^3$, the Auger decay of the 2*s* vacancy is not energetically possible, thus preventing the Auger cascade, and return to ground state is necessarily via radiative transitions.

A schematic energy level diagram showing the main excitation and decay processes involved in this work is shown in Figure 1. It is notable that the photon-excited states include several open shells and sub-shells. This makes the problem of accurate atomic structure calculations a very demanding one, e.g., [28], and the case of N^+ provides a particularly challenging test case for theoretical models. We have carried through extensive calculations using two different theoretical approaches, namely Multi-Configuration Dirac-Fock (MCDF) and R-matrix with Pseudo-States (RMPS) in order to evaluate their predictions compared with experiment and to help in the interpretation of the results.

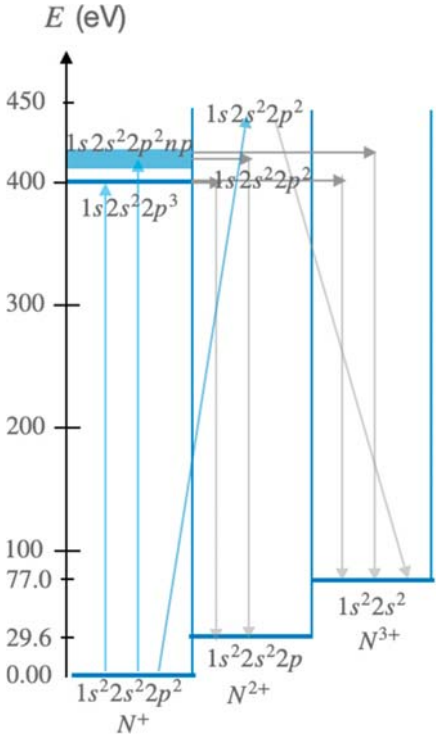

Figure 1. Schematic energy level diagram showing the main excitation and decay processes (upward and downward arrows, respectively) involved in this work. The initial photon absorption process excites a 1*s* electron from the various states of the $1s^22s^22p^2$ and $1s^22s2p^3$ configurations to the $1s2s^22p^3$ (near 400 eV) and $1s2s^22p^2np$ or $1s2s2p^3np$ (between 418 eV and 440 eV) states. The direct ionization process to $1s2s^22p^2$ in N^{2+} followed by Auger decay to $1s^22s^2$ in N^{3+} is also shown.

3.2. Multi-Configuration Dirac-Fock (MCDF)

Multi-configuration Dirac-Fock (MCDF) calculations, based on a full intermediate coupling scheme in a jj-basis, have been performed using a recent version of the code originally developed by Bruneau [29]. The N^+ $(Z = 7)$ photoexcitation and photoionization cross-sections were computed in the Babushkin (velocity) gauge [30] in the photon energy region of the K-edge. Calculations were restricted to electric-dipole (E_1) transitions. The concept of the Slater transition state [31] was used to optimize the one-electron wave functions. Photoexcitation and photoionization cross-sections were evaluated for the five *J*-levels ($^3P_{0,1,2}$ and $^1S_0$) of the ground configuration $1s^22s^22p^2$ and the $^5S_2$ lowest level of the $1s^22s2p^3$ configuration. The $1s^22s^22pnp$ and $1s^22p^3np$ $(n = 3-5)$ configurations were added to optimize the initial state description. Photo-excited levels with $J = 0, 1, 2$ were obtained based on the mixing of the $1s2s^22p^3$, $1s2s^22p^2np$ $(n = 3-5)$, $1s2p^5$, $1s2p^4np$, $n = 3-5$ and $1s2s2p^4$, $1s2s2p^3np$, $n = 3-5$, odd and even parity configurations, respectively. With a view to optimise eigenenergies, different radial functions for the $np_{1/2,3/2}$ $(n = 2-5)$ orbitals were used in the initial and final configurations. The individual photoexcitation cross-sectional profiles were obtained by dressing each E_1 transition with a Lorentzian line shape of full width at half maximum (FWHM) equal to 92.4 meV to represent the Auger width. The latter value was obtained from MCDF calculations performed to calculate the statistical average of the autoionization rates from the $1s2s^22p^3$ configuration to the $1s^22s^22p$, $1s^22s2p^2$ and $1s^22p^3$ configurations, respectively. The same value of 92.4 meV was used for all the members along the aforementioned Rydberg series.

Continuum photoionization cross-sections were calculated using the reduced set of the $1s^2 2s^2 2p^2$, $1s^2 2s 2p^3$, $1s 2s^2 2p^2$ and $1s 2s 2p^3$ configurations.

Additionally, we note the work of Hasoğlu et al. [32] who used multiconfiguration Dirac-Fock (MCDF) and Breit-Pauli (MCBP) theoretical methodologies to calculate the K-shell Auger and radiative decay rates of the ten possible $1s^2 2s^2 2p^3\ ^{2S+1}L_J$ states along the iso-electronic sequence from $Z = 6$ to $Z = 30$, showing the importance of both electron-electron correlation and relativistic effects even at low Z. Some of the Auger rates obtained by Hasoğlu et al. [32] for $Z = 7$ are amenable to direct comparison with the present experimental values (see Section 4.1).

3.3. R-Matrix (RMPS)

The photon energy range of the photoionization (PI) cross-sections presented in [8] has been extended up to 440 eV to include the K-edge region. All PI cross sections were determined using the RMPS method [33–35] in LS—coupling with the parallel version [36] of the programs [34,35,37]. The same 390-level model for the N^{2+} residual ion was used in the present close-coupling PI cross-section calculations as in the work of Gharaibeh et al. [8]. The RMPS resonance parameters were determined using the multi-channel R-matrix QB technique (applicable to atomic and molecular complexes) of Berrington and co- workers [38], Quigley et al. [39] and Ballance et al. [40]. The resonance width Γ may be determined from the inverse of the energy derivative of the eigenphase sum δ at the position of the resonance energy E_r via:

$$\Gamma = 2\left[\frac{d\delta}{dE}\right]^{-1}_{E=E_r} = 2\left[\delta'\right]^{-1}_{E=E_r}, \tag{2}$$

Further relevant theoretical details can be found in Gharaibeh et al. [8].

4. Results and Analyses

The experimental results are presented in Figure 2 showing the measured cross-sections for single and double photo-ionization of N^+ in the 398–450 eV photon energy region. The photon energies at which absolute measurements were carried out are indicated. Both spectra feature a strong discrete resonance region in the 399–405 eV photon range which corresponds with the decay of N^+ ions following $1s \longrightarrow 2p$ electron excitation. The four main peaks observed in the single ionization channel are seen to have counterparts in the double-ionization channel at the same photon energies. Additional, previously unobserved, resonance features appear in the 415–440 eV photon energy region in both the single and double ionisation channels. This is the region corresponding to the decay of N^+ ions following $1s \longrightarrow np$ excitations with $n \geq 3$. Some resonances are seen to form distinctive Rydberg series, particularly in the double-ionization channel, while continuum processes begin to contribute significantly to the cross-section upward of ~430 eV photon energy. Resonance series due to $1s \longrightarrow np$ excitations in the ^1P,^1D and ^1S initial states converge to the $1s2s^2\left(2p^2\ ^3P\right)^{4,2}P$, $1s2s^2\left(2p^2\ ^1D\right)^2D$ and $1s2s^2\left(2p^2\ ^1S\right)^2S$ inner ionisation limits in N^{2+}, respectively. Excitations from the $1s^2 2s 2p^3\ ^5S$ state will result in additional limits. Detailed analyses for the two photon regions 398–403 eV ($1s \longrightarrow 2p$) and 415–450 eV ($1s \longrightarrow np, n \geq 3$) are given below in the light of the MCDF and RMPS theoretical results.

4.1. $1s \rightarrow 2p$ Resonances

Figure 3 shows the ab initio results of our RMPS and MCDF total photoionization cross-section calculations for the resonances in the 398–404 eV region. These arise from the photon excitation of an inner shell 1s electron to a $2p$ valence shell, starting from the assumed initial levels $1s^2 2s^2 2p^2\ ^3P_{0,1,2}$,$^1D_2$,$^1S_0$ and $1s^2 2s 2p^3\ ^5S_2$. Figure 4a shows a high-resolution experimental single-ionisation spectrum (65 meV band pass) in the same region which clearly reveals additional resonances not reported by Gharaibeh et al. [8]. The resonance features in Figure 4a are assigned the numerical labels that are used in Table 2,

which provides the resonance identifications and atomic parameters. Figure 4a also shows the results of Voigt profile numerical deconvolutions of the measured lineshapes.

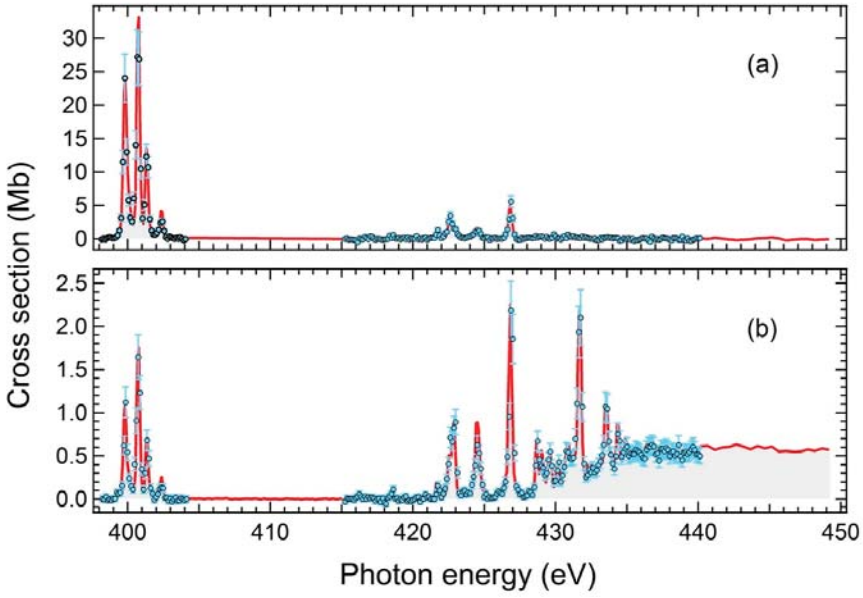

Figure 2. N^+ cross sections measured in (**a**) the single and (**b**) the double photoionisation channels, in the 398–450 eV photon energy range, respectively. In both figures, the photon energies for the absolute measurements (energy band pass of 280 meV) are shown with open circle points. Relative measurements were carried out with an energy band pass varying between 220 meV and 250 meV in the scanned range and shown by a continuous red line.

The $1s^2 2s^2 2p^2\ ^3P_1$ and $1s^2 2s^2 2p^2\ ^3P_2$ states lie 6.04 meV and 16.22 meV, respectively above the $1s^2 2s^2 2p^2\ ^3P_0$ ground state. Such small energy differences are not amenable to discrimination in the present experimental conditions and we, thus, consider initial excitations from these three levels proportionally to their statistical weight. For the sake of simplifying the notation, we shall also generally omit the J-value in the notation of the relevant (LSJ) states in the rest of the paper. From Figure 3, both theoretical approaches predict three strong resonances originating from the ^3P ground state to the $1s2s^2 2p^3\ ^3D, ^3S$ and ^3P states (in increasing order of energy). The strong experimental resonances 1, 3 and 5 in Figure 4a measured at 399.84 eV, 400.73 eV and 401.40 eV, respectively, are readily assigned to these transitions, respectively. The ab initio energies predicted by the MCDF (RMPS) theories are 399.28 (399.709) eV, 400.48 (400.579) eV and 400.53 (401.347) eV, corresponding to experimental vs. calculated energy differences of 0.56 (0.131) eV, 0.25 (0.149) eV and 0.87 (0.05) eV, for the same transitions, respectively. This comparison shows that the RMPS theory, as implemented in the manner described in Section 3, more accurately predicts the experimental values than the MCDF results which show differences of 0.25 eV or greater.

From the theoretical results of Figure 3, it is reasonable to assign the isolated resonance peak 6 observed at 402.36 eV to the $1s^2 2s^2 2p^2\ ^1D \longrightarrow 1s^2 2s 2p^3\ ^1P$ transition (Table 2). It follows that the deconvolved shoulder at 400.85 eV, resonance 4 in Figure 4a, can be attributed to the $1s^2 2s^2 2p^2\ ^1D \longrightarrow 1s 2s^2 2p^3\ ^1D$ transition. RMPS theory results for the resonance energies are again in closer agreement with experiment than the MCDF values (Table 2). Nevertheless, both theoretical approaches agree on these assignments.

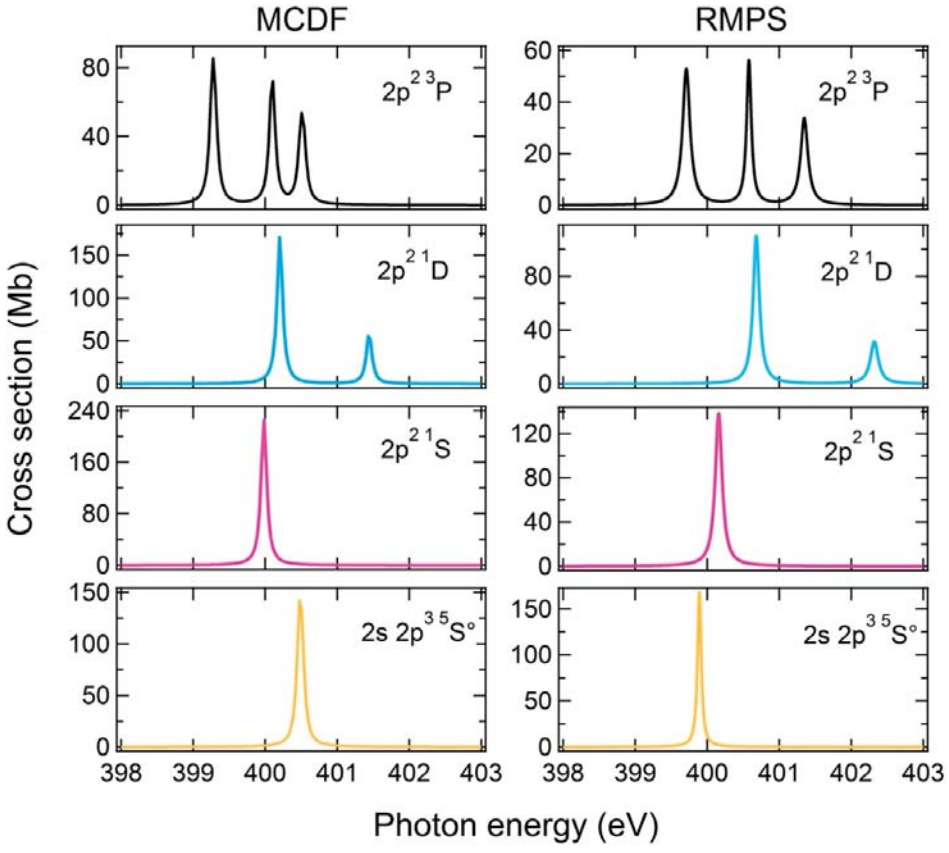

Figure 3. Multiconfiguration Dirac-Fock (MCDF) and R-Matrix with pseudo-states (RMPS) theoretical calculations of the $1s \longrightarrow 2p$ photoexcitation cross sections from the $1s^2 2s^2 p^2\, ^3P$, ^1D, ^1S and $1s^2 2s 2p^3\, ^5S$ LS states of N^+, respectively.

Table 2. Experimentally determined atomic parameters (energy, Auger width and oscillator strength) of the main $1s \longrightarrow 2p$ resonances (~400 eV photon energy) in the N^+ photoionization cross-section spectrum, estimated from the absolute measurements of single-ionisation yields and comparison with theoretical values.

Resonance #Label	Measured Energy [a] (eV)	RMPS Energy (eV)	MCDF Energy (eV)	Experimental Width [a,b] (meV)	RMPS Width (meV)	MCBP/ MCDF Width (meV) [32]	Measured Strength [a,c] (MbeV)	Scaled Strength [d,e] (MbeV)	RMPS Strength [f] (MbeV) This Work	MCDF Strength [g] (MbeV) This Work
1	399.840(2)	399.709	399.275	73(11)	124	171/181	5.7(1.8)	7.6	10.1	14.5
2	399.994(26)	399.891	400.488	167(70)	62		1.4(8)	34.1	16.2	22.9
x	x	400.159	399.98		115				24.6	27.2
3	400.728(2)	400.579	400.094	79(9)	78	33/79	8.6(2.5)	11.5	6.8	9.8
4	400.862(9)	400.681	400.199	116(24)	105		2.9(1.0)	14.9	18.0	26.8
5	401.397(2)	401.347	400.507	70(10)	121	145/148	3.5(1.0)	4.7	6.3	9.0
6	402.378(14)	402.320	401.439	128(48)	132		1.0(0.4)	5.1	6.4	8.4

[a] The number in brackets is the numerical uncertainty on the last digit, i.e., 399.840(2) eV means 399.840 $\pm$ 0.002 eV obtained from a Voigt profile deconvolution of the experimental line shape (peak energy position and width). The overall energy uncertainly must also include the 60 meV energy calibration contribution (see text). [b] This is the Lorentzian width obtained from a Voigt profile deconvolution of the experimental line shape. [c] Obtained from a numerical integration of the measured line profile. [d] Obtained assuming 0.748 ^{3}P + 0.194 ^{1}D + 0.016 ^{1}S + 0.041 ^{5}S initial states contributions (see text). The numbers in this column are comparable with the theoretical RMPS and MCDF strengths. [e] Total strength of 83.2 Mb eV. [f] Total strength of 88.41 Mb eV. [g] Total strength of 118.6 Mb eV.

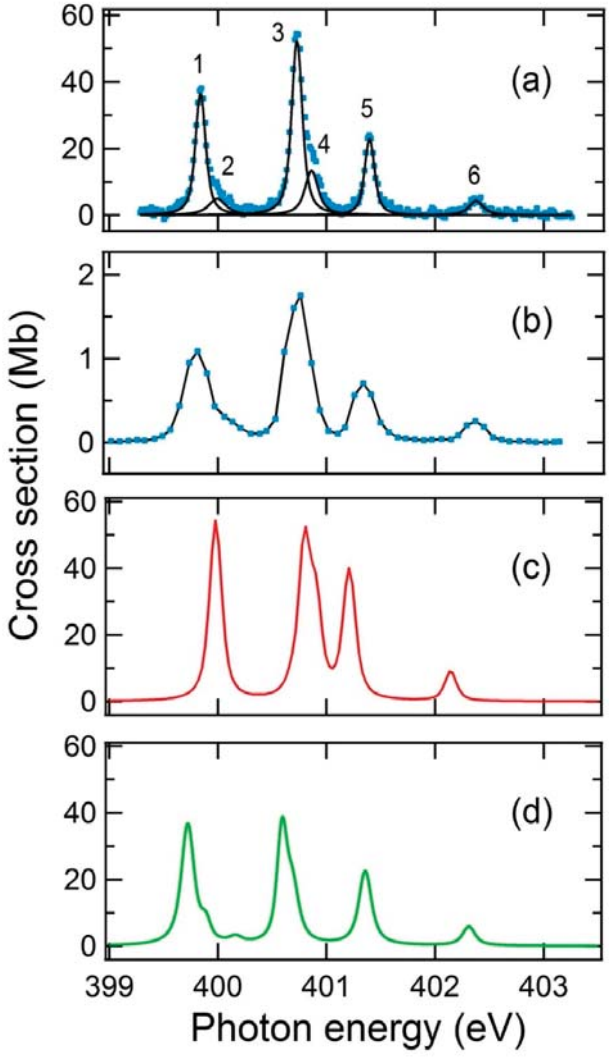

Figure 4. Photoionization cross-sections of the N^+ atomic ion in the photon energy region of the $1s \longrightarrow 2p$ excitations. (**a**) Measured in the single ionisation channel (65 meV energy band pass). (**b**) Measured in the double ionisation channel (225 meV band pass). (**c**) Multiconfiguration Dirac-Fock (MCDF) simulation of the total photoabsorption cross-sections. The theoretical energy values are shifted by +0.7 eV in the figure. (**d**) R-matrix with pseudo-states theoretical (RMPS) simulation of the total photoionization cross-sections.

Figure 4a shows a remaining (deconvolved) resonance 2 at 399.994 eV in the high-energy shoulder of the $^3P \longrightarrow {}^3D$ peak. Figure 3 shows the MCDF and RMPS predictions for transitions arising from the excited states $1s^2 2s^2 2p^2\, {}^1S$ and $1s^2 2s 2p^3\, {}^5S$ and differences exist here between the two theoretical approaches. MCDF suggests resonance 2 to be the $1s^2 2s^2 2p^2\, {}^1S \longrightarrow 1s 2s^2 2p^3\, {}^1P$ transition. RMPS suggests instead that this is a contribution from the $1s^2 2s 2p^3\, {}^5S \longrightarrow 1s 2s 2p^4\, {}^5P$ transition, theoretically predicted at 399.89 eV and closely matching the experimental resonance at 399.98 eV. Taking into account the generally very good agreement between the RMPS predicted energies and experimental values, we

assign resonance 2 to the $^5S \longrightarrow {}^5P$ transition. We note further corroborating evidence for this assignment when the next member of the Rydberg series, for which resonance 2 in Table 2 is the first member, is unequivocally identified (the next member in question is resonance 1 in Table 5 of Section 4 below).

To provide a fuller comparison with experiment the ab initio MCDF and RMPS results of Figure 3 were convolved with Gaussian profiles of 65 meV FWHM to simulate the experimental broadening. The theoretical cross-section values, corresponding to the ground and excited state initial configurations, were weighted by numerical factors representing the relative populations of the initial states. The results are shown in Figure 4c,d. It is clear that the dominant initial configuration is the ground state ^3P, with smaller contributions from the ^1D and ^5S states. The ratios of the measured to the calculated cross-section values can provide an estimate of the initial state fractions. The sum of the integrated experimental intensities (single-ionisation channel only) of the resonances originating in the ^3P state is 6.0 + 9.1 + 3.7 = 18.8 MbeV, while for the RMPS predictions it is 10.1 + 6.8 + 6.3 = 23.2 MbeV, providing a ratio of 0.81 (Table 2). For the ^1D resonances, the numbers are 3.90 MbeV and 24.4 MbeV, respectively, with a ratio of 0.16, while for the ^5S ones the ratio would be $1.4/16.2 \approx 0.09$. We note that these relative population values are quite close to those obtained for a Maxwell-Boltzmann equilibrium at a temperature of ~2.5 eV, for which the weighting factors would be 0.75 ^3P, 0.19 ^1D, 0.016 ^1S and 0.04 ^5S. This agreement may be somewhat fortuitous as it it realised that temperature may not be a meaningful physical concept in this case. However, such factors can be appropriately used to model theoretical cross-sections against experimental ones. Furthermore, the error bars on the experimental/theoretical cross-section ratios are large and include the relative error on the experimental integrated intensities of at least 10% (Table 2) and the contributions to the total cross-section due to the double-ionization channel. Figure 2 shows that the double ionization channel does contribute markedly in the 400 eV region with an estimated contribution of about 5%.

In Figure 4, we scale the theoretical cross-sections by factors of 0.75 ^3P, 0.19 ^1D, 0.016 ^1S and 0.04 ^5S to allow direct comparison with the experiment. The summed results are displayed in Figure 4c,d. From Figure 4, we conclude that the above analyses lead to an overall satisfactory agreement between the MCDF and RMPS theories and experiment in respect of the resonance strengths and energy positions. The RMPS results in Figure 4d reproduce well the experimental observations of Figure 4a in terms of resonance positions and relative intensities, whereas the MCDF peak absolute cross sections seem in better agreement with the experimental values. The very weak feature at 400.16 eV in the RMPS modelled spectrum is associated with the $^1S \longrightarrow {}^1P$ transition (labelled x in Tables 2 and 3). The noise present in the measured data in this region together with an estimated very low scaling factor for ^1S prevent definite confirmation.

Table 3. Resonance Assignments near 400 eV photon energy.

Resonance #Label [1]	Transition
1	$1s^2 2s^2 2p^2\,{}^3P \longrightarrow 1s2s^2 2p^3\,{}^3D$
2	$1s^2 2s 2p^3\,{}^5S \longrightarrow 1s2s2p^4\,{}^5P$
x	$1s^2 2s^2 2p^2\,{}^1S \longrightarrow 1s2s^2 2p^3\,{}^1P$
3	$1s^2 2s^2 2p^2\,{}^3P \longrightarrow 1s2s^2 2p^3\,{}^3S$
4	$1s^2 2s^2 2p^2\,{}^1D \longrightarrow 1s2s^2 2p^3\,{}^1D$
5	$1s^2 2s^2 2p^2\,{}^3P \longrightarrow 1s2s^2 2p^3\,{}^3P$
6	$1s^2 2s^2 2p^2\,{}^1D \longrightarrow 1s2s^2 2p^3\,{}^1P$

[1] Same as Figure 4 and Table 2.

All the results from the RMPS and MCDF calculations in terms of energies (eV) and line strengths (Mb eV) are presented in Table 2 and compared with the experimental measurements. Table 2 also includes the measured line widths (meV) obtained from a Voigt profile numerical deconvolution of the experimental resonance shapes. This allows removal of the 65 meV FWHM Gaussian instrumental broadening from the measured total

line width with the remaining Lorentzian FWHM representing mostly the Auger width of the final state of the resonance. The RMPS resonance widths (see Section 3) either match quite well ($^3S, ^1D, ^1P$) or differ by no more than a factor of about two ($^3D, ^5P, ^3P$) from the measured widths, taking into account the relative uncertainties from ~15% up to ~40%.

Inter-comparing the integrated intensities (resonance strengths) of the resonances originating from the same initial *LS* term allows a relative comparison with theory independent of the initial population fractions. The $^3P \longrightarrow {}^3D$, $^3P \longrightarrow {}^3S$ and $^3P \longrightarrow {}^3P$ intensities are observed in the ratios of 1/1.5/0.6. This is to be compared to the ratio of 1/0.7/0.6 predicted by both the RMPS and MCDF theories. Agreement between experiment and the RMPS and MCDF theories is, thus, reasonably close, although for both theories this is less satisfactory for the $^3S_1$ state. Hasoğlu et al. [32] discussed how peculiar spin-orbit mixing effects with $^3P_1$ affect the Auger and radiative rates of the $^3S_1$ state along the $1s2s^22p^3$ isoelectronic sequence. However, the authors show these effects peak around $Z = 17$ nuclear charge and play only a small part in the present case of $Z = 7$ nuclear charge. For the resonances originating in the $1s^22s^22p^2\,{}^1D_2$ excited state, the 1/0.36 ($^1D \longrightarrow {}^1D/{}^1D \longrightarrow {}^1P$) experimental ratio is well reproduced by both the MCDF and RMPS theories. The total integrated experimental intensities of the six identified resonances, assuming the aforementioned initial state fractions, amounts to (83 ± 12) Mb eV, which is equivalent to a discrete oscillator strength of 0.76 ± 0.15 [41]. These figures compare very favourably with the theoretical RMPS values of 88.4 MbeV and 0.80, respectively, while the MCDF values of 118.6 MbeV and 1.1 are somewhat overestimated.

We have already mentioned the sizeable contribution (~5%) to the total cross section of decay processes leading to double ionisation of the final product (N^{3+}). We see from Figure 3b that in the 400 eV region of $1s \longrightarrow 2p$ excitations, the resonances structure for the doubly-ionisation spectrum is almost exactly coincident in energy and relative intensity with that in the single ionisation channel. This suggests the double-Auger process for the double-ionisation channel, whereby the $1s2s^22p^3$ inner-shell excited configuration non-radiatively decays to the final $1s^22s^2$ configuration of N^{3+} (Auger cascade is not possible here) with a $2p$ electron filling the initial $1s$ hole and the other two highly correlated $2p$ electrons being simultaneously ejected.

The N^{3+} ion yield data of Bari et al. [11] in the 400 eV region are in reasonable agreement with the present data of Figure 4b for both the main resonances energies and relative intensities. However, resonance assignments suggested by Bari et al. [11], based on their own GAMESS configuration interaction (CI) calculations and the previous work of Garabeih et al. [8], differ to some extent from those provided by the detailed analyses of the present work. The more complete comparisons shown between the present absolute measurements (see Section 2) and the results of extended atomic structure calculations from two theoretical approaches lead us to believe that the revised analyses of the present work are conclusive.

4.2. $1s \rightarrow np$ ($n \geq 3$) Resonances

Excitation of a $1s$ electron into np ($n \geq 3$) subshells from a ^3P ground state N^+ ion, leads to the two main series: $1s^22s^22p^{2\,3}P \longrightarrow \left(1s2s^22p^{2\,4}P\right)np_{1/2,3/2}\,{}^3S$, ^3P, ^3D and $1s^22s^22p^{2\,3}P \longrightarrow \left(1s2s^22p^{2\,2}P\right)np_{1/2,3/2}\,{}^3S$, ^3P,^3D converging to the $1s2s^2\left(2p^{2\,3}P\right)\,{}^4P$ and $1s2s^2\left(2p^{2\,3}P\right)\,{}^2P$ inner-shell limits, respectively. Additionally, if $1s$ excitations from the $^1D, ^1S$ and ^5S excited states have contributions, then we obtain several additional series converging on the $1s2s^2\left(2p^{2\,1}D\right)\,{}^2D$, $1s2s^2\left(2p^{2\,1}S\right)\,{}^2S$ and $1s2s\left(2p^{3\,4}S\right)\,{}^6S$ limits, respectively. The contributions of the latter two to the measured total cross-sections are necessarily reduced compared to the ground state contributions as a result of the increasingly lower high n resonance strength coupled to the smaller fractional population factors established in the previous section. The RMPS and MCDF calculated series limits are shown in Table 4. No limits are calculated for the atomic states based on the $1s2s2p^3$ configuration.

Table 4. RMPS, MCDF and experimental (see text) N^{3+} series limits (eV).

Main 1*s* Limits in N^{3+}	RMPS	MCDF	EXPT
$1s2s^2(2p^{2\,3}P)\,^4P$	431.06	431.8	431.49
$1s2s^2(2p^{2\,3}P)\,^2P$	436.23	435.49	436.32
$1s2s^2(2p^{2\,1}D)\,^2D$	435.57	435.51	[1]
$1s2s^2(2p^{2\,1}S)\,^2S$	438.20	439.20	[1]

[1] No measurements.

In Figure 5, we show the ab initio MCDF and RMPS theoretical predictions for the higher energy range of 415–440 eV. These, together with those of Tables 4 and 5, are used as the basis for the analyses of the experimental data presented in Figure 6. In Figure 6a, the absolute cross-sectional data for the single ionisation channel are shown. This channel contains no marked resonance contributions above noise at photon energies greater than ~427/8 eV. Resonance structure above this energy and up to ~436 eV is seen in the double ionisation, shown in Figure 6b, channel only, whereas this channel also contains resonance structures whose energies match those of the single ionisation channel in the region ~418–426 eV. The details of the resonance strengths and energy positions are given in Table 5.

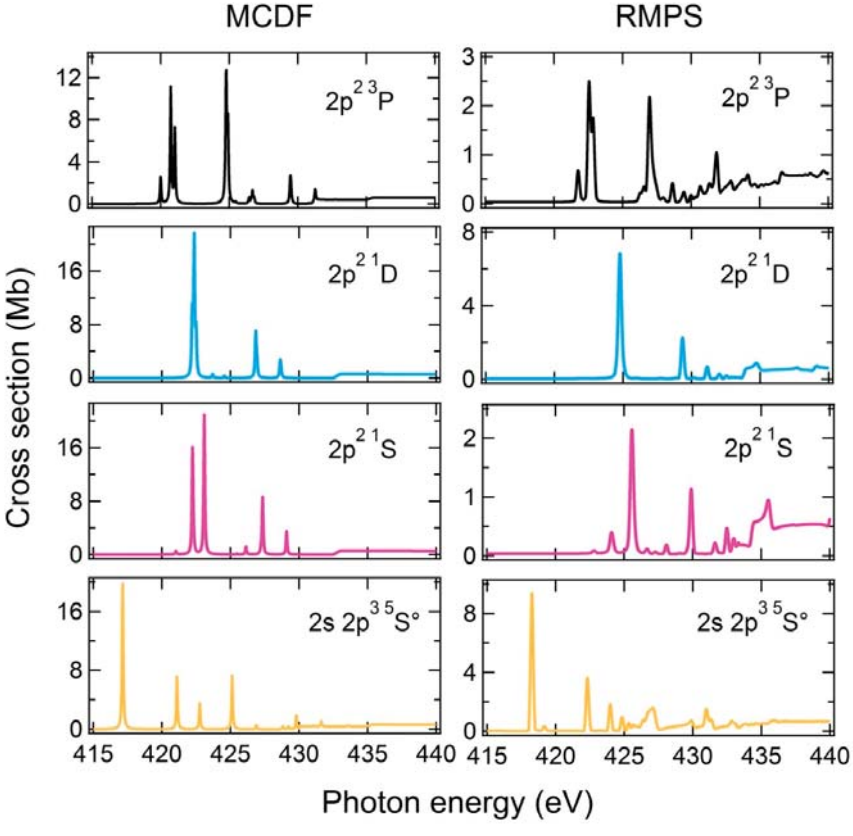

Figure 5. Multiconfiguration Dirac-Fock (MCDF) and R-Matrix with pseudo-states (RMPS) theoretical calculations of the $1s \longrightarrow np, n \geq 3$ photoexcitation and $2p$ photoionization cross sections from the ^3P,^1D,^1S and ^5S states of the $1s^2 2s^2 p^2$ ground and $1s^2 2s 2p^3$ excited configurations of N^+, respectively.

Table 5. Experimentally determined energy and strength of the main $1s \longrightarrow np, n \geq 3$ resonances (415–440 eV photon energy) in the N^+ photoionization cross-section spectrum, estimated from the absolute measurements of single-ionisation and double-ionization yields and comparison with theoretical energy values.

Resonance #Label See Figure 5c	Single Ionization (SI) Channel Energy [a] (eV)	SI Channel Resonance Strength [b] (MbeV)	Double Ionization (DI) Channel Energy [a] (eV)	DI Channel Resonance Strength [b] (MbeV)	RMPS Photon Energy (eV)	MCDF Photon Energy [c] (eV)	Assignment
1	418.53(3)	0.16	418.53(3)	0.03(1)	418.26	419.14	$1s^2 2s 2p^3\,^5S \longrightarrow 1s 2s 2p^3 3p\,^5P$
2	421.74(3)	0.3(1)	421.76(4)	0.03	421.97	421.96	$1s^2 2s^2 2p^2\,^3P \longrightarrow \left[1s2s^2\left(2p^2\,^3P\right)^4P\right]3p\,^3S$
3 [d]	422.25(13)						
4	422.61(2)	1.3(6)	422.66(3)	0.4(1)	422.55	422.66	$1s^2 2s^2 2p^2\,^3P \longrightarrow \left[1s2s^2\left(2p^2\,^3P\right)^4P\right]3p\,^3D$
5	422.96(7)	0.5(4)	422.97(1)	0.22(6)	422.84	422.95	$1s^2 2s^2 2p^2\,^3P \longrightarrow \left[1s2s^2\left(2p^2\,^3P\right)^4P\right]3p\,^3P$
6 [d]	424.13		424.13				
7	424.55	0.6(2)	424.55	0.37(3)	424.78	424.30	$1s^2 2s^2 2p^2\,^1D \longrightarrow \left[1s2s^2\left(2p^2\,^1D\right)^2D\right]3p\,^1L$
8			425.99				$1s^2 2s^2 2p^2\,^3P \longrightarrow \left[1s2s^2 2p^2\right]3p\,^3L$
9 [d]	426.6		426.60				
10	426.88(1)	1.6(3)			426.97	426.66	$1s^2 2s^2 2p^2\,^3P \longrightarrow \left[1s2s^2\left(2p^2\,^3P\right)^4P\right]4p$
10			426.92(1)	0.76(3)		426.78	$1s^2 2s^2 2p^2\,^3P \longrightarrow \left[1s2s^2\left(2p^2\,^3P\right)^2P\right]3p$
11			428.74(3)	0.15	428.63	428.615	$1s^2 2s^2 2p^2\,^3P \longrightarrow \left[1s2s^2\left(2p^2\,^3P\right)^4P\right]5p$
12			429.07(6)	0.12	429.18	428.80	$1s^2 2s^2 2p^2\,^1D \longrightarrow \left[1s2s^2\left(2p^2\,^1D\right)^2D\right]4p$
13			429.61(2)	0.2	429.34	429.46	$1s^2 2s^2 2p^2\,^3P \longrightarrow \left[1s2s^2\left(2p^2\,^3P\right)^4P\right]6p$
14			430.20(2)	0.1			$1s^2 2s^2 2p^2\,^3P \longrightarrow \left[1s2s^2\left(2p^2\,^3P\right)^4P\right]7p$ [e]
15			430.81(5)	0.25	431.13	430.57	$1s^2 2s^2 2p^2\,^1D \longrightarrow \left[1s2s^2\left(2p^2\,^1D\right)^2D\right]5p$
16 [d]			431.56(7)	0.55			
17			431.72(1)	0.45	[f]	431.40	$1s^2 2s^2 2p^2\,^3P \longrightarrow \left[1s2s^2\left(2p^2\,^3P\right)^2P\right]4p$
18 [d]			433.19				
19			433.58(1)	0.26	[f]	433.18	$1s^2 2s^2 2p^2\,^3P \longrightarrow \left[1s2s^2\left(2p^2\,^3P\right)^2P\right]5p$
20			434.41	0.1	[f]	434.09	$1s^2 2s^2 2p^2\,^3P \longrightarrow \left[1s2s^2\left(2p^2\,^3P\right)^2P\right]6p$
21			434.93	0.11			$1s^2 2s^2 2p^2\,^3P \longrightarrow \left[1s2s^2\left(2p^2\,^3P\right)^2P\right]7p$ [e]
22			435.32				$1s^2 2s^2 2p^2\,^3P \longrightarrow \left[1s2s^2\left(2p^2\,^3P\right)^2P\right]8p$ [e]
23 [d]			435.63				
24 [d]			435.95				

[a] Peak energy value obtained from a Voigt profile deconvolution of the experimental line shape. The number in brackets is the numerical uncertainty on the last digit. The overall energy uncertainly must also include the 60 meV energy calibration contribution (see text). [b] Obtained from a numerical integration of the measured line profile. The number in brackets is the numerical uncertainty on the last digit. This is at least 50% if no uncertainty value is quoted in brackets. No entry means that the error is too large for a strength value to be reliably quoted. [c] These energy values are shifted by +2.0 eV. [d] See text. [e] Assignment is based solely on Rydberg analysis of experimental energies. No theoretical RMPS or MCDF data are available. [f] RMPS energy not available.

These data are obtained from Voigt profile numerical fitting of the experimental resonance data profiles including a 250 meV FWHM Gaussian to simulate the energy band pass. Above 428 eV, for reasons of computational stability, Gaussian profiles only were used to extract resonance parameters. The resonances labelled #3, 6, 9, 16, 18, 23, 24 in Table 5 correspond to very low intensity features that are not readily identifiable as peaked atomic resonances, see Figure 6a,b. They arise during the experimental line fitting procedure and are the result of simulating either slightly asymmetric profiles or very weak spectral features and do not affect the general analyses of the data. As remarked earlier, the open

shell nature of N^+ means that the spectral density of resonances in this energy range is very high.

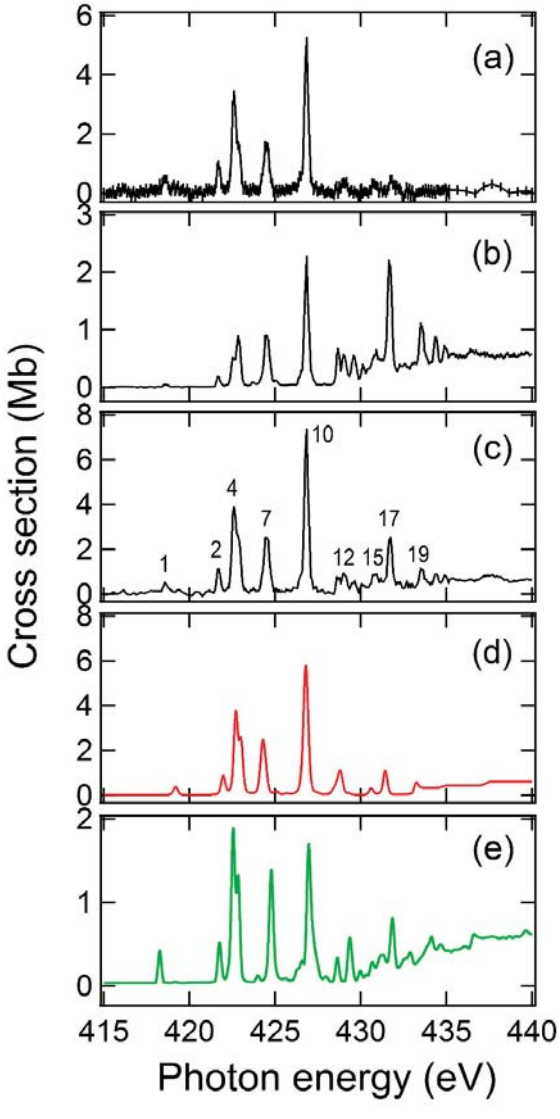

Figure 6. Photoionization cross-sections of the N^+ atomic ion in the photon energy region of the K-shell threshold ($1s \longrightarrow np, n \geq 3$ excitations). (**a**) Absolute measurements in the single-ionisation channel (280 meV band pass). (**b**) Relative measurements in the double-ionisation channel normalised on the data of Figure 5a (250 meV band pass). (**c**) Summation of (**a**,**b**) with added resonance number labels used in the text of the paper. (**d**) Total photoionization cross-section simulation based on multiconfiguration Dirac-Fock calculations (MCDF). The theoretical energies are shifted by +2.0 eV in the figure. (**e**) Total photoionization cross-section simulation based on R-matrix with pseudo-states theoretical (RMPS) calculations.

Both the RMPS and MCDF calculations confirm that the 418.58 eV resonance can only originate from the $^5S_2$ excited state connecting to several $1s2s2p^33p$ final states with

dominant ^5P character (this notation is adopted in Table 4). This assignment was used in Section 4.1 above to establish the assignment of the low-energy resonance (labelled 2 in Tables 2 and 3) in the 400 eV photon region.

The strong resonances at 421.74 eV, 422.61 eV and 422.96 eV are identified as the ^3S, ^3D and ^3P LS components of the $\left[1s2s^2\left(2p^2\,^3P\right)^4P\right]3p$ member of the low energy $\left(2p^2\,^3P\right)^4P\,np$ Rydberg series, respectively. The corresponding single-valued theoretical energies for these and the higher Rydberg states shown in Table 4 are actually the result of the strength-averaged contributions of many mixed LSJ states with $J = 1$ or 2 with almost overlapping energies. As the value of n increases, the energy differences between the (increasingly hydrogenic) LSJ states are almost indistinguishable, allowing Rydberg series analysis based on quantum defect values. The relatively strong resonance (#10) is the contribution of two components at 426.88 eV and 426.91 eV, in the single and double ionisation channels respectively, with about 8 Mb total peak intensity, see Figure 6a–c. Comparison with MCDF theoretical results shows that peak #10 is the blended contribution of the $\left[1s2s^2\left(2p^2\,^3P\right)^4P\right]4p$ and $\left[1s2s^2\left(2p^2\,^3P\right)^2P\right]3p$ resonances. Non-linear least-square fitting of the measured photon energies E_n (eV) of the resonances numbered 10 (426.88 eV), 11, 13 and 14 to the $E_n = I_p - 54.42/(n-\delta)^2$ Rydberg formula where δ is the quantum defect and I_p the ionisation energy (eV) returns best-fit values of $I_p = (431.49 \pm 0.03)$ eV and δ = 0.56 ± 0.02. This value of I_p is in good agreement with the RMPS and MCDF calculations and the δ value is typical for a p electron orbit. These values allow the identification of the $\left[1s2s^2\left(2p^2\,^3P\right)^4P\right]np$ resonances up to $n = 7$. The agreement with the RMPS and MCDF calculated energies is noted. A similar approach for the resonances labelled 10 (426.91 eV), 17, 19, 20, 21 and 22 yields best-fit values of $I_p = (436.32 \pm 0.03)$ eV and δ = 0.59 ± 0.01. This is in good agreement with the RMPS calculations (Tables 4 and 5) and allows the identification of the $\left[1s2s^2\left(2p^2\,^3P\right)^2P\right]np$ series up to $n = 8$. Above 431.4 eV photon energy the most likely process is direct $1s$ ionisation to $1s2s^22p^2$ states followed by KLL Auger decay in N^{2+} leading to a continuous ion signal in the double-ionisation channel only, as observed in Figure 5b. As discussed in Section 3.1, other double-ionisation processes are conceivable for excited $1s2s^22p^2np$, $n \geq 3$ configurations consisting of cascade or double-Auger participator and spectator decays. These processes are energetically possible below the 431.4 eV K-edge and explain satisfactorily the observations of Figure 6b. Single-electron autoionization decay of the $\left[1s2s^2\left(2p^2\,^3P\right)^4P\right]3p$ and $\left[1s2s^2\left(2p^2\,^3P\right)^4P\right]4p$ configurations are the main contributions to the single-ionisation channel as observed in Figure 6a.

Resonance #7 at 424.55 eV corresponds to transitions to $\left[1s2s^2\left(2p^2\,^1D\right)^2D\right]3p\,^1L$ states originating in the $1s^22s^22p^2\,^1D_2$ metastable state with roughly equal contributions in the single and double-ionisation channels. The resonances labelled 12 and 15 measured at 429.07 eV and 430.81 eV may tentatively be assigned to the $4p$ and $5p$ members of this series, respectively. Other contributions from excited states are extremely weak and unambiguous assignments are not possible.

To allow direct comparison with the theoretical data, the single and double ionisation experimental signals are added and the result shown in Figure 6c. In Figure 6d,e, the theoretical data of Figure 5 are adjusted in the manner used and discussed in Section 4.1, i.e., $0.75\,^3P$, $0.19\,^1D$, $0.016\,^1S$ and $0.04\,^5S$ initial state weight coefficients are applied following 225 meV FWHM Gaussian convolution. The MCDF theory shows a very satisfactory agreement with the measured cross-section profile in terms of relative energy positions and absolute intensities for the high energy resonances, although the absolute resonance energies are systematically too low by about 2 eV. Conversely, the RMPS theory predicts quite accurately the measured resonance energies while the peak intensities are typically too small by a factor of 2–3.

Only a qualitative comparison of the N^{3+} ion yield data by Bari et al. [11] (their Figure 3b) is feasible. It indicates a reasonable agreement between the resonance energies and intensity patterns observed in the two works.

5. Conclusions

Enhanced experimental conditions at the MAIA crossed beam facility at SOLEIL allowed substantially improved single- and double-ionisation cross section measurements to be carried out for the N^+ ion in the K-shell excitation regime. In addition to the strong resonances in the 398–405 eV range corresponding to $1s \longrightarrow 2p$ excitations, several well-developed Rydberg resonance series corresponding to $1s \longrightarrow np$, $n \geq 3$ excitations were observed at higher photon energies running to K-shell ionization limits above 430 eV. With three open shells the calculation of such resonance series presents a considerable challenge to theory. Furthermore, contributions due to metastable states had also to be taken into account. Comparison of the measured results with theoretical photoionization cross-section calculations from large-scale MCDF and RMPS photoionization cross section calculations allowed interpretation of the experimental data and benchmarking of the different theoretical approaches. The present theoretical work may be incorporated into astrophysical modelling codes like CLOUDY [42,43], XSTAR [44] and AtomDB [45] used to numerically simulate the thermal and ionization structure of ionized astrophysical nebulae

Author Contributions: J.-P.M., E.T.K., J.-M.B., D.C. and S.G., were involved in the experiments and data taking. The theoretical aspects of the work were contributed by C.B. and B.M.M. The graphs and figures were prepared by J.-M.B. and D.C. All the authors contributed to the analyses presented in the work. J.-P.M., E.T.K., B.M.M. and J.-M.B. prepared the original draft. All the authors reviewed and edited the subsequent versions of the draft. All authors have read and agreed to the published version of the manuscript.

Funding: This research received no external funding.

Acknowledgments: J.-P.M. and E.T.K. wish to thank SOLEIL and the EC for financial assistance with travel, accommodation and subsistence costs. The authors would like to thank the SOLEIL and PLEIADES beam line staff, J. Bozek, C. Nicolas, A. Miloslajevic for their assistance throughout the experiment. This work has benefited from the LabEX PALM's investments (ANR-10-LABX-0039-PALM). B.M.M. acknowledges financial support from the CNRS LabEX PALM programme. The University of Georgia at Athens is thanked for the award of an adjunct professorship, and Queen's University Belfast for the award of a visiting research fellowship. The authors acknowledge this research used grants of computing time at the National Energy Research Scientific Computing Centre (NERSC), which is supported by the Office of Science of the U.S. Department of Energy (DOE) under Contract No. DE-AC02-05CH11231. The authors gratefully acknowledge the Gauss Centre for Supercomputing e.V. (www.gauss-centre.eu) for funding this project by providing computing time on the GCS Supercomputer hazel hen at Höchstleis-tungsrechenzentrum Stuttgart (www.hlrs.de). Itamp is supported in part by NSF Grant No. PHY-1607396.

Conflicts of Interest: The authors declare no conflict of interest.

References

1. Hasoglu, M.F.; Abdel-Naby, S.H.A.; Gorczyca, T.; Drake, J.J.; McLaughlin, B.M. K-shell photoabsorption studies of the carbon isonuclear sequence. *Astrophys. J.* **2010**, *724*, 1296–1304. [CrossRef]
2. McLaughlin, B.M.; Bizau, J.-M.; Cubaynes, D.; Al Shorman, M.M.; Guilbaud, S.; Sahko, I.; Blancard, C.; Gharaibeh, M.F. K-shell photoionization of B-like oxygen (O^{3+}) ions: Experiment and theory. *J. Phys. B At. Mol. Opt. Phys.* **2014**, *47*, 115201. [CrossRef]
3. Bizau, J.-M.; Cubaynes, D.; Guilbaud, S.; Al Shorman, M.M.; Gharaibeh, M.F.; Ababneh, I.Q.; Blancard, C.; McLaughlin, B.M. *K*-shell photoionization of O^+ and O^{2+} ions: Experiment and theory. *Phys. Rev. A* **2015**, *92*, 023401. [CrossRef]
4. McLaughlin, B.M.; Bizau, J.-M.; Cubaynes, D.; Guilbaud, S.; Douix, S.; Al Shorman, M.M.; El Ghazaly, M.O.A.; Sakho, I.; Gharaibeh, M.F. K-shell photoionization of O^{4+} and O^{5+} ions: Experiment and theory. *Mon. Not. R. Astron. Soc.* **2017**, *465*, 4690–4702. [CrossRef]
5. Mathur, S.; Nicastro, F.; Gupta, A.; Krongold, Y.; McLaughlin, B.M.; Brickhouse, N.; Pradhan, A. The O vi Mystery: Mismatch between X-Ray and UV Column Densities. *Astrophys. J.* **2017**, *851*, L7. [CrossRef]

6. Leutenegger, M.A.; Kűhn, S.; Micke, P.; Steinbrűgge, R.; Stierhof, J.; Shah, C.; Hell, N.; Bissinger, M.; Hirsch, M.; Ballhasuen, R.; et al. High-Precision Determination of Oxygen Kα Transition Energy Excludes Incongruent Motion of Interstellar Oxygen. *Phys. Rev. Lett.* **2020**, *125*, 243001. [CrossRef] [PubMed]
7. Stolte, W.C.; Jonauskas, V.; Lindle, D.W.; Sant'Anna, M.M.; Savin, D.W. Inner-shell photoionization studies of neutral atomic nitrogen. *Astrophys. J.* **2016**, *818*, 149. [CrossRef]
8. Gharaibeh, M.F.; Bizau, J.M.; Cubaynes, D.; Guilbaud, S.; El Hassan, N.; Al Shorman, M.M.; Miron, C.; Nicolas, C.; Robert, E.; Blancard, C.; et al. K-shell photoionization of singly ionized atomic nitrogen: Experiment and theory. *J. Phys. B At. Mol. Opt. Phys.* **2011**, *44*, 175208. [CrossRef]
9. Gharaibeh, M.F.; Hassan, N.E.; Al Shorman, M.M.; Bizau, J.-M.; Cubaynes, D.; Guilbaud, S.; Sakho, I.; Blancard, C.; McLaughlin, B.M. K-shell photoionization of B-like atomic nitrogen ions: Experiment and theory. *J. Phys. B At. Mol. Opt. Phys.* **2014**, *47*, 065201. [CrossRef]
10. Al Shorman, M.M.; Gharaibeh, M.F.; Bizau, J.M.; Cubaynes, D.; Guilbaud, S.; El Hassan, N.; Miron, C.; Nicolas, C.; Robert, E.; Sakho, I.; et al. K-shell photoionization of Be-like and Li-like ions of atomic nitrogen: Experiment and theory. *J. Phys. B At. Mol. Opt. Phys.* **2013**, *46*, 195701. [CrossRef]
11. Bari, S.; Inhester, L.; Schubert, K.; Mertens, K.; Schunck, J.O.; Dörner, S.; Deinert, S.; Schwob, L.; Schippers, S.; Müller, A.; et al. Inner-shell X-ray absorption spectra of the cationic series NHy+ (*y* = 0–3). *Phys. Chem. Chem. Phys.* **2019**, *21*, 16505–16514. [CrossRef]
12. Schmidt, M.W.; Baldridge, K.K.; Boatz, J.A.; Elbert, S.T.; Gordon, M.S.; Jensen, J.H.; Koseki, S.; Matsunaga, N.; Nguyen, K.A.; Su, S.; et al. General atomic and molecular electronic structure system. *J. Comput. Chem.* **1993**, *14*, 1347–1363. [CrossRef]
13. Liang, L.; Zhou, C. K-shell photoionization of Be-like nitrogen from the ground state: Energies and Auger widths of the high-lying double-excited states for N IV. *Can. J. Phys.* **2018**, *96*, 1183–1191. [CrossRef]
14. Peng, Y.-G.; Wu, Y.; Zhu, L.-F.; Zhang, S.B.; Wang, J.-G.; Liebermann, H.-P.; Buenker, R.J. Complex multireference configuration interaction calculations for the K-vacancy Auger states of N^{q+} (q = 2-5) ions. *J. Chem. Phys.* **2016**, *144*, 054306. [CrossRef]
15. Bizau, J.M.; Cubaynes, D.; Guilbaud, S.; El Hassan, N.; Al Shorman, M.M.; Bouisset, E.; Guigand, J.; Moustier, O.; Marié, A.; Nadal, E.; et al. A merged-beam setup at SOLEIL dedicated to photoelectron–photoion coincidence studies on ionic species. *J. Electron Spectrosc. Relat. Phenom.* **2016**, *210*, 5–12. [CrossRef]
16. Blancard, C.; Cubaynes, D.; Guilbaud, S.; Bizau, J.-M. Absolute Photoionization Cross Section for Fe^{6+} to Fe^{10+} Ions in the Photon Energy Region of the 2p-3d Resonance Lines. *Astrophys. J.* **2018**, *853*, 32. [CrossRef]
17. Khalal, M.A.; Lablanquie, P.; Andric, L.; Palaudoux, J.; Penent, F.; Bučar, K.; Žitnik, M.; Püttner, R.; Jänkälä, K.; Cubaynes, D.; et al. 4d-inner-shell ionization of Xe+ ions and subsequent Auger decay. *Phys. Rev. A* **2017**, *96*, 013412. [CrossRef]
18. Bizau, J.-M.; Cubaynes, D.; Guilbaud, S.; Penent, F.; Lablanquie, P.; Andric, L.; Palaudoux, J.; Al Shorman, M.M.; Blancard, C. Photoelectron Spectroscopy of Ions: Study of the Auger Decay of the 4d -> nf (n=4,5) Resonances in Xe^{5+} Ion. *Phys. Rev. Lett.* **2016**, *116*, 103001. [CrossRef] [PubMed]
19. Mosnier, J.-P.; Kennedy, E.T.; van Kampen, P.; Cubaynes, D.; Guilbaud, S.; Sisourat, N.; Puglisi, A.; Carniato, S.; Bizau, J.-M. Inner-shell photoexcitations as probes of the molecular ions CH+, OH+, and SiH+: Measurements and theory. *Phys. Rev. A* **2016**, *93*, 061401. [CrossRef]
20. Puglisi, A.; Miteva, T.; Kennedy, E.T.; Mosnier, J.-P.; Bizau, J.-M.; Cubaynes, D.; Sisourat, N.; Carniato, S. X-ray photochemistry of carbon hydride molecular ions. *Phys. Chem. Chem. Phys.* **2018**, *20*, 4415–4421. [CrossRef] [PubMed]
21. Carniato, S.; Bizau, J.-M.; Cubaynes, D.; Kennedy, E.T.; Guilbaud, S.; Sokell, E.; McLaughlin, B.M.; Mosnier, J.-P. Vibrationally and Spin-Orbit-Resolved Inner-Shell X-ray Absorption Spectroscopy of the NH+ Molecular Ion: Measurements and ab Initio Calculations. *Atoms* **2020**, *8*, 67. [CrossRef]
22. Sodhi Rana, N.S.; Brion, C.E. Reference energies for inner shell electron energy-loss spectroscopy. *J. Elec. Spec. Rel. Phenom.* **1984**, *34*, 363–372. [CrossRef]
23. Kato, M.; Morishita, Y.; Oura, M.; Yamaoka, H.; Tamenori, Y.; Okada, K.; Matsudo, T.; Gejo, T.; Suzuki, I.H.; Saito, N. Absolute photoionization cross sections with ultra-high energy resolution for Ar, Kr, Xe and N2 in inner-shell ionization regions. *J. Elec. Spec. Rel. Phenom.* **2007**, *34*, 39–48. [CrossRef]
24. Mosnier, J.-P.; Sayyad, M.H.; Kennedy, E.T.; Bizau, J.-M.; Cubaynes, D.; Wuilleumier, F.J.; Champeaux, J.-P.; Blancard, C.; Varma, R.H.; Banerjee, T.; et al. Absolute photoionization cross sections and resonance structure of doubly ionized silicon in the region of the $2p^{-1}$ threshold: Experiment and theory. *Phys. Rev. A* **2003**, *68*, 052712. [CrossRef]
25. Cooper, J.W. New directions in the study of atomic autoionizing states. *J. Elec. Spec. Rel. Phenom.* **1994**, *67*, 223–231. [CrossRef]
26. Kramida, A.; Ralchenko, Y.; Reader, J.; NIST ASD Team. NIST Atomic Spectra Database (ver. 5.8). 2020. Available online: https://physics.nist.gov/asd (accessed on 18 February 2021).
27. Tachiev, G.; Froese Fisher, C. Breit-Pauli energy levels for the carbonlike sequence. *Can. J. Phys.* **2001**, *79*, 955–976. [CrossRef]
28. Martins, M. Photoionization of open-shell atoms: The chlorine 2p excitation. *J. Phys. B At. Mol. Opt. Phys.* **2001**, *34*, 1321–1355. [CrossRef]
29. Bruneau, J. Correlation and relaxation effects in ns^2-nsnp transitions. *J. Phys. B At. Mol. Opt. Phys.* **1984**, *17*, 3009–3028. [CrossRef]
30. Grant, I.P. Gauge invariance and relativistic radiative transitions. *J. Phys. B At. Mol. Opt. Phys.* **1974**, *7*, 1458–1475. [CrossRef]
31. Slater, J.C. *Quantum Theory of Molecules and Solids Vol. 4: The Self-Consistent Field for Molecules and Solids*; McGraw-Hill: New York, NY, USA, 1974.

32. Hasoğlu, M.F.; Nikolić, D.; Gorczyca, T.W.; Manson, S.T.; Chen, M.H.; Badnell, N.R. Nonmonotonic behavior as a function of nuclear charge of the *K*-shell Auger and radiative rates and fluorescence yields along the $1s2s^2p^3$ isoelectronic sequence. *Phys. Rev. A* **2008**, *78*, 032509. [CrossRef]
33. Burke, P.G. *R-Matrix Theory of Atomic Collisions: Application to Atomic, Molecular and Optical Processes*; Springer: New York, NY, USA, 2011.
34. Burke, P.G.; Berrington, K.A. *Atomic and Molecular Processes: An R-Matrix Approach*; IOP Publishing: Bristol, UK, 1993.
35. Berrington, K.A.; Eissner, W.; Norrington, P.H. RMATRX1: Belfast atomic R-matrix codes. *Comput. Phys. Commun.* **1995**, *92*, 290–420. [CrossRef]
36. Ballance, C.P.; Griffin, D.C. Relativistic radiatively damped R-matrix calculation of the electron-impact excitation of W46+. *J. Phys. B At. Mol. Opt. Phys.* **2006**, *39*, 3617–3628. [CrossRef]
37. Robicheaux, F.; Gorczyca, T.W.; Pindzola, M.S.; Badnell, N.R. Inclusion of radiation damping in the close-coupling equations for electron-atom scattering. *Phys. Rev. A* **1995**, *52*, 1319–1333. [CrossRef] [PubMed]
38. Quigley, L.; Berrington, K.A. The QB method: Analysing resonances using R-matrix theory. Applications to C^+, He and Li. *J. Phys. B At. Mol. Opt. Phys.* **1996**, *29*, 4529–4542. [CrossRef]
39. Quigley, L.; Berrington, K.A.; Pelan, J. The QB program: Analysing resonances using R-matrix theory. *Comput. Phys. Commun.* **1998**, *114*, 225–235. [CrossRef]
40. Ballance, C.P.; Berrington, K.A.; McLaughlin, B.M. Detection and analysis of interloping molecular resonances. *Phys. Rev. A* **1995**, *60*, R4217(R). [CrossRef]
41. Fano, U.; Cooper, J.W. Spectral Distribution of Oscillator Strengths. *Rev. Mod. Phys.* **1968**, *40*, 411. [CrossRef]
42. Ferland, G.J. Quantitative Spectroscopy of Photoionized Clouds. *Ann. Rev. Astron. Astr.* **2003**, *41*, 517–554. [CrossRef]
43. Ferland, G.J.; Korista, K.T.; Verner, D.A.; Ferguson, J.W.; Kingdon, J.B.; Verner, E.M. CLOUDY 90: Numerical Simulation of Plasmas and Their Spectra. *Publ. Astron. Soc. Pac.* **1998**, *110*, 761–778. [CrossRef]
44. Bautista, M.A.; Kallman, T.R. The X-star Atomic Database. *Astrophys. J. Suppl.* **2001**, *134*, 139. [CrossRef]
45. Foster, A.R.; Ji, L.; Smith, R.K.; Brickhouse, N.S. Updated Atomic Data and Calculations for X-ray Spectroscopy. *Astrophys. J.* **2012**, *756*, 128. [CrossRef]

atoms

MDPI

Article

Vibrationally and Spin-Orbit-Resolved Inner-Shell X-ray Absorption Spectroscopy of the NH^+ Molecular Ion: Measurements and ab Initio Calculations

Stéphane Carniato [1], Jean-Marc Bizau [2,3], Denis Cubaynes [2,3], Eugene T. Kennedy [4], Ségolène Guilbaud [2], Emma Sokell [5], Brendan McLaughlin [6] and Jean-Paul Mosnier [4,*]

1 LCPMR, UMR 7614, Sorbonne Université Pierre et Marie Curie Campus, Université Pierre et Marie Curie, 4 Place Jussieu Barre 43-44, F-75005 Paris, France; stephane.carniato@upmc.fr
2 Institut des Sciences Moléculaires d'Orsay, CNRS, Université Paris–Sud, and Université Paris-Saclay, F-91405 Orsay, France; jean-marc.bizau@universite-paris-saclay.fr (J.-M.B.); denis.cubaynes@universite-paris-saclay.fr (D.C.); segolene.guilbaud@universite-paris-saclay.fr (S.G.)
3 Synchrotron SOLEIL, L'Orme des Merisiers, Saint-Aubin, BP 48, F-91192 Gif-sur-Yvette, CEDEX, France
4 School of Physical Sciences and National Centre for Plasma Science and Technology (NCPST), Dublin City University, Dublin 9, Ireland; eugene.kennedy@dcu.ie
5 School of Physics, University College Dublin, Belfield, Dublin 4, Ireland; emma.sokell@ucd.ie
6 Centre for Theoretical Atomic and Molecular Physics (CTAMOP), School of Mathematics and Physics, Queen's University Belfast, Belfast BT7 1NN, UK; bmcl104@gmail.com
* Correspondence: jean-paul.mosnier@dcu.ie

Received: 2 September 2020; Accepted: 29 September 2020; Published: 4 October 2020

Abstract: This article presents N^{2+} fragment yields following nitrogen K-shell photo-absorption in the NH^+ molecular ion measured at the SOLEIL synchrotron radiation facility in the photon energy region 390–450 eV. The combination of the high sensitivity of the merged-beam, multi-analysis ion apparatus (MAIA) with the high spectral resolution of the PLEIADES beamline helped to resolve experimentally vibrational structures of highly excited $[N1s^{-1}H]^{*+}$ electronic states with closed or open-shell configurations. The assignment of the observed spectral features was achieved with the help of density functional theory (DFT) and post-Hartree Fock Multiconfiguration Self-Consistent-Field/Configuration Interaction (MCSCF/CI) ab-initio theoretical calculations of the N1s core-to-valence and core-to-Rydberg excitations, including vibrational dynamics. New resonances were identified compared to previous work, owing to detailed molecular modeling of the vibrational, spin-orbit coupling and metastable state effects on the spectra. The latter are evidenced by spectral contributions from the $^4\Sigma^-$ electronic state which lies 0.07 eV above the NH^+ $^2\Pi$ ground state.

Keywords: NH^+; molecular ion; K-shell; merged-beam

1. Introduction

Small molecules and their cations, notably hydrides, play important roles in laboratory and astrophysical plasma processes [1] and in planetary atmospheric chemistry. Reliable data on their electronic and vibrational structures as well as their interaction with ionizing radiation are key for their identification in astrophysical environments and an understanding of their chemical reactivity [2]. Standard gas-phase chemistry models show that NH and NH^+ are present at various stages of the pathways to ammonia production in the interstellar medium [1–3]. NH has been observed in diffuse clouds [4], but laboratory observations only are known for NH^+. Amero and Vasquez [5] give a comprehensive experimental and theoretical review of the assignments of the observed bands in the NH^+ ultraviolet and visible spectra.

Photoionization studies in the inner-shell regime of neutral molecules of astrophysical interest are well-developed [6]. For the associated cations, however, largely due to experimental difficulties, similar photoionization studies have remained scarce. Hence, only in the past few years has the photo-ion merged-beam technique been successfully applied to several molecular hydride ions [7–11].

Recently, ion yields following X-ray absorption of the cationic series NHy^+ (y = 0–3) were measured and characteristic resonances in the energy range of the atomic nitrogen K-edge were identified by Bari et al. [12]. These authors reported marked changes in the energy of the observed resonances as a function of the number of hydrogen atoms bound to the central nitrogen atom. Theoretical modeling in the framework of molecular group theory was also performed by Bari et al. [12] for the electronic parts of the spectra in order to obtain line assignments.

In this work, we present new high-resolution measurements of the N^{2+} fragment yield following 1 s photo-absorption in the NH^+ molecular ion as a function of the photon energy near the nitrogen K-edge. We implement extended ab-initio theoretical methods to calculate both the electronic and vibrational parts of the N1s absorption spectrum of NH^+. The theoretical results are then compared with the experimental data to provide definitive spectral assignments for the observed resonance energies and a meaningful analysis of their intensity profiles, revealing the importance of vibrational and spin-orbit effects.

2. Experimental Details and Results

The experiments were carried out using the multi-analysis ion apparatus (MAIA), which is located at the SOLEIL synchrotron facility (high-resolution PLEIADES beam line). We only provide the important experimental points here (extensive details on MAIA can be found in Reference [13]). NH^+ ions were optimally produced by heating NH_3 gas in a 12.4 GHz electron cyclotron resonance ion source (ECRIS) with less than 1 mW of radiofrequency power. The ions were extracted at 4 kV and mass-selected by a dipole bending magnet. The resulting NH^+ beam was then merged with the counter-propagating, undulator-monochromatized, synchrotron radiation beam and the overlap between the two beams was optimized. NH^+ ion currents of ~140 nA were typically available in the overlap region. The fragments produced upon the photon–ion interactions were analyzed downstream according to their charge-to-mass ratio by another dipole magnet. The remaining parent NH^+ ions were collected in a Faraday cup while the ionization fragments were counted using microchannel plates. Only the N^{2+} fragmentation channel could be meaningfully measured during the experiments. N^+ and H^+ photo-fragment signals were never above the intense background noise produced by collisions between the fast NH^+ ion beam and the residual gas, despite a background pressure in the low 10^{-9} mbar range. Neutral fragments are not detectable in the MAIA apparatus.

Figure 1a,b present measurements of the variation of the relative cross-section for the production of N^{2+} photofragments as a function of the photon energy between 390 and 450 eV. The spectrum in Figure 1a was obtained with a photon bandwidth (BW) increasing from 220 meV at 390 eV to 250 meV at 450 eV photon energy. Figure 1b displays an enlargement of the 394–401 eV region recorded with a higher resolution bandwidth of 110 meV. The measured cross-sections were corrected for both variations of the NH^+ ion current and the photon flux, which were monitored with a Faraday cup and a calibrated SXUV 300 photodiode, respectively [13]. The statistical uncertainty is displayed on each experimental point using grey bars. Since the N^{2+} fragments are produced with some kinetic energy, the detection of all the fragments is not guaranteed and the cross-section for this fragmentation channel is obtained in arbitrary units only. The photon energy scale was calibrated on the excitation energy of the N^+ 1s → 2p photoexcitation lines [14] recorded during the same beamtime and corrected for the Doppler shift associated with the NH^+ ion velocity. The resulting uncertainty on the photon energy scale is ±40 meV.

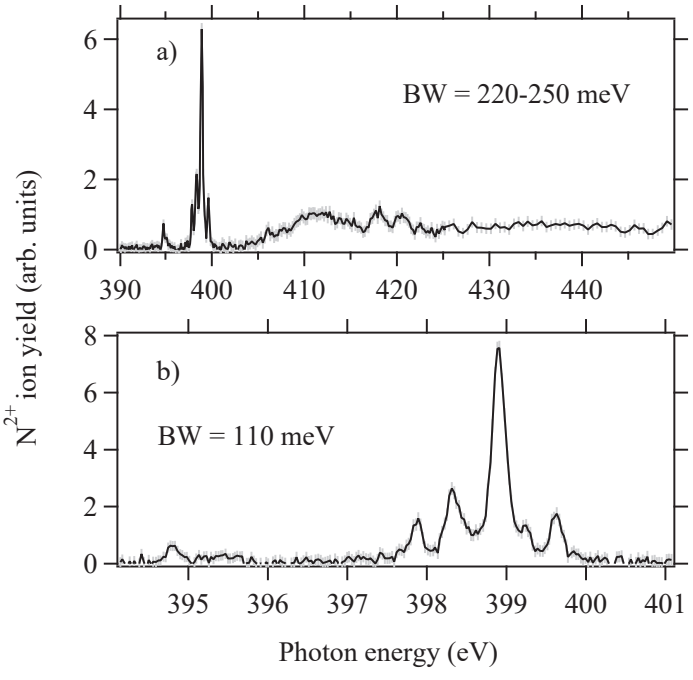

Figure 1. Experimental N^{2+} ion yield spectra of NH^+: (**a**) Recorded on the full photon energy range 390–450 eV with a photon bandwidth (BW) varying between 220 and 250 meV. (**b**) High-resolution spectrum obtained in the region 394–401 eV with a bandwidth of 110 meV.

Taking into account the difference in the photon energy resolution between the two experiments, generally good agreement on the position and shape of the structures is found with Bari et al.'s measurements [12]. The most noticeable difference lies in the relative intensity of the strong lines around 399 eV compared to the continuum above 425 eV.

3. Theoretical Aspects

3.1. Electronic Energies

The simulation of the X-ray absorption spectrum (XAS) of the NH^+ molecular ion consisted of computing the electronic transition energies and dipole moments associated with transitions between the quasi-degenerate fundamental ($^2\Pi$, $^4\Sigma^-$) electronic states and all core-excited states involved in the absorption process up to the $N1s^{-1}$ ionization thresholds. Excitation energies and oscillator strengths for the doublet and quartet states have been computed at both ($^2\Pi$, $^4\Sigma^-$) equilibrium geometries.

In order to calculate accurate energies of peaks in the N1s spectrum, full electronic relaxation energies (RE) with the departure of one N1s inner-shell electron and correlation energies at a post-Hartree-Fock (configuration interaction, CI) level of theory using single and double (SD) valence excitations (CI-SD) accompanying core-valence primary excitation were taken into account. Here, practically, the relaxation of the molecular orbitals (MOs) in the presence of a core vacancy was explicitly taken into account by using the Hartree-Fock Self Consistent Field (HF-SCF) approximation, which consists of a restricted open-shell Hartree-Fock calculation (ROHF) for the (low-lying) quartet core-ionized state $[N(1\sigma)^1 2\sigma^2\, 3\sigma^2 (1\pi_x)^1 (1\pi_y)^1]$, to ensure the degeneracy of the partially filled outermost π orbitals. This approach takes advantage of preparing a set of CI guesses for MOs where the valence-shell density contracts close to the (core) vacancy region.

Our methodology differs from the one adopted by Bari et al. [12], where the final states are described in a CI calculation employing the same orbitals as for the cationic initial state. As a remark, if the initial ground state is in principle correctly described, for the treatment of inner-shell excitations, CI calculations included all configurations that are constructed from the cationic reference configurations by promoting a single electron from the K shell to an unoccupied orbital, involving additional excitations of the valence electrons into virtual/singly occupied orbitals. However, including additional single valence excitations allow recovery of only part of the full relaxation and correlation is poorly described. Consequently, there is a certain imbalance in the description of initial and final electronic states. This imbalance can lead to a calculated transition energy which is slightly too low and varying relative shifts are necessary to be applied along the different orbital relaxation with respective excitation ranges.

Here, for the calculations of the first 100 low-lying core-excited energies, the [N$(1\sigma)^1 2\sigma^2$ $3\sigma^2(1\pi_x)^1(1\pi_y)^1$] molecular orbitals set were next employed within a Post-Hartree-Fock (HF) configuration interaction (CI) procedure, taking into account single and double substitutions (CI-SD) to virtual orbitals from the full valence (FV) manifold and a single hole (SH) in the core manifold (1 or 2 electrons in 1σ), using an iterative Davidson procedure developed by the main author of the present paper.

For the calculation of the oscillator strengths, the same set of MOs has been considered within a CI-SD (SH/FV-SD CI) approach for the description of the ground states of NH^+. This strategy ensures orthogonality of the spin-adapted configuration state functions (CSF) between the ground state and the core-excited states, which simplifies the calculation of the dipole transition moments. Of course, transition moments can be impacted by the description of the initial state. Otherwise, as a mirror to the strategy used by Bari et al. [12], the price to pay is that in principle, core-excitation energies are systematically overestimated by a few eV since the CI-SD ground state is constructed over relaxed core-excited molecular orbitals and not those of the real ground state. For that reason, excitation energies of the first low-lying states, i.e., the $^4\sum^-$ and $^4\Pi$ quartet states, were computed at the DFT level of theory using the Becke 3-parameter hybrid exchange [15] and the Lee-Yang-Parr (B3LYP) gradient-corrected correlation functional [16] with the general atomic and molecular electronic structure system GAMESS (US) quantum chemistry package [17]. These values are considered as energies of reference for prior calibration of the theoretical spectrum. Finally, spin-orbit coupling was also considered. The Breit-Pauli operator was used as implemented in the GAMESS (US) package in order to reveal the key spin-orbit components in the spectrum.

In summary, whatever the two approaches, this balance problem (using either initial MOs or relaxed MOs) is strongly related to the CI approach itself that considers a unique guess of MOs which are not optimal for the description of all of the states of the spectrum.

3.2. Vibrational Analysis, Potential Energy Curves

Assuming that the N K-hole lifetime width is similar to that measured in the nitrogen molecule (105 meV [18]), and because the monochromator bandwidth used in the present measurements was as low as 110 meV, several fine-structure features attributable to vibrational and/or initial population effects were observed in the spectra. In order to take into account the vibrational effects in the core-excited spectra, DFT/B3LYP equilibrium geometries and low-lying one-dimensional potential energy curves (PEC) of the initial and core-excited states of NH^+ have been calculated.

As reported in previous studies (see, for example, Reference [5] and references therein), the electronic ground state of the NH^+ molecular ion is a $^2\Pi$ doublet with seven electrons forming the $1\sigma_{1s}{}^2\ 2\sigma^2\ 3\sigma^2\ 1\pi^1$ electronic configuration. A quartet open-shell $^4\Sigma^-$ ($1\sigma_{1s}{}^2\ 2\sigma^2\ 3\sigma^1\ 1\pi^2$) electronic state is quasi-degenerate with the fundamental state as it lies only 0.07 eV above the $^2\Pi$ state. Consequently, both these configurations must be considered in order to properly describe the experiments. PECs of the $^2\Pi$ and the $^4\sum^-$ ground states were simulated at a Multiconfiguration Self-Consistent-Field (MCSCF) level of theory as implemented in the GAMESS (US) package. Practically, the two N1s

inner-shell electrons ($N1\sigma^2$) have been frozen. The MCSCF expansions comprise single (S) up to double (D) substitutions out of each of the restricted open-shell Hartree-Fock (ROHF) reference configurations. The reference active-space (26 molecular orbitals) includes here the 2σ, 3σ, $1\pi_x$, $1\pi_y$ (five electrons) outermost occupied and the twenty-two lowest-lying unoccupied molecular orbitals. In order to evaluate the energy spacing between the $^2\Pi$ and $^4\sum^-$ potential energy curves, DFT/B3LYP geometry optimizations and frequency calculations have been performed.

In order to determine the vibrational progression and Frank-Condon factors (FC) associated with the most relevant electronic transitions emerging from the x-ray absorption (XAS) N1s inner-shell spectrum of NH^+, the PEC of selected low-lying N1 s^{-1} core-excited states of interest have been calculated for internuclear distances ranging between 0.6 and 5 Å and are displayed in Figure 2 for the internuclear distance region between 0.6 and 3 Å.

In practice, we used the ROHF molecular orbitals of the $N1s^{-1}\,^4\Sigma^-$ quartet low-lying state computed for each interatomic distance. For each distance, a CI-SD calculation was performed with the occupation Restricted Multiple Active Space (ORMAS) method implemented in the GAMESS (US) package, in which the six valence electrons and one N1s inner-shell electron were explicitly correlated at a moderate cost, including up to 65 active molecular orbitals in order to collect the first PECs of the $[N1s^{-1}\ H]^+$ core-excited configurations with $^2\Delta$, $^2\Sigma^+$, $^{2,4}\Sigma$, $^{2,4}\Pi$ symmetries, generating ~7×10^6 configuration state functions (CSF).

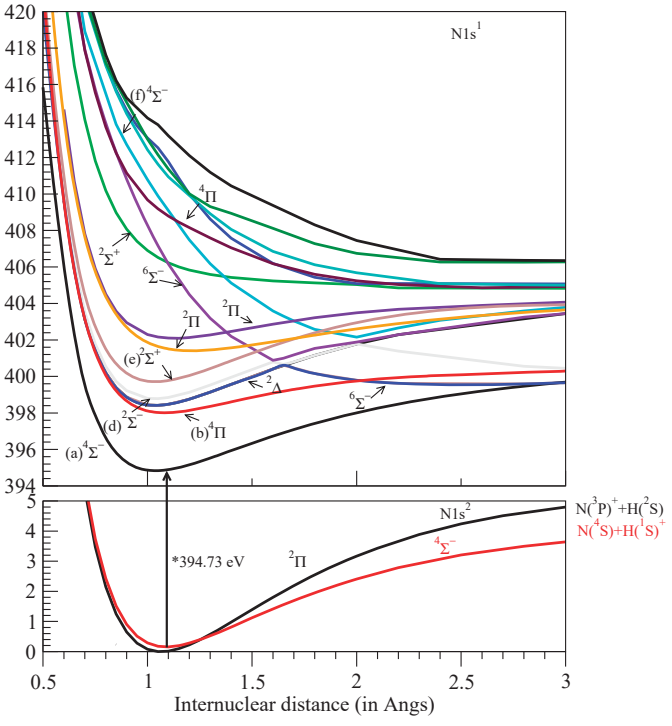

Figure 2. Multiconfiguration Self-Consistent Field (MCSCF) $N1s^2$ doublet $^2\Pi$ and quartet $^4\Sigma^-$ ground states (lower panel) and low-lying configuration interaction single and double substitutions (CI-SD) $N1s^1$ nitrogen K-shell (upper panel) potential energy curves of the NH^+ molecular ion. * The bottom of the lowest $N1s^{-1}\,^4\Sigma^-$ potential energy curve is set to the vertical density functional theory (DFT) energy transition of 394.73 eV represented by the vertical arrow (see text).

As the CI guess of MOs used to describe all the core-excited states is based on the single N1s^{-1} $^4\Sigma^-$ configuration, the CI-SD energy gap between the low-lying state $^4\Sigma^-$ state and the higher states can be overestimated, but the spacing between them can be expected to be satisfactory. In order to reproduce with accuracy the gap between the $^4\Sigma^-$ and the first $^4\Pi$ core-excited state, we performed two single points ($^4\Sigma^-$ and $^4\Pi$) of energy at a larger CI-SDT level, generating ~10^8 CSFs. A global shift of all the core-excited states above $^4\Sigma^-$ was assumed using this new gap value to compare theory vs experiments.

All the calculations were realized with the large aug-cc-pCV5z basis set [19] on all atoms augmented by additional (4s/4p/2d/2f) diffuse functions.

The eigenvalue/eigenfunction problem for the stretching motion taking into account vibrational effects was then solved using the one-dimensional Hamiltonian model that can be written as

$$H = \frac{-\hbar^2}{2\mu}\frac{d^2}{dr^2} + V(r) \tag{1}$$

where μ is the reduced mass of the system, r is the internuclear distance, and $V(r)$ is the molecular potential. The eigenvectors (vibrational wave functions) and eigenvalues (vibrational levels) were obtained by diagonalizing the Hamiltonian in a tridiagonal form using the finite difference approximation and a cubic spline interpolation of the potential energy curves. The matrix elements are

$$H_{i,j} = \frac{-\hbar^2}{2\mu\Delta^2}\left(2\delta_{i,j} - \delta_{i-1,j} + \delta_{i+1,j}\right) + V(r)\delta_{i,j} \tag{2}$$

where Δ is the uniformly spaced mesh. The fundamental frequency (ω_e) and anharmonicity constant (x_e), commonly expressed in terms of the vibrational expression

$$G_v = \omega_e\left(\upsilon + \frac{1}{2}\right) - \omega_e x_e\left(\upsilon + \frac{1}{2}\right)^2, \tag{3}$$

were derived for the ground state and core-excited states of interest in the present study, where υ is the vibrational quantum number.

3.3. Absorption Cross-Section Spectrum

The absorption spectrum was obtained by convolving the mean value of the dipole transition moment for randomly orientated molecular ions in the gas phase, computed at the equilibrium geometry of the system in its ground state, with a Voigt profile which accounts for both the lifetime and instrumental broadenings. The lifetime broadening was assumed to be independent of both core-excited electronic states and the internuclear distance. The transition moments $\mu_{i\to f}$ and the cross-sections were evaluated in the length gauge as follows:

$$\overline{\sigma}_{i\to f}(\omega) = \frac{4}{3}\frac{\pi^2 e^2\hbar}{(4\pi\varepsilon_o)mc}\frac{\left(E_f - E_i\right)^2 m}{\hbar^3\omega}\mu^2_{i\to f}\,\delta\left(\omega - \omega_{fi}\right) = \frac{2}{3}\frac{\left(E_f - E_i\right)^2 m}{\hbar^3\omega}\mu^2_{i\to f}\,C\,\delta\left(\omega - \omega_{fi}\right) \tag{4}$$

where ω is the photon frequency, $\delta\left(\omega - \omega_{fi}\right) = \frac{\gamma}{2\pi\left[(\omega-\omega_{fi})^2 + \frac{1}{4}\gamma^2\right]}$ is the Lorentzian line shape, $\frac{2}{3}\frac{\left(E_f - E_i\right)^2 m}{\hbar^3\omega}\mu^2_{i\to f}$ is the oscillator strength averaged over all possible molecular orientations, and

$$C = \frac{2\pi^2 e^2\hbar}{(4\pi\varepsilon_o)mc} = 109.8 \text{ Mb eV}.$$

The N1s^{-1} spectrum of the NH^+ molecular ion was simulated using a Voigt profile, where γ is the full width at half maximum (FWHM) of the Lorentzian profile corresponding to the N1s^{-1} core-hole lifetime (γ = 105 meV) and a Gaussian function with FWHM equal to ξ = 110 meV to simulate the

experimental broadening. It should be noted that the experimental spectral bandwidth in the higher photon energy was greater (220–250 meV), but in this region, no individual lines are resolved, several of the upper states involved are strongly dissociative, and using the smaller bandwidth for the theoretical spectrum does not affect the simulation. Finally, the average cross-section for a photon of energy ω' is given by

$$\overline{\sigma}(\omega') = \sum_{f=1}^{n} \int \overline{\sigma}_{i\to f}(\omega) \frac{2\sqrt{ln2}}{\xi\sqrt{\pi}} e^{-4ln2\ (\omega'-\omega)^2/\xi^2}\, d\omega \quad (5)$$

where n is the number of final electronic states.

4. Results and Discussion

4.1. Ground States

Both the vibrational frequencies and the equilibrium distances of the quasi-degenerate electronic ground states are key parameters in order to calculate the N1s spectrum of NH^+. The calculated values for the ($^2\Pi$) and ($^4\Sigma^-$) ground states are given in Table 1 and compared to available experimental values [20].

Table 1. NH^+ calculated internuclear distances, d_{NH}, and frequencies, ν_{NH}, for the $^2\Pi$ and $^4\Sigma^-$ ground states compared to experiments (Reference [20]) for the N1s^{-1} core-excited states located in the 394–400 photon energy region (see text).

Main Configuration	State	d_{NH} (Å)	ν_{NH} (cm^{-1})	Type [1]
$1\sigma_1{}^2 2\sigma^2 3\sigma^2 3p_{x,y}{}^1$	$^2\Pi$	1.0776	2974.3	DFT/B3LYP
		1.065	3064.2	MCSCF
		1.0692	3047.58	Experimental value from Ref. [20]
$1\sigma_1{}^2 2\sigma^2 3\sigma^1 3p_x{}^1 3p_y{}^1$	$^4\Sigma^-$	1.1135	2502.0	DFT/B3LYP
		1.096	2716.0	MCSCF
		1.093	2672.57	Experimental value from Ref. [20]
$1\sigma_1{}^1 2\sigma^2 3\sigma^2 3p_x{}^1 3p_y{}^1$	$^4\Sigma^-$	1.0341	3169.0	DFT/B3LYP
		1.040	3182.0	CI-SD
$1\sigma_1{}^1 2\sigma^2 3\sigma^1 3p_x{}^2 3p_y{}^1/3p_x{}^1 3p_y{}^2$	$^4\Pi$	1.0919	2517.0	DFT/B3LYP
		1.082	2557.0	CI-SD
$1\sigma_1{}^1 2\sigma^2 3\sigma^2 3p_x{}^2 3p_y{}^0/3p_x{}^0 3p_y{}^2$	$^2\Delta$	1.0371	3140.0	DFT/B3LYP
		1.035	3250	CI-SD
$1\sigma_1{}^1 2\sigma^2 3\sigma^2 3p_x{}^1 3p_y{}^1$	$^2\Delta$	1.035	3250.0	CI-SD

[1] Definition of acronyms: density functional theory/Becke 3-parameter hybrid exchange and Lee-Yang-Parr gradient-corrected correlation functional (DFT/B3LYP); Multiconfiguration Self-consistent Field (MCSCF); Configuration interaction with single and double substitutions (CI-SD).

For the $^2\Pi$ state, the dissociation energy (D_o = 4.98 eV), equilibrium distance, R_e, and the fundamental vibrational frequency, ω_e, are fairly well reproduced by the present MCSCF-SD calculations compared to the most accurate calculated data (R_e = 1.0687 Å, ω_e = 3052.9 cm^{-1}, D_o = 4.64 eV [21]) and experimental data (D_o = 4.66 eV, R_e = 1.077 Å, ω_e = 2980.65 cm^{-1} [22], or see also Reference [5] and references therein). The calculation of the anharmonicity coefficient from the PEC analysis gives $\omega_e x_e$ = 73.0 cm^{-1}.

For the quartet $^4\sum^-$ state, the MCSCF dissociation energy (D_o = 3.50 eV), equilibrium distance (R_e = 1.096 Å), and fundamental vibrational frequency (ω_e = 2716 cm^{-1}) are also well reproduced by our theoretical calculations compared to experimental data (D_o = 3.33 eV, R_e = 1.093 Å, ω_e = 2652.29 cm^{-1} [5,20]). In this case, the anharmonicity coefficient is $\omega_e x_e$ = 81 cm^{-1}.

In order to evaluate the energy gap between the $^2\Pi$ and $^4\sum^-$ potential energy curves, which is a key parameter for the analyses of the experimental data, DFT/B3LYP geometry optimizations and frequency calculations were performed (see Table 1). For the doublet, the equilibrium distance and ω_e were estimated to be 1.0776 Å and 2974 cm^{-1}, respectively. For the quartet, the DFT equilibrium distance and the harmonic frequency are estimated to be 1.113 Å and 2502 cm^{-1} respectively, in excellent agreement with MCSCF-SD and experimental values [22]. The calculated DFT adiabatic electronic energy gap between the $^2\Pi$ and the $^4\sum^-$ states is estimated to be 0.166 eV. Considering the zero-point energy correction, the vibrational corrected energy gap is finally found equal to 0.137 eV at DFT and 0.143 eV at MCSCF level of theories, somewhat overestimating the experimental value (0.071 eV).

4.2. Core-Excited States

The NH^+ experimental ion yield spectrum covering the full energy window is shown in Figure 1a. Mainly, three distinctive regions are observed: (i) the first region presents a single weak structure close to 395 eV, (ii) the second region is located around 397–400 eV, showing four well-defined components. A high-resolution spectrum of this region is displayed in Figure 1b. (iii) Above 405 eV, the spectrum consists of broad and unresolved features, likely due to the excitation of a 1 s electron to higher empty orbitals, to form Rydberg series converging to the 1 s^{-1} ionization thresholds around 425–430 eV.

In the following, we will separately discuss the three regions. The results of our calculations for the three regions are reported in Table 2.

4.2.1. Region 394–396 eV (Peaks a $^4\Sigma^-$)

The energy position of the low-lying structure (see Figure 1a,b and Figure 3), labeled a, is measured at 394.81 (6) eV. The DFT/B3LYP vertical electronic transition energy is estimated to be 394.53 eV and corresponds to a solely electronic excitation from the N1s inner-shell to the 3σ singly occupied molecular orbital to form the final $^4\Sigma^-$ quartet open-shell $N1\sigma^1 2\sigma^2 3\sigma^2 1\pi_x{}^1 1\pi_y{}^1$ electronic configuration, in agreement with Bari et al. [12]. This assignment is confirmed by analysis of the PEC displayed in Figure 2 showing that the low-lying potential energy curve is well associated with the $^4\Sigma^-$ quartet which dissociates into the $N(^4S) + H^+(^1S)$ final products.

The adiabatic DFT/B3LYP optimized equilibrium distance experiences a substantial shrink by 0.1 Å (R = 1.034 Å) with respect to the quartet ground state PEC of NH^+. This relatively large contraction of the NH bond is corroborated by CI-SD calculations, for which the minimum of the PEC is found at nearly 1.040 Å. The MCSCF numerical vibrational frequency is equal to 3182 cm^{-1}, i.e., ≈470 cm^{-1} larger than for the $^4\sum^-$ quartet electronic ground state. The anharmonicity coefficient $\omega_e x_e$ extracted from PEC analysis is ≈87 cm^{-1}.

Taking into account the differential zero-point energy correction between the initial and final states (MCSCF: +0.03 eV, DFT: +0.04 eV) and the relativistic correction (+0.2 eV) due to departure of one N1s inner-shell electron, the corrected DFT vertical core-excitation energy is finally found at 394.77 eV, in excellent agreement with the experimental data. The CI-SD calculated oscillator strength for the $^4\Sigma^- \rightarrow {}^4\Sigma^-$ transition (peak a) is evaluated to be 0.043, corresponding to a strength of 4.72 Mb eV.

In spite of the weak signal, the band presents an asymmetric tail extending up to ≈395.5 eV (see Figure 1a). As clearly shown by theory, the reason for such asymmetry on the high-energy tail of the peak is due to a vibrational progression. Our simulation shows that the vibrational progression is due to the net shortening of the N-H bond in the N1s core hole state compared to the ground state. The vibrational profile exhibits two significant components with relative intensities 0.82:0.17, lying at 0.19 eV (v = 0→v′ = 0, band a) and 0.56 eV (v = 0→v′ = 1, band a′) above the PEC adiabatic minimum, respectively. Considering the zero-point energy correction of 0.04 eV (at the DFT level of theory) for the $^4\Sigma^- \rightarrow {}^4\Sigma^-$ transition, the energy positions of the theoretical bands a and a′ are finally calculated to be 394.77 eV and 395.14 eV, respectively, in good agreement with the experimental data.

Table 2. Configuration interaction with single and double substitutions (CI-SD) from the full valence manifold results for vertical transitions of valence character from the density functional theory (DFT) doublet (R_e = 1.077Å) and quartet (R_e = 1.113 Å) optimized ground state geometries. Main configurations and weights (W) in %, measured (E_{mea}) and calculated (E_{cal}) transition energies in eV, oscillator strengths f_{theo} above 0.001 only are reported, and labels used to identify the present experimental data. For doublet states, f_{theo} have been calculated for only one (x or y) component.

Electronic Transition	Final State	E_{mea} (eV) [1]	E_{cal} (eV)	W (%)	f_{theo}	Label
Region1						
$1\sigma^2 2\sigma^2 3\sigma^1 1\pi_x^1 1\pi_y^1 \rightarrow 1\sigma^1 2\sigma^2 3\sigma^2 1\pi_x^1 1\pi_y^1$	$^4\Sigma^-$	394.81(6)	394.73 [2]	98.0	0.0430	a
Region2						
$1\sigma^2 2\sigma^2 3\sigma^1 1\pi_x^1 1\pi_y^1 \rightarrow 1\sigma^1 2\sigma^2 3\sigma^1 1\pi_{x(y)}^1 1\pi_{y(x)}^2$	$^4\Pi$	397.87(5)	397.84 [3]	95.6	0.1560	b
$1\sigma^2 2\sigma^2 3\sigma^2 1\pi_{x(y)}^1 \rightarrow 1\sigma^1 3\sigma^2 1\pi_{x(y)}^2\ \pi_{y(x)}^0$	$^2\Delta$	398.31(6)	398.40 [4]	98.7	0.0401	c
$1\sigma^2 2\sigma^2 3\sigma^2 1\pi_{x(y)}^1 \rightarrow 1\sigma^1 2\sigma^2 3\sigma^2 1\pi_x^1\ \pi_y^1$	$^2\Delta$	398.46(11)	398.40	98.7	0.0401	c′
$1\sigma^2 2\sigma^2 3\sigma^2 1\pi_{x(y)}^1 \rightarrow 1\sigma^1 2\sigma^2 3\sigma^2 1\pi_x^1\ \pi_y^1$	$^2\Sigma^-$	398.91(4)	398.70	98.7	0.1208	d
$1\sigma^2 2\sigma^2 3\sigma^2 1\pi_{x(y)}^1 \rightarrow 1\sigma^1 2\sigma^2 3\sigma^2 1\pi_{x(y)}^2\ \pi_{y(x)}^0$	$^2\Sigma^+$	399.63(5)	399.63	92.5	0.0385	e
Region 3						
$1\sigma^2 2\sigma^2 3\sigma^1 1\pi_x^1 1\pi_y^1 \rightarrow 1\sigma^1 2\sigma^2 3\sigma^1 1\pi_x^1 1\pi_y^1\ 4\sigma^1$	$^4\Sigma^-$		409.04	88.0	0.0332	f
$1\sigma^2 2\sigma^2 3\sigma^1 1\pi_x^1 1\pi_y^1 \rightarrow 1\sigma^1 2\sigma^1 3\sigma^2 1\pi_{x(y)}^2 1\pi_{y(x)}^1$	$^4\Pi$		409.14	74.0	0.0012	g
$1\sigma^2 2\sigma^2 3\sigma^2 1\pi_{x(y)}^1 \rightarrow 1\sigma^1 2\sigma^2 3\sigma^2 1\pi_{x(y)}^1\ 4\sigma^1$	$^2\Pi$		412.17	85.0	0.0261	h
$1\sigma^2 2\sigma^2 3\sigma^1 1\pi_x^1 1\pi_y^1 \rightarrow 1\sigma^1 3\sigma^1 1\pi_x^1 1\pi_y^1\ 4\sigma^1$	$^4\Sigma^-$		412.20	77.8	0.0078	i
$1\sigma^2 2\sigma^2 3\sigma^1 1\pi_x^1 1\pi_y^1 \rightarrow 1\sigma^1 3\sigma^1 1\pi_x^1 1\pi_y^1\ 4\sigma^1$	$^4\Sigma^-$		412.40	80.6	0.0189	j
$1\sigma^2 2\sigma^2 3\sigma^2 1\pi_{x(y)}^1 \rightarrow 1\sigma^1 2\sigma^2 3\sigma^2 1\pi_{x(y)}^1\ 4\sigma^1$	$^2\Pi$		414.00	57.8	0.0032	k
$1\sigma^2 2\sigma^2 3\sigma^1 1\pi_x^1 1\pi_y^1 \rightarrow 1\sigma^1 3\sigma^1 1\pi_x^1 1\pi_y^1\ 5\sigma^1$	$^4\Sigma^-$		414.67	89.2	0.0039	l
$1\sigma^2 2\sigma^2 3\sigma^1 1\pi_x^1 1\pi_y^1 \rightarrow 1\sigma^1 3\sigma^1 1\pi_x^1 1\pi_y^1\ 2\pi_{x(y)}^1$	$^4\Pi$		414.70	59.6	0.0174	m
$1\sigma^2 2\sigma^2 3\sigma^2 1\pi_x^1 \rightarrow 1\sigma^1 2\sigma^2 3\sigma^1 1\pi_x^1\ \pi_y^1 4\sigma^1$	$^2\Sigma^-$		414.80	82.0	0.0015	n
$1\sigma^2 2\sigma^2 3\sigma^2 1\pi_{x(y)}^1 \rightarrow 1\sigma^1 2\sigma^2 3\sigma^2 1\pi_{x(y)}^1\ 4\sigma^1$	$^2\Pi$		415.95	57.8	0.0053	o
$1\sigma^2 2\sigma^2 3\sigma^2 1\pi_x^1 \rightarrow 1\sigma^1 2\sigma^2 3\sigma^1 1\pi_x^1\ \pi_y^1 4\sigma^1$	$^2\Delta$		416.09	78.8	0.0015	p
$1\sigma^2 2\sigma^2 3\sigma^2 1\pi_x^1 \rightarrow 1\sigma^1 2\sigma^2 3\sigma^1 1\pi_{x(y)}^2\ \pi_{y(x)}^0 4\sigma^1$	$^2\Delta$		416.09	78.8	0.0015	p′
$1\sigma^2 2\sigma^2 3\sigma^2 1\pi_x^1 \rightarrow 1\sigma^1 2\sigma^2 3\sigma^1 1\pi_x^1\ \pi_y^1 4\sigma^1$	$^2\Sigma^-$		416.51	76.9	0.0032	q
$1\sigma^2 2\sigma^2 3\sigma^2 1\pi_x^1 \rightarrow 1\sigma^1 2\sigma^2 3\sigma^1 1\pi_{x(y)}^2 1\pi_{y(x)}^0 4\sigma^1$	$^2\Sigma^+$		417.68	50.1	0.0016	r
$1\sigma^2 2\sigma^2 3\sigma^2 1\pi_{x(y)}^1 \rightarrow 1\sigma^1 2\sigma^2 3\sigma^2 1\pi_{x(y)}^1\ 4\sigma^1$	$^2\Pi$		418.07	77.4	0.0040	s
$1\sigma^2 2\sigma^2 3\sigma^1 1\pi_x^1 1\pi_y^1 \rightarrow 1\sigma^1 3\sigma^1 1\pi_x^1 1\pi_y^1\ 3\pi_{x(y)}^1$	$^4\Pi$		418.01	94.5	0.0013	t
$1\sigma^2 2\sigma^2 3\sigma^2 1\pi_x^1 \rightarrow 1\sigma^1 2\sigma^2 3\sigma^2 1\pi_x^1\ 2\pi_y^1$	$^2\Sigma^-$		418.14	76.9	0.0012	u
$1\sigma^2 2\sigma^2 3\sigma^1 1\pi_x^1 1\pi_y^1 \rightarrow 1\sigma^1 3\sigma^1 1\pi_x^1 1\pi_y^1\ 3\pi_{x(y)}^1$	$^4\Sigma^-$		418.19	53.5	0.0026	v
$1\sigma^2 2\sigma^2 3\sigma^2 1\pi_x^1 \rightarrow 1\sigma^1 2\sigma^2 3\sigma^2 1\pi_x^1\ 2\pi_y^1$	$^2\Delta$		418.61	76.9	0.0013	x
$1\sigma^2 2\sigma^2 3\sigma^2 1\pi_x^1 \rightarrow 1\sigma^1 2\sigma^2 3\sigma^2 1\pi_x^1\ 2\pi_y^1$	$^2\Delta$		418.61	76.9	0.0013	x′
$1\sigma^2 2\sigma^2 3\sigma^1 1\pi_x^1 1\pi_y^1 \rightarrow 1\sigma^1 3\sigma^1 1\pi_x^1 1\pi_y^1\ 2\pi_{x(y)}^1$	$^4\Pi$		419.55	84.5	0.0027	y
$1\sigma^2 2\sigma^2 3\sigma^1 1\pi_x^1 1\pi_y^1 \rightarrow 1\sigma^1 3\sigma^1 1\pi_x^1 1\pi_y^1\ 5\sigma^1$	$^4\Sigma^-$		419.76	51.3	0.0062	z
$1\sigma^2 2\sigma^2 3\sigma^2 1\pi_x^1 \rightarrow 1\sigma^1 2\sigma^2 3\sigma^1 1\pi_x^1 1\pi_y^1 5\sigma^1$	$^2\Sigma^-$		420.18	69.0	0.0020	za
$1\sigma^2 2\sigma^2 3\sigma^1 1\pi_x^1 1\pi_y^1 \rightarrow 1\sigma^1 3\sigma^1 1\pi_x^1 1\pi_y^1\ 2\pi_{x(y)}^1$	$^4\Pi$		420.27	81.7	0.0099	zb

[1] The number in brackets is the uncertainty on the last digit. [2] Vertical relativistic density functional theory (DFT) value (394.73 eV) corrected by zero-point energy (0.02 eV) used as reference. [3] Vertical transition energy value at 1.096 Å (Multiconfiguration self-consistent Field (MCSCF) minimum distance of the $^4\Sigma^-$ ground state) deduced from Figure 2. [4] Doublet vertical transition energy value at 1.065 Å (Multiconfiguration self-consistent Field (MCSCF) local minimum of the $^2\Pi$ ground state) deduced from Figure 2. 394.77 eV and 395.14 eV, respectively, in good agreement with experimental data.

The presence of the $^4\Sigma^- \rightarrow {}^4\Sigma^-$ transition in the spectrum is due to the plasma source conditions, since the ground electronic state is formally a $^2\Pi$ state, as stated in previous works (see Reference [19] and references therein) and confirmed here by the present calculations, and lies only ≈0.1 eV below the $^4\sum^-$ state. The time of flight of the ions between the source and the interaction region is of the order of a few μ-seconds and, thus, a fraction of the ions interacting with the photons may be vibrationally and/or electronically excited, particularly in a relatively long-lived, low-lying state such as the $^4\Sigma^-$.

4.2.2. Region 397–400 eV

A fitting by Voigt profiles of the experimental data displayed on Figure 3a shows the seven lines, labeled a–e (Table 2). Their energy positions and natural widths extracted from the fits are given in Table 3. Table 3 also shows a comparison with the results of Bari et al. [12] recorded with lower spectral resolution. The calculated XAS spectrum is shown in Figure 3b.

The XAS N1s spectrum of NH^+ is dominated by the peak centered at 398.91 eV (peak d) surrounded by three significant satellite bands (b), (c), and (e) centered at 397.87 eV, 398.31 eV, and 399.63 eV, respectively. We will tackle the identification and discussion of the resonance peaks in the order (b), (c), (e), and (d).

Table 3. Experimental position and natural width of the lines observed in the 394–401 eV photon energy region.

Line Label	Energy (eV)		Natural Width
	This Work	Reference [12] [1]	(meV)
a	394.81(6)	394.9	84(6)
b	397.87(5)	397.8	108(3)
c	398.31(6)	398.8	108(5)
c′	398.46(11)		
d	398.91(4)	398.8	142(20)
d′	399.25(5)		
e	399.63(5)	399.6	94(29)

[1] Uncertainty ± 0.1 eV.

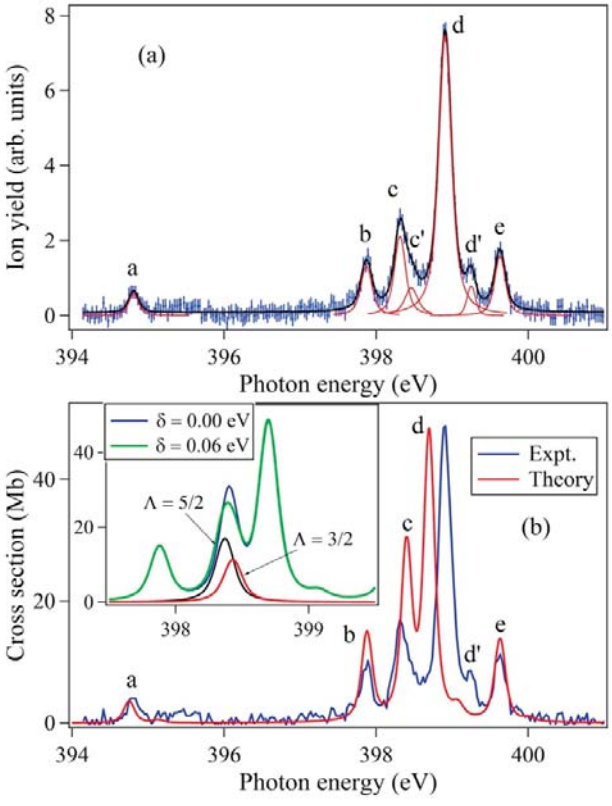

Figure 3. (**a**) Fitting by Voigt profiles of the experimental data, (**b**) NH+ experimental (blue trace Expt.) and calculated (red trace Theory) X-ray absorption spectra (XAS). The most important features are labeled (see Table 2). The experimental spectrum has been normalized to the maximum of peak d. In the insert is shown the splitting of the $^2\Delta$ states components (peak c) due to spin-orbit coupling for two δ values (see text).

Peak b $^4\Pi$

The first satellite line labeled b measured at 397.87 eV corresponds to a second high-spin quartet state associated with the degenerate $^4\Pi$ state involving final N1sσ^1 $2\sigma^2$ $3\sigma^1$ $1\pi_x{}^2$ $1\pi_y{}^1$/N1sσ^1 $2\sigma^2$ $3\sigma^1 1\pi_x{}^1 1\pi_y{}^2$ configurations. The DFT/B3LYP vertical core-excitation energy corresponds to the N1sσ^1 $2\sigma^2$ $3\sigma^1$ $1\pi_x{}^1$ $1\pi y^1$ →N1sσ^1 $2\sigma^2$ $3\sigma^1$ $1\pi_x{}^2$ $1\pi y^1$ and the transition energy is estimated to be 397.34 eV.

The equilibrium distance of the $^4\Pi$ adiabatic curve is very close (DFT 1.0919 Å, CI-SD 1.082 Å) to the internuclear distance found for the $^4\Sigma^-$ initial state. Hence, the N1s inner-shell vacancy does not considerably impact the NH bond length which experiences only a weak shortening of ≈0.01 Å, while the initial and final potential energy curves are found to be nearly parallel (see Figure 2). As a result, the Franck-Condon profile is limited to the v = 0 → v ′= 0 transition and no clear vibrational progression on the high-energy side of the peak at 397.8 eV is expected, as confirmed by the experiments. We note that the vibrational frequency is slightly reduced (CI-SD: 2557 cm^{-1}, DFT: 2516.7 cm^{-1}) compared to a $^4\Sigma^-$ (2716 cm^{-1}) and the anharmonicity coefficient $\omega_e x_e$ deduced from the PEC is ≈71 cm^{-1}. The differential zero-point energy correction (≈−0.01 eV) is rather small, and taking into account the relativistic correction of 0.2 eV, the DFT position of the peak b finally comes to 397.55 eV, i.e., only 2.8 eV above the $^4\Sigma^-$ final core-excited state and ≈−0.3 eV lower than the experimental energy position (397.87 eV). On the contrary, the CI-SD energy gap between the $^4\Sigma^-$ and the $^4\Pi$ core-excited states is rather overestimated (3.5 eV) vs the DFT value and the experiments (3.07 eV). In order to estimate the impact of correlation onto the gap, CI calculations including single up to triple excitations have been performed. As a result, the energy gap is significantly reduced from 3.5 to 3.13 eV, in very good agreement with the experimental value (3.07 eV). Hence, for easier comparison between theory and experiments in Figure 3b, we assumed a global shift (−0.35 eV) of the $^4\Pi$ and higher theoretical core-excited energies reported in Table 2. By this procedure, the $^4\Sigma^- \rightarrow {}^4\Pi$ theoretical transition (397.86 eV) reproduces the experimental excitation energy well (397.84 eV). The calculated oscillator strength is equal to 0.156 (see Table 2), corresponding to a strength of 17.1 Mb eV, so that the theoretical $^4\Sigma^-/{}^4\Pi$ intensity ratio (0.29) is in reasonable agreement with the measured experimental ratio between peaks area (0.33).

Peaks c $^2\Delta$ and e $^2\sum^+$

The peak labeled c on the spectrum is measured at 398.31 eV, i.e., lying 0.44 eV above the resonance b $^4\Pi$. This line is a superposition of two dipole-allowed degenerate doublet $^2\Delta$ states corresponding to the closed-shell N1sσ^1 $2\sigma^2$ $3\sigma^2$ $1\pi_x{}^2$ (or $1\pi_y{}^2$) and open-shell N1sσ^1 $2\sigma^2$ $3\sigma^2$ $1\pi_x{}^1$ $1\pi_y{}^1$ core-excited configurations. The DFT/B3LYP vertical transition energy of the isolated doublet N1sσ^1 $2\sigma^2$ $3\sigma^2$ $1\pi_x{}^2$ configuration at the ground state NH^+ equilibrium distance (R = 1.077 Å) is calculated to be 398.62 eV. This value is slightly overestimated and differs more significantly (398.82 eV) with the experimental one when taking into account the relativistic correction (0.2 eV). The similar analysis developed by Bari et al. [12] for this resonance is confirmed by the present work.

In fact, the calculation of the $^2\Delta$ doublet core-excited energy is not as straightforward as for the single-configuration-like quartet lines, since two former closed-shell spin-doublet configurations (N1sσ^1 $2\sigma^2$ $3\sigma^2$ $1\pi_x{}^2$ (or $1\pi_y{}^2$)) interact through the $J_{3p,3p}$ Coulomb integral, while the open-shell one consists of three different βαα(1), ααβ(2) and αβα (3) configuration spin-state functions, ultimately forming two doublet ($\frac{1}{\sqrt{6}}$(βαα(1) − 2 ααβ(2) + αβα(3)); $\frac{1}{\sqrt{2}}$αβα((3) − ααβ(2)) spin-adapted functions.

The origin of the $^2\Delta$ degeneracy is obvious from an analysis of the nature of the coupling matrix elements (Coulomb and exchange interactions) between the valence closed-shell N1sσ^1 $2\sigma^2$ $3\sigma^2$ $1\pi_x{}^2$ (or $1\pi_y{}^2$) and the three valence open shell N1sσ^1 $2\sigma^2$ $3\sigma^2$ $1\pi_x{}^1$ $1\pi_y{}^1$ configurations. For the former, let us basically consider a two-dimensional matrix (see Table 4) restricted to the $1\pi_x{}^2$ and $1\pi_y{}^2$ valence-shell configurations. The diagonal terms $\langle N1s\alpha^1\, 2\alpha^2\, 3\alpha^2\, 1\pi_{x(y)}{}^2|H|N1s\alpha^1\, 2\alpha^2\, 3\alpha^2\, 1\pi_{x(y)}{}^2\rangle$ are identical, while the off-diagonal elements correspond to the Coulomb integral $J_{3p,3p}$ =

$\left\langle 3p_x(1)3p_y(2)\left|\frac{1}{r_{12}}\right|3p_x(1)3p_y(2)\right\rangle$ between two electrons localized on the nitrogen $3p_{x,y}$ atomic orbitals. This integral has been numerically estimated to be δ = 1.23 eV. The trial diagonalization gives two energies, $\varepsilon'_1 = \varepsilon_1 - \delta$ and $\varepsilon'_2 = \varepsilon_1 + \delta$ and $\Delta = 2\delta = \varepsilon'_2 - \varepsilon'_1 \approx 1.46$ eV. The low-lying state (ε'_1) belongs to a $^2\Delta$ spectroscopic term while the upper one (ε'_2) belongs to a $^2\Sigma^+$ state symmetry. Using a larger CI space of configurations, it is interesting to note that the valence closed shell $1\sigma_1^2 2\sigma^2 3\sigma^2 1\pi_x^2 \pi_y^0$ ($1\pi_x^0 \pi_y^2$) configurations substantially correlate with $1\sigma_1^1\ 2\sigma^2 3\sigma^0 3p_x^2 3p_y^2$, where two electrons contribute to fill the $3p_{x,y}$ orbitals. This interaction of configurations reduces the Δ energy gap to ≈1.2 eV, which roughly corresponds to the energy difference (1.29 eV) between peaks c $^2\Delta$ and e $^2\Sigma^+$ (Table 3). To conclude this part, peak e is therefore attributed to the ($^2\Pi$) $N1s^2\ 2\sigma^2\ 3\sigma^2\ 1\pi_x^1\ (1\pi_y^1) \rightarrow (^2\Sigma^+)\ N1s^1\ 2\sigma^2\ 3\sigma^2\ 1\pi_x^2$ (or $1\pi_y^2$).

Table 4. Diagonal (ε) and sub-diagonal coupling matrix elements between the $N1s\sigma^1 1\pi_x{}^a 1\pi_y{}^b$ (a = 0 or 1; b = 0 or 1) configurations. β and α denote spin configurations. For example, βαα means $\overline{N_{1s^1}}\ \pi_x^1\ \pi_y^1$. J is a Coulomb matrix element. K is a (positive) exchange matrix element.

$N1s\sigma^1$	$1\pi_x^2$	$1\pi_y^2$	βαα	ααβ	αβα
$1\pi_x^2$	$\varepsilon_{\pi_{x^2}}$	$J_{3p,3p}$	0	0	0
$1\pi_y^2$	$J_{3p,3p}$	$\varepsilon_{\pi_{y^2}} = \varepsilon_{\pi_{x^2}}$	0	0	0
βαα	0	0	$\varepsilon_{\beta\alpha\alpha}$	$-K_{1s,3p}$	$-K_{1s,3p}$
ααβ	0	0	$-K_{1s,3p}$	$\varepsilon_{\alpha\alpha\beta}$	$-K_{3p,3p}$
αβα	0	0	$-K_{1s,3p}$	$-K_{3p,3p}$	$\varepsilon_{\alpha\beta\alpha} = \varepsilon_{\alpha\alpha\beta}$

Transition and results from configuration interaction effects: The corresponding calculated CI-SD oscillator strength is found to be 0.038, i.e., 4.17 Mb eV strength. There are three different spin-configurations, denoted βαα (1), ααβ (2), and αβα (3) for the $N1s\sigma^1\ 2\sigma^2\ 3\sigma^2\ 1\pi_x^1\ 1\pi_y^1$ configuration. The spin configuration (1) differs from (2) and (3) since for the former, the two valence electrons have the same (α) spin, leading to spin-dependent diagonal matrix elements. As a result, the coupling matrix element between (1) and (2)/(3) corresponds to the negative of the exchange integral $K_{1s,3p} = \left\langle 1s(1)3p_{x(y)}(2)\left|\frac{1}{r_{12}}\right|1s(2)3p_{x(y)}(2)\right\rangle = 1.38$ eV.

The coupling matrix between (2) and (3) corresponds to the negative of the exchange integral $K_{3p,3p} = \left\langle 3p_x(1)3p_y(2)\left|\frac{1}{r_{12}}\right|3p_x(2)3p_y(1)\right\rangle$, where $K_{3p,3p} = J_{3p,3p}$.

In the spin-adapted space, the 3 × 3 matrix can be compacted to a 2 × 2 matrix form. The diagonalization gives two eigenvalues (ε''_1 and ε''_2). The energy gap $\delta'' = \varepsilon''_2 - \varepsilon''_1$ is found equal to ≈0.3 eV. The spin function associated with the eigenstate with the ε''_1 eigenvalue is constructed with 75% of the $\frac{1}{\sqrt{6}}(\beta\alpha\alpha(1) - 2\,\alpha\alpha\beta(2) + \alpha\beta\alpha(3))$ spin-function and 25% of the $\frac{1}{\sqrt{2}}(\alpha\beta\alpha(3) - \alpha\alpha\beta(2))$ one. Comparing the values, we found that $\varepsilon''_1 = \varepsilon'_1$, both states forming the so-called $^2\Delta$ spectroscopic term, and the corresponding calculated oscillator strengths are similar and each equal to 0.04 (4.35 Mb eV) (see Table 2).

The vertical energy position at the $^2\Pi$ equilibrium distance (1.065 Å) of the $^2\Delta$ band c is finally determined by adding the vertical energy difference between the $^4\Sigma^-$ core-excited state (394.83 eV) and the $^2\Pi$ initial state to the CI-SD vertical energy gap between the $^4\Pi$ and $^4\Sigma^-$ core-excited states (3.17 eV), plus the $^2\Delta$-$^4\Pi$ energy gap (+0.4 eV) extract from the PEC analysis. Following this procedure, the $^2\Delta$ transition energy is finally estimated to be ~398.40 eV while the $^2\sum^+$ transition energy is estimated to be ~399.63 eV, in reasonable agreement with the experiment.

Interestingly, peak c features a pronounced asymmetrical profile, on the high photon energy side. This is particularly intriguing since (see Figure 2) the $^2\Delta$ CI-SD adiabatic potential energy curves have a similar global minimum (R_{min}) at 1.032 Å, thus the NH bond is shrunk by only –0.032 Å from the $^2\Pi$ ($N1s^2\ 2\sigma^2\ 3\sigma^2\ 1\pi_x^1\ 1\pi_y^0$ or $1\pi_x^0\ 1\pi_y^1$) initial state. The PEC of the ($N1s^2\ 2\sigma^2\ 3\sigma^1\ 1\pi_{x(y)}^2\ 1\pi_{y(x)}^0$) $^2\Delta$ configuration presents a characteristic anharmonic behavior with fundamental vibrational frequency, ω_e, and anharmonicity constant, $\omega_e x_e$, equal to 3250 and 120 cm^{-1}, respectively. The Franck-Condon envelope consists mainly (97 %) of the v = 0 → v′ = 0 vibrational transition with a weak contribution

(3%) of v = 0 → v′ = 1 at 0.38 eV from the main band, which may account for the structure labeled *c*′ in Figure 3a. For the second $^2\Delta$ state corresponding to the N1s^1 2σ^2 3σ^2 1π$_x^1$ 1π$_y^1$ configuration, the PEC is parallel to the former $^2\Delta$ state in the 1–1.6 Å range of interatomic distances and shows two regions at 1.6 Å and 2.0 Å, where the curve crosses with other electronic states. However, the Franck-Condon profile is very similar to that found above, i.e., (97%) of the v = 0 → v′ = 0 vibrational transition with a weak contribution (3%) of v = 0 → v′ = 1 at 0.38 eV from the main band, which contributes to enhance the peak c.

We suggest a spin-orbit (SO) coupling effect between the two $^2\Delta$ (S = 1/2, Λ = 2) doublet states as the cause for this wide asymmetric profile. To support this, we have carried out CI-SD + SO calculations limited to the N1s^1 2σ^2 3σ^2 1π$_x^1$ 1π$_y^1$ and N1s^1 2σ^2 3σ^2 1π$_x^2$ (π$_y^0$) configurations. The spin-orbit coupling thus lifts the degeneracy between the two $^2\Delta$ states and the calculations yield the two J_z = 5/2 and J_z = 3/2 SO components in the 3:2 statistical ratio. The corresponding energy gap (δ_{SO}) is theoretically estimated to ~0.02 eV, the value of which appears somewhat underestimated. To illustrate this (see insert in Figure 3b), we have simulated the 394–400 eV energy region considering two different values of δ_{SO} (0.00 eV, 0.06 eV). As observed, the asymmetric tail of peak c to the high photon energy region is reasonably reproduced when the spin-orbit coupling effect is taken into account.

Peak d $^2\sum^-$

The main peak labeled d on the spectrum corresponds to the $^2\Sigma^-$ state with the final N1sσ^1 2σ^2 3σ^2 1π$_x^1$ 1π$_y^1$ electronic configuration. The associated oscillator strength is calculated to be 0.121. The corresponding spin function is built with contributions of 75% and 25% from the $\frac{1}{\sqrt{2}}(\alpha\beta\alpha(3) - \alpha\alpha\beta(2))$ and $\frac{1}{\sqrt{6}}(\beta\alpha\alpha(1) - 2\alpha\alpha\beta(2) + \alpha\beta\alpha(3))$ spin-adapted configurations, respectively. Analyzing the potential energy curves displayed in Figure 2, the energy difference between $^2\Sigma^-$ and $^2\Delta$ at the initial $^2\Pi$ interatomic distance is nearly 0.40 eV, so that the corresponding transition energy is 398.80 eV, in good agreement with the recorded experimental value of 398.91 ± 0.04 eV. As observed, the PEC is nearly parallel to $^2\Delta$. The vibration frequency value is similar to that of $^2\Delta$, where ω_e (b $^2\Delta$) = 3250 cm^{-1}. The Franck-Condon envelope associated with the $^2\Sigma^-$ state consists, as for $^2\Delta$, of two components with 0.96 and 0.03 relative intensities for the v = 0 → v′ = 0 and v = 0 → v′ = 1 transitions, respectively. Due to the high intensity of peak d, the vibrational component v = 0 → v = 1 (labeled d′) is clearly detectable on the theoretical spectrum and also observed experimentally.

To achieve agreement between the first quartet line $^4\Sigma^-$ at 394.81 eV and peak d $^2\sum^-$ theoretical cross-sections with the experimental data, the relative populations of the $^2\Pi$ and $^4\sum^-$ lower states have to be taken into account. A scaling factor of ~0.5 was applied to the quartet states' theoretical data, bringing a satisfactory accord between theory and experiment. Considering the experimental energy gap (ΔE = 0.071 eV) between the $^2\Pi$ and $^4\sum^-$ electronic ground states, this factor would correspond to an equivalent source plasma equilibrium temperature of ~600 K, although it is realized that temperature may not be a good physical concept in this case.

4.2.3. Region 400–430 eV

The experimental spectrum is compared to the calculated XAS spectrum on Figure 4. It presents unresolved broad structures above 405 up to 430 eV. As reported in Table 2, the most intense lines are mainly due to the excitation of a 1s electron, from the initial doublet $^2\Pi$ or quartet $^4\Sigma^-$ states, to the first low-lying empty orbitals (for example 4σ, 2π) to form Rydberg series, converging on various 1s ionization thresholds ranging between 425 and 430 eV with singlet, triplet, and quintet spin state configurations. The calculated energy position of these thresholds is shown in the top right corner of Figure 4 and more theoretical details are given in Table 5. As indicated by the theory in Table 2, the two most intense lines (labeled f) are close, lying in the 409–412 eV energy region. The first $^4\Sigma^-$ state f lying at 409.04 eV corresponds to a multiple excitation, i.e., 1σ^{2}2σ^{2}3σ^{1}1π$_x^1$1π$_y^1$ → 1σ^{1}2σ^{1}3σ^{2}1π$_x^1$1π$_y^1$4σ^1 transition, where a N1s inner-shell electron is promoted simultaneously with an inner-valence electron (2σ) to doubly fill the 3σ and partially fill the 4σ shell. The second $^2\Pi$

state lying at 412.17 eV corresponds to the $1\sigma^2 2\sigma^2 3\sigma^2 1\pi_{x(y)}{}^1 \rightarrow 1\sigma^1 2\sigma^2 3\sigma^2 1\pi_{x(y)}{}^1 4\sigma^1$ transition, where the N1s inner-shell electron is directly promoted to the 4σ shell. Their oscillator strengths are 0.0332 and 0.0261 respectively, corresponding to strengths of 3.64 and 2.86 Mb eV. Comparing the oscillator strength values reported in Table 2, these two lines are expected to be of similar intensities to peaks within the energy region between 397 and 401 eV.

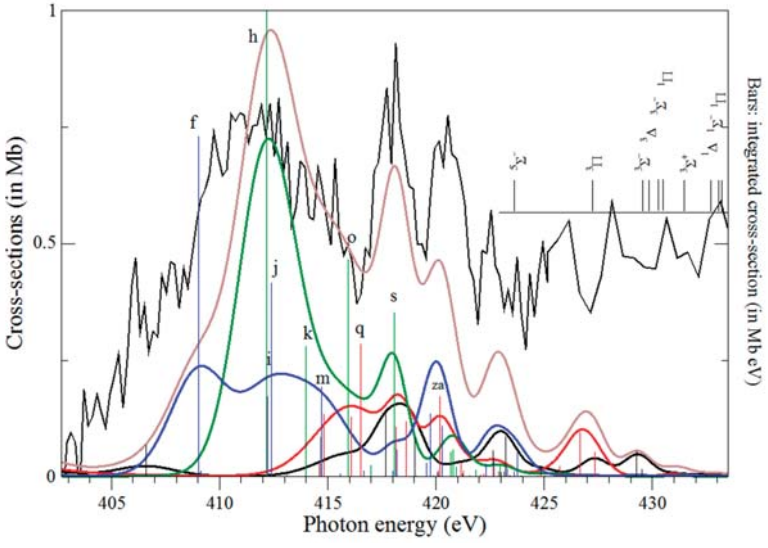

Figure 4. Experimental and simulated spectra in the energy region between 407 and 430 eV. Blue lines/bars: Quartet $^4\Sigma^-$ and $^4\Pi$ states (quartet cross-sections were scaled by a factor of 0.5 to take into account source population effects (see discussion in text)). Green lines: $^2\Pi$ states. Red lines/bars: $^2\Sigma^-$ and $^2\Delta$ states. Black lines/bars: $^2\Sigma^+$ and $^2\Delta$ states. Cross-sections are given in Mb. Bars: Integrated cross-section under the peaks (in Mb eV). Experimental intensities were divided by a factor of eight (see text). The calculated energy positions of the ten lowest lying ionization thresholds are shown in the top right corner.

Table 5. First ten low-lying $N1s^{-1}$ vertical ionization energies calculated at the configuration interaction single and double substitutions (CI-SD) level of theory. *Absolute density functional theory (DFT) triplet ($^2\Pi \rightarrow {}^3\Pi$) and quintet ($^4\Sigma^- \rightarrow {}^5\Sigma^-$) $N1s^{-1}$ vertical ionization energies at R_D = 1.077 Å and R_Q = 1.113 Å respectively, taking into account relativistic corrections (0.2 eV), were used as references. For each final state, the contributions of the main configurations are given in parentheses (%).

Threshold Number	Absolute Energy (eV)	State	Main Configurations
1	423.61 *	$(^5\Sigma^-)_Q$	$1\sigma^1 2\sigma^2 3\sigma^1 1\pi_x{}^1 1\pi_x{}^1$ (97.4)
2	426.93 *	$(^3\Pi)_D$	$1\sigma^1 2\sigma^2 3\sigma^2 1\pi_{x,y}{}^1$
3	429.39	$(^3\Sigma^-)_Q$	$1\sigma^1 2\sigma^2 3\sigma^1 1\pi_x{}^1 1\pi_y{}^1$ (75.6)
4	429.52	$(^3\Delta)_Q$	$1\sigma^1 2\sigma^2 3\sigma^1 1\pi_x{}^1 1\pi_y{}^1$(8.1)/$1\sigma^1 2\sigma^2 3\sigma^1 1\pi_x{}^2$(43.8)/$1\sigma^1 2\sigma^2 3\sigma^1 1\pi_y{}^2$(43.8)
5	429.95	$(^3\Sigma^-)_Q$	$1\sigma^1 2\sigma^2 3\sigma^1 1\pi_x{}^1 1\pi_y{}^1$(87.6)/$1\sigma^1 2\sigma^2 3\sigma^1 1\pi_x{}^2$(4.05)/$1\sigma^1 2\sigma^2 3\sigma^1 1\pi_y{}^2$(4.05)
6	430.22	$(^1\Pi)_D$	$1\sigma^1 2\sigma^2 3\sigma^1 1\pi_x{}^1 1\pi_x{}^1$ (96.2)
7	431.23	$(^3\Sigma^+)_Q$	$1\sigma^1 2\sigma^2 3\sigma^2 1\pi_{x,y}{}^1$
8	432.43	$(^1\Delta)_Q$	$1\sigma^1 2\sigma^2 3\sigma^1 1\pi_x{}^2$(46.0) $1\sigma^1 2\sigma^2 3\sigma^1 1\pi_y{}^2$(46.0)
9	432.79	$(^1\Sigma^-)_Q$	$1\sigma^1 2\sigma^2 3\sigma^1 1\pi_x{}^2$(42.0) $1\sigma^1 2\sigma^2 3\sigma^1 1\pi_y{}^2$(42.0)/$1\sigma^1 2\sigma^2 3\sigma^1 1\pi_x{}^1 1\pi_x{}^1$(8.6)
10	432.87	$(^1\Pi)_Q$	$1\sigma^1 2\sigma^2 3\sigma^1 1\pi_x{}^1 1\pi_x{}^1$(84.0)/ $1\sigma^1 2\sigma^2 3\sigma^1 1\pi_x{}^2$(4.3) $1\sigma^1 2\sigma^2 3\sigma^1 1\pi_y{}^2$(4.3)
			$1\sigma^1 2\sigma^2 3\sigma^1 1\pi_x{}^1 1\pi_y{}^1$ (91.1)
			$1\sigma^1 2\sigma^2 3\sigma^0 1\pi_x{}^1 1\pi_y{}^2$(58.7)/ $1\sigma^1 2\sigma^2 3\sigma^0 1\pi_x{}^2 1\pi_y{}^1$(23.9)
			$1\sigma^1 2\sigma^2 3\sigma^0 1\pi_x{}^2 1\pi_y{}^1$(58.7)/ $1\sigma^1 2\sigma^2 3\sigma^0 1\pi_x{}^1 1\pi_y{}^2$(23.9)

This picture contrasts with the experimental observation which instead shows an unresolved plateau. As displayed in Figure 2, both the PECs associated with the region f clearly present dissociative profiles. For instance, the gradient along the steepest descent (~12.5 eV/Å) at the $^2\Pi$ equilibrium distance is large, and the width of the Franck-Condon profile is estimated to be 2.3 eV. For the $^4\Sigma^-$ state, the gradient is even larger (~16.5 eV/Å) and the energy width of the Franck-Condon profile is estimated to be 3.1 eV.

At higher energies, near 420 eV of photon energy, the spectrum also reveals a number of broad features. The PECs for this energy region have not been explicitly computed. We can assume that high-energy Rydberg core-excited states should present similar behavior as core-ionized states. As a showcase, the DFT numerical gradients F_{NH} were carried out for the triplet ($^3\Pi$, N1s^1 2σ^2 3σ^2 1π$_x$^{1}) and quintet ($^5\Sigma^-$, N1s^1 2σ^2 3σ^1 1π$_x$^{1}1π$_y$^{1}) core-ionized molecular bications, from the formula

$$F_{\nu_{NH}} = \left.\frac{\partial U}{\partial Q_{NH}}\right|_e = \sqrt{\mu_{\nu_{NH}}} \sum_{j=1}^{3N} \frac{A_j^{\nu_{NH}}}{\sqrt{m_j}} \left.\frac{\partial U}{\partial R_j}\right|_e \quad (6)$$

where the gradient $F\nu_{NH}$ is the partial derivative of the final state potential energy surface along the unique stretching normal mode, calculated at the equilibrium geometry, and $A_j^{\nu_{NH}}$ is the output GAMESS (US) column vector of the unitary transformation matrix between the mass weighted Cartesian and normal coordinates for the corresponding mode. As a result, we found $F_{\nu_{NH}}^{^3\Pi}$ = 4.9 eV/Å and $F_{\nu_{NH}}^{^5\Sigma^-}$ = 6.0 eV/Å respectively, corresponding to Gaussian envelopes with FWHMs equal to 0.83 and 1.13 eV. As reported in Table 2, the various spin-state core-ionization thresholds lie over a wide energy range (426–430 eV). In order to simulate the 401–430 experimental energy region of spectrum, we assumed a large FWHM of 2.5 eV for core-excited states lying between 401 and 417 eV and a FWHM of 1.0 eV for core-excited states lying between 417 eV and the ionization thresholds. As observed in Figure 4, the overall shape of the experimental spectrum is fairly well reproduced by theory. However, once the experimental spectrum is normalized to theory on the maximum of peak d, as performed in Figure 3b, the spectral intensity in the energy region 405–430 eV is greater than that of the theoretical spectrum by a factor of 8. One explanation for this discrepancy is that, while theory calculates the absorption spectrum, experiment measures only the N^{2+} fragmentation channel following the creation of the 1s hole. Our results seem to indicate that the relative probability of producing the N^{2+} fragment is higher in the region 405–430 eV than in the region 395–401 eV. A similar argument was proposed by Bari et al. [12] to explain the discrepancy between their theoretical and experimental results. They also observed relative intensity differences between the low- and high-energy regions of their spectra but in their case, by a lower factor of ≈1.8. We also note that the N-K absorption spectrum of NH^+ is characterized by a collection of ionization thresholds extending over more than 10 eV. The low-lying ionization threshold corresponds to ejection of one N1s electron from the $^4\Sigma^-_{(Q)}$ quartet initial state (1σ^{2}2σ^{2}3σ^{1}1π$_x$^{1}1π$_x$^{1}) to form the $^5\Sigma^-_{(Q)}$ state with the 1σ^{1}2σ^{2}3σ^{1}1π$_x$^{1}1π$_x$^{1} open-shell configuration. These direct N1s photoionization processes, contributing to the experimental spectrum of Figure 1a as a more or less constant signal above 425 eV, are not included in the present calculations.

5. Conclusions

We have studied both experimentally and theoretically the excited states of the NH^+ molecular ion by focusing on the N1s inner-shell photo-absorption spectrum in the photon energy region 390–450 eV. The experiments used an ECR plasma molecular ion source coupled with monochromatized synchrotron radiation in a merged-beam configuration. The experimental spectrum was obtained by detection of the N^{2+} photofragments. The photon bandwidth was narrow enough to partially resolve the vibrational distributions in the 1s → π* transitions. The interpretation of the experimental spectrum was undertaken based on a comparison with the total photo-absorption cross-sectional profiles

calculated using ab-initio configuration interaction theoretical methods inclusive of spin-orbit coupling and vibrational dynamics.

Author Contributions: Conceptualization, J.-M.B., D.C., S.G., J.-P.M., and E.T.K.; methodology, E.S., D.C., J.-M.B., J.-P.M., B.M., and E.T.K.; software, S.C., B.M., and D.C.; validation, J.-P.M., D.C., J.-M.B., E.S., and E.T.K.; formal analysis, J.-P.M., E.S., J.M.B., E.T.K., and S.C.; investigation, J.-M.B., J.-P.M., E.T.K., S.C., and E.S.; resources, S.C. and J.-M.B.; data curation, S.G.; writing—original draft preparation, S.C., J.M.B., J.-P.M., and B.M.; writing—review and editing, S.C., J.-M.B., J.-P.M., and E.T.K.; visualization, J.-M.B. and S.C. All authors have read and agreed to the published version of the manuscript.

Funding: This research received no external funding.

Acknowledgments: The authors would like to thank SOLEIL for the award of beamtime and the SOLEIL staff J. Bozek, C. Nicolas, and A. Milosavljevic for assistance in using the PLEIADES beamline. E.K., B.M.L., and J.-P.M. would like to thank SOLEIL for financial help with accommodation and subsistence during beamtime.

Conflicts of Interest: The authors declare no conflict of interest.

References

1. Gerin, M.; Neufeld, D.A.; Goicoechea, J.R. Interstellar Hydrides. *Annu. Rev. Astron. Astrophys.* **2016**, *54*, 181–225. [CrossRef]
2. Rednyk, S.; Roucka, Š.; Kovalenko, A.; Tran, T.D.; Dohnal, P.; Plašil, R.; Glosík, J. Reaction of NH^+, NH_2^+, and NH_3^+ ions with H_2 at low temperatures. *Astron. Astrophys.* **2019**, *625*, A74. [CrossRef]
3. Le Gal, R.; Hily-Blant, P.; Faure, A.; Pineau des Forêts, G.; Rist, C.; Maret, S. Interstellar chemistry of nitrogen hydrides in dark clouds. *Astron. Astrophys.* **2014**, *562*, A83. [CrossRef]
4. Wagenblast, R.; Williams, D.A.; Millar, T.J.; Nejad, L.A.M. On the origin of NH in diffuse interstellar clouds. *Mon. Not. R. Astron. Soc.* **1993**, *260*, 420–424. [CrossRef]
5. Amero, J.M.; Vazquez, G.J. Electronic Structure of NH^+: An Ab Initio Study. *Int. J. Quantum Chem.* **2005**, *101*, 396–410. [CrossRef]
6. Chen, C.T.; Ma, Y.; Sette, F. *K*-shell photoabsorption of the N_2 molecule. *Phys. Rev. A* **1989**, *40*, 6737. [CrossRef]
7. Mosnier, J.-P.; Kennedy, E.T.; Van Kampen, P.; Cubaynes, D.; Guilbaud, S.; Sisourat, N.; Puglisi, A.; Carniato, S.; Bizau, J.-M. Inner-shell photoexcitations as probes of the molecular ions CH^+, OH^+, and SiH^+: Measurements and theory. *Phys. Rev. A* **2016**, *93*, 061401. [CrossRef]
8. Kennedy, E.T.; Mosnier, J.-P.; Van Kampen, P.; Bizau, J.M.; Cubaynes, D.; Guilbaud, S.; Carniato, S.; Puglisi, A.; Sisourat, N. Evolution of L-shell photoabsorption of the molecular-ion series SiH^{n+} (n = 1,2,3): Experimental and theoretical studies. *Phys. Rev. A* **2018**, *97*, 043410. [CrossRef]
9. Klumpp, S.; Guda, A.A.; Schubert, K.; Mertens, K.; Hellhund, J.; Müller, A.; Schippers, S.; Bari, S.; Martins, M. Photoabsorption of the molecular IH cation at the iodine 3d absorption edge. *Phys. Rev. A* **2018**, *97*, 033401. [CrossRef]
10. Lindblad, R.; Kjellsson, L.; Couto, R.C.; Timm, M.; Bülow, C.; Zamudio-Bayer, V.; Lundberg, M.; Von Issendorff, B.; Lau, J.T.; Sorensen, S.L.; et al. X-ray Absorption Spectrum of the N_2^+ Molecular Ion. *Phys. Rev. Lett.* **2002**, *124*, 203001. [CrossRef]
11. Couto, R.C.; Kjellsson, L.; Ågren, H.; Carravetta, V.; Sorensen, S.L.; Kubin, M.; Bülow, C.; Timm, M.; Zamudio-Bayer, V.; von Issendorff, B.; et al. The carbon and oxygen K-edge NEXAFS spectra of CO^+. *Phys. Chem. Chem. Phys.* **2020**, *22*, 16215–16223. [CrossRef] [PubMed]
12. Bari, S.; Inhester, L.; Schubert, K.; Mertens, K.; Schunck, J.O.; Dörner, S.; Deinert, S.; Schwob, L.; Schippers, S.; Müller, A.; et al. Inner-shell X-ray absorption spectra of the cationic series NH_y^+ (y = 0–3). *Phys. Chem. Chem. Phys.* **2019**, *21*, 16505–16514. [CrossRef] [PubMed]
13. Bizau, J.M.; Cubaynes, D.; Guilbaud, S.; El Hassan, N.; Al Shorman, M.M.; Bouisset, E.; Guigand, J.; Moustier, O.; Marié, A.; Nadal, E.; et al. A merged-beam setup at SOLEIL dedicated to photoelectron–photoion coincidence studies on ionic species. *J. Electron Spectrosc. Relat. Phenom.* **2016**, *210*, 5–12. [CrossRef]
14. Gharaibeh, M.F.; Bizau, J.M.; Cubaynes, D.; Guilbaud, S.; El Hassan, N.; Al Shorman, M.M.; Miron, C.; Nicolas, C.; Robert, E.; Blancard, C.; et al. K-shell photoionization of singly ionized atomic nitrogen: Experiment and theory. *J. Phys. B At. Mol. Opt. Phys.* **2011**, *44*, 175208. [CrossRef]

15. Becke, A.D. Density-functional thermochemistry. III. The role of exact exchange. *J. Chem. Phys.* **1993**, *98*, 5648–5652. [CrossRef]
16. Lee, C.; Yang, W.; Parr, R.G. Development of the Colle-Salvetti correlation-energy formula into a functional of the electron density. *Phys. Rev. B* **1988**, *37*, 785–789. [CrossRef] [PubMed]
17. Schmidt, M.W.; Baldridge, K.K.; Boatz, J.A.; Elbert, S.T.; Gordon, M.S.; Jensen, J.H.; Koseki, S.; Matsunaga, N.; Nguyen, K.A.; Su, S.; et al. Montgomery, General atomic and molecular electronic structure system. *J. Comput. Chem.* **1993**, *14*, 1347–1363. [CrossRef]
18. Prince, K.C.; Vondráček, M.; Karvonen, J.; Coreno, M.; Camilloni, R.; Avaldi, L.; de Simonel, M. A critical comparison of selected 1s and 2p core hole widths. *J. Electron Spectrosc. Relat. Phenom.* **1999**, *101*, 141–147. [CrossRef]
19. Woon, D.E.; Dunning, T.H. Gaussian basis sets for use in correlated molecular calculations. V. Core-valence basis sets for boron through neon. *J. Chem. Phys.* **1995**, *103*, 4572–4585. [CrossRef]
20. Colin, R. Perturbations between the $X^2\Pi$ and $a^4\Sigma^-$ states of the NH^+ ion. *J. Mol. Spec.* **1989**, *136*, 387–401. [CrossRef]
21. Feller, D.; Sordo, J.A. A CCSDT study of the effects of higher order correlation on spectroscopic constants. I. First row diatomic hydrides. *J. Chem. Phys.* **2000**, *112*, 5604–5610. [CrossRef]
22. Wilson, D.L. Λ-type doubling in the molecules $^{14}NH^+$, $^{15}NH^+$, and $^{14}ND^+$. *Mol. Phys.* **1978**, *36*, 597–610. [CrossRef]

atoms

MDPI

Article

An Investigation of Laser Produced Lead-Tin Alloy Plasmas between 10 and 18 nm

Enda Scally [1,*], Fergal O'Reilly [2], Patrick Hayden [2], Isaac Tobin [2] and Gerry O'Sullivan [2]

[1] School of Electronic and Electrical Engineering, Technological University Dublin, D08 NF82 Dublin 8, Ireland
[2] School of Physics, University College Dublin, Belfield, D04 N2E5 Dublin 4, Ireland; f.oreilly@ucd.ie (F.O.); patrick.hayden@ucd.ie (P.H.); todindi@tcd.ie (I.T.); gerry.osullivan@ucd.ie (G.O.)
* Correspondence: enda.scally@tudublin.ie

Received: 9 September 2020; Accepted: 14 October 2020; Published: 20 October 2020

Abstract: The results of a systematic study performed on Pb-Sn alloys of concentration 65–35% and 94–6% by weight along with spectra from pure Pb and Sn in the wavelength range of 9.8–18 nm are presented. The dynamics of the Nd:YAG laser produced plasma were changed by varying the focused spot size and input energy of the laser pulse; the laser irradiance at the target varied from 7.3×10^9 W cm^{-2} to 1.2×10^{12} W cm^{-2}. The contributing ion stages and line emission are identified using the steady state collisional radiative model of Colombant and Tonon, and the Cowan suite of atomic structure codes. The Sn spectrum was dominated in each case by the well-known unresolved transition array (UTA) near 13.5 nm. However, a surprising result was the lack of any enhancement or narrowing of this feature at low concentrations of Sn in the alloy spectra whose emission was essentially dominated by Pb ions.

Keywords: Pb-Sn alloys; EUV emission of high Z materials; collisional radiative model; Cowan suite of Codes

1. Introduction

The emission from Sn in a 2% bandwidth at 13.5 nm arising from $\Delta n = 0$, n = 4–4 transitions, has become the definitive source of choice for extreme ultraviolet (EUV) lithography systems. This emission results from an intense unresolved transition array (UTA) whose width and intensity are strongly influenced by plasma opacity [1]. For pure Sn targets, plasmas produced by a solid state $\lambda \sim 1$ μm laser, the UTA is broad and overlaid with numerous strong absorption lines, while with decreasing concentration the intensity increases while the width decreases significantly due to increased radiation transport of the most intense transitions and the intensity reaches a maximum at a concentration of a few % [2]. For plasmas produced with CO_2 lasers ($\lambda = 10.6$ μm) the reduction in critical electron density (and consequently ion density) results in a greater UTA intensity and laser to EUV emission conversion efficiency (CE); again due to the reduction in plasma opacity resulting from a lower ion density [3]. Consequently, CO_2 lasers are used to excite the UTA emission in current lithography sources. Despite the advances in EUV lithography, work is still ongoing regarding metrology sources for reflectometry, surface patterning, surface chemical analysis, etc. [4]. Fahy *et al.* proposed a liquid collector optic to mitigate the debris associated with laser produced plasmas (LPPs) and multilayer optics [5]. Following this Kambali *et al.* proposed using LPPs from Au or an Au-Sn alloy as a metrology source in the 10 to 18 nm region where Au has a relatively flat spectrum with the added attraction that the alloy had a melting temperature of 280 °C and thus could be used as an easily renewable plasma fuel [6]. Similar work by Tobin *et al.* in the 10 to 18 nm region utilised a room temperature gallium alloy (galinstan) source in a laser triggered discharge plasma (LDP), they obtained a relatively flatter spectrum with respect to a pure Sn plasma and an emission structure that reflected the presence of its composite elements [7].

Here the results of a systematic study performed on Pb-Sn alloys of concentration 65–35% and 94–6% by weight, along with spectra from pure Pb and Sn, in the wavelength range of 9.8–18 nm is presented. The dynamics of the Nd:YAG laser plasma were changed by varying the focused spot size and input energy of the laser pulse. The contributing transitions and thus ion stages were identified using the Hartree Fock with configuration interaction (CI) suite of codes written by Cowan [8,9]. To aid in understanding the binary plasmas, the results are compared to the optically thinner CO_2 plasmas and thus contribute to building a database of the spectral emission of high Z materials in the 9.8–18 nm region. The Pb-Sn alloy which in a ratio of 65–35 has a minimum eutectic melting point of ≈ 183 °C, has the potential to provide a clean and bright broadband microscopy or reflectometry EUV source when combined with a suitable renewable liquid optic.

2. Experimental

A schematic of the experimental set-up is shown in Figure 1, where; 1: is a Continuum Surelite III Nd:YAG laser system with a full width at half maximum intensity (FWHM) pulse of 5 ns, and an $M^2 = 3.5$; 2: half wave-plate + beam-splitter energy selector for the Nd:YAG laser; 3: labels the Optosystems Infralight SP10 gas flow transversely excited atmospheric (TEA) pulsed laser system (CO_2 laser; $M^2 = 4$); 4: the CO_2 pulse plasma shutter; 5: the steering optic; 6: the CO_2 pulse profiler; 7: the CO_2 laser focusing lens (f = 20 cm) and 8: the Nd:YAG laser focusing lens (f = 10 cm). Both the lens and target can be moved in vacuum using an interface program to control the actuators to a precision of 1 μm. As seen from Figure 1, the Nd:YAG laser was incident along the target normal, the CO_2 laser was incident at 45 degrees to the target normal and the spectrometer viewed the plasma at 45 degrees to the target normal. The focal position of the lens was found by finding the local minimum value in CE for a 2% bandwidth at 13.5 nm as a function of lens position close to focus [10].

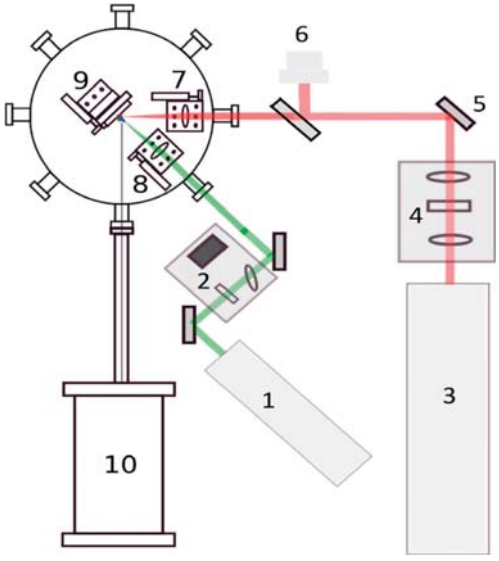

Figure 1. Experimental layout; 1: Nd:YAG laser, 2: Nd:YAG energy selector, 3: CO_2 laser, 4: plasma shutter, 5: steering mirror, 6: pulse profiler, 7: CO_2 focusing lens, 8: Nd:YAG focusing lens, 9: x, y, z target motion, 10: spectrometer.

The CO_2 pulse was shortened to remove the low energy tail using a plasma shutter based on the method pioneered by Hurst and Harilal; the shortened pulse had a FWHM of 21 ns and an energy of

≈100 mJ after the plasma shutter [11]. In this paper, only the shortened CO_2 pulse was used to form a plasma, it will hereafter be referred to as the CO_2 pulse.

The target was cleaned with the first laser shot to remove any contaminants left on the surface of the material; for all Nd:YAG spectra presented an average of five spectra recorded from the second shot was taken whereas for the CO_2, single shot LPP spectra are presented. The target was translated by 1 mm after each spectrum was captured. The chamber and spectrometer were pumped to a base pressure of 10^{-6} mbar.

The spectrometer is a grazing incidence JenOptik E-spec EUV spectrograph, which uses a Hitachi variable line spaced spherical grating (radius of curvature = 0.25 m) to form an image on a vertical plane (flat field effect). The spherical aberration corrected grating has 1200 lines per mm and forms an absolutely calibrated spectrum in the 9.8–18 nm region. The charge coupled device (CCD) camera of the spectrograph was cooled to −13 °C before spectra were captured.

The targets were prepared by melting weighed amounts of Pb and Sn in a dish using a hot plate to give target concentration ratios for Pb-Sn of 65–35 and 94–6 respectively. To check the target concentration before performing the experiment, the targets were sampled using a scanning electron microscopy (SEM) with energy dispersive X-ray spectroscopy (EDX), the results are presented in Table 1 and represent the average of 5 measurements and the variation in elemental composition. The errors in composition arise from the variation noted at different target locations and are reduced over the laser focal spot area. Given that average spectra from 5 shots were taken, the quoted mean composition represents a good estimation of the plasma elemental composition. In addition, the samples were also found to contain a small amount of oxygen and carbon on the surface. The composition for the alloy targets are relative Pb-Sn %, and do not include the % weight of oxygen and carbon that were present on the surface; whereas the % weight for the pure metals are with the inclusion of oxygen and carbon contaminants. The absence of any lines due to oxygen or carbon ions shows the effectiveness of the first laser shot in removing these species.

Table 1. Summary of the percentage weight of lead and tin in the samples and relative compositions of lead and tin in the alloy.

Sn Percentage Weight [%]	Pb Percentage Weight [%]
93 ± 4	
	84 ± 6
6 ± 1	94 ± 10
35 ± 26	65 ± 25

3. Theoretical Calculations

3.1. Collisional Radiative Model

Since both coronal equilibrium (CE) and local thermodynamic equilibrium (LTE) apply to the inner and outer regions of the plasmas respectively, it is best to adopt a model that incorporates both and also describes the region in between which corresponds to the bulk of a LPP. In this study the collisional radiative model (CR model) adapted by Colombant and Tonon (1973 [12] from the collisional radiative recombination coefficients of Bates *et al*. [13] is used). The CR model approximates to the CE model at low electron densities and the LTE model at high electron densities as the dominant recombination mechanism shifts from radiative recombination to three-body recombination with increasing electron density, the ion fractions are obtained on the assumption that the plasma is steady-state. This model provides total charge state densities for each ion, but it neglects the distribution of electrons amongst the excited states within an ion distribution. It also does not account for autoionization and dielectronic recombination but assumes that collisional ionization, radiative recombination, and three body recombination dictate the population state of charge (n_z) at electron temperature (T_e). The plasma is therefore assumed to be optically thin to its own radiation; in this study the required ionization

potentials were calculated using the Cowan code. According to the CR model, Equation (1) gives the electron temperature T_e (eV) as a function of laser irradiance (ϕ in W cm^{-2}):

$$T_e(\text{eV}) \approx 5.2 \times 10^{-6} Z^{\frac{1}{5}} \left[\lambda^2 \phi\right]^{\frac{3}{5}} \quad (1)$$

where Z is the atomic number of the material and λ is the wavelength of the laser in μm. Figure 2 shows the ion fractions for T_e = 10 eV–100 eV for Pb (blue) and Sn (red) plasmas.

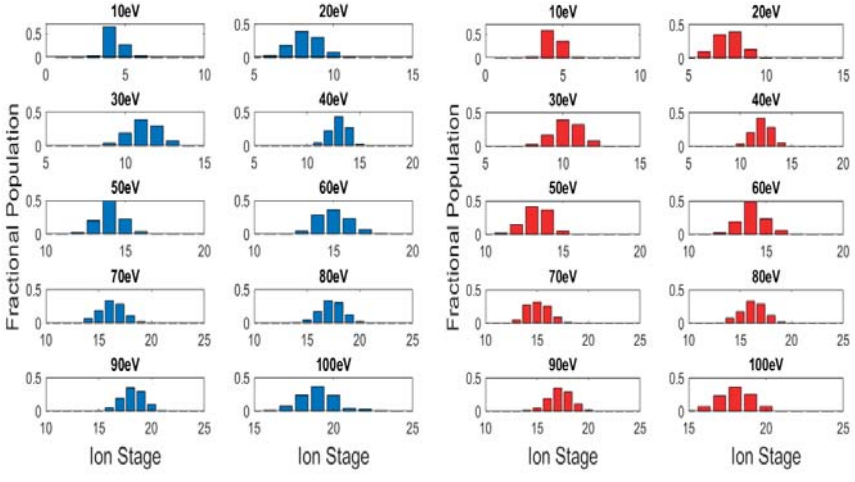

(**a**) (**b**)

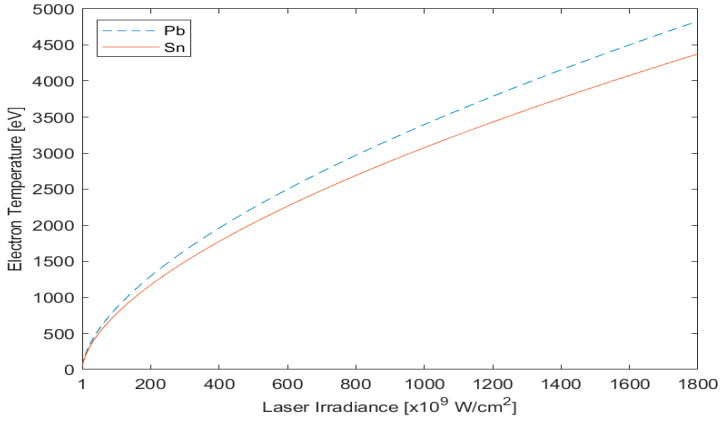

(**c**)

Figure 2. Ion stage populations for Pb (**a**) and Sn (**b**) plasmas for electron temperatures of 10 eV–100 eV. The bottom graph (**c**) shows electron temperature as a function of input laser irradiance.

3.2. Atomic Structure Calculations

Theoretical spectra for a large number of Sn and Pb ion stages were calculated with the CI Cowan RCN, RCN2 and RCG suite of codes [9]. For the calculations performed in this study; the average energy of the configurations was left unchanged as it was found to give good agreement with experiments to

typically within 0.5 eV [14]. Since the calculated values of the Slater-Condon parameters are, in general, overestimated it is necessary to scale them, the scaling factor depends on the configuration of interest and approaches unity when the energy levels are close to hydrogenic. This can be understood as a requirement to take account of internal configuration perturbations not allowed for with a finite wavefunction basis or equivalently the effects of higher electron correlation on the level separation within a configuration [8]. The spectrum of Sn has been well documented in the literature [15–17] and the atomic transitions contributing to the emission in this region have been identified as being predominantly 4p–4d, 4d–4f and 4d–5p [4]. In the case of the Cowan code calculations of Sn, the spin orbit parameter was left unchanged while the F^k, G^k and R^k integrals were reduced by 25% of their ab initio values for Sn V and increased in steps to 85% of their ab initio values for Sn XX, the additional relativistic and correlation corrections were included for both the Sn and Pb calculations. The transitions included in the Sn calculation were the 4p–*m*d + *n*s (*m* = 4–5, *n* = 5–7) and 4d–*m*f + *n*p (*m* = 4–8, *n* = 5–7) for Sn V–Sn XIV; and 4s–*m*p (*m* = 4–7) and 4p–*m*d + *n*s (*m* = 4–7, *n* = 5–7) for Sn XIV–Sn XX.

Figure 3 presents theoretical spectra calculated with the Cowan code for Sn V–Sn XX ions, the weighted transition probabilities (gA values) were convolved with a Gaussian of width 0.01 nm and normalized in the 9.8–18 nm region. The 4d–4f transitions first appear as the feature on the far right in Sn VII, and following the onset of excited state CI of the type $4p^6 4d^N 4f + 4p^5 4d^{N+1}$ at Sn VI shift to shorter wavelength with increasing ionization. For Sn XI the 4d–5p transitions can be seen at 16 nm, which also shift to shorter wavelength with increasing ionization to overlap with the 4p–4d and 4d–4f lines in Sn XIII. From Sn XV onwards the emission observed is solely from 4p–4d excitation in ions with a $4p^N$ ground configuration, many lines of which have been recently identified [18,19].

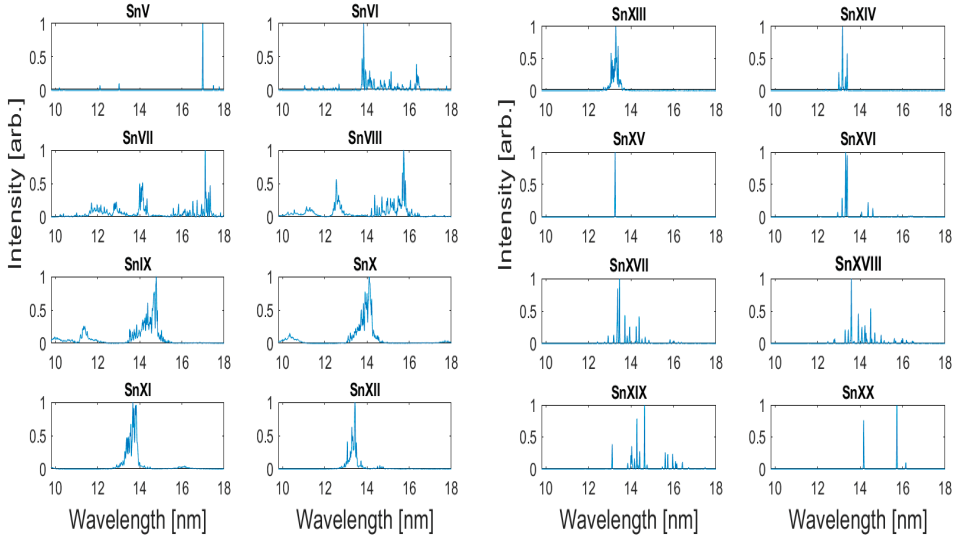

Figure 3. Theoretical spectra calculated with the Cowan suite of codes for Sn V–Sn XX ions, weighted transition probabilities are convolved with a Gaussian of width 0.01 nm and normalized in the 9.8–18 nm region. (See text.).

The emission from Pb in this region is less well documented; earlier work by Bridges *et al.* identified broad UTA features at around 12.5 nm and 16 nm with a dip in the spectrum near 14 nm [20]. Churilov *et al.* identified 9 lines from $5s^2 5p^6 5d$ – ($5s^2 5p^5 5d6s + 5s^2 5p^6 7p$) transitions of PbXIV [21]. In a later study Churilov *et al.* identified 57 lines from $5p^6 5d$ – ($5p^6 5f + 5p^6 6p + 5p^5 5d^2 + 5p^5 5d6s$) transitions in Pb XIV between 9.9 and 20.5 nm [22]; while Kaufman *et al.* identified 6 lines from $5p^6 4f^{14}$ – ($5p^6 4f^{13} 5d^1 + 5p^5 5d^1 + 5p^5 6s$) transitions in Pb XV [23].

In other related work by Carroll *et al.* [24,25] LPP spectra between 7 nm and 13.5 nm from uranium and thorium were found to be dominated by 5d–5f transition array emission which peaks around 9.5 nm and 10.5 nm respectively with a second UTA observed in the thorium spectr a at 8–9.5 nm primarily due to 5p–5d transitions. Liu *et al.* has identified emission bands in Bi plasmas between 8 nm and 17 nm from 5p–5d, 5d–5f, 5s–5p and 5f–5g transitions in ion stages from Bi^{23+}–Bi^{35+} [26]. In other related work Liu *et al.* carried out a study to assess the effects of CI on the UTA emission from $5p^6 5d^{N+1} - 5p^5 5d^{N+2} + 5d^N 5f^1$ transitions in elements Au to U [27].

The line emission from Pb in the 9.8–18 nm region for the range of laser power densities applied originates predominantly from ions with open 5d and 5p subshells. In the case of Pb VII–Pb XIV, emission predominantly originates from 5d–5f, 5p–5d, 5d–6p and 5p–6s transitions. For Pb XV–Pb XX the emission originates from 5p–5d and 5s–5p transitions. Figure 4 shows the calculated positions of 5p–6d (cyan), 5d–6f (magenta), 4f–5d (black), 5p–5d (red), 5d–5f (blue), 5d–6p (yellow), 5p–6s (green) for Pb VI–Pb XIV and 5s–5p (magenta), 5p–5d (red) for Pb XV–Pb XX, plotted as a function of increasing ionization. With increased ionization the emission can be seen to move slightly to higher energy. Each transition array is normalized against the highest gA value for that array in the 9.8–18 nm region.

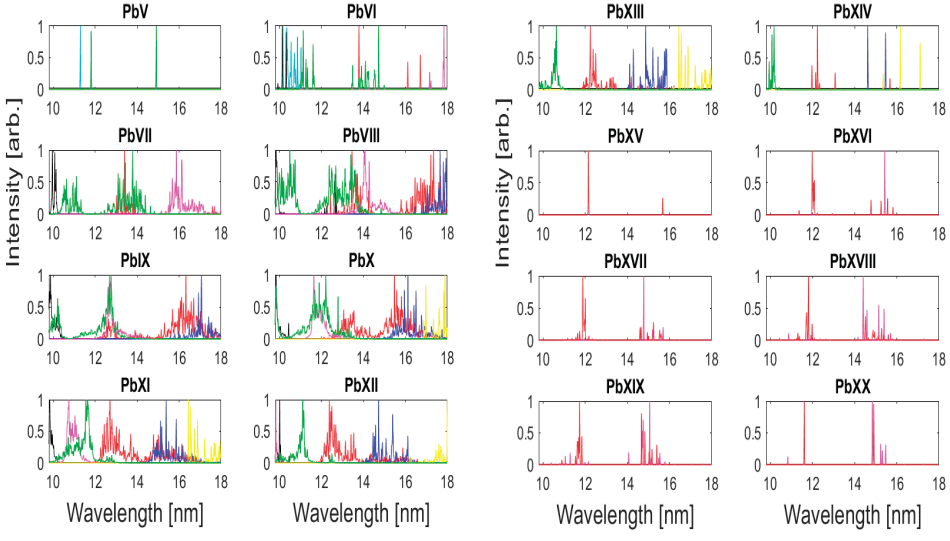

Figure 4. Relative intensity versus wavelength for 5p–6d (cyan), 5d–6f (magenta), 4f–5d (black), 5p–5d (red), 5d–5f (blue), 5d–6p (yellow), 5p–6s (green) for Pb VI–Pb XIV and 5s–5p (magenta), 5p–5d (red) for Pb XV–Pb XX. The weighted transition probabilities are convolved with a Gaussian of width 0.01 nm and while each transition array is normalized against the highest gA value for that array in the 9.8–18 nm region. (Colour online; See text.)

The transitions included in the calculation were the 4f–5d, 5d–*m*f ($m = 5$–7) + *n*p ($n = 6$–7) and 5p–*m*d ($m = 5$–7) + *n*s ($n = 6$–7) for Pb V–Pb XIV, (where the $4f^{13}5s^2 5p^6 5d^N 6s^1$ complex configuration was included to allow for the effects of mixing with the $5p^5 5d^N 6s^1$ configuration); 5p–*m*d + *n*s (m=5–7, n= 6–7), 4f–*m*d (m= 5–6) and 5s–*m*p (m= 5–6) for Pb XV–PbXX. The configurations included in the calculations have been limited to the most important ones, while doubly excited configurations have been neglected to limit calculation time; it is well known that $\Delta n \geq 2$ transitions are, in general, collisionally quenched in LPPs with an electron density of 10^{21} cm^{-3} and are therefore not included in the theoretical spectra presented. Figure 5 presents theoretical spectra calculated with the Cowan code for Pb V–Pb XX ions, the weighted transition probabilities (gA values) were convolved with a Gaussian of width 0.01 nm and normalized in the 9.8–18 nm region.

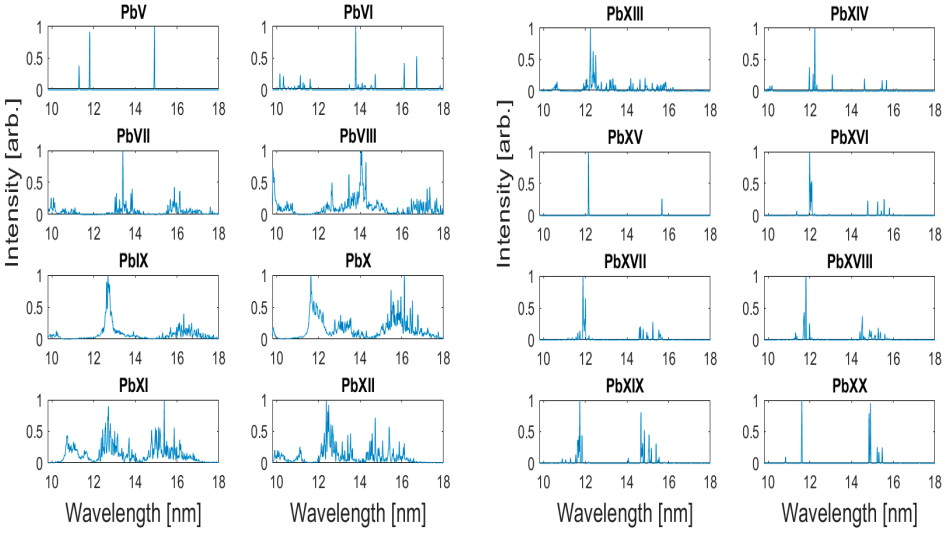

Figure 5. Theoretical spectra calculated with the Cowan code for Pb V–Pb XX ions, the weighted Table 0. nm and normalized in the 9.8–18 nm region. (See text.).

In these calculations the spin orbit parameters were again left unchanged while the F^k, G^k and R^k integrals were reduced by 13% for Pb V to give the best agreement with the $5d^96p^1$ energy levels identified by Goldsmith and Conway [28]. Generally, a reduction in the scaling of F^k, G^k and R^k with increasing ionization is necessary to obtain agreement between calculated and experimental spectra. However, it was found that leaving the values of ζ unchanged, and reducing F^k, G^k and R^k by 13% gave the best agreement with the $5s^25p^65d$ – ($5s^25p^55d6s$ + $5s^25p^67p$) lines of Pb XIV observed by Churilov and Joshi [21]. For Pb XV, ζ value was left unchanged while the F^k, G^k and R^k parameters were reduced by 20% to match the $5p^64f^{14}$ – ($5p^64f^{13}5d^1$ + $5p^55d^1$ + $5p^56s$) lines identified by Kaufman and Sugar [23], no extrapolation beyond Pb XV was carried out and the scaling of the Slater integrals was left unchanged for higher ion stages. Regarding the lines identified by Kaufman and Sugar it should be noted that the $5p^6$ – $5p^55d$ $(3/2,5/2)_1$ line observed at 14.4252 nm in Pb XV was calculated to lie at 15.679 nm, while for all the various scaling ratios tried better agreement was observed if their identification for the $4f^{14}$–$4f^{13}5d$ $(5/2,5/2)_1$ at 7.9564 nm and $5p^6$–$5p^56s$ $(1/2,1/2)_1$ at 7.9959 nm were interchanged; unfortunately, neither of these lines are observed experimentally in the current study.

With increasing ionization, the coupling scheme tends to jj but most commonly, the electronic structure will be best represented by a coupling scheme intermediate between the two extremes of LS or jj, as in general neither the spin-orbit or Coulomb interaction will ever go to zero. In the current study it was found that a higher eigenvector purity could be obtained using a Jj coupling nomenclature, as opposed to the LS coupling labels used by Churilov and Joshi. To remove the ambiguity involved in Jj coupling labels the ground states are labelled with an LS term, as regards the excited states the assignment of the core electrons is done using an LS term for the leading eigenvector followed by a J value for the core electrons, with a j value for the outer subshell being presented and the usual J subscript for the eigenstate.

4. Results

4.1. Effects of Input Laser Energy on Continuum Emission in the 10–18 nm Region

Figures 6–10 show spectra recorded with the Nd:YAG laser for laser focal spots radii of 41 μm (1 mm from focus), 100 μm (2.5 mm from focus), 200 μm (5 mm from focus), 300 μm (7.5 mm from

focus) and 400 μm (10 mm from focus); and energy values of 185 mJ, 270 mJ, 350 mJ and 450 mJ at the target; the power densities range from 7.3×10^9 W cm^{-2}–1.2×10^{12} W cm^{-2}. The focal spot sizes where estimated assuming a Gaussian laser beam and employing the Rayleigh length formula. The dip in the experimental spectrum from 12.36–12.43 nm is due to an error in the intensity calibration of the spectrograph at this wavelength which corresponds to the silicon L-edge. It is present in all spectra and hereafter will be ignored.

As can be seen from Figure 6 to Figure 9, an increase in laser input energy corresponds to an increase in continuum emission. This can be explained by a greater ablated mass, which scales according to $\phi^{5/9}$ for a fixed pulse duration resulting in a larger number of emitting ions present in the plasma [29,30]. Cummings *et al.* performed time dependent spatially resolved calculations of ion and electron density, and found that increasing the laser energy creates a plasma with a shorter high density gradient and a longer low density gradient that reduces self-absorption [31]. The overall peak of the emission also shifts to shorter wavelength for Pb as the 5d subshell empties and the 5p subshell emission takes over. Absorption within the emission band region also increases due to an increase in free electrons available in the outer plasma to repopulate ions of a lower charge state; this is most evident in the Sn spectra.

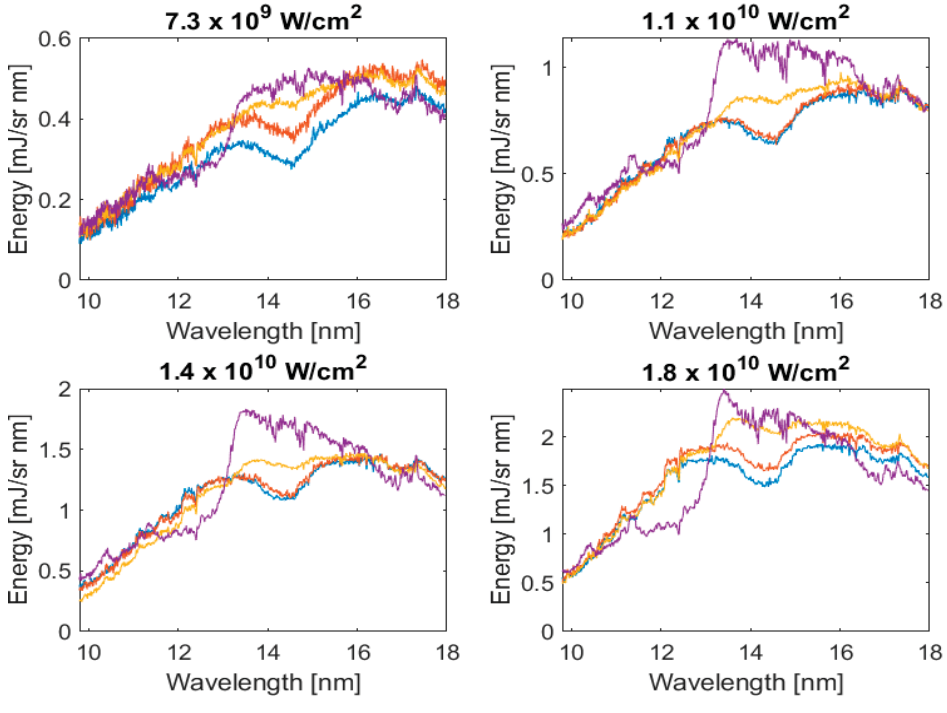

Figure 6. Spectra recorded for a fixed spot radius of 400 μm; the laser energies were 185 mJ, 270 mJ, 350 mJ, 450 mJ; blue: Pb, red: PbSn946, yellow: PbSn6535 and purple: Sn.

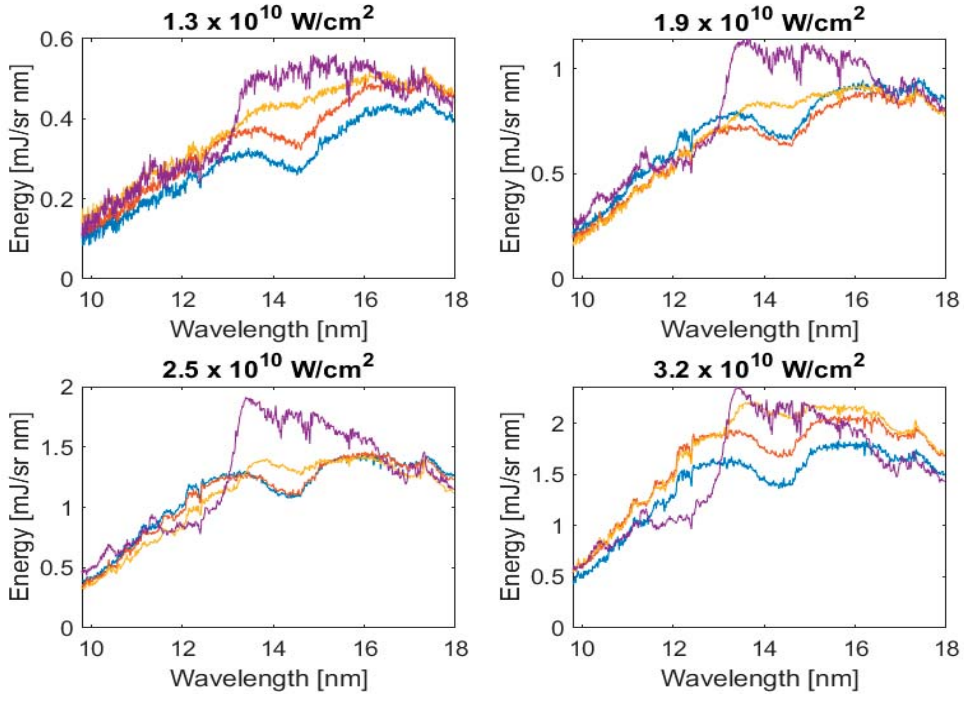

Figure 7. Spectra recorded for a fixed spot radius of 300 μm; the laser energies were 185 mJ, 270 mJ, 350 mJ, 450 mJ; blue: Pb, red: PbSn946, yellow: PbSn6535 and purple: Sn.

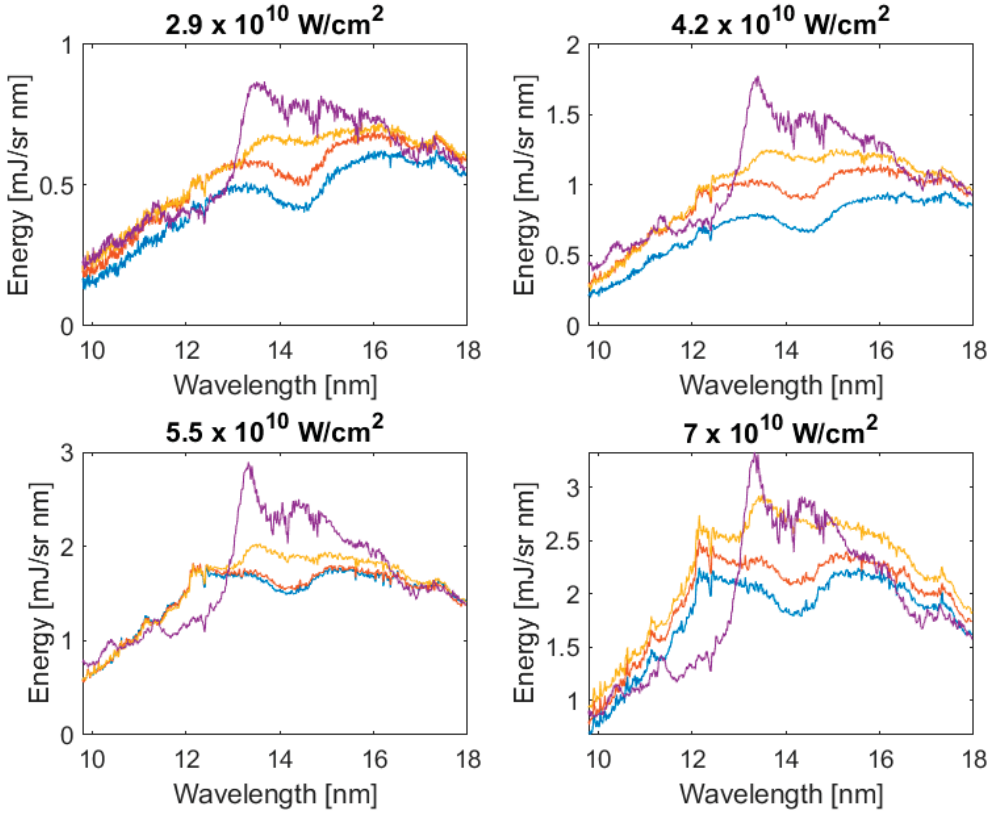

Figure 8. Spectra recorded for a fixed spot radius of 200 μm, the laser energies were 185 mJ, 270 mJ, 350 mJ, 450 mJ; blue: Pb, red: PbSn946, yellow: PbSn6535 and purple: Sn.

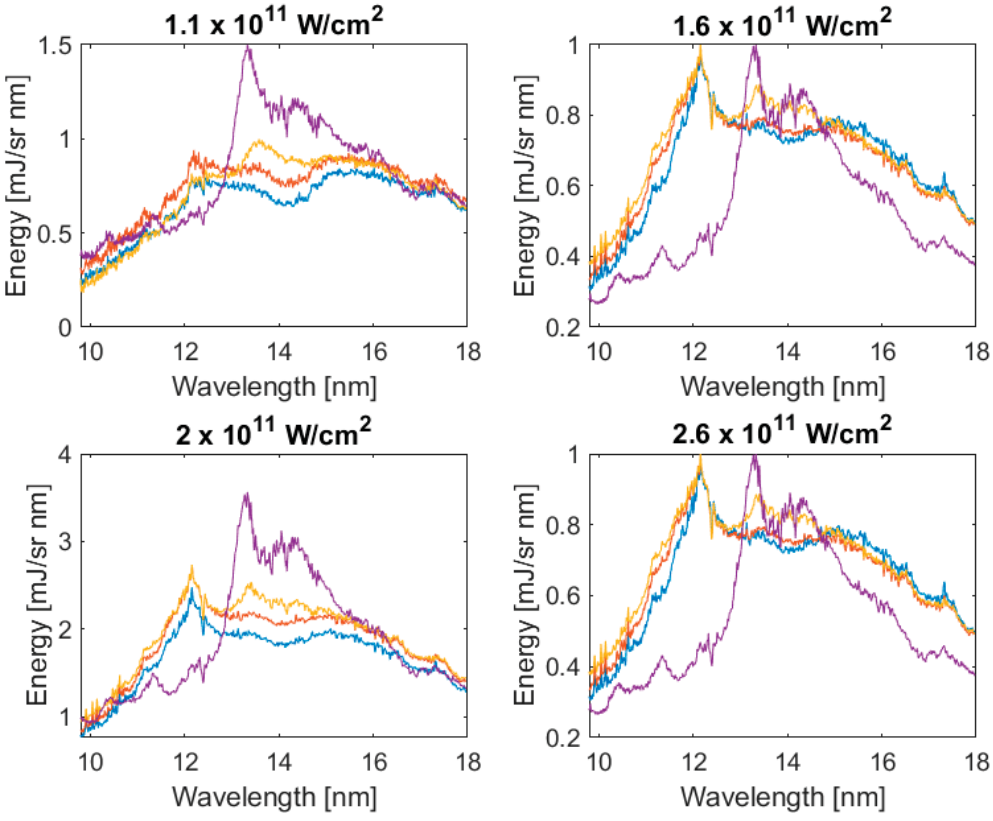

Figure 9. Spectra recorded for a fixed spot radius of 100 μm, the laser energies were 185 mJ, 270 mJ, 350 mJ, 450 mJ; blue: Pb, red: PbSn946, yellow: PbSn6535 and purple: Sn.

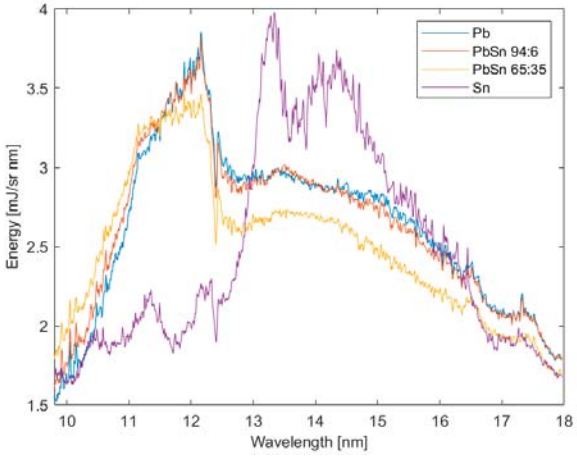

Figure 10. Spectra recorded for a fixed spot radius of 41 μm and laser energy of 450 mJ, 1.2×10^{12} W cm^{-2}; blue: Pb, red: PbSn946, yellow: PbSn6535 and purple: Sn.

One of the most noticeable differences between the Pb and Sn spectra is the growth in spectral efficiency with increasing laser energy for a fixed spot size and the lack of discrete structure due to emission and/or absorption in the Pb plasma. For Sn, absorption features appear at all power densities with the longer wavelength absorption from Sn VII–Sn IX decreasing, while absorption from Sn X and Sn XI becomes more pronounced with increasing power density and average charge in the plasma plume (ξ_{Av}). For Pb the absorption features are much less obvious and are hidden in the continuum; the most dominant absorption features appear between 15–16.5 nm and are present in all spectra. Compared to medium Z elements, high Z elements have been shown to have a more intense continuous spectrum in the EUV region due to the increase in free-free and free-bound radiation, with broad transition array (TA) emission structures superimposed on the continuum resembling bumps as seen here in Pb [32].

Of particular interest is the absence of a pronounced feature due to Sn UTA emission near 13.5 nm in the alloy spectra recorded with the Nd:YAG laser. It is well known that in spectra of Sn plasmas created on targets where the elements other than Sn are low Z elements such as Sn salts or SnO_2 dissolved in plastics that the peak of the Sn UTA emission increased in intensity with decreasing concentration and reached a maximum at a concentration of ~2% due to the decrease in opacity of the highest gA value transitions. For pure Sn targets the plasma is optically thick as evidenced here by the strong absorption features which can be clearly attributed to 4–4 transitions in Sn VII–Sn XI depending on the plasma temperature. Based on these observations it could be expected that the Sn UTA intensity should increase in the alloy, in particular, in that containing a 6% concentration. However, in all of the spectra shown, the emission from the alloys at 13.5 nm is consistently lower than that from pure Sn. Indeed, the emission from the alloys appears to be very similar to that of pure Pb, especially in the case of a 6% concentration and only for the 35% Sn concentration does a weak peak appear in the Sn UTA region. None of the alloy spectra contain features due to either discrete emission or absorption associated with strong individual 4d–4f or 4p–4d lines in Sn and this is particularly evident from Figure 10. Thus the expected increase in UTA emission appears to be quenched by strong 5p–5d absorption in the Pb ions.

It is particularly instructive to compare the absolute emission of the alloys with that of a spectrum generated by combining the emission of pure Sn and Pb summed according to their ratios in the alloys for both Nd:YAG and CO_2 laser produced spectral emission, as shown in Figures 11 and 12. The Nd:YAG spectra of the pure metals are optically thick and one would expect that both the overall intensity should increase and discrete structure such as UTA emission should become more pronounced in the alloy emission due to the reduction in concentration. The overall intensity does indeed increase but the spectra actually appear flatter with less evidence of discrete structure. Indeed, for the spectra presented in Figure 11 the overall emission is most intense for the 65–35 combination where the Pb concentration is lowest. For the CO_2 LPPs, which are essentially optically thin, while there is an increase again in overall emission from the alloys, the UTA at 13.5 nm is particularly clear in the 35% spectrum and essentially mirrors the Sn concentration.

Pure continuum emission originates from recombination and bremsstrahlung, the latter scales with ${\xi_{Av}}^2$, while the former scales as ${\xi_{Av}}^4$ [33]. The ξ_{Av} for Pb is higher than for Sn as ionization potentials decrease for a given charge state with increasing Z along the periodic table and a heavier ion mass results in increased time spent in the deflagration zone [34]. The peak of bremsstrahlung emission corresponds to $\lambda_B = 620/T_e$ nm [35]; at an irradiance of 5.5×10^{10} W cm^{-2} for a Pb LPP, T_e = 38 eV, ξ_{Av} = 13+, λ_B = 16.3 nm, for a Sn LPP, T_e = 34 eV, ξ_{Av} = 11+, λ_B = 18.2 nm corresponding to the longer wavelength limit on the spectra captured.

However, the spectral efficiency is low for Pb compared to Sn at a laser energy of 185 mJ regardless of spot size. If the difference in emission between the Pb and Sn was simply due to continuum emission for a higher ξ_{Av} in the LPP, the spectrum at an irradiance of 1.1×10^{11} W cm^{-2} (spot radius 100 μm) for Pb would be expected to have a greater intensity. For Pb, T_e = 57 eV, ξ_{Av} = 15+ (${\xi_{Av}}^4$ = 50,625),

λ_B = 10.9 nm; for Sn, T_e = 52 eV, ξ_{Av} = 14+ ($\xi_{Av}{}^4$ = 38,416), λ_B = 12 nm, approximately 25% more continuum emission is expected for Pb.

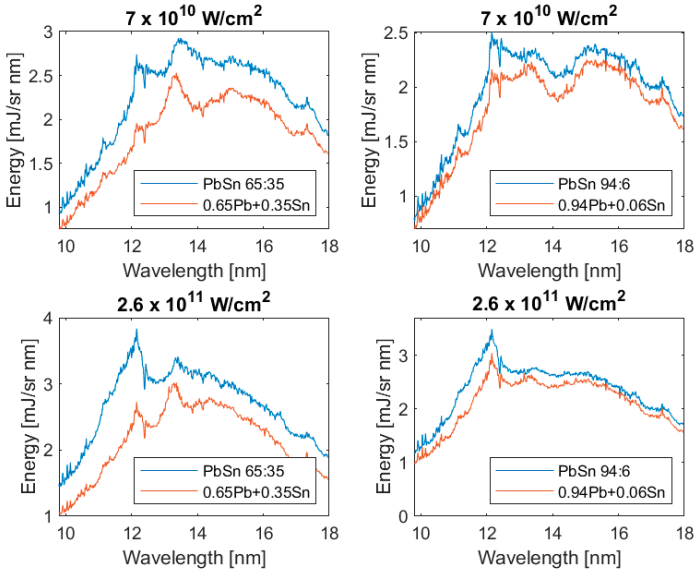

Figure 11. Spectra of Nd:YAG produced plasmas for the alloys compared with those of pure Sn and Pb spectra multiplied by their respective ratios in the alloy targets and summed for laser irradiance of 7×10^{10} W cm^{-2} and 2.6×10^{11} W cm^{-2}.

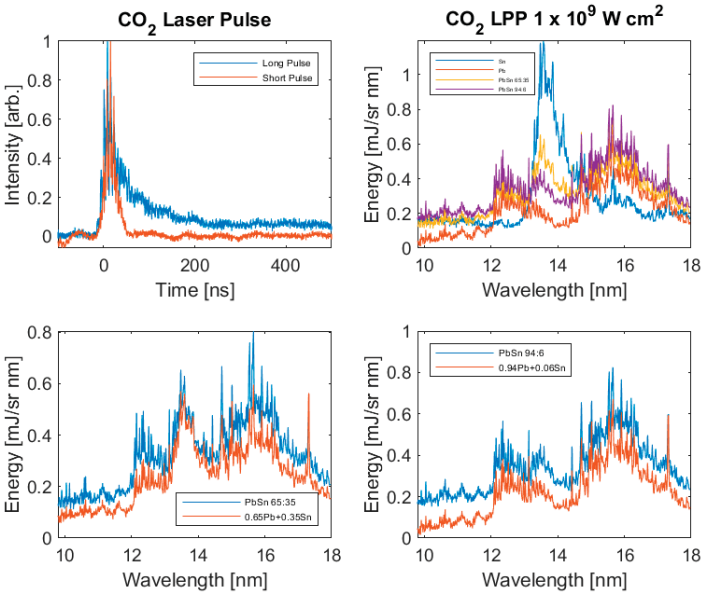

Figure 12. The shortened CO_2 pulse in seen in the top left, the captured spectra are presented in the top right. In the bottom left and right the pure Sn and Pb spectra are multiplied by their respective ratios in the alloy targets and summed. For Pb T_e = 54 eV and ξ_{Av} = 15+, while for Sn T_e = 49 eV and ξ_{Av} = 13+.

4.2. Line Emission in the 10–18 nm Region

The contribution from line emission in the region for Sn (red) and Pb (blue) plasmas for T_e = 10 eV to 100 eV are shown in Figure 13. To obtain these synthetic spectra the theoretical gA values were again weighted assuming a Boltzmann population distribution amongst the levels of each excited configuration and a level degeneracy of 2J+1. The ion fractions for each T_e are calculated using the CR model and the resultant line strengths for each transition are convolved with a Gaussian of width 0.01 nm and summed to give the total emission from a plasma at a single temperature. As seen from Figure 13 4d–4f transitions in Sn (red) create a UTA with emission centered around 13.5 nm. The shift towards shorter wavelength of the 4d–4f array is the result of 4f wavefunction contraction with increasing ion stage [34–36].

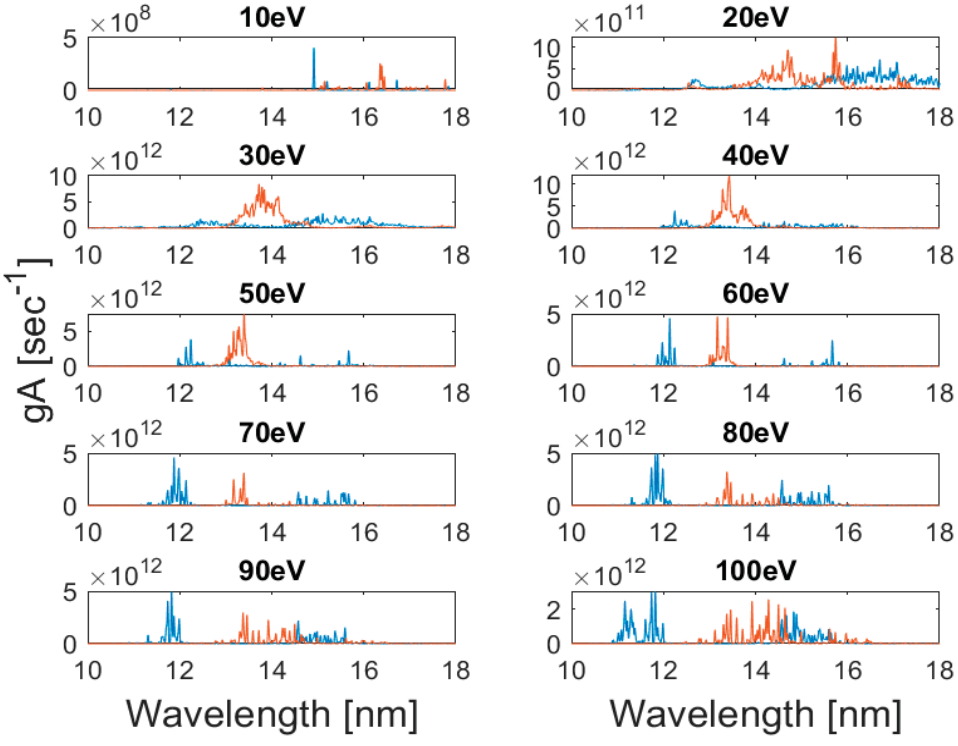

Figure 13. The contribution from line emission in the region for Sn (red) and Pb (blue) plasmas from 10 eV to 100 eV.

Liu *et al.* previously showed that the effect of CI on the 5d–5f and 5p–5d emission arrays along the isoelectronic sequence becomes important for 5d–5f beyond Pb^{7+}, while the effects of CI on 5p–5d emission only becomes important once these transitions overlap with the 5d–5f array [27]. Overall, they found that CI causes a shift to higher energy and a slight increase in array width. Changing the principal quantum number from 5 to 4 gives the configurations leading to the Sn UTA, where emission arrays have a greater overlap and where CI is known to cause a shift to higher energy and a large decrease in array width [37]. Figure 14 shows the positions of calculated Pb energy levels, the importance of including various configurations becomes more obvious from the overlap of their configuration energies. Note the experimental emission range of 69 eV to 127 eV (9.8 nm–18 nm) is marked with red lines in Figure 14. The energy levels are so close that they appear to form a continuous band, the number of levels increases to a maximum and decreases in proportion to the statistical weight

(g) of the subshell; g = [(4l + 2)!/w!(4l + 2 − w)!], where l is the orbital angular momentum number and w is the occupancy of the orbital [9]. The overlapping energy levels of the $5p^5 5d^{N+1}$, $5d^{N-1}5f^1$ and $5d^{N-1}6p^1$ configurations at lower energies and the $5p^5 6s^1$, $5d^{N-1}6f^1$ and $5d^{N-1}7p^1$ at higher energies is significant, warranting their inclusion. The $5p^5 5d^{N+1}$, $5d^{N-1}5f^1$ and $5d^{N-1}6p^1$ configurations do not coalesce to the same degree as the corresponding 4d configurations in Sn ions, with the corresponding emission bands showing greater separation over the range of ion stages considered here. This is especially evident in the $5p^5 5d^{N+1}$ emission to the ground configuration, where the emission array splits into two sub-arrays due to spin-orbital interaction [38]. The preceding section explains the difference in the Pb and Sn calculated spectra, where Pb is seen to have a much broader emission structure compared to Sn.

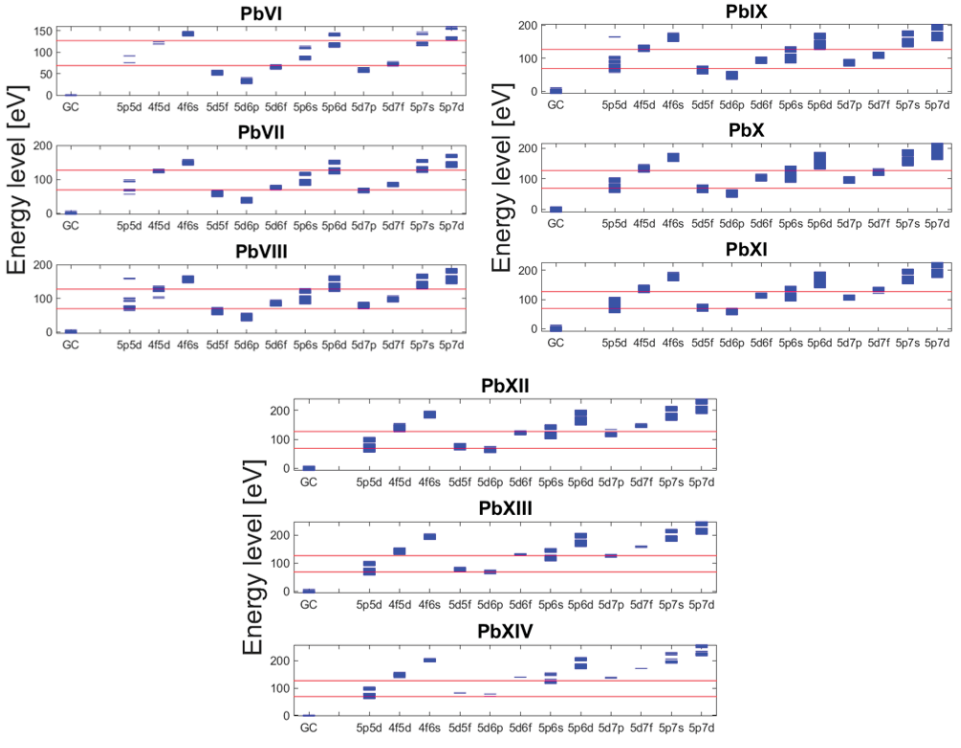

Figure 14. Relevant energy levels of excited configurations in Pb VI to Pb XIV taken from the Cowan code calculations; GC represents the ground configuration, $5d^9$ to $5d^1$. The red lines indicate the approximate region of interest. (See text.).

As stated earlier in calculating the line emission, the plasma was assumed to be optically thin, which a Nd:YAG plasma clearly is not. Previous work by Yan-Biao *et al.* [39] has shown that dielectronic recombination can significantly alter the ion stage population for an optically thick plasma; while work by Sasaki *et al.* [40,41] has shown the contribution from satellite lines increases with opacity of the resonance lines, leading to a broadening of a UTA and the quasicontinuum nature of the observed spectra.

Looking at the difference in the Pb and Sn plasma dynamics, Ahmed *et al.* found that molybdenum LPPs have a slight increase in lateral to normal expansion compared to aluminium LPPs, Mo has slower moving ions and an emission flux that peaks at 40° to the target surface [42]. This would indicate

that the heavier Pb ions form a denser plasma, thus increasing self-absorption and that greater lateral expansion of the plasma reduces coupling with the laser.

4.3. Discussion of Spectra and Line Identification

Plasmas produced at the lower power densities of 7.3×10^9 W cm^{-2} and 1.1×10^9 W cm^{-2} appear to have ion stages up to a maximum of Pb X present. At 1.4×10^{10} W cm^{-2} a number of small peaks between 13 and 15.5 nm corresponding to $5p^65d^5 - 5p^55d^6$ emission from Pb X and $5p^65d^4 - 5p^55d^5$ emission from Pb XI begin to appear; beyond this, line absorption around 16 nm is present with preliminary analysis suggesting $5p^65d^5 - 5d^45f^1$ transitions in Pb X. At shorter wavelengths the emission feature at 10.4 nm in the alloy targets corresponds to $4p^64d^5 - 4d^45f^1 + 4d^46p^1$ emission from Sn X ions [15]. For the Pb plasmas the emission structure on the shorter wavelength side of 12.4 nm become more defined and corresponds to $5p^6 - 5p^56s^1$ transitions in Pb XI and Pb XII. Three peaks are observed at 11.14 nm, 11.16 nm and 11.2 nm and give good agreement with $5p^65d^3 - 5p^55d^36s^1$ transitions of Pb XII; $^2G_{9/2} - (6,1/2)_{11/2}$, $^2H_{11/2} - (7,1/2)_{13/2}$ and $^4F_{3/2} - (1,1/2)_{3/2}$ respectively. All lines observed are summarized in Table 2.

For a power density of 2.5×10^{10} W cm^{-2} the $5p^65d^1 - 5p^55d^16s^1$ lines of Pb XIV; 9.91 nm $^2D_{5/2} - (3,1/2)_{5/2}$, 9.99 nm $^2D_{5/2} - (3,1/2)_{7/2}$, 10.02 nm $^2D_{5/2} - (2,1/2)_{5/2}$, 10.05 nm $^2D_{3/2} - (2,1/2)_{5/2}$, 10.12 nm $^2D_{5/2} - (2,1/2)_{3/2}$, 10.15 nm $^2D_{3/2} - (3,1/2)_{5/2}$ and 10.2 nm $^2D_{5/2} - (4,1/2)_{7/2}$ are visible but weak, becoming apparent at the power density of 1.6×10^{11} W cm^{-2}; these peaks can be seen in Figure 15 where the highest power density for each spot is graphed between 9.8 and 12.5 nm.

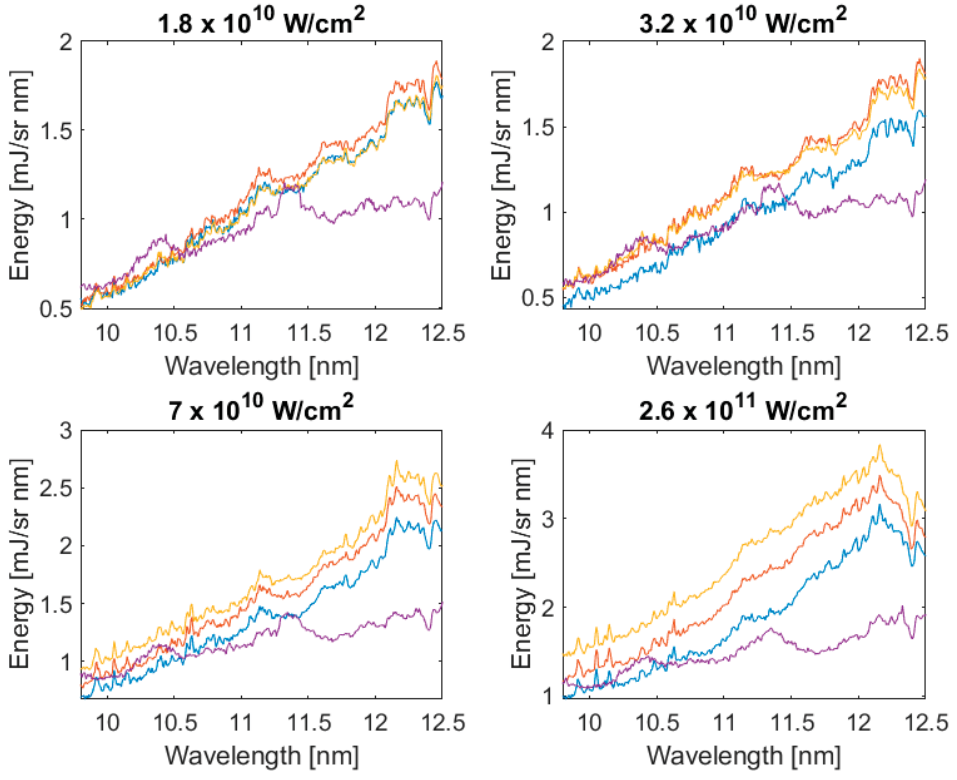

Figure 15. Spectra recorded at the highest power density for spot radii of 100 μm, 200 μm, 300 μm and 400 μm between 9.8 and 12.5 nm; blue: Pb, red: PbSn946, yellow: PbSn6535 and purple: Sn.

Table 2. Observed transitions along with calculated wavelengths and weighted transition probabilities determined from the Cowan suite of codes. The previously observed lines are from the work by Churilov *et al.* (C) [21,22] and Kaufman *et al.* (K) [23].

Ion Stage	Transition Configuration	Jj Composition	Observed λ/nm	Calculated λ/nm	($\times 10^{11}$) gA/s^{-1}	Prev. Observed λ/nm
Pb XIV	$5p^6 5d^1$ ($^2D_{5/2}$) – $5p^5 5d^1 6s^1$	99% ([$^2D_{5/2}$] 3,1/2)$_{5/2}$	9.91	9.950	4.98	9.926 C
Pb XIV	$5p^6 5d^1$ ($^2D_{5/2}$) – $5p^5 5d^1 6s^1$	98.7% ([$^2D_{5/2}$] 3,1/2)$_{7/2}$	9.99	10.023	1.78	10.003 C
Pb XIV	$5p^6 5d^1$ ($^2D_{5/2}$) – $5p^5 5d^1 6s^1$	95.2% ([$^2D_{3/2}$] 2,1/2)$_{5/2}$	10.02	10.079	4.15	10.063 C
Pb XIV	$5p^6 5d^1$ ($^2D_{3/2}$) – $5p^5 5d^1 6s^1$	48.6% ([$^2D_2$] 2,1/2)$_{5/2}$ + 45% ([$^2D_3$] 3,1/2)$_{5/2}$	10.05	10.087	6.38	10.070 C
Pb XIV	$5p^6 5d^1$ ($^2D_{5/2}$) – $5p^5 5d^1 6s^1$	91.2% ([$^2D_2$] 2,1/2)$_{3/2}$	10.12	10.143	3.07	10.132 C
Pb XIV	$5p^6 5d^1$ ($^2D_{3/2}$) – $5p^5 5d^1 6s^1$	54.1% ([$^2D_3$] 3,1/2)$_{5/2}$ –42.8% ([$^2D_2$] 2,1/2)$_{5/2}$	10.15	10.151	1.56	10.137 C
Pb XIV	$5p^6 5d^1$ ($^2D_{5/2}$) – $5p^5 5d^1 6s^1$	97.4% ([$^2D_4$] 4,1/2)$_{7/2}$	10.2	10.179	9.22	10.176 C
Pb XIII	$5p^6 5d^2$ ($^1G_4$) – $5p^5 5d^2 6s^1$	62.7% ([$^1G_4$] 9/2,1/2)$_4$ –35.8% ([$^3F_4$] 9/2,1/2)$_4$	10.48	10.495	6.07	
Pb XIII	$5p^6 5d^2$ ($^3F_3$) – $5p^5 5d^2 6s^1$	88.4% ([$^3F_3$] 9/2,1/2)$_4$ –3% ([$^3F_2$] 7/2,1/2)$_4$	10.6	10.607	9.81	
Pb XIII	$5p^6 5d^2$ ($^3F_4$) – $5p^5 5d^2 6s^1$	50.8% ([$^3F_4$] 11/2,1/2)$_5$ – 44.3% ([$^1G_4$]11/2,1/2)$_5$	10.63	10.648	11.90	
Pb XII	$5p^6 5d^3$ ($^2G_{9/2}$) – $5p^5 5d^3 6s$	38.8% ([$^2G_{9/2}$] 6,1/2)$_{11/2}$ –29.6% ([$^2H_{9/2}$]6,1/2)$_{11/2}$ –22.6% ([$^4F_{9/2}$] 6,1/2)$_{11/2}$	11.14	11.133	12.21	
Pb XII	$5p^6 5d^3$ ($^2H_{11/2}$) – $5p^5 6s$	90.2% ([$^2H_{11/2}$]7,1/2)$_{13/2}$	11.16	11.162	10.45	
Pb XII	$5p^6 5d^3$ ($^4F_{3/2}$) – $5p^5 5d^3 6s$	31.5% ([$^4F_{1/2}$] 1,1/2)$_{3/2}$ + 25.7%([$^4F_{1/2}$]2,1/2)$_{3/2}$ + 28.1% ([$^2D_{1/2}$]2,1/2)$_{3/2}$	11.20	11.195	3.80	
Pb XV	$5p^6$ ($^1S_0$)–$5p^5 5d^1$	90% ([$^2P_{1/2}$] 1/2,3/2)$_1$ – 9.3% ([$^3P_{3/2}$] 3/2,5/2)$_1$	12.11	12.116	23.82	12.160 K
Pb XIV	$5p^6 5d^1$ ($^2D_{5/2}$) – $5p^5 5d^2$	54.1% ([$^3P_1$] 3/2,0)$_{3/2}$ – 22.6% ([$^3P_2$] 3/2,0)$_{3/2}$	12.16	12.159	32.30	12.162 C
Pb XIV	$5p^6 5d^1$ ($^2D_{5/2}$) – $5p^5 5d^2$	68.8% ([$^1G_4$] 7/2,0)$_{7/2}$ + 12.2% ([$^3F_3$] 7/2,0)$_{7/2}$	12.20	12.237	64.89	12.230 C
Pb XIV	$5p^6 5d^1$ ($^2D_{5/2}$) – $5p^5 5d^2$	47.5% ([$^3F_3$] 5/2,0)$_{5/2}$ – 18.9% ([$^3P_2$] 5/2,0)$_{5/2}$ + 10.5% ([$^1D_2$] 5/2,0)$_{5/2}$	12.25	12.243	55.98	12.249 C
Pb XIV	$5p^6 5d^1$ ($^2D_{3/2}$) – $5p^5 5d^2$	65.9% ([$^3F_2$] 5/2,0)$_{5/2}$ – 8.9% $5d^0 5f^1$([$^1S_0$]0,5/2)$_{5/2}$ + 7.9% ($_{(1}$$^1D_2$]5/2,0)$_{5/2}$	13.04	13.078	30.98	13.137 C
Pb XIII	$5p^6 5d^2$ ($^3F_4$) – $5p^5 5d^3$	62.3% ([$^2H_{9/2}$]5,0)$_5$ + 13.2% ([$^2H_{11/2}$]5,0)$_5$ – 10.6% ([$^4F_{9/2}$]5,0)$_5$	13.14	13.176	23.14	

Increasing irradiance to 3.2×10^{10} W cm^{-2} the Pb emission on the short wavelength side of 12 nm becomes more defined. For the PbSn946 plasma the emission from Sn at 10.34 nm is present but no visible contribution from Sn at 11.35 nm in the alloy spectra is seen. Using the convolved synthetic spectra for each ion stage as an aid it can be seen the emission between 11.1–11.2 nm corresponds to $5p^65d^3 - 5p^55d^36s^1$ transitions in Pb XII, while the feature between 10.6–10.8 nm corresponds to $5p^65d^4 - 5p^55d^46s^1$ transitions in Pb XI, with a small contribution to the feature between 11.6–11.8 nm. The feature at 11.6–11.8 nm corresponds to $5p^65d^5 - 5p^55d^56s$ transitions in Pb X, for wavelengths shorter than 14 nm the Pb spectrum peaks in emission around 12.88 nm corresponding to $5p^65d^N - 5p^55d^{N+1}$ (where N = 3–5) emission from Pb X–Pb XII ions. The falloff in emission at wavelengths longer than 16.5 nm indicates a shift away from ion stages lower than Pb IX with Sn absorption features still present in the alloy plasmas, while the emission from Pb VIII and Pb IX at 17.33 nm involving 5d–5f and 5p–6d arrays stays constant; this feature is observed for higher laser power densities and corresponds to the emission from the outer plasma.

When the focal spot is further reduced to 400 μm the spectra shift slightly back to longer wavelengths and lower ion stage emission for a laser irradiances of 2.9×10^{10} W cm^{-2} and 4.2×10^{10} W cm^{-2}, a point of note here is that when calculating T_e for a given laser irradiance the CR model does not take into account laser plasma coupling. For the alloys at 2.9×10^{10} W cm^{-2} and 4.2×10^{10} W cm^{-2} the emission from Sn at 10.34 nm has now disappeared while the emission at shorter wavelength is pronounced compared to the Pb plasma. For a laser irradiance of 4.2×10^{10} W cm^{-2} a number of Pb peaks form between 12 and 12.5 nm persist up to a power density of 7×10^{10} W cm^{-2}. At 5.5×10^{10} W cm^{-2} five peaks can be identified at 12.11 nm $^1S_0 - (1/2,3/2)_1$, 12.16 nm $^2D_{5/2} - (3/2,0)_{3/2}$, 12.20 nm $^2D_{5/2} - (7/2,0)_{7/2}$, 12.25 nm $^2D_{5/2} - (5/2,0)_{5/2}$ and 13.04 nm $^2D_{3/2} - (5/2,0)_{5/2}$ corresponding to $5p^65d^N - 5p^55d^{N+1}$ transitions of Pb XIV and Pb XV, with the 12.11 nm and 12.16 nm lines remaining fixed for all spectra at higher power densities. At 7×10^{10} W cm^{-2} the three prominent peaks at 10.48 nm $^1G_4 - (9/2,1/2)_4$, 10.6 nm $^3F_3 - (9/2,1/2)_4$ and 10.63 nm $^3F_4 - (11/2,1/2)_5$ correspond to $5p^65d^2 - 5p^55d^26s^1$ transitions in Pb XIII are visible.

For the higher power density of 1.1×10^{11} W cm^{-2} the plasmas appear slightly cooler and the emission from Sn has its comparative maximum and shifts the spectrum to longer wavelengths for the PbSn6535 plasma. It is also worth noting at this laser irradiance, Sn emission peaks at a slightly longer wavelength for the PbSn6535 plasma, due to a reduction in Sn absorption. For Pb a number of small emission peaks appear around 13 nm, the peaks at 13.04 nm $^2D_{3/2} - (5/2,0)_{5/2}$ and 13.14 nm $^3F_4 - (5,0)_5$ corresponding to the $5p^65d^N - 5p^55d^{N+1}$ transitions in Pb XIV and Pb XIII respectively, and remain visible up to a power density of 1.2×10^{12} W cm^{-2}.

For these higher laser power densities, there is an obvious contribution from higher ion stages with a 5p ground configuration, however it is not possible to assign a label to any of these lines without ambiguity. Increasing the power density to 1.6×10^{11} W cm^{-2} the Pb spectrum now appears relatively flat, a number of lines around 14.8 nm are visible but weak, and with increasing power density the intensity of the transitions decreases and appear as photoabsorption features at the highest power density of 1.2×10^{12} W cm^{-2}. At 2×10^{11} W cm^{-2} and 2.6×10^{11} W cm^{-2} a number of lines on the short wavelength side of the peak at 12.16 nm are evident, which is now the longest wavelength peak of the cluster. These peaks again originate from 5p–5d transitions of ion stages Pb XVI to Pb XX. A relatively flat band of emission between 13 and 15 nm is observed with preliminary analysis suggesting a significant contribution from satellite lines in this region, additionally emission at wavelengths longer than 15 nm falls off more sharply.

At the highest power density of 1.2×10^{12} W cm^{-2} the PbSn6535 plasma shows a significant reduction in emission at longer wavelengths, with the emission now falling off beyond 13 nm. The pure Sn plasma exhibits a number of lines between 14.3 and 15 nm from ion stages in the high teens, while longer wavelength emission is significantly reduced compared to the plasma produced at 1.1×10^{11} W cm^{-2}. However, the shorter wavelength features from lower ion stages are still present indicating emission from the outer plasma. For the PbSn6535 plasma relative to the pure Pb plasma

the reduced intensity of the $5p^6 5d^1 - 5p^5 5d^2$ line at 12.16 nm indicates a reduction in self-absorption. The Sn emission from the alloy target decreases with increasing concentration indicating a T_e too high for Sn ions with an opened 4d subshell, while the small emission feature from Sn at 13.5 nm in the PbSn946 results from recombining ions in the outer plasma and has an overlap with the 5p – 5d subarray emission from recombined Pb ions seen in the pure Pb spectrum. While the PbSn6535 plasma has emission from lower ion stages, it appears to favor Pb emission which is again evident at longer wavelengths where emission from Pb VIII to Pb X is present at 16.5 nm and 17.33 nm. The crest of the emission now spans from 11.15 nm to 12.16 nm for PbSn6535, with peaks that appear in all three Pb plasmas and arise from ion stages ranging between Pb XIV and approximately Pb XXII.

4.4. Influence of Spot Size on Plasma Expansion

When comparing spectra from different spot sizes it was found that for a larger focal spot similar spectral flux can be achieved at a lower power density albeit a greater laser energy; with an emission structure that resembles a lower average charge. The effects of spot size on plasma dynamics has been studied by Harilal *et al.* [43] and Tao *et al.* [44], combining their work and applying to the current spectra; when the spot size increases the plasma propagation dynamics change from being spherical in nature to expanding more cylindrically. The smaller focal spot undergoes more lateral expansion but has a reduced plasma scale length and thus less self-absorption explaining the stronger emission at shorter wavelengths. For larger focal spots there is increased coupling between the plasma and laser due to the cylindrical expansion; as the laser energy is now shared between a greater number of emitting ions a lower average charge is obtained but an increase in continuum emission is observed for the same reason, bremsstrahlung emission scales with $\xi_{Av}{}^2 n_i$, where n_i is the ion density. It is also worth noting the increased scale length for larger focal spots leads to greater self-absorption and emission from lower ion stages at longer wavelengths from recombined ions and free electrons in the outer plasma [45,46].

5. Conclusions

Spectra from Sn, Pb and Sn-Pb alloys have been recorded in the EUV spectral region from both Nd:YAG and CO_2 LPPs. With increasing power density, the spectra of pure Sn targets are dominated by the 13.5 nm UTA emission. However, in the alloys this feature appears to be quenched by absorption due to Pb 5p–5d transitions, here the overall intensity does indeed increase but the spectra actually appear flatter with less evidence of discrete structure. Further evidence for this behavior is provided by the emission from optically thinner CO_2 LPPs where the emission structure reflects the Sn target concentration and ions present. The greater spectral efficiency for the alloys indicates that they should have a useful role as LPP sources for metrology applications. In addition, the contributing ions stages were discussed and a number of transitions in ion stages Pb XII to Pb XV have been identified.

Author Contributions: E.S. performed the experimental setup, experiments, calculations, data analysis and writing of original draft; supervision performed by G.O. and F.O.; review and editing performed by G.O., F.O., P.H. and I.T. All authors have read and agreed to the published version of the manuscript.

Funding: Science Foundation Ireland: Award 07/IN.1/B1771.

Conflicts of Interest: The authors declare no conflict of interest.

References

1. Carroll, P.K.; O'Sullivan, G. Ground-state configurations of ionic species I through XVI for Z = 57–74 and the interpretation of 4 d–4 f emission resonances in laser-produced plasmas. *Phys. Rev. A* **1982**, *25*, 275. [CrossRef]
2. Hayden, P.; Cummings, A.; Murphy, N.; O'Sullivan, G.; Sheridan, P.; White, J.; Dunne, P. 13.5 nm extreme ultraviolet emission from tin based laser produced plasma sources. *Appl. Phys. Lett.* **2006**, *99*, 093302.
3. White, J.; Dunne, P.; Hayden, P.; O'Reilly, F.; O'Sullivan, G. Optimizing 13.5 nm laser-produced tin plasma emission as a function of laser wavelength. *Appl. Phys. Lett.* **2007**, *90*, 181502. [CrossRef]

4. White, J. Opening the Extreme Ultraviolet Lithography Source Bottleneck: Developing A 13.5-Nm Laser-Produced Plasma Source for the Semiconductor Industry. Ph.D. Thesis, National College of Ireland, Dublin, Ireland, 2006.
5. Fahy, K.; O'Reilly, F.; Scally, E.; Kambali, I.; Sheridan, P. Robust Liquid Metal Collector Mirror for EUV and Soft X-ray Plasma Sources. In Proceedings of the International Workshop on Extreme Ultraviolet Sources, Dublin, Ireland, 13–15 November 2010.
6. Kambali, I.; Scally, E.; Dunne, P.; O'Sullivan, G.; Sheridan, P.; Sokell, E.; O'Reilly, F. A tin–gold alloy based EUV source for metrology applications. *J. Phys. D Appl. Phys.* **2013**, *46*, 5014–5020. [CrossRef]
7. Tobin, I.; Juschkin, L.; Sidelnikov, Y.; O'Reilly, F.; Sheridan, P.; Sokell, E.; Lunney, J.G. Laser triggered Z-pinch broadband extreme ultraviolet source for metrology. *Appl. Phys. Lett.* **2013**, *102*, 203504. [CrossRef]
8. Cowan, R.D. Theoretical Calculation of Atomic Spectra Using Digital Computers. *J. Opt. Soc. Am.* **1968**, *58*, 808–818. [CrossRef]
9. Cowan, R.D. *The Theory of Atomic Structure and Spectra*; University of California Press: Berkeley, CA, USA, 1981.
10. Harilal, S.S.; Coons, R.W.; Hough, P.; Hassanein, A. Influence of spot size on extreme ultraviolet efficiency of laser-produced Sn plasmas. *Appl. Phys. Lett.* **2009**, *95*, 221501. [CrossRef]
11. Hurst, N.; Harilal, S.S. Pulse shaping of transversely excited atmospheric CO_2 laser using a simple plasma shutter. *Rev. Sci. Instrum.* **2009**, *80*, 035101. [CrossRef]
12. Colombant, D.; Tonon, G.F. X-ray emission in laser-produced plasmas. *J. Appl. Phys.* **1973**, *44*, 3524–3537. [CrossRef]
13. Bates, D.R.; Kingston, A.E.; McWhirter, R.W.P. Recombination between electrons and atomic ions, I. Optically thin plasmas. *Proc. R. Soc. A* **1962**, *267*, 298–313.
14. Cowan, R.D. Theoretical Study of p^m–$p^{(m-1)}$l Spectra. *J. Opt. Soc. Am.* **1968**, *58*, 924–930. [CrossRef]
15. Svendsen, W.; O'Sullivan, G. Statistics and characteristics of xuv transition arrays from laser-produced plasmas of the elements tin through iodine. *Phys. Rev. A* **1994**, *50*, 3710–3718. [CrossRef] [PubMed]
16. Churilov, S.S.; Ryabtsev, A.N. Analysis of the spectra of in XII–XIV and Sn XIII–XV in the far-VUV region. *Opt. Spectrosc.* **2006**, *101*, 169–178. [CrossRef]
17. Torretti, F.; Sheil, J.; Schupp, R.; Basko, M.M.; Bayraktar, M.; Meijer, R.A.; Witte, S.; Ubachs, W. Prominent radiative contributions from multiplyexcited states in laser-produced tin plasma for nanolithography. *Nat. Commun.* **2020**, *11*, 2334. [CrossRef] [PubMed]
18. Churilov, S.S.; Ryabtsev, A.N. Analyses of the Sn IX–Sn XII spectra in the EUV region. *Phys. Scr.* **2006**, *73*, 614. [CrossRef]
19. Bouza, Z.; Scheers, J.; Ryabtsev, A.; Schupp, R.; Behnke, L.; Shah, C.; Sheil, J.; Bayraktar, M.; López-Urrutia, J.R.C.; Ubachs, W.; et al. EUV spectroscopy of Sn5+–Sn10+ ions in an electron beam ion trap and laser-produced plasmas. *J. Phys. B At. Mol. Phys.* **2020**, *53*, 1–10. [CrossRef]
20. Bridges, J.M.; Cromer, C.L.; Mcllrath, T.J. Investigation of a laser-produced plasma VUV light source. *Appl. Opt.* **1986**, *25*, 2208–2214. [CrossRef]
21. Churilov, S.S.; Joshi, Y.N. Observation of the strongest $5s^25p^65d$–($5s^25p^55d6s + 5s^25p^57p$) Transitions in Au XI to Bi XV ions. *Phys. Scr.* **2001**, *63*, 363–366. [CrossRef]
22. Churilov, S.S.; Joshi, Y.N.; Reader, J. Analysis of $5p^65d$–($5p^65f+5p^66p+5p^55d^2+5p^55d6s$) Transitions in Tl XIII, Pb XIV, and Bi XV and Revised Wavelengths for $5p^6\ {}^1S_0$–$5p^55d\ (3/2, 5/2)_1$ Transitions in Hg XIII, Tl XIV, Pb XV, and Bi XVI. *Phys. Scr.* **2002**, *66*, 213–221. [CrossRef]
23. Kaufman, V.; Sugar, J. Wavelength, classification, and ionization energies in the isoelectronic sequences fr om Yb II and Yb III through Bi XV and Bi XVI. *J. Opt. Soc. Am.* **1976**, *66*, 1019–1025. [CrossRef]
24. Carroll, P.K.; Costello, J.T.; Kennedy, E.T.; O'Sullivan, G. XUV emission from Thorium plasmas; the identificationof Th XI and Th XIII. *J. Phys. B At. Mol. Phys.* **1986**, *19*, L651–L656. [CrossRef]
25. Carroll, P.K.; Costello, J.T.; Kennedy, E.T.; O'Sullivan, G. XUV emission from Uranium plasmas; the identification of U XIII and U XV. *J. Phys. B At. Mol. Phys.* **1984**, *17*, 2169–2176. [CrossRef]
26. Liu, L.; O'Sullivan, G.; O'Reilly, F.; Long, E.; Wang, X.; Dunne, P. EUV spectral analysis of ns-laser produced bismuth plasmas at 8–17 nm. *Opt. Express* **2017**, *25*, 9974–9985. [CrossRef] [PubMed]
27. Liu, L.; Kilbane, D.; Dunne, P.; Wang, X.; O'Sullivan, G. Configuration Interaction Effects in Unresolved $5p^65d^{N+1}$, $5p^55d^{N+2}+5p^65d^N5f^1$ Transition Arrays in Ions Z = 79–92. *Atoms* **2017**, *5*, 20. [CrossRef]
28. Goldsmith, S.; Conway, J.G. Analysis of the configurations $5d^86s^2$ in Pt I through Hg II and $5d^96p$ in Pt I through Bi VI. *J. Opt. Soc. Am.* **1975**, *65*, 1371–1375. [CrossRef]

29. White, J.; Dunne, P.; Hayden, P.; O'Sullivan, G. Simplified one-dimensional calculations of 13.5 nm emission in a tin plasma including radiation transport. *J. Appl. Phys.* **2009**, *106*, 113303. [CrossRef]
30. Burdt, R.A.; Yuspeh, S.; Sequoia, K.L.; Tao, Y.; Tillack, M.S.; Najmabadi, F. Experimental scaling law for mass ablation rate from a Sn plasma generated by a 1064 nm laser. *Appl. Phys. Lett.* **2009**, *106*, 033310. [CrossRef]
31. Cummings, A.; O'Sullivan, G.; Dunne, P.; Sokell, E.; Murphy, N.; White, J.; Hayden, P.; Sheridan, P.; Lysaght, M.; O'Reilly, F. A spatio-temporal study of variable composition laser-produced Sn plasmas. *J. Phys. D Appl. Phys.* **2006**, *39*, 73–93. [CrossRef]
32. Mehlman, G.; Burkhalter, P.G.; Newman, D.A.; Ripin, B.H. *Soft X-ray Emission Spectra from Laser-Irradiated High Z-Targets*; NRL Memorandum Report 6674; Dynamics of Solids Branch: Washington, DC, USA, 1990.
33. Salzman, D. *Atomic Physics in Hot Plasmas*; Oxford University Press: New York, NY, USA, 1998.
34. O'Sullivan, G.; Cummings, A.; Dong, C.Z.; Dunne, P.; Hayden, P.; Morris, O.; Sokell, E.; O'Reilly, F.; Su, M.G.; White, J. Emission and absorption in laser produced plasmas: Processes and applications. *J. Phys. Conf. Ser.* **2009**, *163*, 012003. [CrossRef]
35. O'Sullivan, G. The origin of line-free XUV continuum emission from laser-produced plasmas of the lelements $62 < Z < 74$. *J. Phys. B At. Mol. Phys.* **1983**, *16*, 3291–3304.
36. Hayden, P.; White, J.; Cummings, A.; Dunne, P.; Lysaght, M.; Murphy, N.; Sheridan, P.; O'Sullivan, G. Tin based laser-produced plasma source development for EUVL. *Microelectron. Eng.* **2006**, *83*, 699–702. [CrossRef]
37. D'Arcy, R.; Ohashi, H.; Suda, S.; Tanuma, H.; Fujioka, S.; Nishimura, H.; Nishihara, K.; Suzuki, C.; Kato, T.; Koike, F.; et al. Transitions and the effects of configuration interaction in the spectra of Sn XV–Sn XVIII. *Phys. Rev. A* **2009**, *79*, 042509. [CrossRef]
38. Bauche, J.; Bauche-Arnoult, C.; Klapisch, M. Unresolved Transition Arrays. *Phys. Scr.* **1988**, *37*, 659–663. [CrossRef]
39. Yan-Bia, F.; Chen-Zhang, D.; Mao-Gen, S.; O'Sullivan, G. Dielectronic Recombination of Sn10+ Ions and Related Satellite Spectra. *Chin. Phys. Lett.* **2008**, *25*, 927. [CrossRef]
40. Sasaki, A.; Nishihara, K.; Koike, F.; Kagawa, T.; Nishikawa, T.; Fujima, K.; Kawamura, T.; Furukawa, H. Simulation of the EUV SPectrum of Xe and Sn Plasmas. *IEEE J. Sel. Top. Quantum Electron.* **2004**, *10*, 1307–1314. [CrossRef]
41. Sasaki, A.; Nishihara, K.; Murakami, M.; Koike, F.; Kagawa, T.; Nishikawa, T.; Fujima, K.; Kawamure, T.; Furukawa, H. Effect of the satellite lines and opacity on the extreme ultraviolet emission from high-density Xe plasmas. *Appl. Phys. Lett.* **2004**, *85*, 5857–5859. [CrossRef]
42. Elsieda, M.; Diwakar, P.K.; Polek, M.; Hassanein, A. Dynamics of low- and high-Z metal ions emitted during nanosecond laser-produced plasmas. *J. Appl. Phys.* **2016**, *120*, 173104. [CrossRef]
43. Harilal, S.S. Influence of spot size on propagation dynamics of laser-produced tin plasma. *J. Appl. Phys.* **2007**, *102*, 123306. [CrossRef]
44. Tao, Y.; Harilal, S.S.; Tillack, M.S.; Sequoia, K.L.; O'Shay, B.; Najmabadi, F. Effect of focal spot size on in-band 13.5 nm extreme ultraviolet emission from laser-produced Sn plasma. *Opt. Lett.* **2006**, *31*, 2492–2494. [CrossRef]
45. White, J.; Cummings, A.; Dunne, P.; Hayden, P.; O'Sullivan, G. Simplified calculation of nonlocal thermodynamic equilibrium excited populations contributing to 13.5 nm emission in a tin plasma. *J. Appl. Phys.* **2007**, *101*, 043301. [CrossRef]
46. Coons, R.W.; Campos, D.; Crank, M.; Harilal, S.S.; Hassanein, A. Comparison of EUV spectral and ion emission features from laser produced Sn and Li plasmas. In Proceedings of the SPIE Advanced Lithography, San Jose, CA, USA, 21–25 February 2010; Volume 7636, pp. 1–7.

atoms

MDPI

Article

The 5d-6p VUV Photoabsorption Spectrum of Bi^+

Hu Lu [1,*], Lazaros Varvarezos [1], Patrick Hayden [2], Eugene T Kennedy [1], Jean-Paul Mosnier [1] and John T Costello [1]

[1] School of Physical Sciences and NCPST, Dublin City University, 9 D09 V209 Dublin, Ireland; lazaros.varvarezos2@mail.dcu.ie (L.V.); eugene.kennedy@dcu.ie (E.T.K.); jean-paul.mosnier@dcu.ie (J.-P.M.); john.costello@dcu.ie (J.T.C.)

[2] School of Physics, University College Dublin, Belfield, 4 D04 V1W8 Dublin, Ireland; patrick.hayden@ucd.ie

* Correspondence: hu.lu3@mail.dcu.ie

Received: 8 August 2020; Accepted: 2 September 2020; Published: 4 September 2020

Abstract: The photoabsorption spectrum of Bi^+ was measured in the wavelength range between 37 and 60 nm, using the dual laser plasma technique in which one plasma is used as the source of vacuum ultraviolet continuum radiation and the other plasma is used as the sample of atoms and/or ions to be probed. A number of features in the Bi^+ spectrum was identified with the aid of the Cowan suite of atomic codes. The 5d → 6p transitions from the ground configuration ($5d^{10}6s^26p^2$) gave rise to the most prominent features in the measured spectrum. Transitions from low-lying excited states associated with the four excited configurations, $5d^{10}6s^26p6d$, $5d^{10}6s^26p7s$, $5d^{10}6s^26p7p$ and $5d^{10}6s6p^3$, were found to make small contributions to the observed spectrum in the 47–50 nm spectral region. To the best of our knowledge, for Bi^+, this spectral region is rather unexplored and spectroscopic data are absent from the literature.

Keywords: atomic ions; photoionization; dual-laser plasma technique

1. Introduction

Although the interaction of atomic ions with radiation is sometimes regarded as purely of fundamental atomic physics interest, it is often encountered in other research fields such as plasma physics and astrophysics [1]. For example, lowly charged ions such as Pb^+ and Bi^{2+} play an important role in investigations regarding e.g., stellar evolution [2] and the chemical composition of peculiar stars [3,4]. High Z atoms such as Bi are important in fusion research and extreme-UV (EUV) light source development. For example, Bi is among the candidates for developing a broadband emission water window source (region 2.3–4.4 nm) for high-contrast biological microscopy [5]. Due to the needs for spectral databases of high Z elements, soft X-ray emission measurements and EUV emission measurements on heavy ions including Bi were performed in the TEXT tokamak [6] and Large Helical Device (LHD) [7], respectively.

Photoabsorption studies of atomic ions have been reported using the merged synchrotron-ion beams technique [8–10]. In this case, accelerated beams of ions are merged with synchrotron radiation. The advent of third generation radiation sources exhibiting high brilliance, such as SOLEIL [11] and PETRA III [12] has yielded measurements of total, inner-shell photoionization cross sections [13]. Despite the apparently straightforward nature of this method, and the fact that it can provide absolute photoionization cross sections, the difficulty inherent in obtaining high currents of mono charge state ion beams and the need for access to large scale synchrotron facilities limits the wider applicability of this technique.

Analogous measurements yielding relative photoabsorption cross sections can be performed by means of table-top or laboratory scale techniques. One possibility is to perform photoabsorption measurements in atoms and the corresponding photoionized plasmas using radiation emitted from a

laser produced plasma (LPP)-based source where a gas target serves as the active medium [14–16]. Another well-established method is the so-called dual laser plasma (DLP) technique [17,18]. When a high-power laser pulse is focused onto a solid target, a short-lived plasma (some tens of nanoseconds) is formed that can be used as a back-lighting vacuum-UV (VUV) to soft X-ray (SXR) light source. A second laser is used to generate an absorbing plasma that includes the atomic or ionic species of interest. This technique can be used to perform photoabsorption measurements to study the inner-shell and multiple electron excitations in a wide range of atoms and ions e.g., [19–22]. The DLP technique has previously been used to carry out photoabsorption measurements on several lowly charged ions such as: Si^{+} [23], Si^{2+} [24], Si^{3+} [25] and Cr^{+} [26]. Furthermore, the DLP technique was applied by Banahan and coworkers [27] to measure the photoabsorption spectrum of Pb^{2+} and Bi^{3+} in the 19–41 nm spectral region, where excitation of the 5d subshell plays an important role. More recently, photoabsorption spectra of the Ti-like ions, Pb^{+} and Bi^{2+} in the 37–70 nm spectral region were reported. In this case, contributions of the 5d → 6p excitations to the photoabsorption spectra were found to be the most significant [28].

In this work, we report photoabsorption measurements in Bi^{+} in the 37–60 nm spectral region. To the best of our knowledge, this part of the spectrum for Bi^{+} is rather unexplored, and spectroscopic data are absent from the literature. Such spectroscopic data could prove to be useful additions to the existing atomic and molecular databases e.g., the VAMDC project which integrates more than 30 such databases [29,30].

In Section 2, we describe the experimental setup and how we obtained the spectral data. In Section 3, we present our experimental results and compare them with calculations using the Cowan suite of atomic structure codes. We show the contributions of 5d → 6p transitions from both ground state and low-lying excited states to the Bi^{+} spectrum. Finally, in Section 4, our conclusions are presented.

2. Experiment

The results presented in this work were recorded using the well-established DLP experimental facility at Dublin City University [31]. The output of a Q switched Nd:YAG laser (0.4 J, 15 ns) was focused onto a tungsten rod to produce the back-lighting continuum plasma. A second time-synchronized Nd:YAG laser pulse (0.45 J, 6ns) was focused by means of a cylindrical lens onto a bismuth target to produce an absorbing line plasma in the experiment. By appropriate choices of laser irradiation conditions and the position of the absorbing plasma with respect to the optical axis and inter-plasma time delay, the photoabsorption spectrum of Bi^{+} was obtained. Initially, the background continuum intensity (I_0) was recorded by firing the back-lighting Nd:YAG laser alone onto the tungsten rod, while the transmitted intensity (I) was obtained by firing both lasers onto the tungsten rod and bismuth plate with an adjustable time delay, respectively. The measured spectrum is displayed here as $\mathrm{Log}(I_0/I)$ versus the wavelength, corresponding to the quantity αL, where α is the absorption coefficient and L is the absorbing plasma column length. αL can also be written as σNL, where "σ" is the photoabsorption cross section and "NL" is the column density and is sometimes referred to as the relative absorption cross section or the optical depth $\tau = A^{-1}$, where A is the absorbance.

VUV spectra were recorded for a range of time delays and positions of the Bi target surface with respect to the optical axis of an Acton Research Corporation VM510 normal incidence spectrometer. The spectrometer was equipped with a concave grating of 1200 grooves/mm and operated with an entrance slit width of 50 μm for the current experiment. The adjustable fore-slit, located between the target chamber and entrance slit of the spectrometer, was used in the experiment to reduce the intensity of line emission coming from outside of the dense core region of the tungsten plasma used as a continuum source. In other experiments, e.g., on VUV LIBS, it has been used to occlude the continuum emission and favour the line emission coming from the cooler outer region of the plasma plume [32]. It was set to a width of 250 μm for the current experiment. Spectral image readout was provided by a back illuminated CCD (charge-coupled device) camera (Andor Technology Model No. DV420-BN). Spectra with good signal to noise ratio values were obtained by summing 10 single laser

shot "I" and "I_0" spectra. All spectra were calibrated by comparison with the wavelengths of known emission lines from a laser produced aluminium plasma from the same setup.

3. Results and Discussion

The absorption spectrum of Bi^+ in the spectral region ranging from 37 to 60 nm is shown in Figure 1. It was acquired at an inter-laser delay of 1000 ns and with the absorbing plasma formed a distance of 8.7 mm away from the optical axis of the system. By looking at valence excited lines of Bi^+ at longer wavelengths, it was found that the bismuth plasma was dominated by singly charged ions for these experimental conditions. The laser was tightly focused onto the Bi target via the cylindrical lens. In order to identify the observed absorption features, we carried out a series of calculations using the Cowan suite of atomic structure codes [33]. The suite comprises a number of core codes, three of which, labelled RCN, RCN2 and RCG, were used in this work. RCN uses the Hartree–Fock method or a number of variations of this method such as the Hartree–Slater (HS) or Hartree plus statistical Exchange (HX) methods to calculate one-electron radial wavefunctions along with direct, exchange and spin-orbit interaction integrals. RCN2 uses the output wavefunctions from RCN to calculate the configuration-interaction Coulomb integrals. Finally, RCG sets up energy matrices for each possible value of the total angular momentum J, diagonalizes each matrix to obtain the eigenvalues (level energies) and eigenvectors (from which the state mixing coefficients can be obtained) and then computes spectra, with wavelengths, oscillator strengths, radiative transition probabilities, and radiative lifetimes.

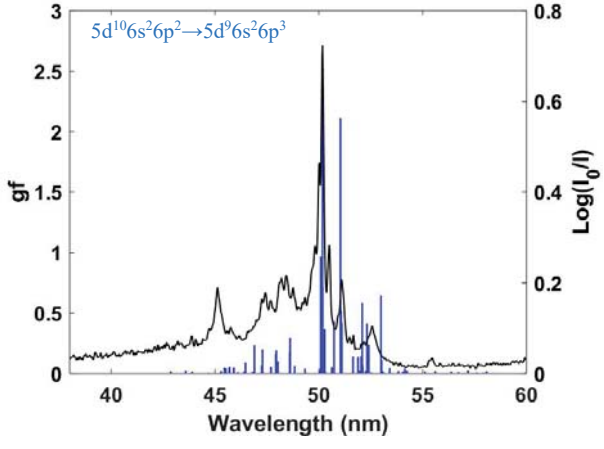

Figure 1. The experimentally recorded spectrum (black) of Bi^+ together with the gf values (blue) for the 5d→6p transition array, i.e., $5d^{10}6s^26p^2 \rightarrow 5d^96s^26p^3$ transitions.

After testing a number of possible pairs of upper and lower state configurations, the final electron configurations for each of the low-lying states were finally chosen and are given in Table 1. In order to optimize the calculations, the values of Slater integrals were reduced. Specifically, the direct (F_k) and exchange (G_k) integrals were reduced by 15%, as were the configuration interaction (R_k) integrals. In addition, the spin-orbit integrals were reduced by 5%.

Table 1. Ground and lowly lying electron configurations of Bi^+ included in the Cowan code photoabsorption calculations.

Ground Configuration	Low-Lying (Excited) Configurations
$5d^{10}6s^26p^2$	$5d^{10}6s6p^3$
	$5d^{10}6s^26p6d$
	$5d^{10}6s^26p7s$
	$5d^{10}6s^26p7p$

In Figure 1, we show the gf values for the 5d → 6p transitions from the ground electron configuration of Bi^+. The photoabsorption cross section is related to the oscillator strength, which is in turn given by the weighted oscillator strength normalized to the multiplicity of the lower state, so the gf values were used to compare with the experiment in this work. As can be seen, 5d subshell photoabsorption from the ground configuration $5d^{10}6s^26p^2$ dominated the spectrum and resulted in the strong observed photoabsorption peaks at 50.02, 50.18 and 51.08 nm. According to calculations with the Cowan suite of atomic structure codes, these three peaks are mainly due to the transitions $5d^{10}6s^26p^2$ (^1S) $^1D_2$ → $5d^96s^26p^3$ (^2D) $^1D_2$, $5d^{10}6s^26p^2$ (^1S) $^1D_2$ → $5d^96s^26p^3$ (^2D) $^1F_3$, $5d^{10}6s^26p^2$ (^1S) $^3P_2$ → $5d^96s^26p^3$ (^4S) $^3D_3$, respectively.

In Figure 2, we show the contribution of 5d → 6p transitions from low-lying excited configurations of Bi^+ to the overall absorption spectrum. The plasma temperature was expected to be less than 2 eV for the prevailing experimental conditions [34], and so the population of low-lying excited states would be expected to be a low % of the ground state population. Their contribution to the measured spectrum was thus expected to be finite, but small.

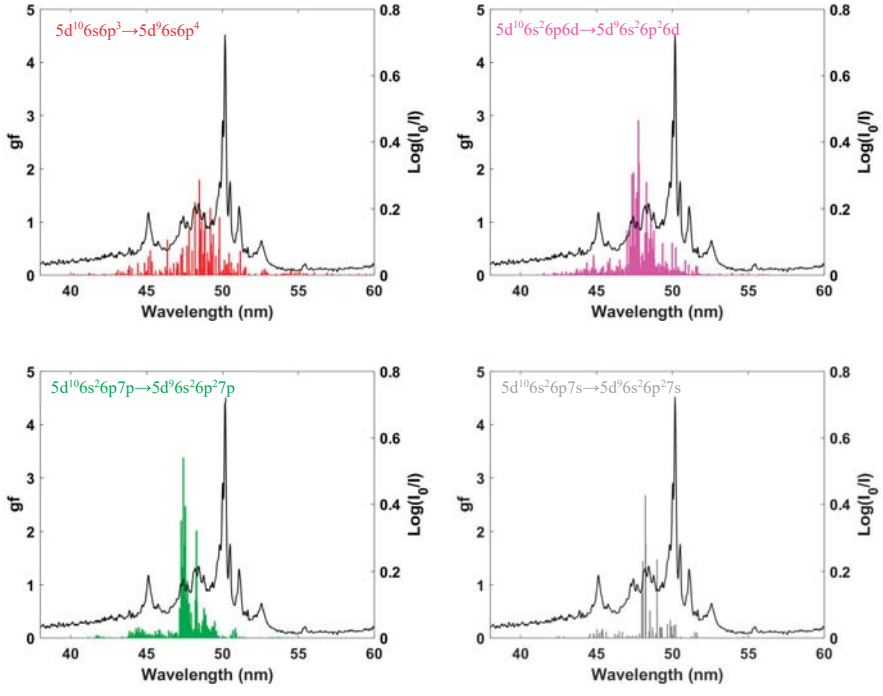

Figure 2. Calculated gf values for 5d–6p transitions from low-lying, excited configurations of Bi^+ compared to the observed spectrum. From top to bottom and from left to right: $5d^{10}6s6p^3$→$5d^96s6p^4$, $5d^{10}6s^26p6d$→$5d^96s^26p^26d$, $5d^{10}6s^26p7p$→$5d^96s^26p^27p$ and $5d^{10}6s^26p7s$→$5d^96s^26p^27s$.

Table 2 includes some of the strongest predicted transitions arising from low-lying (excited) electron configurations of Bi^+. The contributions from the excited states were particularly complex as many transitions were possible. For $5d^{10}6s^26p^2 \rightarrow 5d^96s^26p^3$, there were 97 transitions in the calculation, 61 of them with a gf value bigger than 0.01. For $5d^{10}6s6p^3 \rightarrow 5d^96s6p^4$, there were 353 transitions in the calculation, 180 of them with a gf value bigger than 0.01. For $5d^{10}6s^26p6d \rightarrow 5d^96s^26p^26d$, there were 1506 transitions in the calculation, 591 of them with a gf value bigger than 0.01. For $5d^{10}6s^26p7p \rightarrow 5d^96s^26p^27p$, there were 860 transitions in the calculation, 297 of them with a gf value bigger than 0.01. For $5d^{10}6s^26p7s \rightarrow 5d^96s^26p^27s$, there were 123 transitions in the calculation, 69 of them with a gf value bigger than 0.01.

Table 2. Transitions arising from lowly lying (excited) electron configurations of Bi^+.

Wavelength Region (nm)	Transitions	λ (nm)	gf Values
48.01–48.85	$5d^{10}6s6p^3\ (^2D)\ ^3D_2 \rightarrow 5d^96s6p^4\ (^1D)\ ^3F_3$	48.48	1.7998
	$5d^{10}6s6p^3\ (^2D)\ ^3D_3 \rightarrow 5d^96s6p^4\ (^1D)\ ^3F_4$	48.19	1.3768
	$5d^{10}6s^26p6d\ (^2P)\ ^3F_3 \rightarrow 5d^96s^26p^26d\ (^3P)\ ^3G_4$	48.29	1.7533
	$5d^{10}6s^26p6d\ (^2P)\ ^3F_2 \rightarrow 5d^96s^26p^26d\ (^3P)\ ^3G_3$	48.58	1.0639
	$5d^{10}6s^26p7p\ (^2P)\ ^3D_2 \rightarrow 5d^96s^26p^27p\ (^3P)\ ^3F_3$	48.29	2.0222
	$5d^{10}6s^26p7p\ (^2P)\ ^3D_1 \rightarrow 5d^96s^26p^27p\ (^3P)\ ^3F_2$	48.27	1.1598
	$5d^{10}6s^26p7s\ (^2P)\ ^3P_2 \rightarrow 5d^96s^26p^27s\ (^3P)\ ^3D_3$	48.21	2.6750
	$5d^{10}6s^26p7s\ (^2P)\ ^1P_1 \rightarrow 5d^96s^26p^27s\ (^3P)\ ^1D_2$	48.24	1.7633
	$5d^{10}6s^26p7s\ (^2P)\ ^3P_2 \rightarrow 5d^96s^26p^27s\ (^3P)\ ^3P_2$	48.05	1.1502
47.15–47.82	$5d^{10}6s^26p6d\ (^2P)\ ^3F_4 \rightarrow 5d^96s^26p^26d\ (^3P)\ ^3G_5$	47.75	2.9095
	$5d^{10}6s^26p6d\ (^2P)\ ^1F_3 \rightarrow 5d^96s^26p^26d\ (^3P)\ ^1G_4$	47.80	2.1086
	$5d^{10}6s^26p6d\ (^2P)\ ^3F_4 \rightarrow 5d^96s^26p^26d\ (^3P)\ ^3F_4$	47.45	1.9398
	$5d^{10}6s^26p6d\ (^2P)\ ^3P_2 \rightarrow 5d^96s^26p^26d\ (^1D)\ ^3D_3$	47.34	1.9009
	$5d^{10}6s^26p7p\ (^2P)\ ^3D_3 \rightarrow 5d^96s^26p^27p\ (^3P)\ ^3F_4$	47.43	3.3784
	$5d^{10}6s^26p7p\ (^2P)\ ^3D_3 \rightarrow 5d^96s^26p^27p\ (^3P)\ ^3D_3$	47.28	2.2064
	$5d^{10}6s^26p7p\ (^2P)\ ^1D_2 \rightarrow 5d^96s^26p^27p\ (^3P)\ ^1F_3$	47.55	2.4676

In Figure 3, we show the measured photoabsorption spectrum of Bi^+ compared with synthetic spectra built from the convolution of the gf values with a Gaussian function (0.045 nm FWHM), chosen to represent the spectrometer instrument function. In Figure 3a, the simulation included photoabsorption from the ground electron configuration only. The resulting synthetic spectrum exhibited reasonable agreement with the experimental data. The relative heights and positions of the overall spectrum and some discrete features were reproduced by the calculation, specifically, the discrete photoabsorption features at 50.02 nm ($5d^{10}6s^26p^2\ (^1S)\ ^1D_2 \rightarrow 5d^96s^26p^3\ (^2D)\ ^1D_2$), 50.18 nm ($5d^{10}6s^26p^2\ (^1S)\ ^1D_2 \rightarrow 5d^96s^26p^3\ (^2D)\ ^1F_3$) and 51.08 nm ($5d^{10}6s^26p^2\ (^1S)\ ^3P_2 \rightarrow 5d^96s^26p^3\ (^4S)\ ^3D_3$). As shown in Figure 2, there were features in the 47–50 nm region due to the 5d → 6p transitions from excited states of Bi^+. Specifically, there were quite strong features in the 48.01–48.85 nm and 47.15–47.82 nm spectral regions. Some of the most intense of these transitions are listed in Table 2. In Figure 3b, we added contributions due to photoabsorption from these low-lying excited states to Figure 3a. The gf values for the associated transitions were multiplied by a small factor (5%) before including them in this synthetic spectrum. This in line with the low plasma temperature alluded to the above. It is clear that the transitions did indeed make a small but finite contribution to the overall spectral distribution.

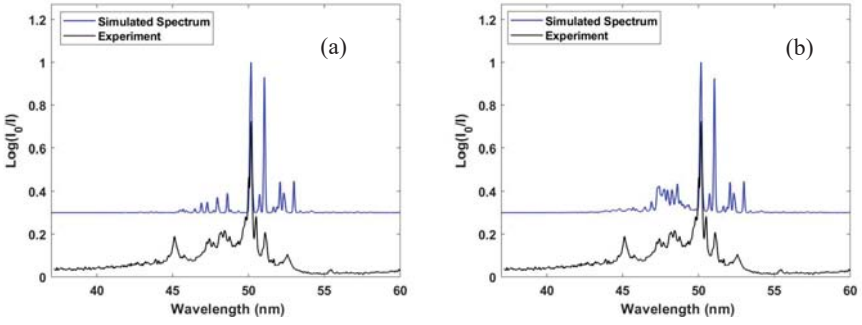

Figure 3. A comparison between the synthetic spectra and experimental data. (**a**) Simulated spectrum including photoabsorption from the ground electron configuration of Bi^+ only. (**b**) Simulated spectrum including photoabsorption both from the ground and from low-lying excited states of Bi^+.

4. Conclusions

To conclude, the rather unexplored spectral region (37–60 nm) of the Bi^+ spectrum was investigated. The 5d → 6p transitions, arising from levels associated with the ground state electron configuration, were identified as the dominant contributors to the observed spectrum. The experimental findings were complemented by theoretical calculations performed with the aid of the Cowan suite of atomic structure codes. Using the computed data, the synthetic spectrum of Bi^+ was constructed in the spectral region of interest and reproduced the overall shapes and some of the discrete features of the experimental spectrum quite well. Importantly, 5d → 6p transitions from low-lying excited states are believed to make a small but finite contribution to the Bi^+ spectrum for our experimental conditions, mostly in the 47–50 nm spectral range.

Author Contributions: Data curation, H.L. and P.H.; formal analysis, H.L. and L.V.; writing—original draft preparation, H.L. and L.V.; writing—review and editing, P.H., E.T.K., J.-P.M. and J.T.C.; analytical calculations and visualization, H.L.; supervision, J.T.C. All authors have read and agreed to the published version of the manuscript.

Funding: The work is supported by the Education, Audio-visual and Culture Executive Agency (EACEA) Erasmus Mundus Joint Doctorate Programme EXTATIC, Project No. 2012-0033, Sustainable Energy Authority of Ireland (SEAI) Grant No. 19/RDD/556 and Science Foundation Ireland (SFI) Grant Nos. 19/FFP/6956 and 13/SIRG/2100. The work is associated with EU H2020 COST Action No. CA17126 (TUMIEE).

Acknowledgments: The authors gratefully acknowledge the support from the listed funding.

Conflicts of Interest: The authors declare no conflict of interest.

References

1. Larsson, M.; Geppert, W.D.; Nyman, G. Ion chemistry in space. *Rep. Prog. Phys.* **2012**, *75*, 066901. [CrossRef]
2. Cardelli, J.A.; Federman, S.R.; Lambert, D.L.; Theodosiou, C.E. Ultraviolet Transitions of Low Condensation Temperature Heavy Elements and New Data for Interstellar Arsenic, Selenium, Tellurium, and Lead. *Astrophys. J.* **1993**, *416*, L41. [CrossRef]
3. Leckrone, D.S.; Johansson, S.G.; Wahlgren, G.M.; Brage, T.; Proffitt, C.R. Atomic Data Requirements for the Analysis of Chemically Peculiar Spectra. In *Highlights of Astronomy*; Andersen, J., Ed.; International Astronomical Union/Union Astronomique Internationale: Paris, France, 1998; Volume 11B, pp. 650–652.
4. Wahlgren, G.M.; Brage, T.; Brandt, J.C.; Fleming, J.; Johansson, S.; Leckrone, D.S.; Proffitt, C.R.; Reader, J.; Sansonetti, C.J. The bismuth abundance in the hgmn stars χ lupi and hr 7775 and improved atomic data for selected transitions of Bi I, Bi II, and Bi III. *Astrophys. J.* **2001**, *551*, 520. [CrossRef]
5. Higashiguchi, T.; Otsuka, T.; Yugami, O.; Jiang, W.; Endo, A.; Li, B.; Dunne, P.; O'Sullivan, G. Feasibility study of broadband efficient "water window" source. *Appl. Phys. Lett.* **2012**, *100*, 014103. [CrossRef]
6. Finkenthal, M.; Lippmann, S.; Huang, L.K.; Zwicker, A.; Moos, H.W. O-shell emission of heavy atoms in an optically thin tokamak plasma. *Phys. Rev. A* **1992**, *45*, 5846. [CrossRef] [PubMed]

7. Suzuki, C.; Koike, F.; Murakami, I.; Tamura, N.; Sudo, S.; Sakaue, H.A.; Nakamura, N.; Morita, S.; Goto, M.; Kato, D.; et al. EUV spectroscopy of highly charged high Z ions in the Large Helical Device plasmas. *Phys. Scr.* **2014**, *89*, 114009. [CrossRef]
8. Schippers, S.; Kilcoyne, A.L.D.; Phaneuf, R.A.; Müller, A. Photoionization of ions with synchrotron radiation: From ions in space to atoms in cages. *Contemp. Phys.* **2016**, *57*, 215–229. [CrossRef]
9. Phaneuf, R.A.; Kilcoyne, A.L.D.; Müller, A.; Schippers, S.; Aryal, N.; Baral, K.; Hellhund, J.; Aguilar, A.; Esteves-Macaluso, D.A.; Lomsadze, R. Cross-section measurements with interacting beams. *AIP Conf. Proc.* **2013**, *1545*, 72–78.
10. West, J.B. Photoionization of atomic ions. *J. Phys. B At. Mol. Opt. Phys.* **2001**, *34*, R45–R91. [CrossRef]
11. Gharaibeh, M.F.; Bizau, J.M.; Cubaynes, D.; Guilbaud, S.; El Hassan, N.; Al Shorman, M.M.; Miron, C.; Nicolas, C.; Robert, E.; Blancard, C.; et al. K-shell photoionization of singly ionized atomic nitrogen: Experiment and theory. *J. Phys. B At. Mol. Opt. Phys.* **2011**, *44*, 175208. [CrossRef]
12. Schippers, S.; Ricz, S.; Buhr, T.; Hellhund, J.; Müller, A.; Klumpp, S.; Martins, M.; Flesch, R.; Rühl, E.; Lower, J.; et al. Photon-ion spectrometer PIPE at the variable polarization XUV beamline of PETRA III. *J. Phys. Conf. Ser.* **2012**, *388*, 142016. [CrossRef]
13. Kjeldsen, H. Photoionization cross sections of atomic ions from merged-beam experiments. *J. Phys. B At. Mol. Opt. Phys.* **2006**, *39*, R325. [CrossRef]
14. Varvarezos, L.; Lu, H.; Costello, J.T.; Bartnik, A.; Wachulak, P.; Fok, T.; Węgrzyński, Ł.; Fiedorowicz, H. Soft X-ray photoabsorption spectra of photoionized CH_4 and CO_2 plasmas. *J. Phys. B At. Mol. Phys.* **2019**, *53*, 045701. [CrossRef]
15. Varvarezos, L.; Lu, H.; Costello, J.T.; Bartnik, A.; Wachulak, P.; Fok, T.; Węgrzyński, Ł.; Fiedorowicz, H. Oxygen K-shell photoabsorption spectra of photoionized CO_2 plasmas. *J. Phys. B At. Mol. Opt. Phys.* **2020**, *53*, 105701. [CrossRef]
16. Fiedorowicz, H.; Bartnik, A.; Jarocki, R.; Rakowski, R.; Szczurek, M. Enhanced X-ray emission in the 1-keV range from a laser-irradiated gas puff target produced using the double-nozzle setup. *Appl. Phys. B* **2000**, *70*, 305–308. [CrossRef]
17. Costello, J.T.; Mosnier, J.P.; Kennedy, E.T.; Carroll, P.K.; O'Sullivan, G. X-UV Absorption Spectroscopy with Laser-Produced Plasmas: A Review. *Phys. Scr.* **1991**, *34*, 77–92. [CrossRef]
18. D'Arcy, R.; Costello, J.T.; McGuinness, C.; O'Sullivan, G. Discrete structure in the 4d photoabsorption spectrum of antimony and its ions. *J. Phys. B At. Mol. Phys.* **1999**, *32*, 4859. [CrossRef]
19. Chakraborty, H.S.; Gray, A.; Costello, J.T.; Deshmukh, P.C.; Haque, G.N.; Kennedy, E.T.; Manson, S.T.; Mosnier, J.-P. Anomalous behavior of the near-threshold photoionization cross section of the neon isoelectronic sequence: A combined experimental and theoretical study. *Phys. Rev. Lett.* **1999**, *83*, 2151. [CrossRef]
20. Van Kampen, P.; O'Sullivan, G.; Ivanov, V.K.; Ipatov, A.N.; Costello, J.T.; Kennedy, E.T. Dramatic changes in the 3s autoionization process at the beginning of the Ar I sequence. *Phys. Rev. Lett.* **1997**, *78*, 3082. [CrossRef]
21. Jannitti, E.; Nicolosi, P.; Tondello, G. Photoionization and double excitation spectrum of Be^{2+}. *Opt. Commun.* **1984**, *50*, 225–230. [CrossRef]
22. Nicolosi, P.; Villoresi, P. Experimental measurement of the C II L-shell photoabsorption spectrum. *Phys. Rev. A* **1998**, *58*, 4985. [CrossRef]
23. Costello, J.T.; Kennedy, E.T.; Mosnier, J.P.; Sayyad, M.H.; McGuinness, C. Extreme-UV photoabsorption spectrum of a laser-produced silicon plasma: Evidence for metastable Si^+ ions. *J. Phys. B At. Mol. Opt. Phys.* **1998**, *31*, L547. [CrossRef]
24. Mosnier, J.P.; Costello, J.T.; Kennedy, E.T.; Kiernan, L.; Sayyad, M.H. Even-parity autoionizing states in the extreme-ultraviolet photoabsorption spectra of Mg, Al^+, and Si^{2+}. *Phys. Rev. A* **1994**, *49*, 755. [CrossRef] [PubMed]
25. Brilly, J.; Kennedy, E.T.; Mosnier, J.P. 2p photoabsorption spectra of valence excited configurations in Al^{2+} and Si^{3+} observed in a dual laser produced plasma experiment. *Phys. Scr.* **1990**, *41*, 30. [CrossRef]
26. McGuinness, C.; Martins, M.; Wernet, P.; Sonntag, B.F.; Van Kampen, P.; Mosnier, J.P.; Kennedy, E.T.; Costello, J.T. Metastable state contributions to the measured 3p photoabsorption spectrum of Cr^+ ions in a laser-produced plasma. *J. Phys. B At. Mol. Opt. Phys.* **1999**, *32*, L583. [CrossRef]
27. Banahan, C.; McGuinness, C.; Costello, J.T.; Kilbane, D.; Mosnier, J.P.; Kennedy, E.T.; O'Sullivan, G.; Van Kampen, P. The 5d photoabsorption spectra of Pb III and Bi IV. *J. Phys. B: At. Mol. Opt. Phys.* **2008**, *41*, 205001. [CrossRef]

28. Lu, H.; Varvarezos, L.; Alli, M.B.; Nicolosi, P.; Costello, J.T.; Hayden, P. The 5d → 6p EUV photoabsorption spectra of Pb II and Bi III: Evidence of excited states. *J. Phys. B At. Mol. Opt. Phys.* **2020**, *53*, 115001. [CrossRef]
29. Dubernet, M.L.; Boudon, V.; Culhane, J.L.; Dimitrijevic, M.S.; Fazliev, A.Z.; Joblin, C.; Kupka, F.; Leto, G.; Le Sidaner, P.; Loboda, P.A.; et al. Virtual atomic and molecular data centre. *J. Quant. Spectrosc. Radiat. Transf.* **2010**, *111*, 2151–2159. [CrossRef]
30. Dubernet, M.L.; Antony, B.K.; Ba, Y.A.; Babikov, Y.L.; Bartschat, K.; Boudon, V.; Braams, B.J.; Chung, H.K.; Daniel, F.; Delahaye, F.; et al. The virtual atomic and molecular data centre (VAMDC) consortium. *J. Phys. B At. Mol. Phys.* **2016**, *49*, 074003. [CrossRef]
31. Kennedy, E.T.; Costello, J.T.; Mosnier, J.-P.; Cafolla, A.A.; Collins, M.; Kiernan, L.; Köble, U.; Sayyad, M.H.; Shaw, M.; Sonntag, B.F.; et al. Extreme-ultraviolet studies with laser-produced plasmas. *Opt. Eng.* **1994**, *33*, 3984–3993. [CrossRef]
32. Meighan, O.E. XUV and VUV Photoabsorption and Emission Studies in Thorium and other High-Z Laser Plasmas. Ph.D. Thesis, Dublin City University, Dublin, Ireland, 2000.
33. Cowan, R.D. *The Theory of Atomic Structure and Spectra*; University of California Press: Berkeley, CA, USA, 1981.
34. Banahan, C. One and Two Photon Absorption of Atoms and Ions. Ph.D. Thesis, Dublin City University, Dublin, Ireland, 2009.

atoms

MDPI

Article

Investigation of a Collisional Radiative Model for Laser-Produced Plasmas

Nicholas L. Wong *, Fergal O'Reilly and Emma Sokell

School of Physics, University College Dublin, Belfield, Dublin 4, D04 V1W8, Ireland; f.oreilly@ucd.ie (F.O.); emma.sokell@ucd.ie (E.S.)

* Correspondence: nicholas.wong1@ucdconnect.ie

Received: 31 July 2020; Accepted: 24 August 2020; Published: 1 September 2020

Abstract: Plasmas of a variety of types can be described by the collisional radiative (CR) model developed by Colombant and Tonan. From the CR model, the ion distribution of a plasma at a given electron temperature and density can be found. This information is useful for further simulations, and due to this, the employment of a suitable CR model is important. Specifically, ionization bottlenecks, where there are enhanced populations of certain charge states, can be seen in these ion distributions, which in some applications are important in maintaining large amounts of a specific ion. The present work was done by implementing an accepted CR model, proposed by Colombant and Tonon, in Python and investigating the effects of variations in the ionization energy and outermost electron subshell occupancy term on the positions of ionization bottlenecks. Laser Produced Plasmas created using a Nd:YAG laser with an electron density of $\sim n_e = 10^{21}$ cm^{-3} were the focus of this work. Plots of the collisional ionization, radiative recombination, and three-body recombination rate coefficients as well as the ion distribution and peak fractional ion population for various elements were examined. From these results, it is evident that using ionization energies from the NIST database and removing the orbital occupancy term in the CR model produced results with ionization bottlenecks in expected locations.

Keywords: collisional-radiative model; laser-produced plasma, ion distribution; ionization bottleneck; radiative recombination; collisional ioniztion; three-body recombination

1. Introduction

Laser-produced plasmas (LPPs) are important to many fields of research. They have found uses in laser-induced breakdown spectroscopy [1], extreme ultraviolet lithography [2], and are laboratory scale sources of astrophysical plasmas [3,4], therefore, it is important to understand the characteristics of LPPs. In this regard, a collisional-radiative (CR) model was proposed by Colombant and Tonon to describe LPPs [5]. This CR model finds the charge state distribution for an LPP, utilizing rate equations for three dominant processes: collisional ionization, three-body recombination, and radiative recombination [5].

The CR model continues to be used to estimate charge state distributions for the emission spectra of a variety of elements, for example C ($Z_A = 6$), Ge ($Z_A = 32$), and Gd ($Z_A = 64$) [6–8]. Typically in these experiments laser pulse lengths are on the order of 10 ns, with wavelengths of 1064 or 532 nm [6–10]. The CR model has seen further use in investigating LPPs through the three-body and radiative recombination rate coefficients [9]; and it has also been extended, for example into a time-dependent version taking into account photoionization [10]. Su et al. investigated the evolution of Al ($Z_A = 13$) LPPs and, as might be expected, determined that the impact of photoionization on the charge state distribution was more important for plasmas with lower electron densities in which relative collisional ionization rates are lower [10]. The photoionization rates reported by Su et al.

for Al^{3+} to Al^{6+} have orders of magnitude in the same range as the other rate coefficients. Colombant and Tonan [5] used units of cm^3s^{-1} for rate coefficients for the three dominant processes and to express photoionization rates in these units Su et al. considered rates/electron number density (n_e). These authors found rate coefficents for photoionization between 10^{-9} to 10^{-15} cm^3s^{-1} depending on the electron temperature and density [10]. Other photoionization rates have been reported [11], but these rates describe multi-photon ionization during the formation of LPPs and thus are not applicable to the CR model considered here. However, it is noteworthy that these high photoionization rates during the laser pulse duration play a significant role in creating LPPs when the laser beam is of sufficient intensity. Comparing the order of magnitude of the photoionization rate coefficients determined by Su et al. with the multi-photon rate coefficients, clearly shows the difference between the two. For the photoionization of O ($Z_A = 8$) with laser intensities on the order of 10^{13} W/cm^{-2}, Sharma et al. report the multi-photon rates being between 10^8 to 10^{10} s^{-1}, where n_e is on the order of 10^{14} to 10^{15} cm^{-3} [11], corresponding to rate coefficients between 10^{-6} to 10^{-5} cm^3s^{-1}. The resonant process of dielectronic recombination (DR) has recently been shown to have a significant effect upon the charge state distribution of Si ($Z_A = 14$) LPPs [12]. Due to their resonant nature, DR rates are sensitive to electron temperature. Whilst there are relatively few studies on the effect of DR on charge state distributions in plasmas at electron temperatures below 100 eV, some studies indicate that it dominates over radiative recombination [12]. It is worth bearing in mind that this recent study does not include the influence of autoionization, a resonant process that will drive the charge balance in the opposite direction to DR. The work presented here does not take into account photoionization, DR or autoionization and instead focuses on the original CR model developed by Colombant and Tonon.

The basis of the CR model is a set of analytical expressions for the rate coefficients, that have been compared to empirical formulas or experimental data [13,14]. This model was presented in 1973, and the aim of the original publication was not the CR model itself but instead an extension of it [5]. Colombant and Tonan were mainly concerned with the optimization of LPPs as heavy-ion or X-ray sources. However, the reasonable correspondence of the expressions used in the CR model with experiments has proven to be adequate, and the model is still utilized today. Despite this widespread use, little investigation into the original model has been reported. In some cases the results of the CR model are compared to other more rigorous models (such as FLYCHK [7] or a CR model based on output from HULLAC [15,16]), but this comparison is not always carried out. Thus, any inconsistencies within the CR model may go unnoticed. In the present work, the effects of altering different parameters within the CR model, namely the ionization energy of ion stage Z (χ_Z) and the number of electrons in the outermost subshell of ion stage Z (ξ_Z), were examined. A representative range of elements, spanning carbon to lead, has been studied, and the main findings are presented in this article.

2. The CR Model

2.1. Limits of Applicability

The CR model described by Colombant and Tonon assumes there are three main processes in the plasma that give the ratio of two ion populations of adjacent charge states (n_{Z+1} and n_Z), when the system is in a steady state [5]. The processes are collisional ionization, radiative recombination, and three-body recombination. These assumptions constrain the model to certain electron densities (n_e) and temperatures (T_e) [5]. The plasma must also be optically thin, and the electrons must have a Maxwellian velocity distribution [5]. The constraints on n_e and T_e come from the need for the population of the more highly charged state (Z+1) to remain steady, while the less charged state (Z) approaches its equilibrium population [5]. In other words, lower charged ion stages must reach an equilibrium population, before the populations of more highly charged ion stages significantly change. Colombant and Tonon presented a plot of this constraint, and they show for $n_e = 10^{21}$ cm^{-3} the T_e must be at least 10 eV and for $n_e = 10^{19}$ cm^{-3} at least 3 eV [5]. The constraint

requiring an optically thin plasma necessitates $T_e \geq 30$ eV for $n_e = 10^{21}$ cm^{-3}, but the T_e minimum remains the same for $n_e = 10^{19}$ cm^{-3} [5].

Equation (1) is the electron critical density formula, with n_{ec} in cm^{-3} and λ in μm. From Equation (1), a wavelength of 1064 nm produces $n_e \approx 10^{21}$ cm^{-3}, and a wavelength of 10.6 μm produces $n_e \approx 10^{19}$ cm^{-3}.

$$n_{ec} = \frac{1.12 \times 10^{21}}{\lambda^2} \quad [\text{cm}^{-3}] \tag{1}$$

Colombant and Tonon also provide the following estimate for T_e (Equation (2)), which is valid for plasmas that are not fully ionized and have small radiation losses [5].

$$T_e \approx 5.2 \times 10^{-6} Z_A^{1/5} [\lambda^2 \phi]^{3/5} [eV] \tag{2}$$

In Equation (2), Z_A is the target material's atomic number, λ is the laser wavelength in μm, and ϕ is the laser flux in W/cm^2. Equation (2) can be used to determine indicative temperatures to find laser parameters that produce LPPs, for which the CR model is applicable. The temperature determined from the equation should fall within the temperature constrains specified by Colombant and Tonan [5] mentioned above. Since $Z_A^{1/5}$ is on the order of 1 to 2 for elements as heavy as Pb, $T_e = 30$ eV and $\lambda = 1064$ nm in Equation (2) yields a laser flux on the order of 10^{11} W/cm^2. This minimum laser flux can be achieved easily with typical Nd:YAG lasers, with laser pulse energies, pulse widths, and focal spot diameters on the order of 1 J, 10 ns, and 100 μm, respectively. Where spot sizes are on the order of 10s of μm the minimum laser flux is greatly exceeded [6,8–10]. Similarly, with $T_e = 3$ eV and $\lambda = 10.6$ μm, a laser flux on the order of 10^7 W/cm^2 is found, which can be exceeded by laser energies, pulse widths, and focal spot diameters on the order of 1 J, 1 μs, and a few mm, respectively. These parameters can be achieved by CO_2 lasers, for example as reported in [7].

The CR model no longer applies when the n_e is on the order of 10^{17} cm^{-3} or smaller [5], such as in inductively coupled plasmas with n_e on the order of 10^{14} cm^{-3} [17], as there are not enough electron-electron collisions to ensure that the constraints of the CR model are met. This minimum order of n_e magnitude (10^{17} cm^{-3}) along with Equation (1) gives a limit of $\lambda \leq 10^2$ μm for lasers used in LPP production. Furthermore, the time to achieve a charge of Z and the time an ion is in the conduction region of the plasma must be shorter than the laser pulse [5]. Colombant and Tonon show for $n_e = 10^{21}$ cm^{-3} and $n_e = 10^{19}$ cm^{-3} the laser pulse must be greater than $10^{-10} - 10^{-9}$ s and $10^{-8} - 10^{-7}$ s, respectively [5]. Thus, the CR model is not applicable for LPPs from ps laser such as those in [18,19], which have $n_e \approx 10^{21}$ given $\lambda = 1064$ nm.

2.2. Basis of the Model

The ion population ratio and rate coefficient for each process are given in Equations (3)–(6), respectively [5].

$$\frac{n_{Z+1}}{n_Z} = \frac{S(Z, T_e)}{\alpha_r(Z+1, T_e) + n_e \alpha_{3b}(Z+1, T_e)} \tag{3}$$

$$S(Z, T_e) = \frac{9 \times 10^{-6} \xi_Z (\frac{T_e}{\chi_Z})^{1/2}}{{\chi_Z}^{3/2}(4.88 + \frac{T_e}{\chi_Z})} \exp\left(\frac{-\chi_Z}{T_e}\right) \quad [\text{cm}^3 \cdot \text{s}^{-1}] \tag{4}$$

$$\alpha_r(Z, T_e) = 5.2 \times 10^{-14} (\frac{T_e}{\chi_Z})^{1/2} Z [0.429 + \frac{1}{2} \ln(\frac{\chi_Z}{T_e}) + 0.469 (\frac{T_e}{\chi_Z})^{1/2}] \quad [\text{cm}^3 \cdot \text{s}^{-1}] \tag{5}$$

$$\alpha_{3b}(Z, T_e) = \frac{2.97 \times 10^{-27} \xi_Z}{T_e {\chi_Z}^2 (4.88 + \frac{T_e}{\chi_Z})} \quad [\text{s}^{-1}] \tag{6}$$

Here n_e is the electron density (in cm^{-3}), ξ_Z is the number of electrons in the outermost orbital subshell for an ion of charge Z, χ_Z is the ionization energy for an ion of charge Z (in eV), and T_e is the electron temperature (in eV). In the present work, n_e was set to 10^{21} cm^{-3}, ξ_Z was found using

the normal rules for electron removal (removing electrons in descending order, starting with the least tightly bound electrons with the largest nl values), two different sets of χ_Z were used (the NIST database [20] values and estimates using Equation (7), as in [5]), and T_e was either a range of values or a set value. For the ratio of the bare nucleus population over the ions with one electron remaining, a non-zero χ_Z for the bare nucleus is needed, since Equations (5) and (6) require this value in several places including denominators. The bare nucleus was assumed to have an χ_Z similar to the Bohr Hydrogen atom and was calculated as $\chi_Z = 13.5984(Z)^2$ [eV], with $Z = Z_A$ being the charge of the bare nucleus.

The population ratio (n_Z/n_{Total}) for all charge states of an ion at a given temperature can be found, by setting the ion population for the ground state to an arbitrary value (e.g. 1), iteratively solving Equation (3) from the ground state up to the highest charge state to obtain each ion population, and then dividing each charge state's population by the sum of all populations. Repeating this process for different temperatures and plotting the results gives an ion distribution plot of population ratio against temperature as shown in Figure 1, which shows an example charge state, or ion, distribution for Sn ($Z_A = 50$). The computing requirements are not high and the work here was done using Python.

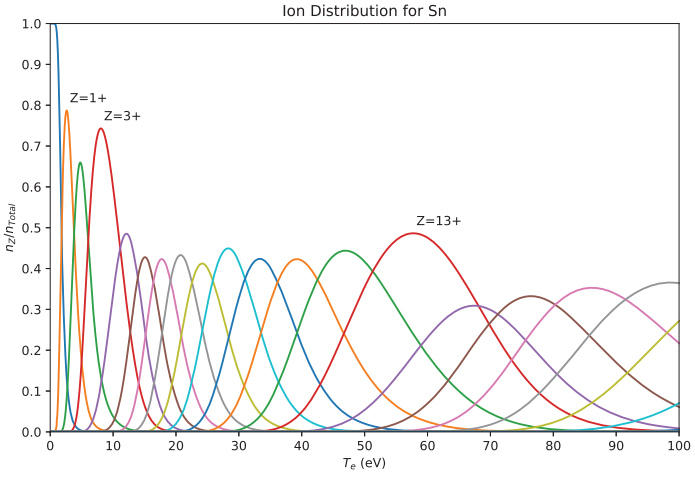

Figure 1. A Sn ion distribution generated using the traditional CR model by Colombant and Tonon [5], with different ion stages denoted by the different colored curves and the 1^+, 3^+, and 13^+ ion stages marked.

2.3. Parameters Used

During the investigation some changes were made to the parameters used in the Colombant and Tonan CR model [5], which will be referred to as the traditional CR model. A major consideration was the change in determination of ξ_Z, when the phenomena known as $4f$ collapse, or contraction occurs. $4f$ contraction is where electrons in the $4f$ subshell become more tightly bound than $5p$ and $5s$ electrons, thus changing the typical electron configuration expected as the $4f$ orbital is filled before the $5p$ and $5s$ shells are completely filled [21,22]. To observe the effects of this phenomenon on the lanthanides, the electronic configurations reported in [22] were used. The outermost orbital was chosen to be the one, which appeared to lose an electron, when comparing an ion stage of charge Z to the next highest ion stage, with charge Z+1. For elements heavier than the lanthanides, the standard electron removal method was used again for simplicity.

In addition to this, the ionization energy used is an important factor within the model, but the actual values used are not reported in many of the papers using the CR model. Complicating the issue is that Colombant and Tonon provide an estimated ionization energy shown in Equation (7) [5], which will be referred to as CT χ_Z, and small variations in the ionization energy can produce significantly different results. Within Equation (7), χ_Z is the ionization energy to obtain an ion of charge Z, Z is the charge of the ion, and Z_A is the atomic number of the element.

$$\chi_Z \approx \frac{45Z^2}{Z_A^{2/3}} \quad [\text{eV}] \tag{7}$$

2.4. Correction to the Traditional CR Model

While investigating the rate equations, a discrepancy was found in the radiative recombination rate coefficient (Equation (5)). Colombant and Tonon and their cited source for Equation (5) [23] differ from the original sources [14,24] in the power on the last T_e/χ_Z term, which has a coefficient of 0.469. Instead of a $\frac{1}{2}$ power, it is a $\frac{1}{3}$ power as shown in Equation (8) [14,24]. The $\frac{1}{3}$ power comes from the fitting of an equation to the asymptotic expansion of the Kramers-Gaunt factor for bound to free transitions [14]. Furthermore, no explanation is given for the change to $\frac{1}{2}$, nor could one be determined [23].

$$\alpha_r(Z, T_e) = 5.2 \times 10^{-14}(\frac{T_e}{\chi_Z})^{1/2} Z[0.429 + \frac{1}{2}\ln(\frac{\chi_Z}{T_e}) + 0.469(\frac{T_e}{\chi_Z})^{1/3}] \quad [\text{cm}^3 \cdot \text{s}^{-1}] \tag{8}$$

Changing the power to $\frac{1}{3}$ causes the ion distribution peaks to shift slightly toward higher temperatures, and Equation (8) was used for the majority of the data presented here. To differentiate this choice from the traditional CR model which uses the $\frac{1}{2}$ power, the method using the $\frac{1}{3}$ will be referred to as the standard CR model. Table 1 lists the terms used to describe the different methods and parameter configurations used. Many elements were examined and general trends are described from this examination. The elements Sn and Pb are presented as illustrative examples, as these elements show many of the important characteristic features observed in the studies of other elements.

Table 1. A list of the terms used to describe the model and parameter configurations used throughout this work, along with a brief description of each.

Name	Description
Traditional	The CR model using Equations (3)–(6)
Standard	The CR model using Equations (3), (4), (6), and (8)
NIST χ_Z	Use of the χ_Z values reported by NIST [20]
CT χ_Z	Use of χ_Z values calculated from Colombant and Tonon's estimate, Equation (7) [5]
No ξ_Z	Removal of the ξ_Z term from Equations (4) and (6)

3. Ionization Bottlenecks

A possible error and part of the impetus for this work can be seen in Figure 1. In this distribution, there are large peaks in the maximum ion population for Sn^{1+}, Sn^{3+}, and Sn^{13+}. However, given the phenomena known as ionization bottlenecks, these peaks are not expected. An ionization bottleneck is a build up of the ion population that occurs in ion stages with a full outermost electron orbital, due to the difference between ionization energies [25]. Therefore, the peak population of an ion stage corresponding to a full outermost subshell is expected to be greater than the peak population of its neighboring ion stages, especially the one of higher charge. The electron configurations for Sn^{1+}, Sn^{3+}, and Sn^{13+} do not correspond to full orbitals and are instead $[Kr]4d^{10}5s^25p^1$, $[Kr]4d^{10}5s^1$, and $[Kr]4d^1$, respectively. It would be expected that ionization bottlenecks should be observed at Sn^{2+}, Sn^{4+} and Sn^{14+}. Examples of this discrepancy in other research can be seen in the ion distribution plots of Gd [8,26,27] and Sn [28].

4. Results and Discussion

4.1. Sn ($Z_A = 50$)

Ion distributions, such as the one shown in Figure 1, were the initial basis for comparisons. To further examine the ionization bottleneck discrepancy, ion distribution curves were extended to higher temperatures (up to $5 \cdot 10^6$ eV), and the peak fractional populations were plotted against the number of electrons in the ionization stage for different methods, as summarized in Table 1. These results are shown in Figure 2. For the peak population plots, the standard method was plotted along with the standard method without ξ_Z. In both plots of Figure 2, the standard method with the ξ_Z term is the solid line, and the standard method without the ξ_Z term is the dashed line. These two cases utilize the NIST χ_Zs and the CT χ_Zs, as shown in Figure 2a,b respectively. For each plot, the number of electrons remaining corresponding to noble gas configurations and configurations whose outermost subshell was a filled n*d* subshell were marked as dashed vertical lines. The vertical lines show where ionization bottlenecks are expected to occur.

Using the standard CR model and NIST χ_Zs for Sn (solid line in Figure 2a), a possible ionization bottleneck can be seen at the He-like configuration (Sn^{48+}), as the peak fractional population is much larger than the more highly charged configuration (Sn^{49+}) and slightly larger than the less charged configuration (Sn^{47+}). All further expected ionization bottlenecks are not observed. Instead the peak fractional population for the closed subshell configurations are either much lower than their neighbors, or the lower charged neighboring configuration (Z−1) exhibits an ionization bottleneck. The Ar-like configuration (Sn^{32+}) is an example of the former behaviour, with a dip, while the Ne-like, Ni-like, Kr-like, and Pd-like configurations (Sn^{40+}, Sn^{22+}, Sn^{14+}, and Sn^{4+}) are closer to the latter behaviour. Similarly, when the CT χ_Zs are used (solid line in Figure 2b), there are dips at all of the expected ionization bottleneck locations, with only the Pd-like configuration having a significant bottleneck at a lower charged state. Removing ξ_Z produces the expected ionization bottlenecks with the NIST χ_Zs but removes all features with the CT χ_Zs, as shown by the dashed lines in Figure 2a,b respectively.

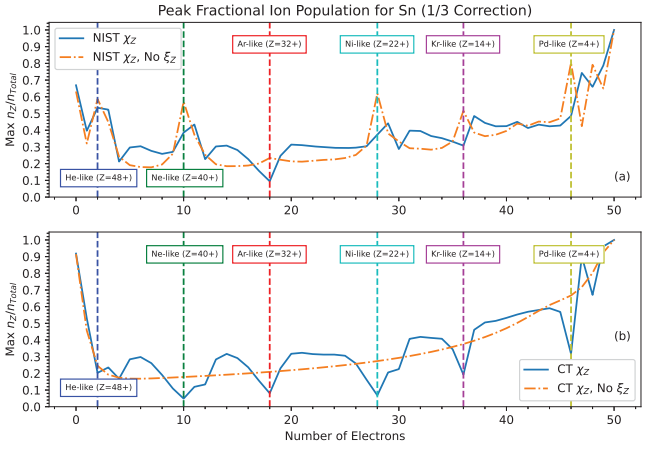

Figure 2. Plots of the peak fractional ion population for Sn calculated with the standard CR model, using Equation (3) (solid lines) and the standard CR model without the ξ_Z term (dashed lines). Two different χ_Zs were used, the NIST values [20] (**a**) and the estimated CT values from Equation (7) (**b**). The vertical lines mark noble gas configurations and configurations whose outermost subshell was a filled nd^{10} subshell.

While rate coefficients plots were not shown by Colombant and Tonon, they were examined here, in an effort to interpret the unusual behaviour observed for the ionization bottlenecks. The results from Equations (4), (6), and (8) were plotted for consecutive ion stages. The ground state and up to the sixth ion stage (Sn^{5+}) were chosen, because several changes in the outermost occupied subshell could be observed. As with the peak fractional population plots, the NIST and CT χ_Zs were used, with and without ξ_Z. Figure 3 shows these plots for the collisional ionization rate coefficient.

Curves for ion stages with the same outermost occupied subshell tended to group together for all of the rate coefficients. The rate equations given above indicate that the collisional ionization and three-body recombination rates decrease as ionization increases, while the radiative recombination rates would increase as ionization increased. However, as illustrated in Figure 3, some curves of ion stages with the same outermost electron orbital cross. In particular, crossing can be observed in Figure 3a,c between Sn^{3+}, Sn^{4+}, and Sn^{5+}. An important note here is that this crossing was not seen in the radiative recombination curves; and unlike the other two rates, the radiative recombination rate does not depend on the occupancy term (ξ_Z). Again, the effect of removing this occupancy was investigated. For the NIST χ_Zs, the curve crossing observed before was no longer present in Figure 3b. For the CT χ_Zs, removing ξ_Z also removed the curve crossing. All rate coefficient plots followed the ionization orders seen before, but the ion stage curves were no longer clustered. Instead the first few curves corresponding to low ionization stages appeared to have larger differences than later stages, and the differences decreased in size as ionization increased. The rate coefficient differences themselves were small and gave some curves the appearance of equal spacing. This can be seen in Figure 3d for neutral Sn to Sn^{5+}. This behaviour indicates that the occupancy term (ξ_Z) may be associated with the appearance of ionization bottlenecks at unexpected charge states, evident in Figure 1. This association is supported by further consideration of the three-body recombination rates, as shown in Figure 4. The rates would be expected to decrease with charge state [10], however the rate for Sn^{3+} is between that for Sn^{6+} and Sn^{7+}. When the occupancy (ξ_Z) was removed, the exception evident in Figure 4 using the standard method was no longer present.

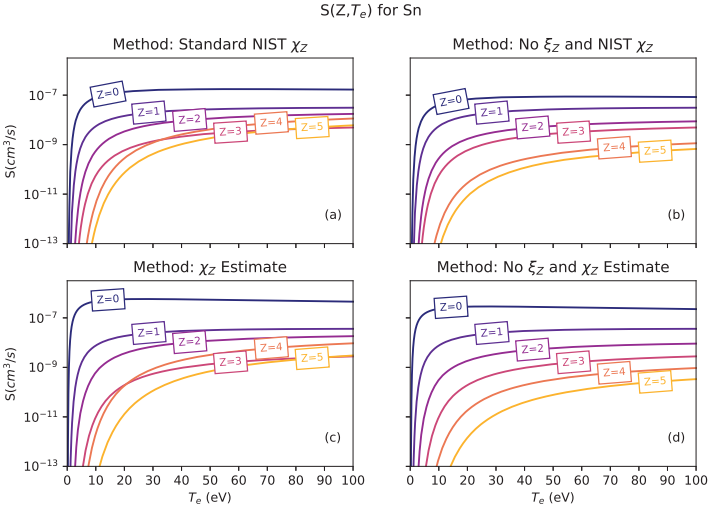

Figure 3. Plots of the collisional ionization rate coefficient for neutral Sn to Sn^{5+}. Each plot was made using Equation (4) without any changes with the NIST χ_Zs (**a**), without the orbital occupancy term, ξ_Z (**b**), with the estimated ionization energies from Equation (7) (**c**), and with the estimated ionization energies and without ξ_Z (**d**).

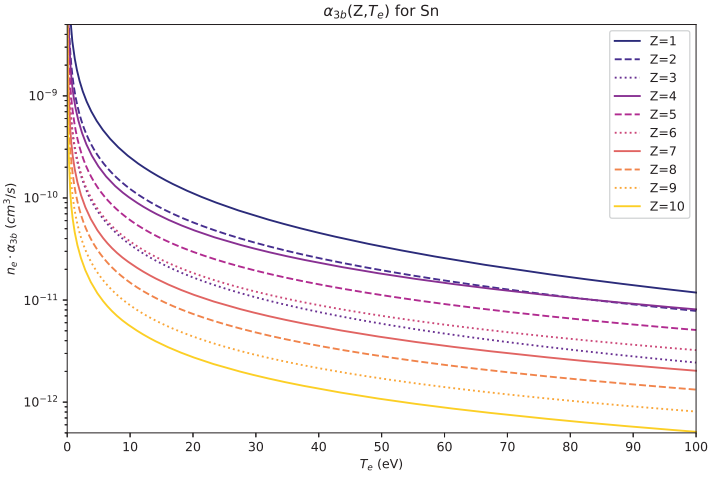

Figure 4. A plot of the 3-body recombination rate coefficient for Sn made with NIST χ_Zs and ξ_Z included. Here the Sn^{3+} curve is not in the same order of charge as the other curves, and is instead between the Sn^{6+} and Sn^{7+} curves. The Sn^{2+} curve can also be seen crossing the Sn^{4+} curve.

One final consideration for Sn was the population behavior of ion stages with very few to no electrons remaining, which corresponds to the far right side of the plots in Figure 2. Without the $\frac{1}{3}$ correction to Equation (5) and using the NIST χ_Zs, with or without the occupancy factor (ξ_Z), the peak population of the final stage ($Z = 50^+$) was smaller than the three preceding stages ($Z = 49^+$, 48^+, and 47^+). It would be expected that at sufficiently high temperatures bare ions would be the dominate species in the plasma. When the $\frac{1}{3}$ correction was used with the NIST χ_Zs, the final stage had a higher peak population than the three lower charged stages, as shown in Figure 2a. In all cases using the CT χ_Zs, the peak population of the final stage exceeded those of the neighboring states. Nevertheless, the improved behavior of the model using the NIST χ_Zs, when $\frac{1}{3}$ (rather than $\frac{1}{2}$) was used, supports the adoption of the standard (as opposed to the traditional) model used for most of the work described here.

4.2. Common Trends Observed across the Periodic Table

The Sn plots showed many of the common trends observed in the peak fractional population and rate coefficient plots obtained for other elements investigated using the NIST χ_Zs. In particular, the peak fractional population plots for other elements also exhibited ionization bottleneck discrepancies, peaks occurring before filled outermost subshell configurations or dips at these locations. For He-like and Ne-like configurations, these discrepancies were not seen throughout the elements examined. Instead, the expected ionization bottleneck was observed, with the peak population of these stages being greater than both of their neighbors. As atomic number increased though, the peak population of the preceding neighbor ($Z-1$) of the Ne-like ionization bottlenecks increased with respect to the bottleneck's peak population. At Ru ($Z_A = 44$), the peak population before the Ne-like configuration exceeded the ionization bottleneck, leading to what is observed for Sn in Figure 2a. While this trend was also seen for the He-like bottlenecks, for heavier elements the ion stages themselves went outside of the range of the plot, due to insufficient computing power and the need to maintain good resolution at lower temperatures. When the ξ_Z term was removed, the peaks corresponding to ionization bottlenecks shifted to ion stages with full outermost orbitals.

The CT χ_Zs also produced discrepancies throughout the elements examined. However, there were more dips at the number of electrons for a full outermost orbital than observed using the NIST χ_Zs. This difference was often seen at lower numbers of electrons, namely He-like and Ne-like configurations. Removing ξ_Z while using the CT χ_Zs did not produce expected ionization bottlenecks. Instead, the peaks and dips were flattened, as shown in Figure 2b.

As with Sn, for the rate coefficient plots, generated using the NIST χ_Zs, the curves tended to group according to their configurations' outermost subshell. The rate coefficients also decreased or increased as ionization increased as described previously. In some cases the curves of ion stages with the same outermost electron orbital would cross, like with Sn; and no connection between the crossing point and the peak populations of the crossed curves could be found. As with Sn, in other cases one curve would not be in the ionization order for the three-body recombination plots. Again, no exceptions were observed in the radiative recombination curves. When the occupancy (ζ_Z) was removed, the exceptions seen before using the standard method were no longer present, and the grouping of curves for the collisional ionization and three-body recombination curves became more distinct, as was observed for Sn.

In comparing the NIST and CT χ_Zs, using the CT values produced the same discrepancies of crossing and out of order curves. The difference between the two methods was that the clustering of ionization stages based on the outermost electron orbital was diminished if not completely lost, when using the CT χ_Zs. The observations for Sn, when ξ_Z was removed, was the common trend. The curves remained in the increasing ionization order, but were not clustered; and the difference between curves appeared to be slowly decreasing.

Heavier elements continued to show the previously described trends; however, once ground state configurations have electrons in the $4f$ orbital ($Z_A \geq 58$), additional complications arise. These complications are mainly seen in configurations where the now occupied $4f$ orbital begins to be emptied and $4f$ contraction becomes relevant.

4.3. Pb ($Z_A = 82$)

To illustrate the difference in behavior between the lighter elements and the lanthindes or heavier elements, Figure 5 shows peak fractional population plots for Pb, which has a ground state electronic configuration of $[Xe]4f^{14}5d^{10}6s^26p^2$. Continuing to use the standard electron removal method, the peak corresponding to the ionization bottleneck for an outermost electron configuration of $4f^{14}5s^25p^6$ should occur at Pb^{14+} (Er-like, 68 electrons). It is clear from Figure 5a that using the standard CR model with NIST χ_Zs produced an ionization bottleneck at a charge state Pb^{13+} rather than Pb^{14+}. This discrepancy vanishes when the ξ_Z is removed. However, the entire region between between the Pb^{36+} ion stage (Pd-like), which corresponds to a full outermost $4d$ subshell, and Pb^{14+} has no obvious ionization bottlenecks associated with the $4f$, $5s$, or $5p$ subshells. Using the occupancies (ζ_Z), there is a dip at Pb^{22+} (Nd-like, 60 electrons) indicating a possible bottleneck, since this matches the discrepancies described previously for Sn and is observed for the Kr-like and Pd-like ion stages for Pb in Figure 5a. This dip could correspond to a full outermost $4f$ subshell after the $5s$ and $5p$ electrons are removed. Furthermore for the CT χ_Zs, the dips observed at the expected bottlenecks are deeper than those observed for lighter elements. These additional observations from the Pb plots were common to period 6 elements with $Z_A \geq 72$ (transition metals and heavier elements).

The lanthanides exhibited the same ionization bottleneck discrepancies described for lighter elements up to Pd-like configurations (46 electrons), as discussed for Pb. At ion stages with more electrons than the Pd-like peak population trends varied, being sensitive to the ordering of shells from which electrons are stripped. This variation was most likely due to $4f$ contraction [21,22], since the value of ξ_Z was ambiguous as the outermost subshell was no longer easily determined [22]. In other words, due to the contraction of the $4f$ orbital, ions with the same number of electrons as Xe are no longer likely to exhibit closed-shell behaviour as the ground state configuration corresponds to a mixture of open $5p$ and open $4f$ shells. However, if the ξ_Z term is removed this issue becomes moot.

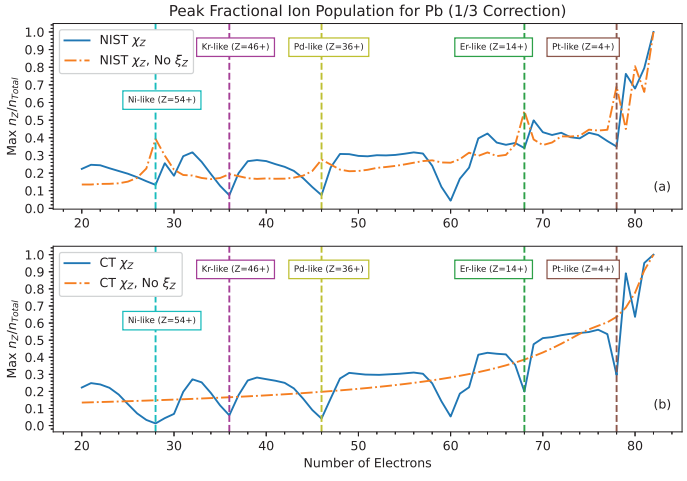

Figure 5. Plots of the peak fractional ion population Pb, calculated with the standard CR model using Equation (3) (solid lines), and from the standard CR model without the ξ_Z term (dashed lines). Two different χ_Zs were used, the NIST values [20] (**a**) and the estimated values from Equation (7) (**b**). The vertical lines mark noble gas configurations and configurations whose outermost subshell is a filled nd^{10} subshell. The Er-like line corresponds to the electronic configuration: [Xe]$4f^{14}$.

4.4. Gd ($Z_A = 64$) Comparison

In order to further emphasize the importance of ξ_Z and χ_Z, an attempt was made to reproduce an ion distribution plot for Gadolinium ($Z_A = 64$, [Xe]$4f^7 5d^1 6s^2$) from another work [8]. The exact distribution could not be reproduced, but the closest agreement was achieved using the NIST χ_Zs, with no ξ_Z term, and without the $\frac{1}{3}$ correction to the recombination term. As described above, the removal of the occupancy term automatically negates the need to consider $4f$ contraction and the ordering of shells. The resulting plot is shown in Figure 6. In this plot ionization bottlenecks can be seen at Gd^{3+}, Gd^{11+}, and Gd^{18+}. Gd^{3+} corresponds to the removal of the $5d^1$ and $6s^2$ electrons, whilst Gd^{18+} corresponds to a full outermost $4d$ subshell with the electronic configuration [Kr]$4d^{10}$ [22], so that these two are bottlenecks as expected. Gd^{11+} falls into the region where the ground configurations have both open $5p$ and open $4f$ shells [22], where the ground state configuration is given as [Kr]$4d^{10}5s^2 4f^5$. This bottleneck could be attributed to the removal of all the $5p$ electrons, but it is important to keep in mind that the corresponding configurations for Gd^{10+} and Gd^{9+} are [Kr]$4d^{10}5s^2 4f^6$ and [Kr]$4d^{10}5s^2 5p^2 4f^5$ respectively [22]. It is noteworthy that the Gd^{11+} bottleneck is much less distinct than those for Gd^{3+} and Gd^{18+}, this being directly associated with the complex, mixed nature of the ground state configurations for ion stages in this range of charge states.

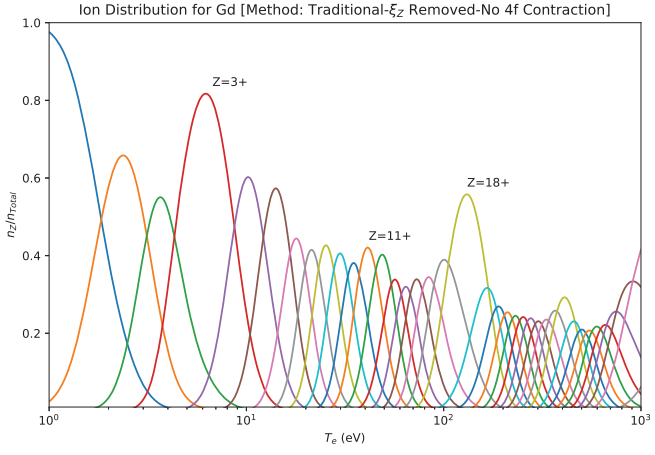

Figure 6. A Gd ion distribution generated using the traditional CR model by Colombant and Tonon using the NIST χ_Zs, with no ξ_Z term, and without the $\frac{1}{3}$ correction. Since the ξ_Z was removed, whether or not $4f$ contraction is taken into account produces the same distribution. Here ion stages are denoted by the different colored curves, and the 3^+, 11^+, and 18^+ stages are marked, due to the observed ionization bottlenecks.

4.5. Overall Findings

The effect of the ξ_Z term within Equation (3) was investigated by comparing when the term was set to 1, effectively removing the term, and when the term was used normally. This effect was investigated using both the NIST χ_Zs and the CT χ_Zs. Using the NIST χ_Zs and removing ξ_Z produced rate coefficient plots, ion distributions, and consequently peak fractional population plots that better supported the theory of ionization bottlenecks. In other words, given the current availability of accurate ionization energy data, which were not accessible when the CR model was developed [5], it is now better to use actual ionization energies rather than to estimate them and subsequently correct for quantum effects with an occupancy factor. There is of course no physical justification for using the occupancy factor with the NIST χ_Zs. ξ_Z was probably introduced in an attempt to mitigate against the continuous nature of the expression used for the ionization potentials (Equation (7)) in the original CR model [5].

Examining the results using the NIST χ_Zs, it was found that He-like and Ne-like configurations were clearly shown to be ionization bottlenecks, having peak populations greater than both the ion stage before (Z−1) and after (Z+1). However, ion stages corresponding to full outermost configurations with larger n (e.g. Ar-like, Kr-like configurations) had peak populations lower than at least one neighbor, indicating no ionization bottleneck at the anticipated configuration. Removing ξ_Z caused these ion stages to then become ionization bottlenecks. Figure 2a. and the region below 60 electrons in Figure 5a are some examples of this. Therefore, with the NIST χ_Zs, the ξ_Z term seems to be the cause of the discrepancies between the charge states of observed and expected ionization bottleneck peaks.

These results suggest that the ξ_Z term could have been an early correction factor to help account for the unrealistic smoothness of the estimated χ_Zs. Equation (7) models processes that are quantum mechanical in nature; therefore, a term to account for an ion's quantum state, (i.e., electronic configuration), could be needed. The introduction of such a term was discussed in the sources for Equation (4) [13,29,30]. However, the ion distributions for C and U ($Z_A = 92$) presented by Colombont and Tonon [5] do not appear to have been made using the estimated χ_Zs with the occupancy factor, since the plots were not reproduced in the present study using these parameters. The C distribution

is close to one that was generated using the NIST χ_Zs with no occupancy factor. This suggests that Colombont and Tonon [5] may have used experimentally determined χ_Zs when they were available. This difference between the plots demonstrates the value of carefully considering what χ_Zs are used in plasma models. In addition to this, the removal of ξ_Z, with the use of the CT estimated χ_Zs, demonstrates the importance of utilizing the correct χ_Zs, since under these conditions all bottleneck features are removed (as shown in Figure 2b) instead of producing the expected ionization bottlenecks.

Furthermore, within the rate coefficient plots, for some elements an ion stage curve was out of the commonly observed ion stage order. By removing ξ_Z this order discrepancy was also removed. Some ion stage curves would also cross others. No reason could be found for this sort of crossing to occur, and when ξ_Z was removed the curve crossing was no longer observed. Additionally, ion stages began to group according to outermost electron orbital. An example of each of these trends is shown in Figure 3a,b. Equations (4), (6), and (8) indicate that without the ξ_Z factor, χ_Z is the only other variable for a given temperature (T_e) within the rate coefficient equations and therefore the only influence on the ion stage distributions for a fixed n_e. The grouping of ion stages according to the outermost electronic orbital, which are observed when the NIST χ_Zs are used with no occupancy factor, makes sense as χ_Z most drastically changes between ion stages with different outermost subshells. These larger differences are in turn the reason for ionization bottlenecks [25], and therefore the observed grouping of ion stages also supports the use of experimental χ_Zs, with no ξ_Z term. This sole reliance of the rate equations, and thus the CR model, upon χ_Z underlines the benefit of using the real values of χ_Z, which are now available [20].

5. Conclusions

In conclusion, the importance of careful consideration of the values for the ionization energies (χ_Z) and occupancy factors (ξ_Z) within the traditional CR model proposed by Colombant and Tonon [5] has been shown. This point was emphasised by consideration of the charge states at which ionization bottlenecks occur. The effect of a number of different variants of the CR model were explored, revealing unphysical behaviour in rate coefficients and the associated occurrence of ionization bottlenecks at unexpected charge states. It was found that eliminating ξ_Z, removed these discrepancies, when using NIST χ_Z values. However, when using the CT estimated χ_Z values, all features indicating any ionization bottlenecks were removed if the occupancy factor was not included. A minor correction from [14,24] to the radiative recombination rate coefficient term was also found. This correction being the change of a $\frac{1}{2}$ power to a $\frac{1}{3}$ power in Equation (5).

The continuation of this work will be to compare the generated ion distributions to experimental plasmas. In this comparison, an investigation of ionization bottlenecks could also be done, since they have been the impetus for the current work with extremely visible discrepancies in the traditional CR model plots. Furthermore, the addition of the photoionization, dielectronic recombination and autoionization rate coefficients to the CR model could be tested.

Author Contributions: All authors contributed to conceptualization, writing—review and editing, and discussion of the data. Under the supervision of E.S., software modeling, investigation, and writing—original draft preparation was carried out by N.L.W. All authors have read and agreed to the published version of the manuscript.

Funding: This research received no external funding. N.L.W. acknowledges the support of the UCD Scholarship in Research and Teaching.

Conflicts of Interest: The authors declare no conflict of interest.

References

1. Kaiser, J.; Novotný, K.; Martin, M.Z.; Hrdlička, A.; Malina, R.; Hartl, M.; Adam, V.; Kizek, R. Trace elemental analysis by laser-induced breakdown spectroscopy—Biological applications. *Surf. Sci. Rep.* **2012**, *67*, 233–243. [CrossRef]
2. Versolato, O.O. Physics of laser-driven tin plasma sources of EUV radiation for nanolithography. *Plasma Sources Sci. Technol.* **2019**, *28*, 83001. [CrossRef]

3. Cross, J.E.; Reville, B.; Gregori, G. Scaling of magneto-quantum-radiative hydrodynamic equations: From laser-produced plasmas to astrophysics. *Astrophys. J.* **2014**, *795*, 59. [CrossRef]
4. O'Sullivan, G.; Li, B.; D'Arcy, R.; Dunne, P.; Hayden, P.; Kilbane, D.; McCormack, T.; Ohashi, H.; O'Reilly, F.; Sheridan, P.; et al. Spectroscopy of highly charged ions and its relevance to EUV and soft X-ray source development. *J. Phys. B At. Mol. Opt. Phys.* **2015**, *48*, 144025. [CrossRef]
5. Colombant, D.; Tonon, G.F. X-ray emission in laser-produced plasmas. *J. Appl. Phys.* **1973**, *44*, 3524–3537. [CrossRef]
6. Min, Q.; Su, M.; Wang, B.; Cao, S.; Sun, D.; Dong, C. Experimental and theoretical investigation of radiation and dynamics properties in laser-produced carbon plasmas. *J. Quant. Spectrosc. Radiat. Transf.* **2018**, *210*, 189–196. [CrossRef]
7. Maguire, O.; Kos, D.; O'Sullivan, G.; Sokell, E. EUV spectroscopy of optically thin Ge VI-XI plasmas in the 9–18 nm region. *J. Quant. Spectrosc. Radiat. Transf.* **2019**, *235*, 250–256. [CrossRef]
8. Otsuka, T.; Kilbane, D.; White, J.; Higashiguchi, T.; Yugami, N.; Yatagai, T.; Jiang, W.; Endo, A.; Dunne, P.; O'Sullivan, G. Rare-earth plasma extreme ultraviolet sources at 6.5–6.7 nm. *Appl. Phys. Lett.* **2010**, *97*, 111503. [CrossRef]
9. Wubetu, G.A.; Kelly, T.J.; Hayden, P.; Fiedorowicz, H.; Skrzeczanowski, W.; Costello, J.T. Recombination contributions to the anisotropic emission from a laser produced copper plasma. *J. Phys. B At. Mol. Opt. Phys.* **2020**, *53*, 65701. [CrossRef]
10. Su, M.G.; Wang, B.; Min, Q.; Cao, S.Q.; Sun, D.X.; Dong, C.Z. Time evolution analysis of dynamics processes in laser-produced Al plasmas based on a collisional radiative model. *Phys. Plasmas* **2017**, *24*, 13302. [CrossRef]
11. Sharma, A.; Slipchenko, M.N.; Shneider, M.N.; Wang, X.; Rahman, K.A.; Shashurin, A. Counting the electrons in a multiphoton ionization by elastic scattering of microwaves. *Sci. Rep.* **2018**, *8*, 1–10. [CrossRef]
12. Lu, H.; Su, M.; Min, Q.; Cao, S.; He, S.; Dong, C.; Fu, Y. Effect of dielectronic recombination on charge-state distribution in laser-produced plasma based on steady-state collisional-radiative models. *Plasma Sci. Technol.* **2020**, *22*, 105001. [CrossRef]
13. McWhirter, R.W.P. Spectral Intensities. In *Plasma Diagnostic Techniques*; Huddlestone, R.H., Leonard, S.L., Eds.; Academic Press Inc.: New York, NY, USA, 1965; pp. 201–264.
14. Seaton, M.J. Radiative Recombination of Hydrogenic Ions. *Mon. Not. R. Astron. Soc.* **1959**, *119*, 81–89. [CrossRef]
15. Shimada, Y.; Kawasaki, H.; Watanabe, K.; Hara, H.; Anraku, K.; Shoji, M.; Oba, T.; Matsuda, M.; Jiang, W.; Sunahara, A.; et al. Optimized highly charged ion production for strong soft X-ray sources obeying a quasi-Moseley's law. *AIP Adv.* **2019**, *9*, 115315. [CrossRef]
16. Sasaki, A.; Sunahara, A.; Nishihara, K.; Nishikawa, T. Investigation of the ionization balance of bismuth-to-tin plasmas for the extreme ultraviolet light source based on a computer-generated collisional radiative model. *AIP Adv.* **2016**, *6*, 105002. [CrossRef]
17. Lee, K.; Lee, Y.; Jo, S.; Chung, C.W.; Godyak, V. Characterization of a side-type ferrite inductively coupled plasma source for large-scale processing. *Plasma Sources Sci. Technol.* **2008**, *17*, 015014. [CrossRef]
18. Wu, T.; Higashiguchi, T.; Li, B.; Arai, G.; Hara, H.; Kondo, Y.; Miyazaki, T.; Dinh, T.H.; Dunne, P.; O'Reilly, F.; et al. Spectral investigation of highly ionized bismuth plasmas produced by subnanosecond Nd:YAG laser pulses. *J. Phys. B At. Mol. Opt. Phys.* **2016**, *49*, 35001. [CrossRef]
19. Li, B.; Otsuka, T.; Sokell, E.; Dunne, P.; O'Sullivan, G.; Hara, H.; Arai, G.; Tamura, T.; Ono, Y.; Dinh, T.H.; et al. Characteristics of laser produced plasmas of hafnium and tantalum in the 1–7 nm region. *Eur. Phys. J. D* **2017**, *71*, 1–9. [CrossRef]
20. Kramida, A.; Ralchenko, Y.; Reader, J.; NIST ASD Team. *NIST Atomic Spectra Database (Ver. 5.7.1)*; National Institute of Standards and Technology: Gaithersburg, MD, USA, 2019. Available online: https://physics.nist.gov/asd (accessed on 12 February 2020).
21. Carroll, P.K.; O'Sullivan, G. Ground-state configurations of ionic species I through XVI for Z = 57−74 and the interpretation of $4d-4f$ emission resonances in laser-produced plasmas. *Phys. Rev. A* **1982**, *25*, 275–286. [CrossRef]
22. Kilbane, D.; O'Sullivan, G. Ground-state configurations and unresolved transition arrays in extreme ultraviolet spectra of lanthanide ions. *Phys. Rev. A At. Mol. Opt. Phys.* **2010**, *82*. [CrossRef]
23. Kolb, A.C.; McWhirter, R.W.P. Ionization Rates and Power Loss from θ-Pinches by Impurity Radiation. *Phys. Fluids* **1964**, *7*, 519–531. [CrossRef]

24. Menzel, D.H.; Pekeris, C.L. Absorption Coefficients and Hydrogen Line Intensities. *Mon. Not. R. Astron. Soc.* **1935**, *96*, 77–110. [CrossRef]
25. Attwood, D.T.; Sakdinawat, A.; Geniesse, L. *X-rays and Extreme Ultraviolet Radiation: Principles and Applications*, 2nd ed.; Cambridge University Press: Cambridge, UK, 2016. [CrossRef]
26. Otsuka, T.; Higashiguchi, T.; Yugami, N. Rare-Earth Plasma Beyond Extreme Ultraviolet (BEUV) Sources at 6.x nm. *Electron. Commun. Jpn.* **2015**, *98*, 52–58. [CrossRef]
27. Higashiguchi, T.; Otsuka, T.; Yugami, N.; Jiang, W.; Endo, A.; Dunne, P.; Li, B.; O'Sullivan, G. *Shorter-Wavelength Extreme-UV Sources below 10 nm*; SPIE: Washington, DC, USA, 2011. [CrossRef]
28. White, J.; Hayden, P.; Dunne, P.; Cummings, A.; Murphy, N.; Sheridan, P.; O'Sullivan, G. Simplified modeling of 13.5 nm unresolved transition array emissionof a Sn plasma and comparison with experiment. *J. Appl. Phys.* **2005**, *98*, 113301. [CrossRef]
29. Drawin, H.W. Zur formelmäßigen Darstellung der Ionisierungsquerschnitte gegenüber Elektronenstoß. *Zeitschrift für Physik* **1961**, *164*, 513–521. [CrossRef]
30. Thomson, J.J. XLII. Ionization by moving electrified particles. *Lond. Edinb. Dublin Philos. Mag. J. Sci.* **1912**, *23*, 449–457. [CrossRef]

MDPI
St. Alban-Anlage 66
4052 Basel
Switzerland
Tel. +41 61 683 77 34
Fax +41 61 302 89 18
www.mdpi.com

Atoms Editorial Office
E-mail: atoms@mdpi.com
www.mdpi.com/journal/atoms

MDPI
St. Alban-Anlage 66
4052 Basel
Switzerland

Tel: +41 61 683 77 34
Fax: +41 61 302 89 18

www.mdpi.com

ISBN 978-3-0365-2431-3